THEORY OF METAL-INSULATOR-SEMICONDUCTOR (MIS) AND SEMICONDUCTOR-INSULATOR-SEMICONDUCTOR (SIS) SOLAR CELLS

By

RAJENDRA SINGH, B.Sc., M.Sc.

A Thesis

Submitted to the School of Graduate Studies

in Partial Fulfilment of the Requirements

for the Degree

Doctor of Philosophy

McMaster University

April 1979

© RAJENDRA SINGH 1979

THEORY OF MIS AND SIS SOLAR CELLS

DOCTOR OF PHILOSOPHY (1979)
(Physics)

McMASTER UNIVERSITY
Hamilton, Ontario

TITLE: Theory of Metal-Insulator-Semiconductor (MIS) and Semiconductor-Insulator-Semiconductor (SIS) solar cells

AUTHOR: Rajendra Singh, B.Sc. (Agra University)
M.Sc. (Meerut University)
M.Sc. (Dalhousie University)

SUPERVISOR: Professor J. Shewchun

NUMBER OF PAGES: xxii, 266

ABSTRACT

This thesis describes the theory of tunnel metal-insulator-semiconductor (MIS) and semiconductor-insulator semiconductor (SIS) solar cells. In both cases, the thickness of the insulating layer is < 40 Å and the current flow has been described by quantum mechanical tunneling process. The base-semiconductor in both cases is single-crystal and non-degenerate.

The introduction of a thin insulating layer [< 16 Å in the case of Al-SiO_x-(p-type)Si solar cells] eliminates the pinning effect observed in Schottky barrier diodes, so that the minority carrier quasi-Fermi level is now pinned to the Fermi level in the metal to produce a higher open-circuit voltage. Recent experimental work on oxide-semiconductor/base-semiconductor solar cells indicates that the performance of such devices also could be dramatically controlled by the presence of a thin interfacial layer or insulator. We have developed a mathematical model to calculate the photovoltaic respose of the MIS diodes. The theory of SIS solar cells is an expansion of the MIS solar cell theory, where the metal is now allowed the property of a variable band gap which can be set at any value from zero to several electron volts. The theory is valid when the top semiconductor is an amorphous or heavily doped (degenerate) wide-gap oxide-semiconductor. The SIS model is capable of explaining why some oxide-semi-

conductor/base - semiconductor solar cells indicated good performance of such heterojunction devices while others show poor performance.

Our work shows that optimized MIS and SIS solar cells can have efficiencies comparable to p-n junction solar cells. The effect of various parameters on the device performance has been studied. The most important parameters are the thickness of the insulating layer and the metal work function.

The theory of tunnel MIS solar cells has been compared with the available experimental data and an excellent agreement is observed. The open-circuit voltage below a certain thickness of insulating layer (SiO_x) shows slight deviation from the theory. This experimental observation has been accounted for by the presence of pin-holes associated with ultra-thin oxides and a composite model of Schottky barrier and MIS solar cells has been developed. Based on this model, we have calculated the complex dielectric constant of SiO_x as a function of its thickness. Measurement of dark I-V characteristics as a function of temperature confirms the pseudo p-n junction behaviour of MIS solar cells and discards thermionic emission models.

The calculation of SIS solar cells has been compared with the experimental work. The measurement on the temperature effect, intensity effect, insulator thickness effect and the spectral response supports the SIS model. We have also discussed various main loss mechanisms associated with SIS solar cells. This includes the transmission-reflection loss from the top layer, recombination in the depletion layer, open-circuit lowering

and series and shunt resistance losses. At the end of the thesis, we have shown that simple methods based on the electrical measurements of oxide-semiconductor/base-semiconductor systems often lead to incorrect values for the electron affinity of oxide-semiconductors.

ACKNOWLEDGMENT

I gratefully acknowledge the supervision and guidance of my thesis supervisor, Professor J. Shewchun. The help of various colleagues, namely K. Rajkanan, J. St. Pierre, M. Spitzer and D. Burk is acknowledged with many thanks. It is a pleasure to acknowledge C. D. Bennewitz who helped in the preparation of the final draft. The assistance of A. Kazandjian for the art work is gratefully acknowledged. The help of Prof. J. Dubow of Colorado State University in providing experimental data on ITO/Si solar cells is acknowledged with many thanks. Mrs. Helen Kennelly typed the final draft very efficiently. I am grateful to her for typing the thesis, as well as for the love and affection shown to me during my stay at McMaster. The financial assistance of McMaster University and the funding provided by the Department of Energy, U.S.A. and the National Research Council of Canada is also gratefully acknowledged. I wish to express regards to my parents, brothers, sister and a large number of relatives and friends who have given me constant encouragement and moral support during the course of this work. Finally, I wish to thank my wife Reeta Singh for her understanding and assistance in many ways. She also typed the first draft of this thesis, and I dedicate this work to her.

TABLE OF CONTENTS

CHAPTER		PAGE
1	INTRODUCTION	1
2	GENERAL DESCRIPTION OF SOLAR CELLS AND APPROACH TO PROBLEM FORMULATION	
	2.1 Introduction	7
	2.2 Phenomenological Description and Electrical Characteristics of Solar Cells	8
	2.3 Limitations of Phenomenological Models and the Exact Calculational Method of Solar Cells	15
	2.4 Outline of the Method Used to Model MIS and SIS Solar Cells	17
3	THEORETICAL CALCULATIONS OF METAL-INSULATOR-SEMICONDUCTOR (MIS) AND SEMICONDUCTOR-INSULATOR-SEMICONDUCTOR (SIS) SOLAR CELLS	
	3.1 Introduction	20
	3.2 General Remarks on MIS and SIS Solar Cells	22
	3.2.1 MIS solar cells	22
	3.2.2 SIS Solar Cells	25
	3.3 Description of MIS and SIS Solar Cell Model	35
	3.3.1 Background Material	35
	3.3.2 Mathematical Model	37
	3.3.3 Effect of Wide Band Gap of Oxide-Semiconductor on SIS Tunnel Diode	43
		46
	3.3.4 Physical Description of MIS and SIS Solar Cells	

CHAPTER PAGE

3.3.5 Dark I-V Characteristics of MIS and SIS Solar Cells 54

3.4 Effect of Various Parameters on the Performance of MIS and SIS Solar Cells 60

3.4.1 Effect of Interfacial layer thickness 60

3.4.2 Effect of Substrate Resistivity 71

3.4.3 Effect of Surface States and Surface Charge 76

3.4.4 Effect of Metal and Oxide-semiconductor Work Function 80

3.4.5 Effect of Temperature 92

3.4.6 Effect of Intensity 99

3.4.7 Effect of Minority Carrier Life Time 105

3.4.8 Effect of Crystal Orientation 107

3.4.9 Effect of Semiconductor Band-gap 107

3.4.9.1 ITO/InP SIS Solar Cell 108

3.4.9.2 ITO/GaAs SIS Solar Cell 117

3.5 Spectral Response of MIS and SIS Solar Cells 118

3.6 Capacitance Voltage (C-V) and Conductance Voltage (G-V) Characteristics of MIS and SIS Solar Cells 121

3.7 Summary 129

4 COMPARISON OF MIS SOLAR CELL THEORY WITH EXPERIMENTAL WORK AND OTHER THEORIES AND Si-SiO_x INTERFACE STUDY

CHAPTER PAGE

4.1 Introduction 131

4.2 Comparison with Experimental Work 132

4.2.1 Effect of Insulator Thickness 132

4.2.2 Effect of Substrate Resistivity 143

4.2.3 Effect of Metal Work Function 146

4.2.4 Effect of Temperature 149

4.2.5 Effect of Crystal Orientation 156

4.2.6 Spectral Response 159

4.3 Comparison with MIS and Schottky Barrier Calculations 161

4.3.1 Comparison with Other MIS Solar Cell Models 161

4.3.2 Comparison with Schottky Barrier Solar Cell Calculations 162

4.4 Si-SiO_x Interface Study 163

4.4.1 Introduction 163

4.4.2 Effects of Oxide Thickness on Open-Circuit Voltage 166

4.4.3 Composite Model of MIS Solar Cells 171

4.4.4 Dielectric Properties of the Interface 176

4.5 Summary 178

5 COMPARISON OF SIS SOLAR CELL THEORY WITH EXPERIMENTAL WORK

5.1 Introduction 181

5.2 Effect of Various Parameters on SIS Solar Cell Performance 182

5.2.1 Existence of the Interfacial Layer 182

CHAPTER PAGE

5.2.2 Effect of Insulator Thickness 182

5.2.3 Effect of Temperature 183

5.2.4 Effect of Intensity 198

5.2.5 Effect of Oxide-Semiconductor Work Function 201

5.3 Spectral Response 204

5.4 Loss Mechanism in SIS Solar Cells 205

5.4.1 Transmission-Reflection Loss Associated with Oxide-Semiconductor 207

5.4.2 Recombination in the Surface Depletion Layer 211

5.4.3 Lowering of the Open-Circuit Voltage 217

5.4.4 Series and Shunt Resistance Losses 217

5.5 The Importance of the Electron Affinity of Oxide-Semiconductors 220

5.6 Summary 226

6 CONCLUSION 229

APPENDIX A EFFECT OF SERIES RESISTANCE ON THE SOLAR CELL PERFORMANCE 234

APPENDIX B SILICON PARAMETERS AND SOLAR SPECTRUMS USED IN THE CALCULATIONS 239

APPENDIX C EXPRESSION FOR THE OPEN-CIRCUIT VOLTAGE OF A COMBINED MODEL OF THE SCHOTTKY BARRIER AND MIS SOLAR CELLS 251

REFERENCES 254

LIST OF TABLES

TABLE		PAGE
3.1	Some Properties of Base-Semiconductors and Oxide-Semiconductors	29
3.2	Typical Properties of ITO Films	34
3.3	Effect of the Magnitude of the Wide Band-Gap Semiconductor on SIS Tunnel Currents. No Surface States are Considered	44
3.4	Effect on the Magnitude of the Wide Band-Gap Semiconductor on SIS Tunnel Currents. Surface States are Present at the Insulator-Base-Semiconductor Interface.	45
3.5	Numerical Values Assigned to System Parameters for Calculating Si MIS and SIS Solar Cell Performance	59
3.6	Desired Work Function of Metals and Highest Possible AM1 Efficiency for some MIS Solar Cells	83
3.7	Desired Electron Affinity of Oxide-Semiconductors and Highest Possible AM1 Efficiency for Some Base-Semiconductors	84
3.8	Some Properties of SiO_2 and P_2O_5	114
3.9	Numerical Values Assigned to System Parameters for Calculating ITO-InP SIS Solar Cell Performance	115
3.10	Numerical Values Assigned to System Parameters for Calculating ITO-GaAs SIS Solar Cell Performance	119
4.1	Experimental Data on Single Crystal Si and GaAs MIS Solar Cells	147
4.2	Measured n values and Saturation Currents as a Function of Temperature for Al-SiO_x-(p-type)Si Solar Cells	154

TABLE		PAGE
4.3	Estimation of the Width of Transition Layer at the Interface by Various Diagnostic Techniques	164
5.1	Measured n Values and Saturation Currents as a Function of Temperature for ITO on (0.2 Ω-cm) p-type Si Diode No. 12-G	187
5.2	Measured n Values and Saturation Currents as a Function of Temperature for ITO on (1.0 Ω-cm) p-type Si Diode No. 170	191
5.3	Experimental Results on SIS Solar Cells	202
5.4	List of Some Anti-reflection Coating Materials and Their Index of Refraction	210
B1	Parameters Used in the Calculation of Si Mobility	240
B2	AM0, AM1, AM2 Spectral Distributions	243

LIST OF FIGURES

FIGURE		PAGE
2.1	Equivalent circuit of a solar cell, including series and shunt resistance.	9
2.2	I-V characteristics of a solar cell with and without illumination.	12
3.1	Simple equilibrium energy-band diagram of the p-type MIS solar cell.	24
3.2	Schematic energy-band diagram for a p-type tunnel MIS solar cell when a forward bias V_a is applied under zero illumination.	26
3.3	Simple representation of the interface that controls electrical characteristics of Schottky barrier and MIS solar cells.	27
3.4	Simple equilibrium energy-band diagram of the ITO-SiO_x-(p-type) Si tunnel diode system.	32
3.5	Schematic energy band diagram of the MIS tunnel diode system with a p-type semiconductor region.	48
3.6	Schematic energy-band diagram for a p-type tunnel SIS solar cell when a forward bias V_a is applied under zero illumination.	50
3.7	Energy band diagram of ITO-SiO_x-(p-type) Si solar cell near the maximum power condition.	51

FIGURE PAGE

FIGURE		PAGE
3.8	Computed dark I-V characteristics of the MIS and SIS solar cells.	55
3.9	Assumed distribution of surface states across the energy band gap of silicon.	58
3.10	Computed effect of insulator thickness on the conversion efficiency of silicon MIS and SIS solar cells.	62
3.11	The variation of short-circuit current density J_{sc}, open-circuit voltage V_{oc}, and fill factor as a function of insulator thickness for silicon MIS and SIS solar cells.	64
3.12	Schematic energy-band diagram for a p-type MIS solar cell under short circuit condition.	68
3.13	Effect of doping density on the conversion efficiency, open-circuit voltage short circuit current density and fill factor of an Al-SiO_x-(p-type)Si solar cell.	72
3.14	Effect of doping density on conversion efficiency of an ITO-SiO_x-(p-type)Si tunnel diode.	73
3.15	The effect of surface state density and insulator charge on conversion efficiency versus insulator thickness on an Al-SiO_x-(p-type)Si solar cell.	79

FIGURE		PAGE
3.16	The effect of insulator charge on conversion efficiency of an Al-SiO_x-(p-type)Si solar cell with surface state density as the variable parameter.	81
3.17	Calculation of efficiency as a function of metal work function of an M-SiO_x-(p-type)Si solar cell.	86
3.18	Effect of metal work function on the open-circuit voltage, short circuit current density and fill factor of an M-SiO_x-(p-type)Si solar cell.	87
3.19	The effect of surface state density and insulator charge on conversion efficiency for various ϕ_{mi} and doping density combinations.	89
3.20	Computed effect of barrier heights variation on the conversion efficiency η, and open-circuit voltage, V_{oc} of an ITO-Si SIS tunnel diode.	91
3.21	Effect of temperature upon the forward dark I-V characteristics of ITO-SiO_x-(p-type)Si tunnel diode.	94
3.22	Effect of temperature upon the reverse dark I-V characteristics of ITO-SiO_x-(p-type)Si tunnel diode.	96

FIGURE | PAGE

3.23 Effect of temperature on the efficiency, open-circuit voltage, short circuit current density and fill factor of an ITO-SiO_x-(p-type)Si solar cell. 97

3.24 Calculated efficiency of nITO-SiO_x-(p-type)Si solar cell as a function of solar intensity with insulator thickness as the variable parameter. 100

3.25 Calculated resistance of the interfacial layer as a function of its thickness. 101

3.26 Calculated efficiency η and fill factor FF of ITO-Si SIS tunnel diodes as a function of solar intensity. 103

3.27 Calculated open-circuit V_{oc}, and short-circuit current density, J_{sc}, of ITO-Si SIS tunnel solar cell as a function of solar intensity. 104

3.28 Effect of minority carrier lifetime on the conversion efficiency of an Al-SiO_x-(p-type)Si solar cell. 106

3.29 Schematic energy-band diagram of the minority carrier ITO-P_2O_5-(p-type)InP tunnel diode system when a forward bias V_a is applied under zero illumination. 112

FIGURE		PAGE
3.30	Computed effect of insulator thickness on conversion efficiency of an ITO-P_2O_5-(p-type)InP tunnel diode under AM2 illumination.	116
3.31	Computed effect of insulator thickness on the conversion efficiency of an nITO-Ga_2O_3-(p-type) GaAs solar cell.	120
3.32	Computed Spectra response (A/W) versus wavelength of an ITO-SiO_x-(p-type)Si solar cell.	122
3.33	Theoretical C-V characteristics of p-type MIS solar cell as a function of insulator thickness.	124
3.34	Theoretical G-V characteristics of p-type MIS solar cell as a function of insulator thickness.	125
3.35	Theoretical C-V characteristics of p-type MIS solar cell as a function of signal frequency.	127
3.36	Theoretical G-V characteristics of p-type MIS solar cell as a function of signal frequency.	128
4.1	The measured variation of efficiency as a function of insulator thickness for an Al-SiO_x-(p-type)Si diode with 0.2 Ω-cm Si.	133
4.2	The measured dependence of J_{sc} as a function of insulator thickness for an Al-SiO_x-(p-type)Si diode with 0.2 Ω-cm Si.	134

FIGURE		PAGE
4.3	The measured dependence of V_{oc} as a function of insulator thickness for an Al-SiO_x-(p-type)Si diode with 0.2 Ω-cm Si.	135
4.4	The measured dependence of V_{oc} as a function of insulator thickness for an Al-SiO_x-(p-type)Si solar cell.	136
4.5	The measured dependence of FF as a function of insulator thickness for an Al-SiO_x-(p-type)Si solar cell.	138
4.6	The measured dependence of FF as a function of insulator thickness for an Al-SiO_x-(p-type)Si solar cell.	139
4.7	The increase in short circuit current density as a function of normalized diffusion length for small area solar cells.	141
4.8	Calculated fill factor of a solar cell as a function of area, with series resistance as the variable parameter.	142
4.9	Measured open circuit voltage of an Al-SiO_x-(p-type)Si solar cell as a function of doping density for an Al-SiO_x-(p-type)Si solar cell.	144
4.10	Measured short circuit current, open-circuit voltage and fill factor as a function of doping density for Si p-n junction solar cells.	145

FIGURE		PAGE
4.11	Experimentally measured forward dark I-V characteristics of Al-SiO_x-(p-type)Si solar cell as a function of temperature.	151
4.12	Theoretical fit to the experimental data of Figure 4.11, using diffusion current dominated tunnel MIS solar cells theory.	155
4.13	Theoretical fit to the experimental data of Figure 4.11, with thermionic emission process as the current conduction mechanism in MIS solar cells.	157
4.14	I-V characteristics under solar illumination for Al-SiO_x-(p-type)Si solar cells of <100> and <111> crystal orientation.	158
4.15	Calculated and measured spectral response of Al-SiO_x-(p-type)Si solar cell.	160
4.16	Experimental and theoretical open circuit voltage of tunnel MIS solar cell as a function of oxide thickness.	167
4.17	Calculated n, k and percent pinhole area of SiO_x as a function of oxide thickness.	167
5.1	Calculated effect of temperature upon the forward dark I-V characteristics of ITO-SiO_x-(p-type)Si tunnel diode.	184

FIGURE		PAGE
5.2	Experimentally measured forward dark forward I-V characteristics of ITO-SiO_x-(p-type)Si solar cells No. 12-G as a function of temperature.	186
5.3	Theoretical fit to the experimental data of Figure 5.2.	189
5.4	Experimentally measured forward dark forward I-V characteristics of ITO-(p-Si) solar cell No. 170.	190
5.5	Theoretical fit to the experimental data of Figure 5.4.	192
5.6	Experimentally measured reverse dark I-V characteristics of ITO-(p-Si) solar Cell No. 170.	193
5.7	Calculated effect of temperature upon the reverse dark I-V characteristics of ITO-SiO_x-(p-type)Si tunnel diode.	195
5.8	Theoretical fit to the experimental data of Figure 5.6.	196
5.9	Reverse current at V_R = 1 volt as a function of temperature for diode No. 170.	197
5.10	Effect of temperature on the efficiency, open-circuit voltage, short-circuit current density and fill factor of n-ITO/p-Si solar cell.	199

FIGURE PAGE

5.11 Experimentally measured effect of intensity on the efficiency, open-circuit voltage, short-circuit current density and fill factor of nITO/p-Si solar cell. 200

5.12 Calculated and experimentally measured spectral response of n-ITO/p-Si solar cell. 206

5.13 Typical transmission and reflection curves for argon sputtered indium-tin-oxide films (10% Sn) of approximately the same thickness (∿ 3000 Å). 208

5.14 Calculated dark I-V characteristics of n-ITO/p-Si tunnel diode with depletion lifetime as the variable parameter. 213

5.15 Calculated conversion efficiency of n-ITO/p-Si SIS solar cell as a function of depletion region lifetime, with bulk lifetime as the variable. 215

5.16 Experimentally measured forward dark I-V characteristics of n-ITO/p-Si solar cell at 298°K. 216

5.17 Calculated resistance of the interfacial layer as a function of its thickness. 219

5.18 Semi-log plots of I_{01}/T^2 and I_{01}/T^3 vs $10^3/T$ for n-ITO/p-Si solar cells. 222

FIGURE | PAGE

5.19 Simple equilibrium energy-band diagram for n-oxide-semiconductor/p-base-semiconductor solar cell, neglecting the presence of an interfacial layer. 224

A1 Calculated effect of series resistance on the short-circuit current density of a solar cell. 235

A2 Effect of series resistance on the fill factor and efficiency of optimized MIS and SIS solar cells. 238

CHAPTER 1

INTRODUCTION

Recent research work on photovoltaic solar energy conversion for large scale terrestrial application indicates that the major handicap is the high cost of solar cells. Possible cost reduction may emerge from the technological breakthrough in the manufacture of solar cells, utilizing polycrystalline or amorphous semiconductors instead of the presently used single-crystal semiconductors. The characteristics of homojunction solar cells are well understood, but such devices are not compatible with non-crystalline semiconductors due to high reverse saturation currents [1]. Other options are heterojunction or surface barrier devices (commonly known as Schottky barrier diodes). The Schottky barrier solar cells are very simple to fabricate, but in the past these devices did not draw much attention due to their lower conversion efficiency. Recent experimental work [2-4] has shown that the presence of a thin interfacial layer or oxide between the metal and the semiconductor of a Schottky barrier can considerably increase the photovoltaic conversion efficiency of such solar cells. The useful range of oxide layers is < 40 Å. These experimental observations can be explained in terms of a tunnel metal-

insulator-semiconductor (MIS) diode that is formed when the interfacial layers are introduced [5].

Recently there have been a number of reports on high efficiency oxide-semiconductor/base-semiconductor solar cells [6-9]. The suitability of an oxide-semiconductor as a conducting window material in heterojunction solar cells is due to its wide-band gap and low sheet resistivity. An examination of the crystal structure, lattice constant and linear coefficients of thermal expansion of the semiconductor components of these heterojunction solar cells shows that they are not particularly compatible and thus not likely to form good devices. In examining the experimental data, it became apparent that the performance of such devices also could be dramatically controlled by the presence of a thin interfacial layer or insulator. The behaviour of these devices can be explained in terms of a semiconductor-insulator-semiconductor (SIS) diode [10].

This thesis is concerned with the theory of metal-insulator-semiconductor (MIS) and semiconductor-insulator-semiconductor (SIS) solar cells. The SIS theory is an expansion of the MIS solar cell theory, where the metal is now allowed the property of a variable bandgap which can be set at any value from zero to several electron volts. The SIS theory is valid for any system where one side of the junction is an amorphous or heavily doped (degenerate) wide-gap oxide semiconductor.

The first portion of this thesis, Chapter 2, describes the general operation of solar cells and the background material related to the formulation of MIS and SIS solar cell theory. The electrical characteristics of and the phenomenological model for solar cells are discussed. The limitations of phenomenological approaches and the exact calculational method for solar cells are described. At the end of this chapter, we have described the approach which has been used to calculate the theoretical performance of MIS and SIS solar cells.

The next portion of this thesis, Chapter 3, is devoted to the theoretical calculations for MIS and SIS solar cells. In Chapter 3, a general picture of MIS and SIS solar cells is presented in the beginning. Without giving any mathematical details, the superior performance of MIS and SIS solar cells over Schottky barrier and heterojunction solar cells is explained. This is followed by the description of the MIS and SIS solar cell model. In the next section, the effect of various parameters on the performance of MIS and SIS solar cells is described. The most important parameters in controlling the conversion efficiency of MIS and SIS solar cells are the top layer work function and the insulator thickness. Theoretically, we have shown that the conversion efficiency of optimum MIS and SIS solar cells can be similar to the p-n junction solar cells. The spectral response of MIS and SIS diodes has also been calculated in this chapter. Since there is no damaged diffusion region near the surface in the MIS and SIS

solar cells, these devices display a superior ultra-violet response compared to p-n junction solar cells. At the end of this chapter the C-V and G-V characteristics of MIS and SIS solar cells have been calculated by using the method of reference 11.

In Chapter 4, the theory of MIS solar cells is compared to the experimental measurements. The effect of insulator thickness on the open-circuit voltage, fill factor and short circuit current density of an Al-SiO_x-(p-type)Si solar cell is compared. The open-circuit voltage data below a certain thickness of insulator (about 13 Å in the case of SiO_x) show slight deviation from the theory. A composite model is developed for non-uniform insulator layers. The model takes into account the pin-holes associated with ultra thin oxides. This model has been used to estimate the complex dielectric constant of SiO_x as a function of its thickness. Dark I-V characteristics of Al-SiO_x-(p-type)Si solar cells as a function of temperature supports the pseudo p-n junction behaviour of MIS solar cells. These results show that the dark current is diffusion limited as predicted by theory. The spectral response is also compared with the theory. Overall, the MIS solar cell theory is in excellent agreement with the available experimental data. At the end of this chapter, we compare our MIS solar cell theory with the theories proposed by other workers. Most of the theories are based on the assumption that the dark current of MIS solar cells is due to thermionic emission (majority carriers). The experimental results contra-

dict these theories and support our minority carrier tunnel MIS model.

The theory of semiconductor-insulator-semiconductor (SIS) solar cells is compared with the experimental data in chapter 5. Most of the experimental work reported in the literature is on Si. In the case of InP, a 14.4% efficient device has been reported [9]. The model is capable of explaining why some reports in the literature have indicated good performance of such heterojunction devices while others have not. Experimental data are presented which support our model. In particular, the effect of temperature on the dark I-V characteristics of n-ITO/p-Si heterojunction solar cells is compared with the SIS theory. The calculated effect of temperature on the open-circuit voltage, short circuit current density and fill factor of n-ITO/p-Si solar cells is compared. The spectral response and intensity measurements are also compared with theoretical calculations. In all cases the experimental work is in good agreement with the theoretical SIS model.

The last part of Chapter 5 also deals with the loss mechanisms in SIS solar cells. In particular, the transmission-reflection loss, recombination in the surface depletion layer, open-circuit voltage lowering and series and shunt resistance losses are discussed. Some workers have reported on the value of

electron affinity of oxide semiconductors by using simple methods based on the electrical measurements of oxide-semiconductor/base-semiconductor solar cells [12]. We have shown that such methods often lead to incorrect results, due to the uncertainty in the Fermi level position in the oxide-semiconductors and other interface parameters [13].

CHAPTER 2

GENERAL DESCRIPTION OF SOLAR CELLS AND APPROACH TO PROBLEM FORMULATION

2.1 INTRODUCTION

The photovoltaic effect (Becquerel effect) is defined as the generation of an electromotive force by the absorption of light (or any other ionizing radiation) in a non-homogeneous medium. A solar cell is a photovoltaic device that converts solar energy directly into electrical energy. Basically, for the operation of a solar cell, one needs: (i) generation of electron-hole pairs in excess of the thermal equilibrium value and (ii) separation of charges at some electrical non-homogeneity in the system.

In principle, the photovoltaic effects can occur in any material (solid, liquid or gas). However, acceptable efficiency for conversion of sunlight into electricity occurs, at present, only in semiconductors. The semiconductor may be an elemental semiconductor (Si, Ge, Se, etc.) or a compound semiconductor (GaAs, CdS, Cu_2S, InP, etc.). The electrical non-homogeneity in a semiconductor can be due to a metal-semiconductor contact (commonly known as a Schottky diode), or a p-n junction formed by introducing a suitable impurity into the opposite type semiconductor. The p-n junction can be a homojunction of hetero-junction depending on whether the junction is composed of the

same semiconductors on both sides or two different semiconductors.

In this chapter the general description of solar cells and the background material related to the formulation of MIS and SIS solar cell theory will be presented. In Section 2.2, we shall describe the phenomenological description and electrical characteristics of solar cells. These phenomenological approaches can be used in a very limited sense. These limitations and the exact calculational method for solar cells are described in Section 2.3. In Section 2.4, we shall present the approach we have used to calculate the theoretical performance of MIS and SIS solar cells.

2.2 PHENOMENOLOGICAL DESCRIPTION AND ELECTRICAL CHARACTERISTICS OF SOLAR CELLS

The electrical characteristics of a solar cell can be understood in a phenomenological sense from the use of an equivalent circuit diagram as shown in Figure 2.1. This simple equivalent circuit of a solar cell under illumination consists of a non-linear junction, constant current generator and an external load. In an ideal junction, the series and shunt resistance effects are negligible. The constant current, I_L, results from the collection of light generated carriers. The junction current is related to the voltage across the junction by the ideal Shockley diode equation [14].

Figure 2.1

Equivalent circuit of a solar cell, including series and shunt resistance.

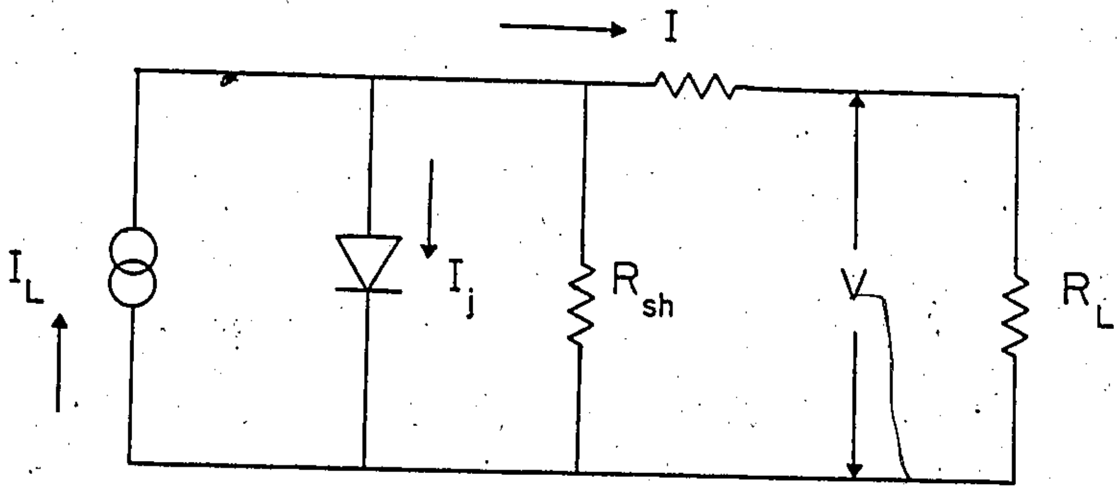

EQUIVALENT CIRCUIT OF A SOLAR CELL

Figure 2.1

$$I_j = I_0\{\exp(\frac{V}{V_{th}}) - 1\} \qquad (2.1)$$

where $V_{th} = \frac{nkT}{q}$ with $n = 1$, at 300°K, V_{th} = 25.9 mV. The ideal p-n junction saturation current is given by

$$I_0 = q\, n_i^{\,2}[\frac{1}{N_D}\sqrt{\frac{D_p}{\tau_p}} + \frac{1}{N_A}\sqrt{\frac{D_n}{\tau_n}}] \qquad (2.2)$$

where

$$n_i^{\,2} = N_c N_v \exp(-E_g/kT). \qquad (2.3)$$

The total current-voltage characteristic of an ideal cell under illumination is expressed as

$$I = I_0\{\exp \frac{V}{V_{th}} - 1\} - I_L . \qquad (2.4)$$

Figure 2.2 shows the I-V characteristic of a solar cell in the dark and under illumination. The dark characteristics are given by equation (2.1) and under light by equation (2.4). The I-V curve in the fourth quadrant represents the region of power generation. The maximum power delivered, P_m, is given by the largest rectangle that can be fitted in the fourth quadrant. As shown in Figure 2.2, the solar cell can be characterized by three main parameters, (i) open circuit voltage, V_{oc}, (ii) short circuit current, I_{sc}, (iii) Fill factor, FF. The open circuit voltage V_{oc} is the voltage output, when the load impedance is much greater than the device impedance. Setting I = 0 in equation (2.4), the open circuit voltage is given by

Figure 2.2

I-V characteristics of a solar cell with (lower curve) and without illumination.

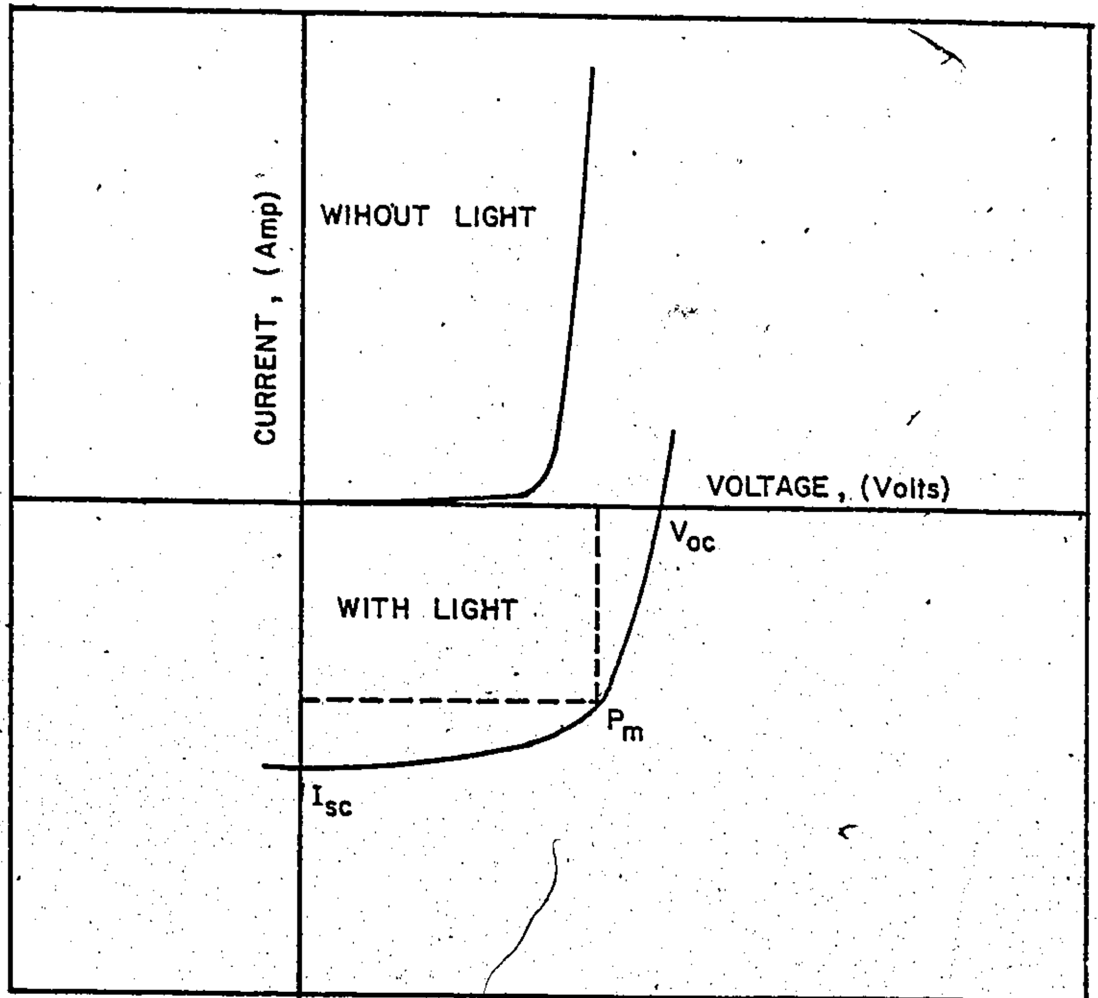

Figure 2.2

$$V_{oc} = V_{th} \ln(1 + \frac{I_L}{I_0}) . \tag{2.5}$$

The short circuit current I_{sc} is the current output, when the load impedance is much smaller than the device impedance. Setting V=0 in equation (2.4), the short circuit current is given by,

$$I_{sc} = -I_L . \tag{2.6}$$

The ratio of maximum power output P_m ($P_m = V_m \times I_m$, where I_m and V_m denote current and voltage at maximum power point) to the product of I_{sc} and V_{oc} is called the fill factor, and is given by

$$FF = \frac{V_m \times I_m}{V_{oc} \times I_{sc}}. \tag{2.7}$$

The three parameter open-circuit voltage, short-circuit current and fill factor can be used to estimate the efficiency η of a solar cell and is given by

$$\eta = \frac{\text{maximum power output}}{\text{power input}}$$

$$= \frac{V_{oc} \times I_{sc} \times FF}{P_{in} \times A} \tag{2.8}$$

where P_{in} is the input solar power density and A is the area of the device. An examination of equations (2.5) to (2.7) shows that the operation of an ideal solar cell depends basically on two parameters, I_L and I_0. The former one depends

primarily on the incident light and the latter depends on the material parameters. Highest efficiency will be observed if the photon generated current, I_L, is high and the diode saturation current, I_o, is low. Only photons with energy greater than E_g, the band gap of the semiconductor, are effective in creating electron-hole pairs. This consideration shows that highest short circuit current will be observed in solar cells made of semiconductors with smallest band gap. On the other hand, the saturation current I_0, will be minimum for semiconductors with highest energy band gap. These considerations lead to the conclusion that with an increase in band gap of the semiconductor, the open circuit voltage, V_{oc}, will increase and the short circuit current, I_{sc}, will decrease. The optimum band gap for solar cells is around 1.5 eV [15]. Logically, this result shows the compromise between small and large band gaps, which means either many photons are used relatively inefficiently or few photons are used relatively efficiently.

The efficiency of any solar cell can be estimated in a very simple way. Taking the sun as a black body of temperature T = 6000°K, the solar cells must satisfy the Carnot constraint on efficiency, i.e.,

$$\eta < 1 - \frac{300}{6000} = 95\% \; . \qquad (2.9)$$

Here we have assumed that the device is operating at about 300°K. As mentioned earlier, only photons with energy $h\nu > E_g$

can create electron-hole pairs in the semiconductor. In the case of silicon, with a band gap of about 1.1 eV, the efficiency will be reduced to about 44%. This number of 44% is based on the assumption that the device can have open circuit voltage, V_{oc} equal to the energy band gap at normal (AM1) solar intensity. In practical situations the efficiency will be reduced by

$$\text{voltage factor} = \frac{qV_{oc}}{E_g} \quad . \tag{2.10}$$

For silicon solar cells, the voltage factor is about 0.6 for the highest open circuit voltage devices. The fill factor for a good solar cell is about 0.8. Both the voltage factor and the fill factor reduce the efficiency of silicon solar cells to about 21% at AM1 [15].

So far we have described an ideal solar cell and equation (2.4) represents the I-V characteristics without considering the effect of series and shunt resistance. Also, in practical solar cells, the dark current flow is governed by various mechanisms. The diode ideality factor "n" is also not equal to one. The effect of various dark current mechanisms may be considered by assuming several diodes in the parallel with each other. Considering these non-idealities, the I-V relation for real solar cells is given by

$$I - \frac{V-IR_s}{R_{sh}} = \sum_i I_{oi}\{\exp[(\frac{V-R_sI}{V_{thi}})] - 1\} - QI_L \tag{2.11}$$

where R_s and R_{sh} represent the series and shunt resistance and Q is the collection efficiency of the device. The collection efficiency is defined as the ratio of the number of carriers collected to the number of carriers generated. In good solar cells, the shunt resistance is so large that its effect is negligible. In bad solar cells, the shunt resistance reduces the open circuit voltage drastically. A device with low value of R_{sh} shows gross defects in the junction and represents the basic weakness of a particular fabrication process or the structure itself. The series resistance, R_s, reduces the fill factor of a device. If the current passing through the devices is large, R_s may also decrease the short circuit current I_{sc}. The effect of R_s on fill factor and short circuit current is discussed at length in Appendix A.

2.3 LIMITATIONS OF PHENOMENOLOGICAL MODELS AND THE EXACT CALCULATIONAL METHOD OF SOLAR CELLS

Equation (2.11) of the last section can be used to estimate the performance characteristics of any solar cell. Such simple methods, either underestimate or overestimate the true behaviour of the device, which depends on the various simplifications used in the calculations. One such example related to our work is the use of the phenomenological method to estimate the efficiency of Schottky barrier solar cells [16]. According to the calculations of Pulfrey and McOut [16], a maximum theoretical efficiency of 22-24% should be possible with silicon. The experimental results on Si Schottky barrier

solar cells [17-20] never approached even 10%. As we pointed out in reference [21], these calculations are based on various unusual physical conditions which cannot be readily met in practice. Using the thermionic emission approach, various workers calculated the performance of MIS solar cells [22-24]. All these underestimate the actual potential of MIS solar cells, as evident by the experimental work [25,26]. Thus, in order to know the true behaviour of any solar cell we have to start with the basic semiconductor equations.

The basic semiconductor equations in one dimension are as follows [27(a)]:

$$\frac{dF}{dx} = \frac{q}{\varepsilon_s}(p - n + N_D^+ - N_A^-) \quad (2.12(a))$$

$$\frac{1}{q}\frac{dJ_n}{dx} + G = U \quad (2.12(b))$$

$$\frac{1}{q}\frac{dJ_p}{dx} - G = -U \quad (2.12(c))$$

$$J_n = q\mu_n nF + qD_n\frac{dn}{dx} \quad (2.12(d))$$

$$J_p = q\mu_p pF - qD_p\frac{dp}{dx} \quad (2.12(e))$$

In the above equations, U is the net thermal recombination-generation rate which is usually modelled by the Shockley-Read-Hall (SRH) model [28] as

$$U = \frac{np - n_i^2}{[\tau_{po}(n+n_1) + \tau_{no}(p+p_1)]} \quad (2.12(f))$$

The function G is the external generation rate due to incident light and is given by

$$G = \int_0^{\lambda_c} [1-R(\lambda)]\alpha(\lambda)N(\lambda)\exp[-\alpha(\lambda)x]d\lambda \ . \qquad (2.12(g))$$

where R is the reflection coefficient, N is the incident photon density per wavelength interval, α is the absorption coefficient and λ_c is the cutoff wavelength corresponding to the band gap of the semiconductor.

For any solar cell, the solution of this non-linear set of equations with appropriate boundary conditions gives the electron and hole densities throughout the device as well as the current-voltage relationship. While certain approximations can sometimes be used to simplify this non-linear set of equations, an accurate analysis requires a numerical computer solution.

2.4 OUTLINE OF THE METHOD USED TO MODEL MIS AND SIS SOLAR CELLS

Experimental work on MIS and SIS solar cells [2-4,6-9] shows that these devices rely on a thin interfacial layer (10-30 Å) between the top contact (metal or conducting semiconductor) and the base-semiconductor. The exact nature of the transition from metal to interface, or semiconductor to interface on either side of the interfacial layer is not known. In principle, a material composition profile of each structure can be

constructed by using techniques such as Auger analysis. However, such a profile is often highly colored by the details of the specific fabrication procedure employed. In order to model these devices, we have chosen a sharp interfacial layer model, even though the transitions are more likely to be graded. The justification is that the behaviour of MIS and SIS diodes in a solar conversion mode is not particularly sensitive to the exact nature of these transitions [10]. With such thin interfacial layers (10-30 Å), the obvious current transport mechanism through the interface is tunneling.

Tunneling is a process in which current flows through a normally non-conducting medium (non-conducting in a classical sense) by a non-destructive process. The insulating medium is so thin that the wave function of the charge carrier is of the same order of magnitude in extent as the interface. Thus part of the wave function can penetrate the interface and appear on the other side. This constitutes a current flow. There are various ways to deal with the problem of tunneling through thin interfacial layers [29-31]. We have used Harrison's [30] approach in our model, since other methods are beyond the scope of our work. The current transmitted by tunneling through an interfacial layer (generally insulator in its bulk form) separating two materials is given by [30].

$$J = \frac{q}{2\pi^2 h} \int_{-\infty}^{\infty} dE(f_1 - f_2) \int ds \, T \qquad (2.13)$$

where q is the magnitude of the electronic charge, h is Planck's constant, and f_1 and f_2 are the respective carrier occupation probabilities in the material to the left and right of the interfacial layer for carriers of energy E. The "shadow" of a constant energy surface is defined as its projection in wave number (k) space on a plane parallel to the barrier and the integral over S is the overlap of the shadows from the top layer and the base-semiconductor for the energy E.

The transmission coefficient through the potential barrier of the insulator, T, is obtained by the WKB approximation in Harrison's approach. Although this approach can be criticized on a number of theoretical grounds [32], the procedure provides a reasonable representation of the average potential variation in the interfacial region and is capable of explaining the experimental results of MIS and SIS solar cells.

After specifying the characterization of the tunneling process, the modelling is straight forward. The non-linear set of equations presented in the last section (Eq. (2.12(a)-2.12(g)) are solved numerically under the boundary conditions imposed by the tunneling contact to the semiconductor. By using numerical methods throughout, self-consistent solutions satisfying both the equations describing tunneling through the interfacial layer and carrier transport in the semiconductor were obtained at each bias point. This allowed the dominant features of the MIS and SIS solar cells to be recognized and provides an accurate method for finding optimum parameters of the device.

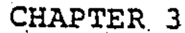

CHAPTER 3

THEORETICAL CALCULATIONS OF METAL-INSULATOR SEMICONDUCTOR (MIS) AND SEMICONDUCTOR-INSULATOR SEMICONDUCTOR (SIS) SOLAR CELLS

3.1 INTRODUCTION

The conventional way of forming a solar cell is to create a p-n junction by introducing a suitable impurity into the opposite type semiconductor. Mostly, a high temperature diffusion process is used to change the conductivity type of the base semiconductor to the opposite type. Such diffusion processes to create a p-n junction can be expensive and also unsuitable for polycrystalline and amorphous semiconductors. Thus, there has been a steady search for alternate and potentially lower cost methods of forming a photovoltaic junction. One such technique consists of inducing a conductivity-type change at the surface of the semiconductor by the application of an ultra thin metal or a relatively thick transparent (wide band gap) conducting semiconductor of proper work function. Such solar cells rely on a thin interfacial layer (10-30 Å) between the top "inducing" contact (metal or conducting semiconductor) and the base semiconductor. This interfacial layer is generally an oxide or some other compound which is normally an insulator in its bulk form. Hence these

cells are referred to as metal-insulator-semiconductor (MIS) or semiconductor-insulator-semiconductor (SIS) solar cells.

We shall describe the general remarks on MIS and SIS solar cells in section 3.2.1 and 3.2.2. In the next section 3.3, the details of the model used to investigate the properties of MIS and SIS solar cells will be discussed. The work of reference 52 was extended to study the photovoltaic response of MIS diodes. The SIS solar cell operation is an expansion of MIS solar cell theory, where the metal has the property of a variable bandgap, which can be set at any value from zero to several electron volts. In section 3.4, the effect of various parameters on the performance of MIS and SIS solar cells will be discussed. In particular, the effect of insulator thickness, substrate resistivity, surface states and insulator charge, metal or conducting oxide-semiconductor work function, temperature, intensity, minority carrier life time, crystallographic orientation and the band gap of the base semiconductor will be studied. The calculated spectral response of MIS and SIS solar cells will be discussed in section 3.5. The C-V and G-V characteristics of MIS and SIS solar cells will be described in section 3.6. Summary of this chapter will be presented in section 3.7.

3.2 GENERAL REMARKS ON MIS AND SIS SOLAR CELLS

3.2.1 MIS Solar Cells:

When a metal of proper work function is brought into contact with a clean surface of a semiconductor, the charge carriers flow from one material to the other. This flow continues until the Fermi levels are adjusted to the same height, resulting in the thermal equilibrium condition. Due to band bending at the interface, such metal-semiconductor junctions (commonly known as Schottky barrier diodes) can be used in place of a p-n junction. Schottky-barrier solar cells are currently being examined for their suitability in large-scale terrestrial applications since they are significantly simpler to fabricate with an associated lower-cost technology. They are also formed at low temperatures without any appreciable degradation in the bulk properties of the semiconductor. It is conceivable that these structures can be adapted to polycrystalline film materials, where such unwanted effects as grain-boundary diffusion of the dopant in conventional p-n junction formation may be eliminated. Unfortunately, the conversion efficiencies in experimental devices are much lower than the anticipated theoretical values.

Recent experimental work [2-4] has shown that the presence of a thin interfacial insulating layer or oxide between the metal and the semiconductor of a Schottky barrier can considerably increase the photovoltaic conversion efficiency of such solar cells. A Schottky diode retains its essential

characteristics even when a thin layer (oxide) is introduced, provided that this layer is about 10 Å or so (in the case of metal-SiO_2-Si structures). Above this thickness of oxide layer a tunnel MIS diode will be formed [21].

An investigation of Schottky barrier solar cells shows that their photovoltaic conversion efficiencies are poor due to their open-circuit voltage, V_{oc}. Experimental values of V_{oc} for Si Schottky barrier solar cells is about 0.2-0.3 V [17-20] while for Si homojunction solar cells, V_{oc} is about 0.6 V [33]. Similar results are obtained for GaAs and other Schottky barrier solar cells. The low V_{oc} is basically due to high dark current, which indicates a low barrier height for the device. A clear picture of the electronic structure at a metal-semiconductor interface is not completely known. However, the experimental observation can be explained by the presence of large density of surface states at the interface which effectively "pin" the Fermi level in the semiconductor valance band. The barrier height for an n-type Schottky barrier is about $\frac{2}{3}$ of the band gap and is about $\frac{1}{3}$ of the band gap for p-type barriers [34(a)].

An equilibrium energy-band diagram for a MIS solar cell is shown in figure 3.1, where the case of a p-type semiconductor is illustrated and the band gap of the insulator and the semiconductors are represented by E_{gi}, and E_{gs}, respectively. The energy difference between the semiconductor and insu-

Figure 3.1

Simple equilibrium energy-band diagram of the p-type MIS solar cell. E_{gi} and E_{gs} denote the band gap of insulator and semiconductor respectively. ϕ_{mi} and ϕ_{si} are the metal to insulator and semiconductor to insulator work functions. ϕ_p is the barrier height which governs V_{oc} of the device.

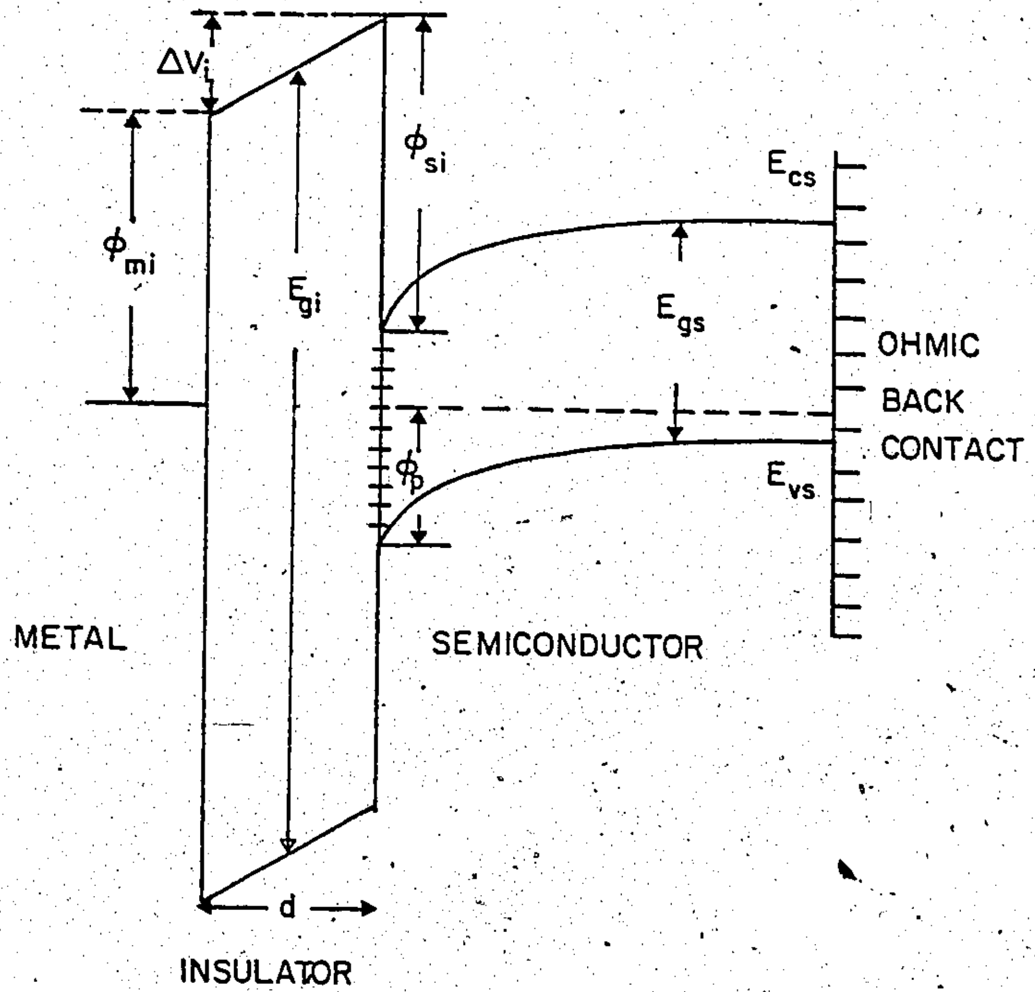

Figure 3.1

lator conduction band edges (3.2 eV for silicon-silicon dioxide) is represented by ϕ_{si}. The metal-to-insulator barrier height, which is related to the vacuum work function of the metal, is represented by ϕ_{mi}. Measurements on thick oxide devices indicate that it has a value of 3.2 eV for the Al-SiO_2 interface and 4.1 eV for Au-SiO_2 [27(c)].

The introduction of an ultra thin insulating layer eliminates the pinning effect, observed in Schottky barrier solar cells, so that the minority carrier quasi-Fermi level is now pinned to the Fermi level in the metal to produce a higher open-circuit voltage. These features can be observed in the energy band diagram shown in figure 3.2, in which the device is biased positively with respect to the top metal contact. As shown in figure 3.3, the insulator-semiconductor (IS) interface is relatively "clean" and the metal-insulator (MI) interface (the less important) is "dirty". Thus, in an MIS solar cell the electrical characteristics are controlled by a clean interface, while in a Schottky diode the controlling interface is "dirty". This is the reason why Schottky barrier solar cells have lower conversion efficiency [1]

3.2.2 <u>Semiconductor-Insulator-Semiconductor (SIS) Solar Cells</u>

Recently there have been a number of reports of oxide semiconductors in conjunction with low band gap semiconductors, (< 1.5 eV) to form solar cells. The base semiconductors investigated are Si [6-8,12,35-43], InP [9,44-47], GaAs [44,46,47], Ge [46,47], CdTe [48] and $CuInSe_2$ [49]. The oxide semiconductors

Figure 3.2

Schematic energy-band diagram for a p-type tunnel MIS solar cell when a forward bias V_a is applied under zero illumination.

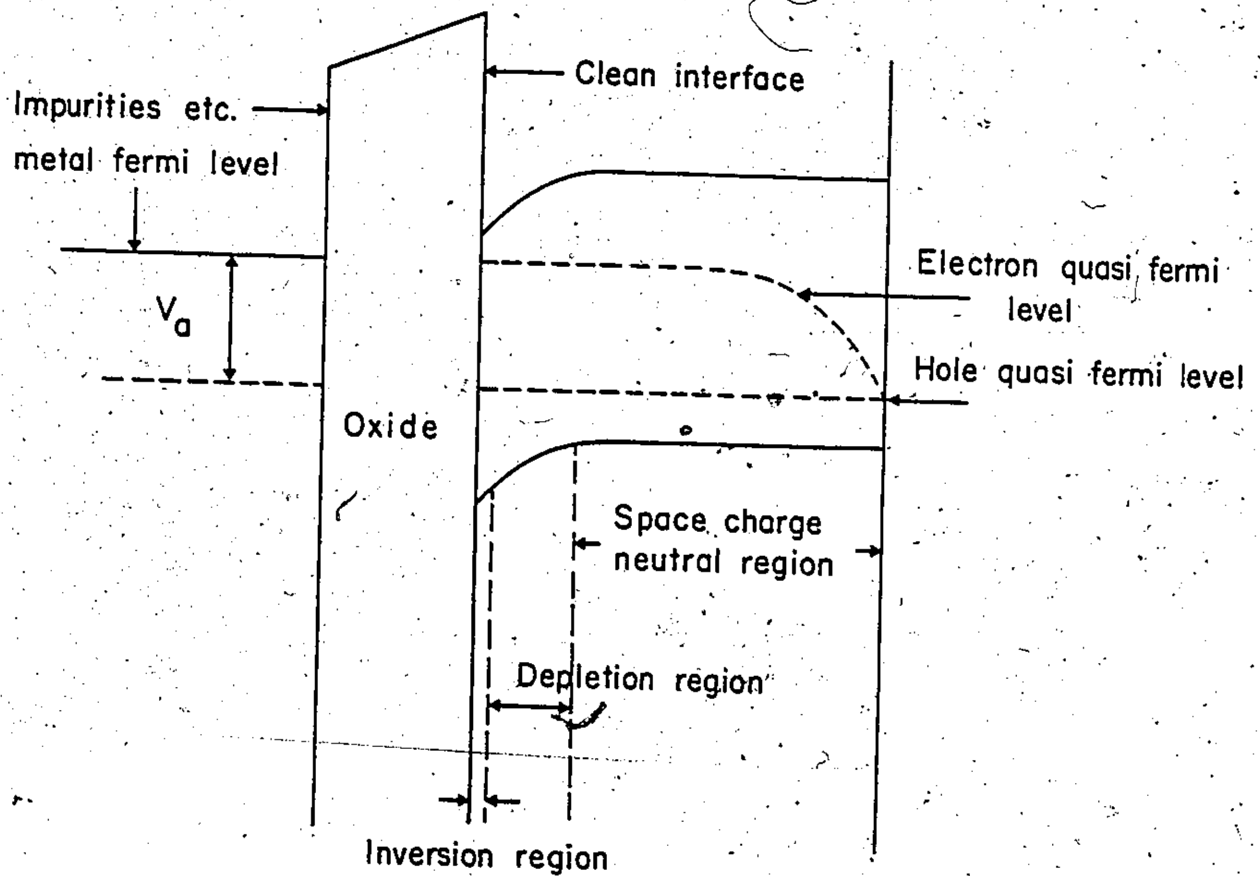

Figure 3.2

Figure 3.3

Simple representation of the interface that controls electrical characteristics of Schottky barrier and MIS solar cells. For the Schottky barrier devices, the interface is "dirty". In the case of MIS solar cells, the oxide-semiconductor interface is "clean".

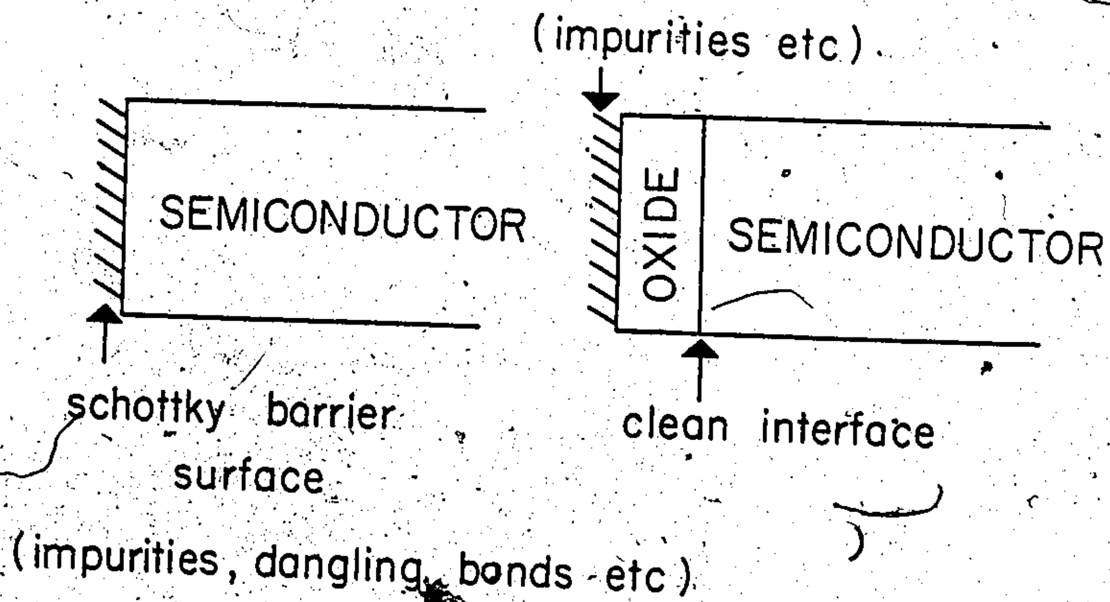

Figure 3.3

used to form devices are SnO_2, In_2O_3 or SnO_2/In_2O_3 mixtures (indium tinoxide or ITO) and ZnO. Not all investigations reported in the literature have yielded high efficiency for photovoltaic conversion. Only in the case of ITO-Si (p-type) [6] SnO_2-Si (n-type) [43], and ITO-InP (p-type) [9] has an efficiency greater than 10% been observed. In the first instance these devices can be considered as belonging to a family of heterojunctions in which one side is a wide band gap semiconductor, such as SnO_2, mated to a much narrower band gap material, such as Si. The suitability of oxide-semiconductor as a conducting window material in heterojunction solar cells is due to their wide-band gap and low sheet resistivity.

It is well known that only heterojunctions with appropriate electron affinities, good lattice and crystal match and negligibly small difference in the thermal-expansion coefficient will form good photovoltaic devices. Table 3.1 contains crystal structure, lattice parameters and thermal expansion coefficients of some oxide-semiconductors and base semiconductors. We ignore the question of affinities for the moment. An examination of Table 3.1 shows that no combination of base semiconductor and oxide-semiconductor is particularly compatible and thus there is no combination likely to form good devices. Although Table 3.1 contains only a small section of possible semiconductors and oxides, it nonetheless serves to illustrate what a wider search would reveal [50]. The question is why

TABLE 3.1

SOME PROPERTIES OF BASE SEMICONDUCTORS AND OXIDE-SEMICONDUCTORS

Semiconductor	Type of Crystal Structure	Lattice Constant (Å)			Linear Coefficient of Thermal Expansion (10^{-6}/°C)	Electron Affinity (eV)
		a	b	c		
Si	Diamond	5.431	-	-	2.3	4.1
Ge	Diamond	5.657	-	-	5.8	4.0
InP	Zinc blend	5.869	-	-	4.5	4.4
GaAs	Zinc blend	5.653	-	-	5.8	4.7
CdTe	Zinc blend	6.477	-	-	5.9	4.3
$CuInSe_2$	Chalopyrite	5.782	-	11.620	-	4.3
In_2O_3	Cubic	10.118	-	-	10.2	4.3-4.4
SnO_2	Tetragonal	4.737	-	3.185	4.0	4.8-4.9
ITO	Cubic	10.118	-	-	~10.2	4.2-4.5
ZnO	Hexagonal	3.249	-	5.205	7.2	4.2
$Cd_2S_nO_4$	Orthorhombic	5.568	9.887	3.902	-	4.3 (estimated)
CdS_nO_3	Rhombohedral	5.458	5.577	7.874		4.5 (estimated)
Bi_2O_3	Cubic	10.245	-	-		4.5 (estimated)

have some reports in the literature indicated good performance of such heterojunction devices while others have not.

In examining the available experimental data, it became apparent that the performance of such devices could be dramatically controlled by the presence of a thin interfacial layer or insulator. They appear capable of accommodating in some way, which is not as yet completely understood, the strains due to crystal structure, lattice parameters and perhaps thermal-expansion coefficient mismatch, thus in effect grading one side of the junction into the other.

In a device such as the SIS diode, it is often difficult to know how to approach the electronic modeling problem. A material composition profile of the structure with distance would be desirable, however, such a profile is often highly influenced by the details of the specific fabrication procedure employed. Structurally, the two semiconductors are separated by an interfacial region, but the exact nature of the transitions on either side of the interfacial layer is not known. A perfectly general description is obviously out of the question at this time. In order to make any headway, we choose a sharp interfacial layer model, as a first approximation, even though the semiconductor to insulator transitions are more likely to be graded. The justification is that the behaviour of the SIS diode is not particularly sensitive to the exact nature of these transitions. The insulator is sufficiently thin (10-30 Å)

so that current transport through, the interface is by tunneling. While the tunneling process is sensitive, to a degree, to the shape of the barrier, we shall show that in the device as described, it is charge transport in the semiconductors that determines the I-V characteristics. The tunneling serves largely to provide an "ohmic contact". These statements are true, within certain qualifications which will be discussed later.

Figure 3.4 shows a simple equilibrium energy band diagram for the SIS diode. The band gaps and barrier heights have been chosen to reflect the (n-type) ITO-(p-type) Si system whose experimental characteristics will be compared with theory. The numerical values on the silicon side are known to a good degree of precision but this is not the case on the ITO side. We are using the best parameter values culled from the literature. ITO is a more complicated material than depicted by this simple band diagram. However, at this point in time, this description is sufficient for our purposes.

The degenerate ITO and the moderately doped p-type silicon are separated by an interfacial layer whose thickness (d) lies between 10 and 20 Å. This interfacial layer is shown as a wide band gap material or insulator. Experiments indicate that SiO_2 is present so that this proposition is reasonable. However, constituents from the ITO have undoubtedly entered the composition and the exact nature is yet to be resolved. For

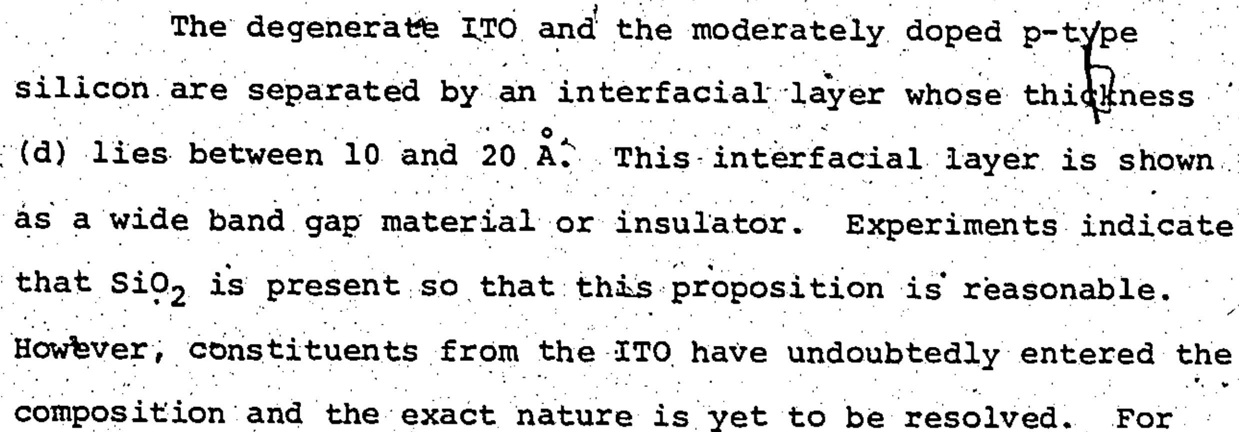

Figure 3.4

Simple equilibrium energy-band diagram of the ITO-SiO_x-(p-type)Si tunnel diode system. E_{gos}, E_{gi} and E_{gs} denote the band gap of ITO, SiO_2 and Si respectively. ϕ_{osi} is the oxide semiconductor-to-insulator barrier height and is related to work function of ITO. ϕ_B is the barrier height which governs V_{oc} of the device.

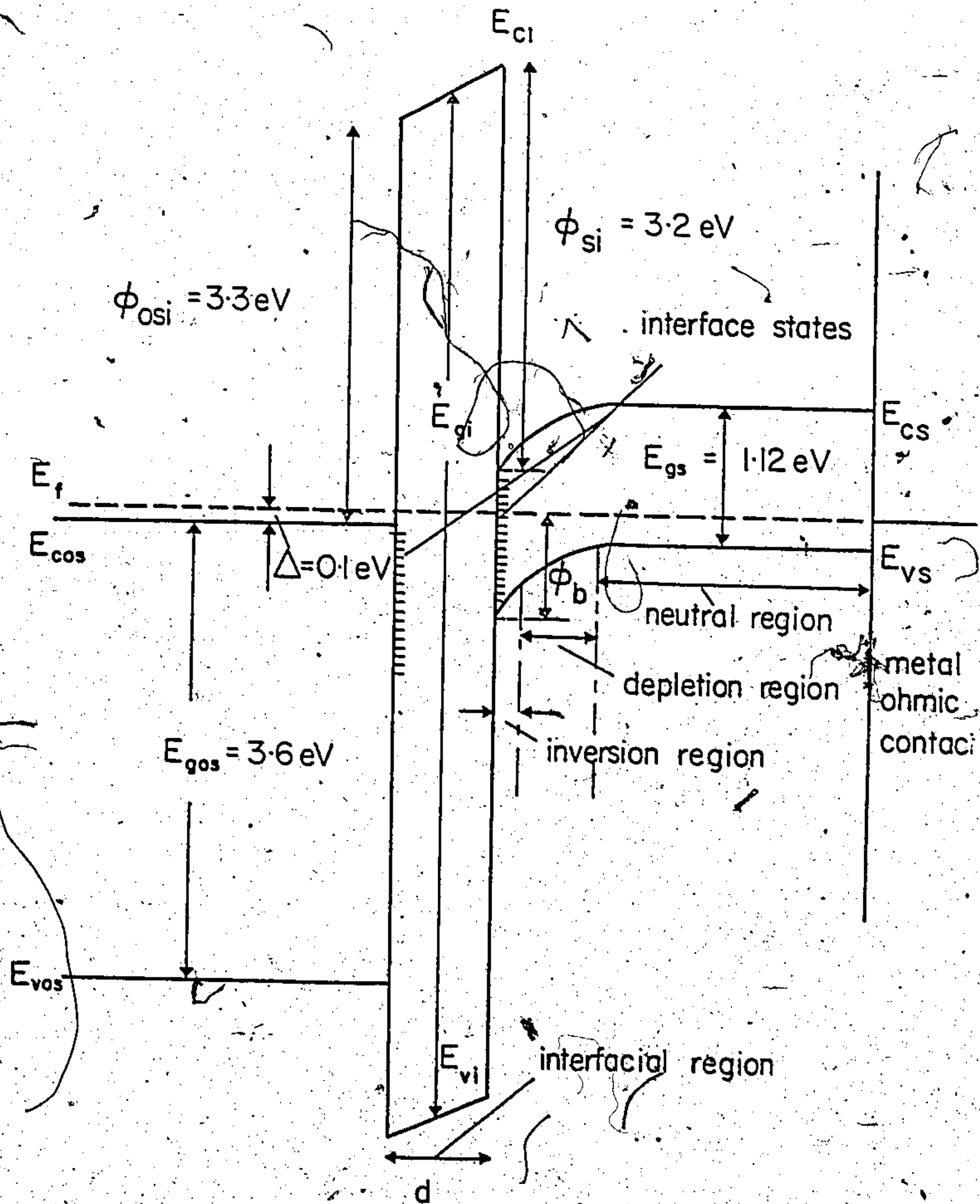

Figure 3.4

example, a $Sn_xSi_yO_z$ compound could be present.

The surface of the base-semiconductor (p-type silicon) is inverted by virtue of oxide-semiconductor (ITO) and base-semiconductor (Si) work functions. The work function of ITO has not been measured directly but has been inferred from electrical data [12]. Based upon the experimental data available from the literature, Table 3.2 of estimated parameters for ITO has been prepared and used in the cell performance analyses [51]. We regard ITO to be a low-work function material in our nomenclature. A high-work function material ($\phi_{osi} > 3.6$ eV) would yield a surface which was accumulated rather than inverted. Such devices may be of interest in their own right and high work function MIS diodes have already been reported in the literature [52].

An inspection of the equilibrium energy band diagram of the SIS diode (Figure 3.4) shows that the Fermi level lies close to the minority carrier conduction band edge. The dominant dark current will be minority carrier current. In addition, the wide band gap of the oxide-semiconductor suppresses those majority carriers which might consider band to band tunneling. The resulting photovoltaic performance of an SIS diode appears to be the same as that of an MIS diode. In a later section, we will show that the two structures indeed behave in the same way.

TABLE 3.2

TYPICAL PROPERTIES OF ITO FILMS

Crystal structure	cubic
Lattice constant	10.118 Å
Linear coefficient of thermal expansion	10.2×10^{-6}/°C
Band gap	2.62-3.75 eV
Resistivity	1.77×10^{-4}-1.2×10^{-2} Ωcm
Carrier concentration	1×10^{19}-1.3×10^{21} cm^{-3}
Effective mass	0.3-0.55 m_0
Hall mobility	26-40 cm^2/v.sec.
Refractive index	1.68-2.48
Electron affinity	4.1-4.3 eV
Position of Fermi level below or above the conduction band edge	0-0.4 eV

3.3 DESCRIPTION OF MIS AND SIS SOLAR CELL MODEL

3.3.1 Background Material

The fundamental equations for the characterization of any semiconductor device are non-linear [27(a)]. Due to this non-linearity, only in very few cases can an analytical solution be obtained to describe the true behaviour of the device. The same problem exists in characterization of the MIS tunnel diode. In spite of various attempts [27(b),53-54], there is no satisfactory theory of Schottky diodes, primarily due to a lack of understanding of the electronic properties of the metal-semiconductor interface. In the past, the tendency to describe the current flow in thin insulator diodes has been in terms of Schottky diode theory modification to include the non-idealities introduced by the insulating layer [55-57]. This kind of approach has not given a clear understanding of these structures. Recent theoretical and experimental work done at McMaster University [2,11,52,58-60] established that these thin insulating diodes constitute a unique class of their own and have very interesting properties from a device point of view. Previous investigations have shown that when the insulator in a MIS diode is less than about 60 Å (for Al-SiO_2-Si) significant tunnel currents can flow between the metal and the semiconductor. These currents are initially of such small magnitude that the semiconductor is essentially in thermal equilibrium. If the insulator thickness is further decreased,

the tunnel currents increase to the point where they are sufficiently large enough to disturb the semiconductor from thermal equilibrium. This occurs at around 28 Å for Al-SiO_2-(p-type) Si diodes. Thus, in general, below some critical value of insulator thickness, "nonequilibrium" tunnel MIS diodes are formed. Over a certain bias range, the MIS tunnel diode operates in this non-equilibrium mode where the diode current is semiconductor limited (due to generation-recombination in the bulk) and the tunnel current merely acts as an ohmic contact. Indeed, we should point out that the tunneling process becomes of secondary importance in this non-equilibrium mode. Any current conduction process through the oxide which is of sufficient magnitude to establish a non-equilibrium in the semiconductor will produce the same result. This could even conceivably be a leakage current through a badly formed interfacial layer. Such non-equilibrium diodes can be further classified as majority-carrier, surface-state or minority-carrier devices depending on whether the dominant tunnel-current flow near zero bias is between the metal and the majority-carrier band, the surface states, or the minority-carrier band. Which diode is formed depends on whether the semiconductor-insulator interface at zero bias is accumulated, depleted, or in strong inversion. The contact-metal work function is the most important parameter in determining which of these states exists.

For example, minority-carrier diodes can be formed on p-type silicon substrates by selecting metals, such as aluminum, which have a low value of work function ϕ_{mi}. The ϕ_{mi} for aluminum has a value of 3.2 eV. Conversely, a high value of ϕ_{mi} such as gold at ϕ_{mi} 4.2 eV, is needed to form a minority-carrier diode on n-type silicon. For majority-carrier diodes, the converse of the above description applies. The transition from a minority- to majority-carrier diode diode occurs at around 3.6 eV and in this region tunneling via surface states can dominate. Majority-carrier tunnel diodes show current multiplication properties and are not necessarily suitable for photovoltaic purposes, but are useful in transistor-type devices [52]. Minority-carrier devices, on the other hand, can show I-V characteristics which obey the ideal Shockley diode equation [14] and are suitable for photovoltaic conversion. Before the fabrication of any MIS solar cell, the potential of the MIS tunnel diode in an energy conversion structure for electron-voltaic conversion was experimentally demonstrated by Shewchun, Green and King [2]. The work of reference 52 has been extended to develop the theory of MIS solar cells and will be discussed in the next section.

3.2.2 Mathematical Model

A detailed description of the self-consistent numerical technique for the characterization of the MIS tunnel diode is given in reference 52. For solar cell application, this approach is new and for completeness, we describe below the pertinent

equations mentioning the necessary changes made in the original program.

The approach that is adopted here formulates the problem in such a way that numerical solutions to an accuracy of 0.5% are obtained.

(1) Characterization of the Semiconductor Region

The basic equations describing the semiconductor region are following, where the symbols have their usual meaning [27(a)].

(a) Poisson's Equation

$$\frac{dF}{dx} = \frac{q}{\varepsilon_s} (p - n + N_D^+ - N_A^-) \tag{3.1}$$

(b) Continuity Equations

$$\frac{1}{q} \frac{dJ_n}{dx} + G = U \tag{3.2}$$

$$\frac{1}{q} \frac{dJ_p}{dx} - G = - U \tag{3.3}$$

where the electron-hole generation rate is given by

$$G = \int_0^{\lambda_c} [1-R(\lambda)]\alpha(\lambda)N(\lambda)\exp[-\alpha(\lambda)x]d\lambda \ . \tag{3.4}$$

Here $R(\lambda)$ is the reflection coefficient, $\alpha(\lambda)$ is the absorption coefficient, $N(\lambda)$ is the number of photons per second per unit area, and λ_c is the cutoff wavelength corresponding to the band-gap energy of the semiconductor. If we set $G = 0$, the above equation reduces to equation (A2) and (A3) of reference 52 .

(c) Current Density Equations

$$J_n = q\mu_n nF + q D_n \frac{dn}{dx} \qquad (3.5)$$

$$J_p = q\mu_p pF - q D_p \frac{dp}{dx} \qquad (3.6)$$

(d) Shockley-Read-Hall (SRH) Recombination Formula

$$U = \frac{(np - n_i^2)}{[\tau_{po}(n + n_1) + \tau_{no}(p + p_1)]} \qquad (3.7)$$

(e) Electric Field and Electrostatic Potential Relationship

$$F = -\frac{d\psi}{dx} \qquad (3.8)$$

The above set of equations can be solved to any desired accuracy using numerical techniques once an electron and hole concentration at the semiconductor-insulator interface and the electrostatic potential change across the semiconductor are specified. The iterative algorithm proposed by Gummel [61] was employed to solve the set of non-linear equations.

(2) Characterization of Tunneling Through the Insulator

The equations employed were Equation (A8) and (A9) of reference [52]:

$$J = \frac{q}{2\pi^2 h} \int_{-\infty}^{\infty} dE(f_m - f_s) \int ds\, e^{-n} \qquad (3.9)$$

$$\eta = \frac{2}{h} \int_{x_a}^{x_b} (P_{Ti}{}^2 - p_i{}^2)^{1/2} \, dx \qquad (3.10)$$

A two band model of the insulator was used. The energy momentum relationship in the insulator is given by

$$P_i{}^2/2m_{Ti} = [E - \phi_{CB}(x)]\{1 + [E - \phi_{CB}(x)]/E_{gi}\} \qquad (3.11)$$

where $\phi_{CB}(x)$ represents the energy of the insulator conduction band edge. Assuming there exists a parabolic relationship between the transverse energy E_T and the transverse momentum, P_T, for a particle in all three regions of the device, this gives the following expression for the electron current flow between the metal and the semiconductor conduction band,

$$J_{CT} = 4\pi q \frac{m_{Ti}}{h^3} \int_0^{E_{max}} dE (f_m - f_s) \int_0^{(m_{Ts}/m_{Ti})E} dE_T \, e^{-\eta} \qquad (3.12)$$

where

$$\eta = \frac{2}{h} (2m_{Ti})^{1/2} \int_{x_a}^{x_b} \{E_T - (E - \phi_{CB})$$

$$\times \; [1 + (E - \phi_{CB})/E_{gi}]\}^{1/2} dx \qquad (3.13)$$

and the semiconductor conduction band edge is taken as the reference. A similar relation can be obtained for current flow density between the metal and valence band of the semiconductor.

The above formulation is applicable only for tunneling into <100> oriented silicon and not for <111> silicon, since we have assumed a parabolic relationship between the transverse energy and momentum. For the latter case, we have to use the expression derived in Appendix B of reference 52.

(3) Characterization of Surface States

Surface states associated with the semiconductor-insulator interface were characterized using SRH kinetics modified to include the effects of tunneling between these states and the metal. This yields the following expression for the occupancy of each independent level under steady state conditions.

$$f_{to} = \frac{n_s S_n + p_1 S_p + J/q}{(n_s + n_1) S_n + (p_s + p_1) S_p} \qquad (3.14)$$

where n_s and p_s are the surface concentrations of electrons and holes, n_1 and p_1 are parameters familiar from conventional single-level SRH theory, and S_n and S_p are surface recombination velocities given by

$$S_{n,p} = N_t \langle \sigma_{n,p} v_{th} \rangle \qquad (3.15)$$

N_t is the density of surface states, v_{th} is the thermal velocity of electrons and $\sigma_{n,p}$ are capture cross-sections. The net rate of capture of electrons in the conduction band by these states is

$$U_{cn} = \frac{S_n S_p(n_s p_s - n_i^2) - (n_s + n_1) S_n J/q}{(n_s + n_1) S_n + (p_s + p_1) S_p} \quad (3.16)$$

and a similar expression for U_{cp}. J is the current density tunneling into the surface states level which was computed by the expression [62]

$$J = \sigma_T N_t A(f_m - f_{to}) \quad (3.17)$$

where σ_T is an effective tunneling capture cross-section and A depends upon the trap energy and bias conditions.

A continuous distribution of surfaces states was modelled as a large number (20) of distinct surface state levels. Each of these levels was assumed to be independent, i.e., it was assumed that each level exchanged carriers more rapidly with the semiconductor valence and conduction bands than with each other.

(4) Voltage Relationship

In addition to the above equations, a relationship involving the semiconductor, surface states, insulator and metal parameters was the expression for the total voltage applied to the solar cell:

$$V_a = \psi_s + \frac{\varepsilon_s}{\varepsilon_i} F_s d - q \frac{(Q_i + Q_{SS})}{\varepsilon_i} d - \phi_{si} + \phi_{mi} - \delta \quad (3.18)$$

(5) Solutions Technique

The approach used to solve the overall system of equations was to specify the electrostatic potential drop ψ_s, across the

semiconductor. Then if the electron and hole concentrations at the interface are specified, a solution for the semiconductor region can be found. Once this is found, it is possible to find a solution for the charge in the surface states, recombination at the surface states, and the tunnel currents. The current densities at the interface will not match unless the correct values of electron and hole concentrations at the interface are found. The technique used was to vary the carrier concentrations at the interface until the current conservation conditions were satisfied. The iteration procedure is rapidly convergent if the initial guesses of interface quasi-Fermi level shifts are with 5 kT of the correct value. Poor initial guesses require more iterations and with very poor guesses, the iteration procedure may diverge. Using a CDC 6400 computer, a computational time of between 7 and 55 sec. (depending upon initial guess) was required to obtain solutions to an accuracy of better than 0.5 percent.

3.3.3 Effect of the Wide Band Gap of Oxide-Semiconductor on SIS Tunnel Diode: Using the calculational method described earlier, we have examined the effect of the band gap of the oxide semiconductor or the wide band gap semiconductor side of the junction on the tunneling current flows in the SIS diode. This data is presented in Tables 3.3 and 3.4. Table 3.3 shows the variation of the hole and electron (J_{CT} and J_{VT}) currents as a function

TABLE 3.3

EFFECT OF THE MAGNITUDE OF THE WIDE BAND GAP SEMICONDUCTOR ON SIS TUNNEL CURRENTS. DARK CHARACTERISTICS WITH ϕ_{osi} = 3.7 eV AND INTERFACIAL LAYER THICKNESS = 12 Å. NO SURFACE STATES ARE PRESENT AT THE INSULATOR-SILICON INTERFACE. $N_A = 1.5 \times 10^{23}/m^3$ FOR SILICON.

E_{gos} (eV)	V_A (V)	Electron Current J_{CT} (A/m^2)	Hole Current J_{VT} (A/m^2)
0.0	0.375	4.33×10^{-3}	1.95×10^{-1}
0.5	0.375	4.33×10^{-3}	1.95×10^{-1}
1.0	0.375	4.27×10^{-3}	0.0
1.5	0.375	4.27×10^{-3}	0.0
3.6	0.375	4.27×10^{-3}	0.0

TABLE 3.4

EFFECT OF THE MAGNITUDE OF THE WIDE BAND GAP SEMICONDUCTOR ON SIS TUNNEL CURRENTS. DARK CHARACTERISTICS WITH ϕ_{osi} = 3.7 eV AND INTERFACIAL LAYER THICKNESS = 12 Å. SURFACE STATES ARE PRESENT AT INSULATOR-SILICON INTERFACE. $N_A = 1.5 \times 10^{23}/m^3$ FOR SILICON.

E_{gos} (eV)	V_A (V)	Surface State Current J_{ST} (A/m^2)	Electron Current J_{CT} (A/m^2)	Hole Current J_{VT} (A/m^2)
0.0	0.372	43.9	2.07×10^{-4}	0.192
0.5	0.379	57.6	8.66×10^{-3}	0.192
1.0	0.379	54.7	8.66×10^{-3}	0
1.5	0.379	54.7	8.66×10^{-3}	0
3.6	0.379	54.7	8.66×10^{-3}	0

of bandgap for the surface state free case. As expected, the hole tunnel current vanishes as the energy gap gets larger. In Table 3.4 for the case of surface states at the insulator-semiconductor interface, the situation is more complicated. In this case considerable current can be transported across the interfacial layer via surface states. However, the effect of the band gap is again quite distinct. The calculation routine is capable of describing the MIS structure as a limiting case (i.e. $E_{gos} \rightarrow 0$, SIS $\rightarrow$ MIS).

3.3.4 Physical Description of MIS and SIS Solar Cells

Figures 3.1 and 3.4 show simple equilibrium energy band diagrams for the MIS and SIS solar cells. The base-semiconductor is p-type in both cases. The key parameters in these diagrams are the potential barrier heights ϕ_{mi}, ϕ_{osi} and ϕ_{si}. As shown in Figures 3.1 and 3.4, the surface of p-type base-semiconductor is inverted due to low work function of the top layer. The following is a simple description of current transport in the MIS and SIS diodes. The inverted p-type base-semiconductor surface provides a supply of minority carriers (electrons) which can tunnel into the top layer (J_{CT}). The current flow from the valance band of the base-semiconductor to the top contact is represented by J_{VT}. In the case of SIS diodes, the majority carriers are blocked from tunneling by the wide band-gap of the oxide-semiconductor. This need not be the case if the band gap on the left hand is made smaller.

The limiting case is, of course, a metal. Tunneling can also occur via defect states at the two interfaces. We have considered J_{ST} to be the dominant tunnel transition via defects at the insulator-base-semiconductor interface. The effective current flows due to the interchange of the charge between the conduction and valence bands of the semiconductor and these defects by recombination-generation processes are represented by J_{CI} and J_{VI}, respectively.

One can see from Figures 3.1 and 3.4 that the Fermi level of the system is much closer to the minority carrier band edge. Thus, when the device is biased, the dominant current in strong inversion will be from the minority carrier band. Figure 3.5 shows the energy band diagram when the MIS diode is biased positively with respect to the top metal layer under zero illumination. Thus, in both MIS and SIS diodes, the dominant dark current near zero bias will be of minority carriers, provided the interface is inverted. This requires a low work function metal or conducting semiconductors for the p-type base-semiconductor and a high work function top layer for the n-type base semiconductor. Such non-equilibrium minority carriers MIS and SIS diodes are best suited for photovoltaic action. The operation of the two diodes is similar.

The minority carrier non-equilibrium model of operation is interesting in that the minority carrier quasi-fermi levels in the semiconductors can be pinned effectively to their respec-

Figure 3.5

Schematic energy band diagram of the MIS tunnel diode system witha p-type semiconductor region. J_{CT} and J_{VT} are the current flows from the conduction and valance bands of the metal contact. J_{ST} is a flow from surface states to the metal and is supplied by J_{CI} and J_{VI}. The semiconductor is biased positiviely with respect to the top metal contact by a voltage, V_a.

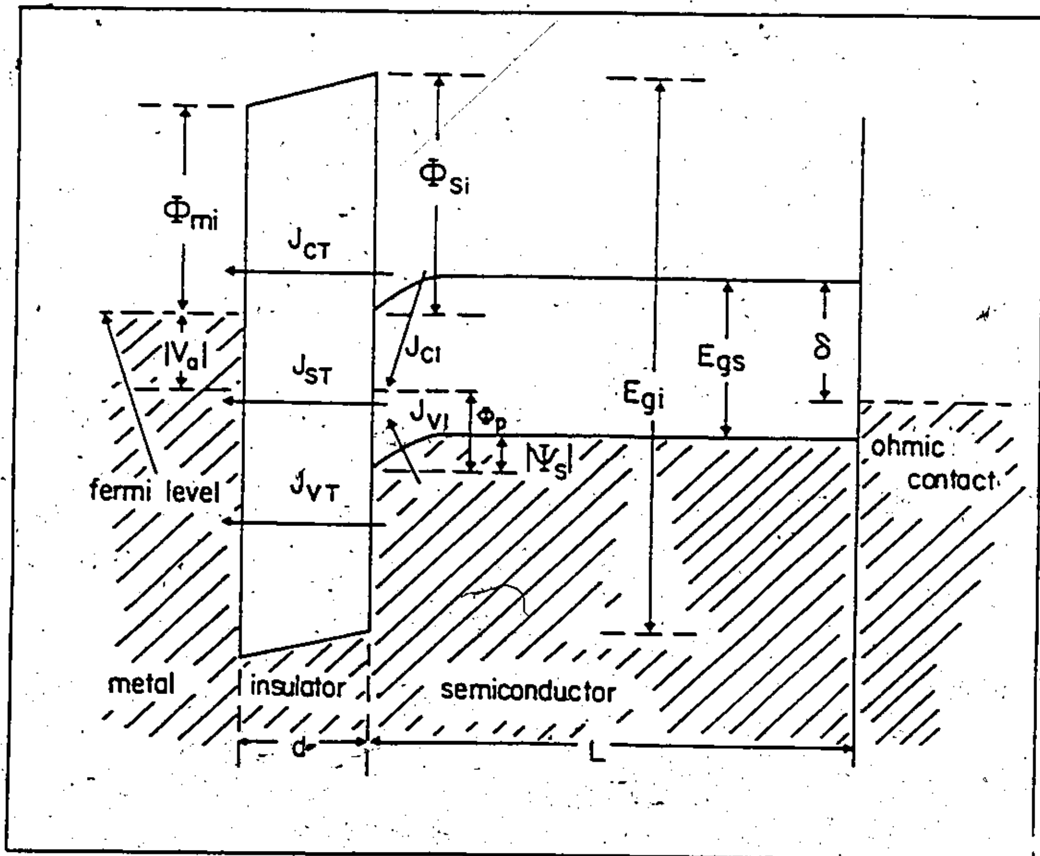

Figure 3.5

tive minority carrier bands over a limited bias range. This is shown in Figure 3.6 where the SIS diode has a forward vias V_A. As the junction is further forward biased, the semiconductor current increases eventually to a value larger than that which can be supported by the tunneling process. This becomes the tunnel limited regime of operation. At the start of this regime the electron quasi-fermi level becomes unpinned with respect to the conduction band edge. Prior to this bias point, the SIS diode operates as a pseudo p-n junction and, in the absence of defects, would be an ideal Shockley diode. Figure 3.7 shows a band diagram with the diode operating in the photovoltaic mode near the maximum power point. The electron and hole quasi-Fermi levels reflect the light induced generation of carriers.

We shall now find an expression for the barrier height of MIS and SIS solar cells. An inspection of the energy band diagram shown in figure 3.1 gives the following relation:

$$\phi'_{mi} + \Delta v_i = \phi_{si} + E_{gs} - \phi_p$$

or

$$\phi_p = E_{gs} + \phi_{si} - \phi'_{mi} - \Delta v_i . \qquad (3.19)$$

Here ϕ_p is the barrier height of a p-type MIS solar cell, which governs the open-circuit voltage V_{oc} of the device. Δv_i is the potential drop across the insulator and ϕ'_{mi} is the effective metal-insulator work function given by:

Figure 3.6

Schematic energy-band diagram of the minority carrier ITO-SiO_x-(p-type)Si tunnel diode system without illumination. The device is biased positively by a voltage V_a with respect to the top ITO layer. J_{CT} and J_{VT} are the current flows from the conduction and valance bands of the Si to the ITO layer. J_{ST} is a flow from surface states to the ITO and is supplied by J_{CI} and J_{VI}. Also shown in the diagram are the electron and hole Fermi levels in the semiconductor.

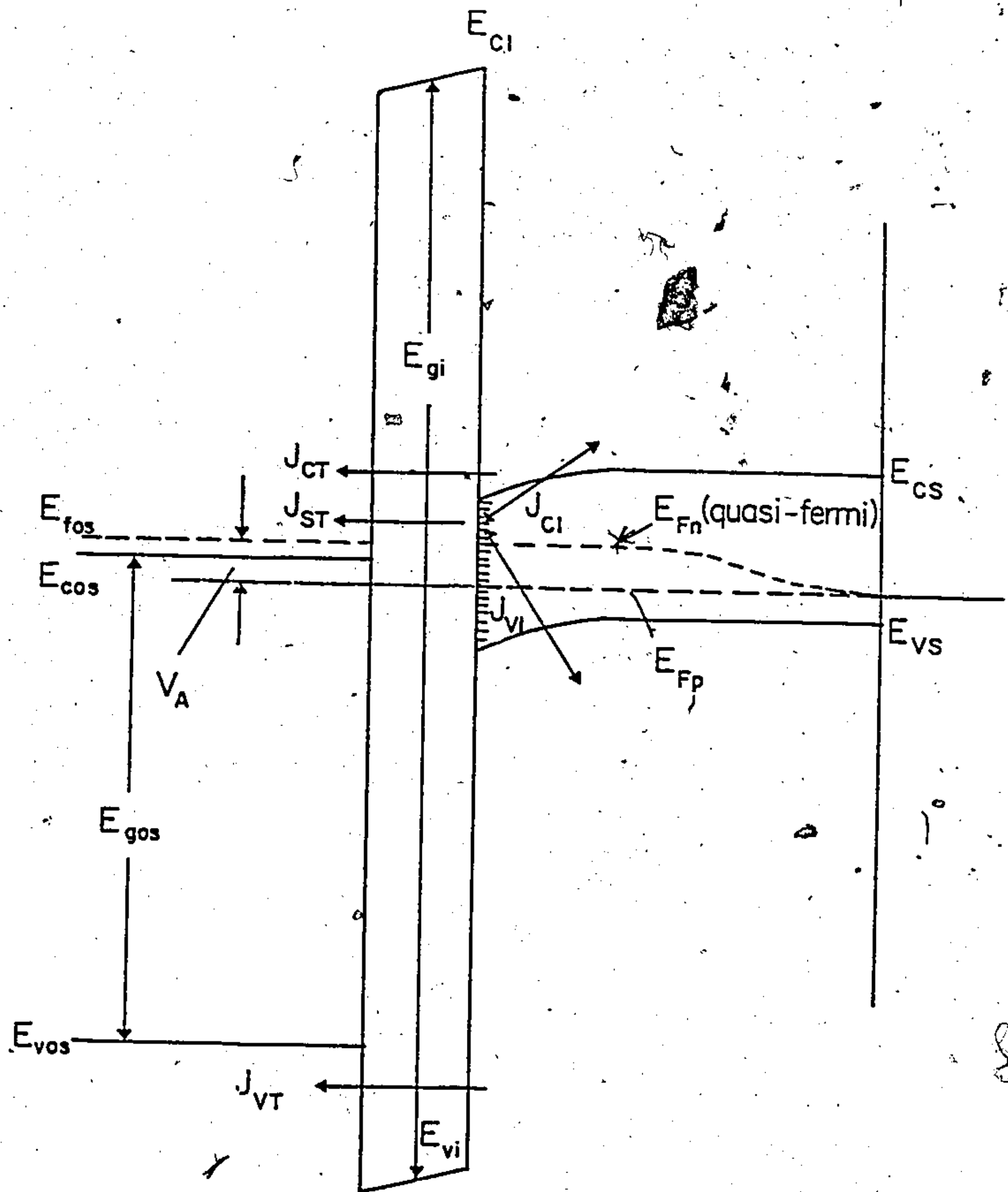

Figure 3.6

Figure 3.7

Energy band diagram of the ITO-SiO_x-(p-type)Si tunnel diode system near the maximum power conditions under illumination.

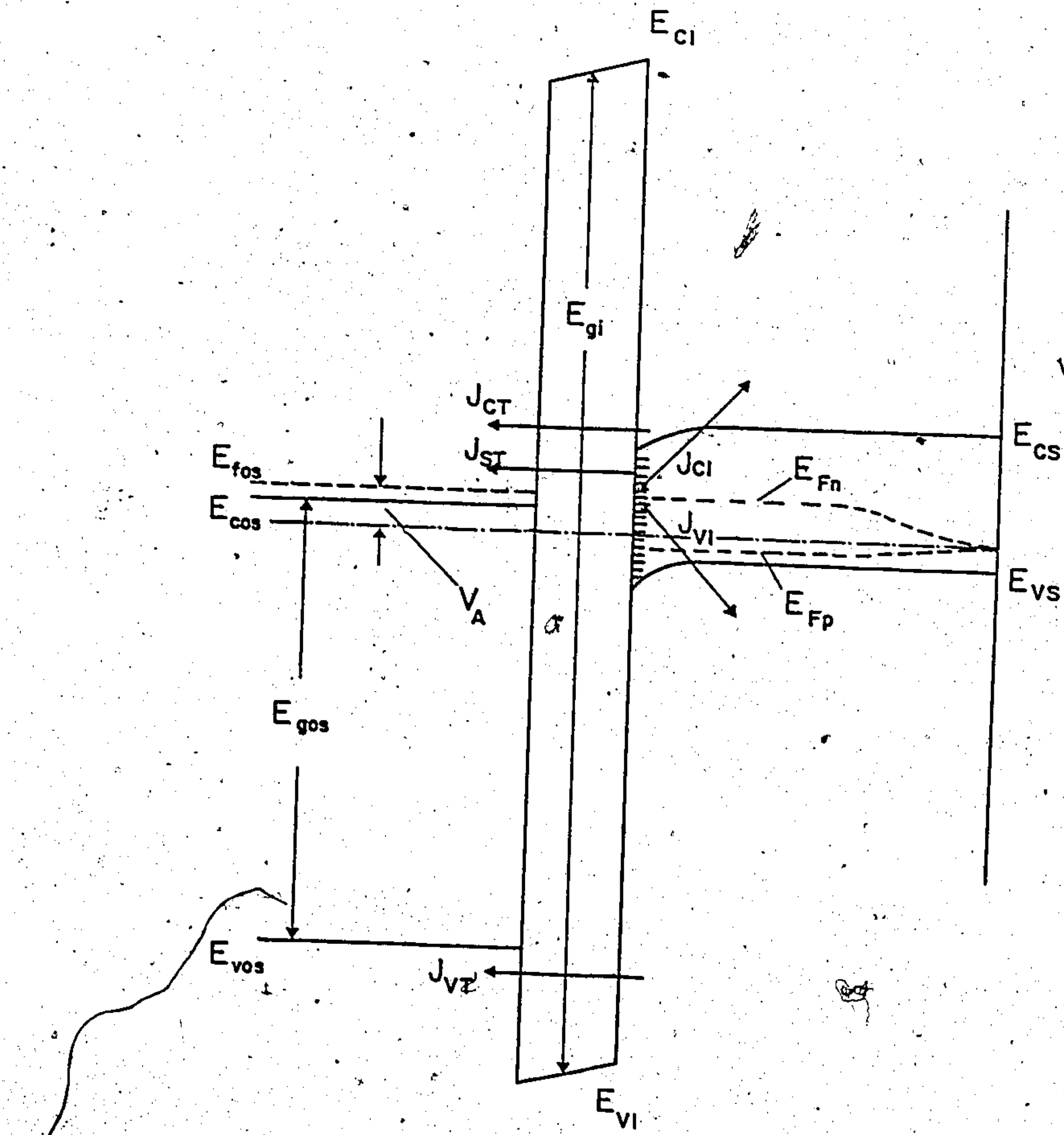

Figure 3.7

$$\phi'_{mi} = \phi_{mi} - \frac{q(Q_{ss}+Q_i)d}{\varepsilon_i} . \quad (3.20)$$

In the above expression Q_{ss} and Q_i are the charge densities due to charges in the surface states and insulator. The potential drop across the insulator is given by:

$$\Delta v_i = F_s d \quad (3.21)$$

where F_s is the electric field strength at the surface. Substituting equation (3.20) and (3.21) into equation (3.19), the barrier height of a p-type MIS solar cell is given by:

$$\phi_p = E_{gs} + \phi_{si} - \phi_{mi} - F_s d + \frac{q(Q_{ss}+Q_i)d}{\varepsilon_i} . \quad (3.22)$$

Similiar consideration of Figure 3.4 gives the barrier height of a p-type SIS solar cell and is given by

$$\phi_p = E_{gs} + \phi_{si} - \phi_{osi} + \Delta - F_s d + \frac{q(Q_{ss}+Q_i)d}{\varepsilon_i} . \quad (3.23)$$

For an n-type MIS solar cell the barrier height is given by

$$\phi_n = \phi_{mi} - \phi_{si} - F_s d - \frac{q(Q_{ss}+Q_i)d}{\varepsilon_i} . \quad (3.24)$$

The barrier height of an n-type SIS solar cell is given by

$$\phi_n = \phi_{osi} - \Delta - \phi_{si} - F_s d - \frac{q(Q_{ss}+Q_i)d}{\varepsilon_i} . \quad (3.25)$$

From equations (3.22) and (3.23) one can observe that

in order to have a barrier height ϕ_p close to the energy-band gap of the base-semiconductor, one has to select the top contact such that the work function of the metal or the conducting oxide-semiconductor is less than or equal to the electron affinity of the semiconductor. For n-type MIS and SIS solar cells, the top layer work function should be roughly equal to or greater than the sum of the energy-band gap and the electron-affinity of the base-semiconductor. This agrees with the earlier conclusion that for MIS and SIS tunnel diodes, ϕ_{mi} or ϕ_{osi} should have low values for the p-type base-semiconductors and high values for n-type base-semiconductors. The thickness of the insulator should be kept small, in order to have minimum potential drop across it. For p-type base-semiconductors, positive insulator charge increases the barrier height, and the converse applies for n-type semiconductors. Donor-type surface states increase the barrier height of p-type MIS solar cells, while the acceptor-type states decrease it. Converse argument holds for n-type MIS solcar cells.

Most of the numerical calculations have been done for p-type Si MIS and SIS solar cells. The results are equally valid for n-type Si and other semiconductors. One problem faced during this work was lack of an analytical expression for Si parameters. We have collected expressions for minority carrier lifetime, intrinsic carrier concentration, mobility and energy

gap from the literature. These Si parameters in analytical forms are discussed in Appendix B.

The data for photon-flux were taken from NASA Lewis [63(a), 63(b)] for various air masses and have been tabulated in the interval of 0.005 μm in Appendix B. Most of the calculations have been done for AM2 with solar constant 74.9 mw/cm^2. Some calculations have also been done for AM1 (solar constant 92.2 mw/cm^2 or 100 mw/cm^2).

3.3.5. Dark I-V Characteristics of MIS and SIS Solar Cells

Figure 3.8 contains the calculated dark I-V characteristics for an MIS and SIS diode. Characteristics for an Al-SiO_2-Si diode with a 2 Ω-cm, p-type base semiconductor are shown in Figure 3.8a. This calculation was for the ideal case without defects at the oxide-semiconductor interface or within the oxide itself. The variable parameter is the insulator thickness. It is seen that as the insulator thickness is decreased, the characteristics tend to converge to a locus curve in both the forward and reverse directions of bias. This is the ideal Shockley-diode characteristic. The equation for the ideal diode or Shockley diode is of the form

$$J = J_S[\exp(\frac{qV}{nkT}) - 1]$$

with n = 1. The convergence of the reverse bias curves on the Shockley diode characteristic at around 28 Å is an indication

Figure 3.8

(a): Computed dark I-V characteristics of the MIS tunnel diode. The substrate is 2 Ω-cm p-type <100> silicon, ϕ_{mi} is equal to 3.2 eV, and the variable parameter is d, the thickness of the insulator. Other device parameters are listed in Table 3.5.

(b): Computed I-V characteristics of the ITO-Si-SIS tunnel diode demonstrating "non-equilibrium" effects for minority-carrier devices. The substrate is 2 Ω-cm, p-type <100> silicon. The variable is d, the thickness of the interfacial layer. Other device parameters are given in Table 3.5. Surface states have the distribution of Figure 3.9 and the insulator charge Q_i was taken as 5×10^{15} m^{-2}.

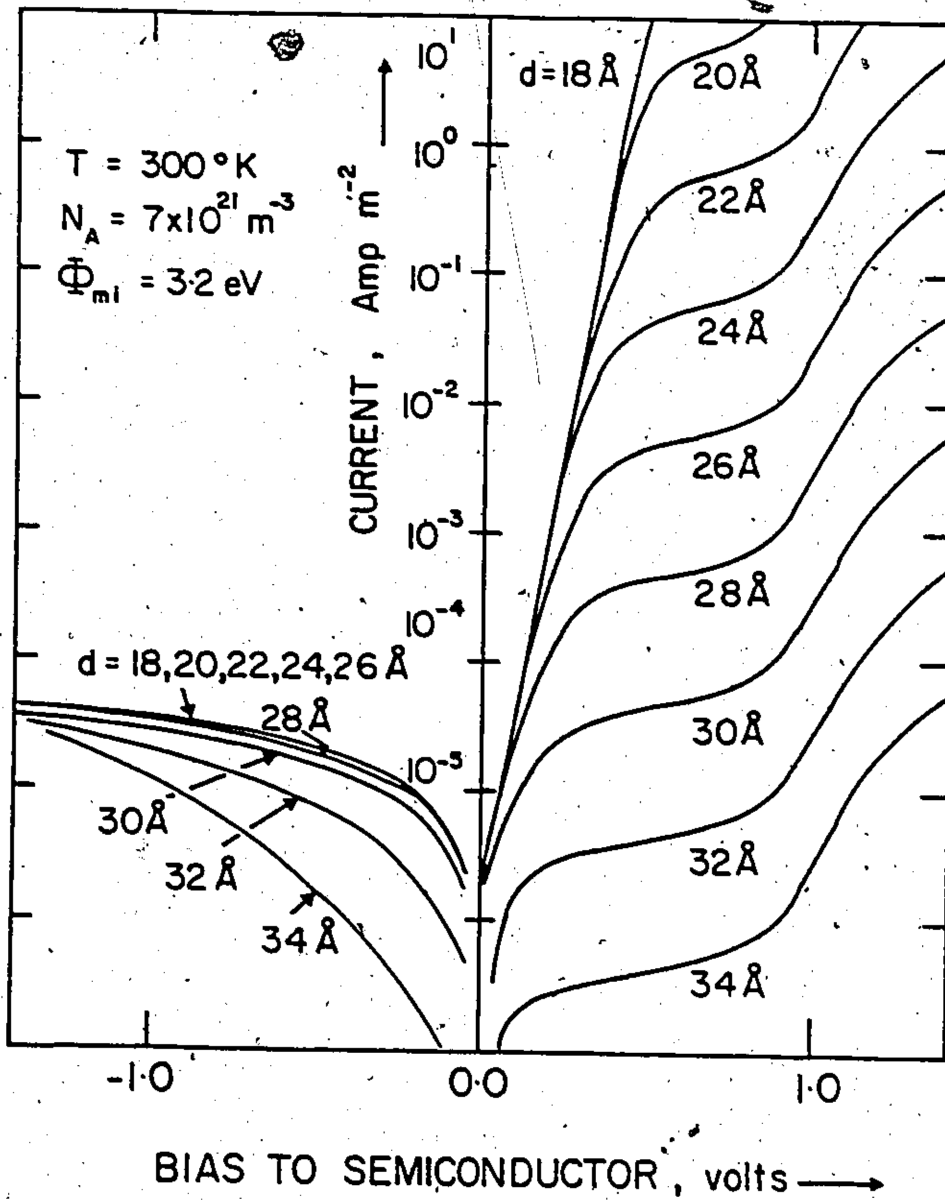

Figure 3.8(a)

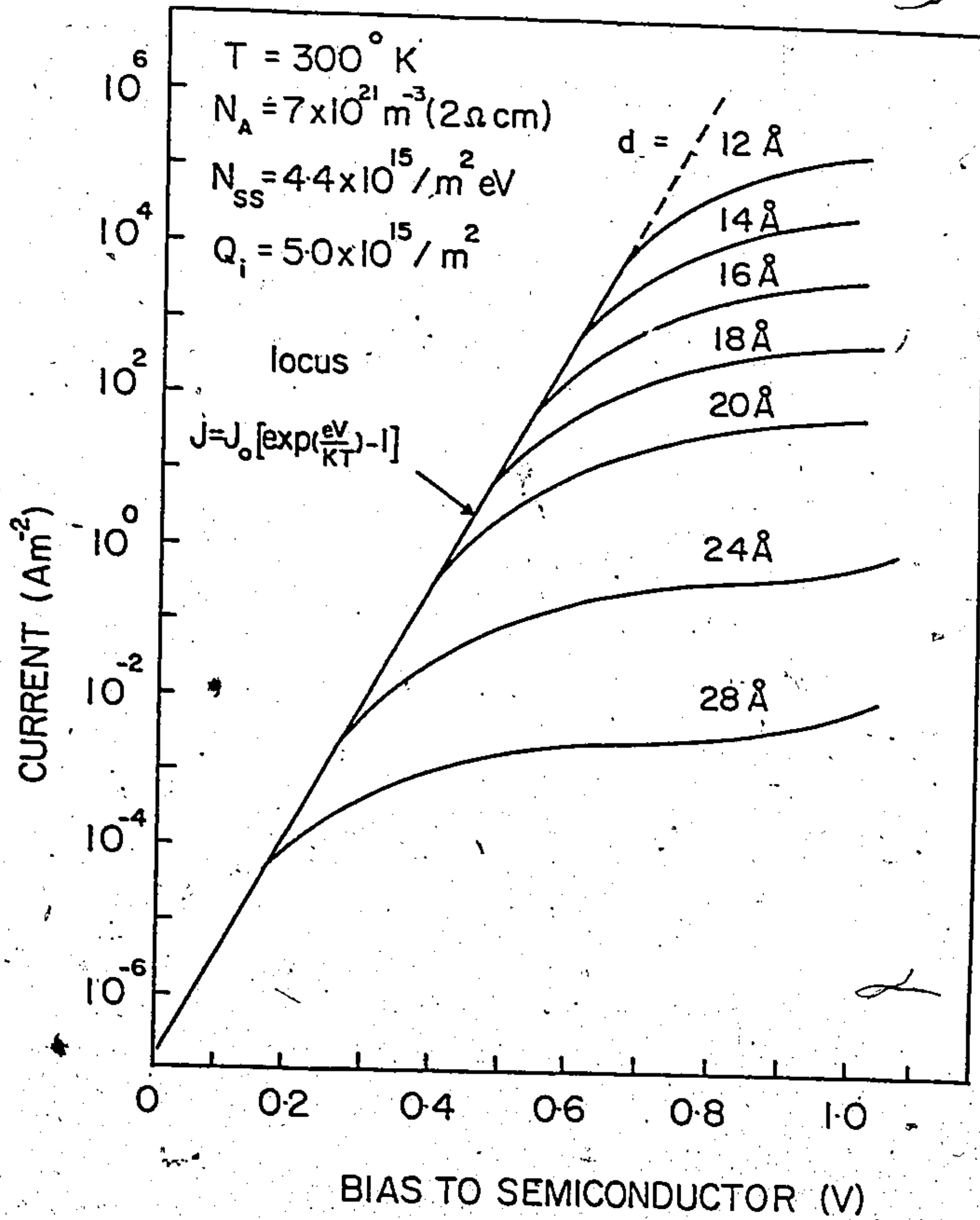

Figure 3.8(b)

of the transition from equilibrium to non-equilibrium operation. In forward bias, the departure from the ideal diode locus indicates the changeover from semiconductor limited operation to tunnel limited operation. Even at 28 Å this departure point occurs at very low forward biases. As the interfacial layer or oxide layer thickness decreases, the departure point shifts to higher and higher biases. Since, with silicon p-n junctions under normal AM1 illumination, about 0.5-0.7 volts is developed across the junction, Figure 3.8a indicates that significant conversion efficiency would not occur for insulator thicknesses much above 20 Å. Above 20 Å one would expect a large degree of photocurrent suppression due to the I-V characteristic, much as observed in p-n junction solar cells with a large series resistance. In fact, we can think of the tunnel limited regions as being equivalent to series resistance.

Figure 3.8b shows a similar calculation for an SIS diode, also on a 2 Ω-cm p-type silicon base semiconductor. In this calculation, oxide defects and interface states of Figure 3.9 have been included and the region below 28 Å plotted more extensively. Numerical values assigned to system parameters are given in Table 3.5. It can be seen more readily that for a solar cell output voltage of 0.5 v, interfacial layers of less than 16 Å are required to avoid tunnel limited operation and its incumbent series resistance effect.

Figure 3.9

Assumed distribution of surface states across the energy band gap of silicon. The states below midgap were treated as donor-type levels while those aboce midgap were modelled as having acceptor-type properties. At midgap, the density of surface states $N_{SS} = 4.4\times10^{15}\ eV^{-1}\ m^{-2}$.

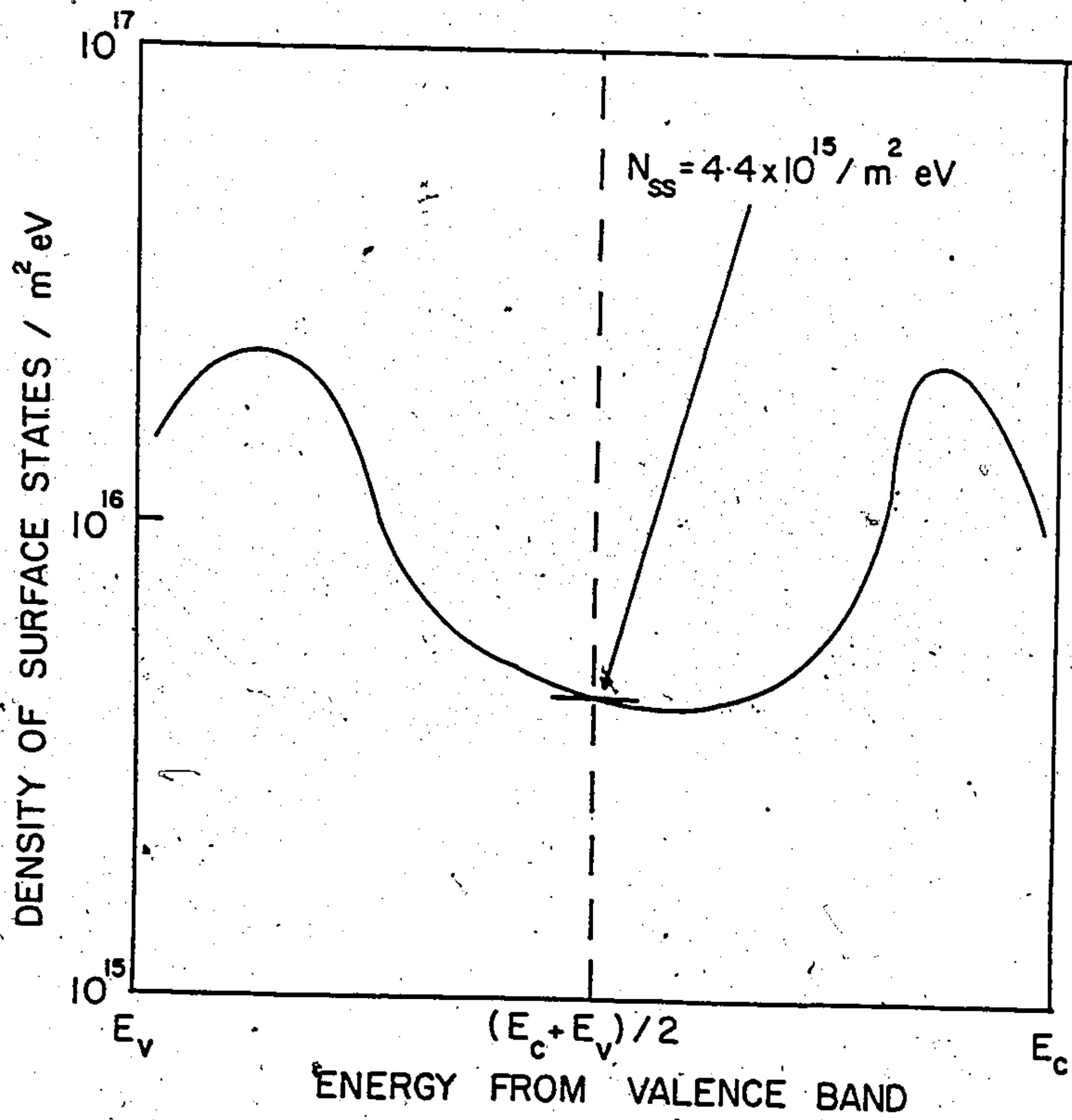

Figure 3.9

TABLE 3.5

NUMERICAL VALUES ASSIGNED TO SYSTEM PARAMETERS FOR CALCULATING Si MIS AND SIS SOLAR CELL PERFORMANCE

Parameter	Numerical Value
T	300 °K
ϕ_{si}	3.2 eV
E_{gi}	8.0 eV
E_{gs}	1.1 eV
n_i	1.5×10^{16} m^{-3}
N_c/N_v	1.73
ε_i	3.82 ε_0
ε_s	11.7 ε_0
Δ	-0.1 eV
n_1	n_i
p_1	n_i
m_i, m_{Ti}, m_{Ts}	0.65 m_0
σ_n	10^{-19} m^{-2}
σ_p	10^{-19} m^{-2}
σ_t	10^{-19} m^{-2}
v_{th}	1.17×10^{5} m/sec
L	2.5×10^{-4} m
F_A	0.045 eV

3.4 EFFECT OF VARIOUS PARAMETERS ON THE PERFORMANCE OF MIS AND SIS SOLAR CELLS

Due to lack of available experimental data, in most of the calculations we have assumed a zero optical reflection at the front surface. Some calculations have been done for n-ITO/p-Si solar cells with reflection loss. The following are the main parameters that affect the performance of MIS and SIS solar cells:

i) interfacial layer thickness
ii) resistivity of the substrate
iii) surface states and insulator charge
iv) metal or oxide-semiconductor work function
v) temperature
vi) intensity
vii) minority carrier life time
viii) crystallographic orientation
ix) band gap of the base-semiconductor .

The effects of the above mentioned parameters will be examined in turn in the following sections.

3.4.1 Effect of Interfacial Layer Thickness

Obviously, one key parameter which controls the conversion efficiency of tunnel MIS and SIS solar cells is the interfacial layer thickness. In Al-SiO_x-Si and ITO-SiO_x-Si, the appropriate range of thickness is 10-30 Å, the upper limit being the value at which the Si MIS and SIS diodes would revert

to equilibrium mode operation and the lower limit being the value beyond which Schottky diode behaviour sets in. That there should be a dependence of conversion efficiency on insulator thickness over this range has already been commented on and is readily apparent from Figure 3.8.

Figure 3.10 shows the results of calculations of conversion efficiency of MIS and SIS solar cells as a function of insulator thickness. In the case of MIS solar cells the calculations have been carried out for two typical values of substrate resistivity (0.07 Ω-cm and 2.0 Ω-cm). The calculations for SIS solar cells have been carried out for substrate resistivities of 0.2 Ω-cm and 2.0 Ω-cm. As expected, the efficiency is very low until the interfacial layer thickness drops below about 20 Å and then there is a rapid rise with a saturation in a plateau at about 15 Å. These calculations are not for an "ideal" case since moderate values of surface state density and oxide charge have been included as indicated.

In the region between 15 Å and 20 Å, the drop in efficiency with increasing thickness can be thought of as due to an increasingly effective series resistance as a result of two components: (a) the exponential change in tunnel current with thickness, (b) the change in the I-V characteristic due to the transition from the semiconductor current-limited mode to the tunnel current-limited mode. This is supported by the calculations of short-circuit current, J_{sc}, and fill factor, FF, which are presented in Figure 3.11. Both show a marked simi-

Figure 3.10

(a): Computed effect of insulator thickness on conversion efficiency of an Al-SiO_x-(p-type)Si solar cell with carrier concentration as a parameter. Surface states have the distribution of Figure 3.9 and the insulator charge has the value 5×10^{15} m^{-2}. All other parameters are listed in Table 3.5.

(b): Computed effect of insulator thickness on conversion efficiency of an ITO-SiO_2-(p-type)Si tunnel diode with carrier concentration as a parameter. Surface states have the distribution of Figure 3.9 and the insulator charge has the value 5×10^{15} m^{-2}. All other parameters are listed in Table 3.5.

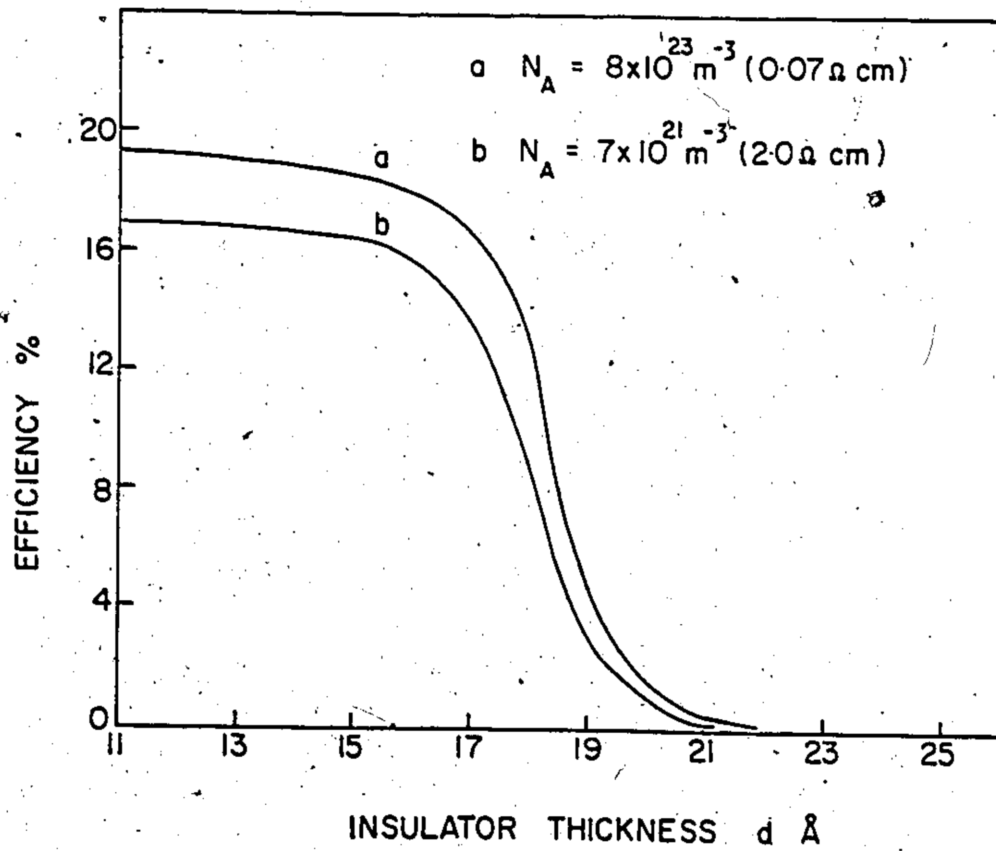

Figure 3.10(a)

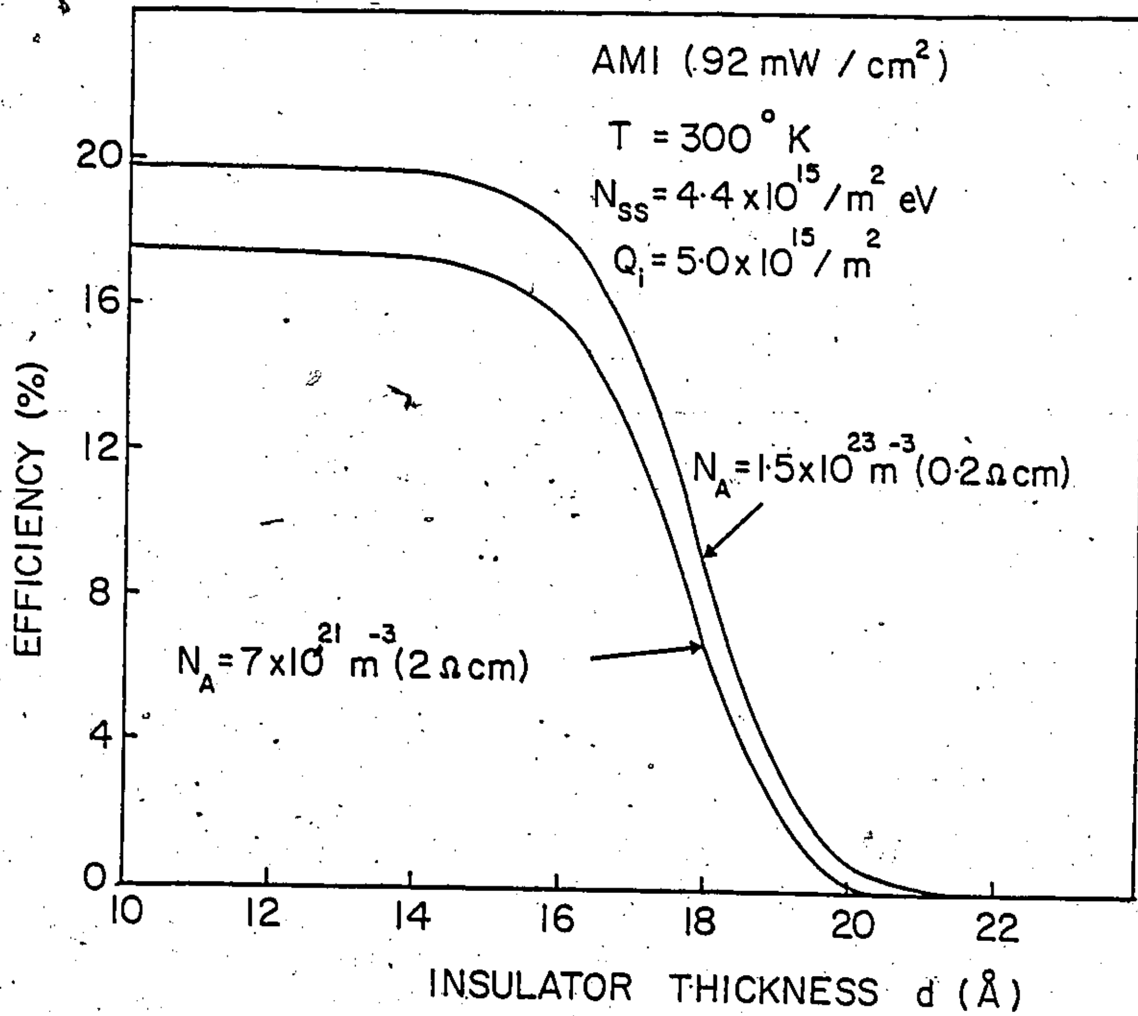

Figure 3.10(b)

Figure 3.11

(a): The variation of short-circuit current Density J_{SC}, open-circuit voltage V_{oc}, and fill factor as a function of insulator thickness for an Al-SiO_x-(p-type) diode with carrier concentration of 8×10^{23} m^{-3}. All other parameters are the same as for data in Figure 3.10(a).

(b): The variation of short-circuit density J_{SC}, open-circuit voltage V_{oc}, and fill factor, FF, as a function of insulator thickness for an ITO-SiO_x-(p-type)Si tunnel diode with carrier concentration as a parameter. All other parameters are the same as for data in Figure 3.10(b).

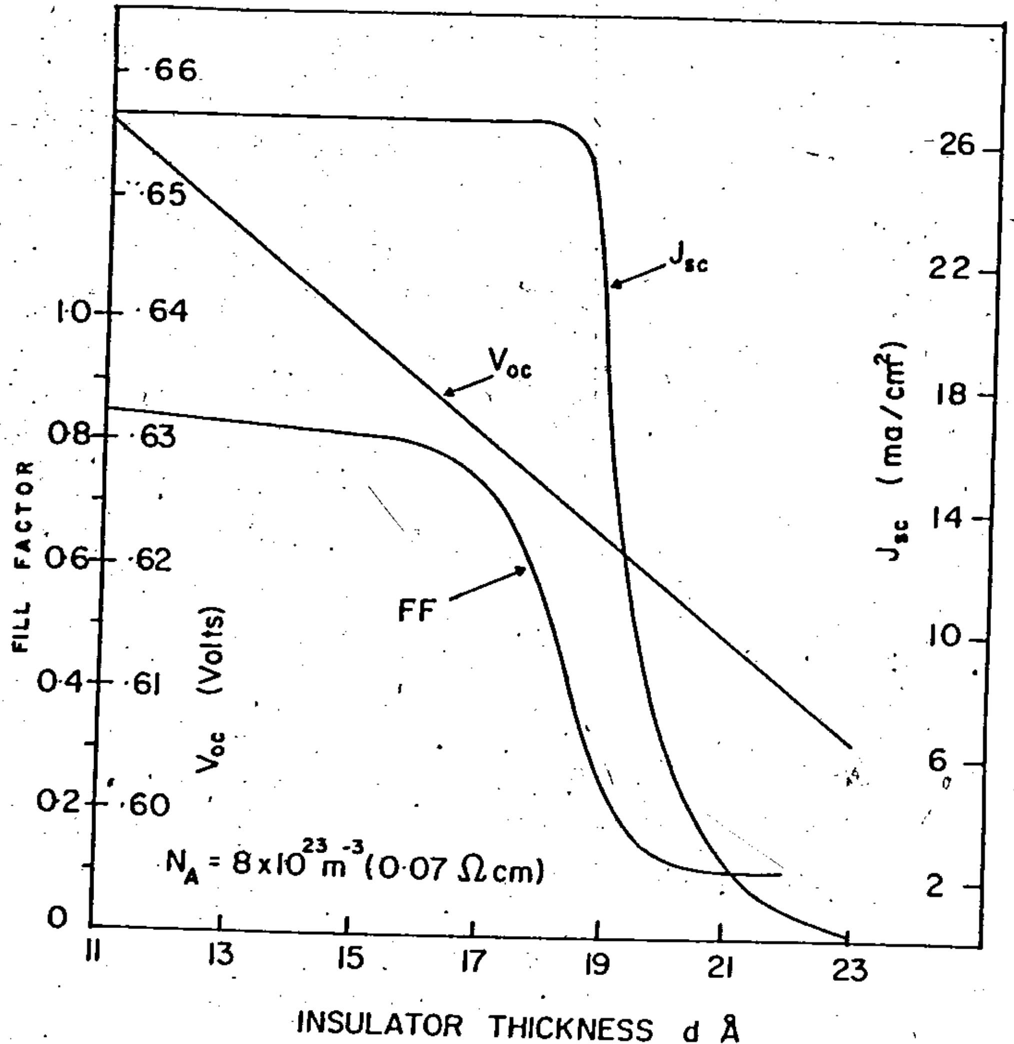

Figure 3.11(a)

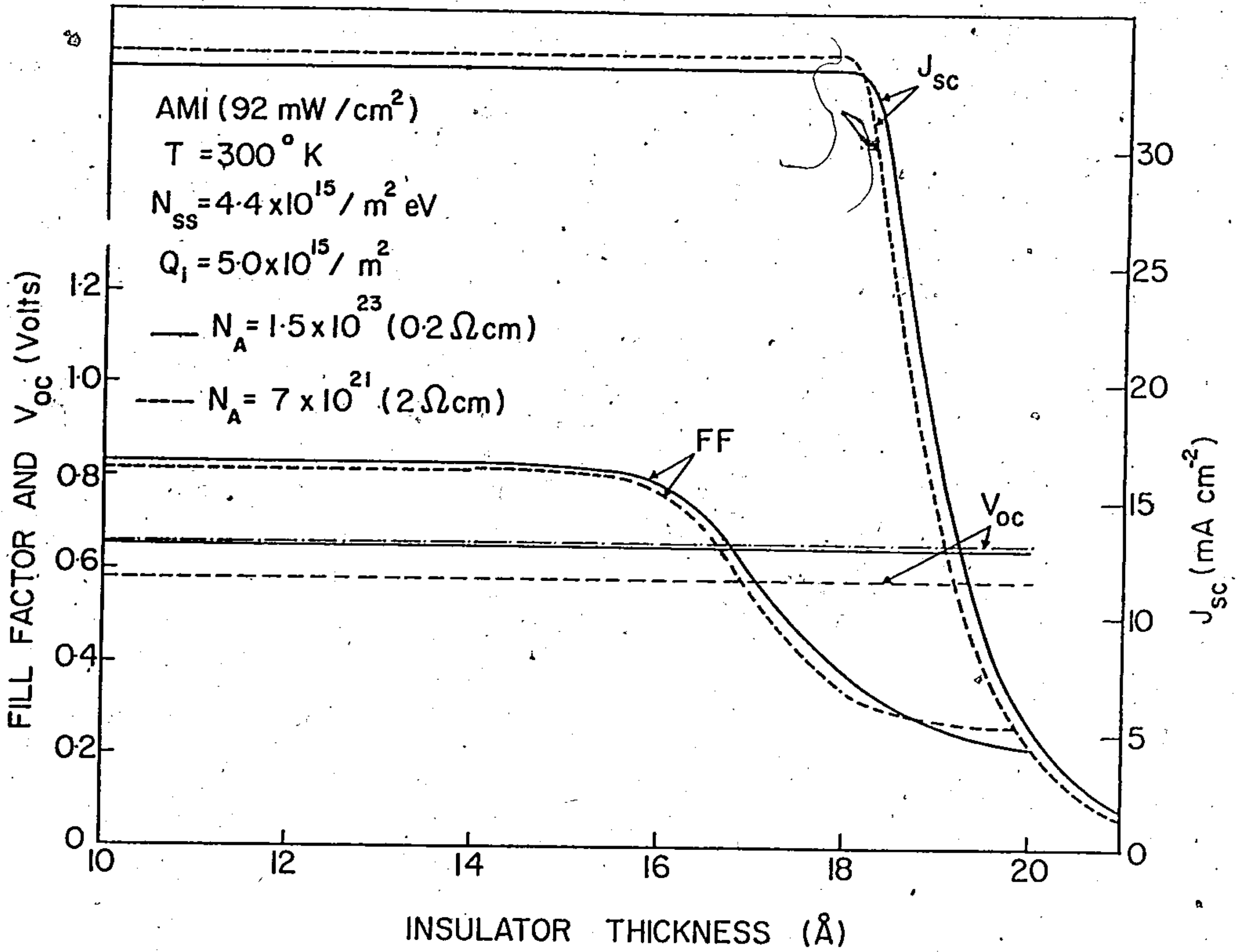

Figure 3.11(b)

larity in form to the efficiency curves in Figure 3.10. As noted, below about 15 Å, the efficiency curves saturate in a plateau. The explanation is that at some point the tunneling occurs at such a rate that the resistance via this process is insignificant. All possible current from the semiconductor is being extracted and changes can only occur with changes in illumination. thus the efficiency saturates.

It is also seen in Figure 3.10 that an increase in doping also causes an increase in the conversion efficiency. This is attributable to an increase in the barrier height, more about which will be said in a later section. This behaviour is similar to a p-n junction solar cell, since the increase in doping level decreases the dark current, which corresponds to an increase in the open-circuit voltage of the device.

From Figure 3.11, it is seen that the open-circuit voltage, V_{oc}, varies rather slowly with insulator thickness and in an apparently linear fashion. Also, it is observed from Figure 3.11 that the rate of decrease of V_{oc} increases with increase in the doping density of the base-semiconductor. These features can be explained by considering that in the thickness range of interest, the base-semiconductor surface is inverted. Under such conditions, the difference of the electron and hole quasi fermi levels will be approximately equal to the open-circuit voltage. In other cases, where the minority-carrier quasi fermi level is not pinned to the fermi level in the metal, the open-circuit voltage will be small compared to the pinned case.

with increase in doping density, the degree of semiconductor surface inversion also decreases. As the thickness of the insulator increases, the potential drop across the insulator also increases, which reduces the open-circuit voltage of the device. The linear dependence can be explained from equation (3.22) or (3.23) i.e.

$$\phi_p = E_{gs} + \phi_{si} - \phi_{mi} - F_s d + \frac{q(Q_{ss}+Q_i)d}{\varepsilon_i} \quad \text{-- MIS case} \quad (3.22)$$

$$\phi_p = E_{gs} + \phi_{si} - \phi_{osi} + \Delta F_s d + \frac{q(Q_{ss}+Q_i)d}{\varepsilon_i} \quad \text{-- SIS case} \quad (3.23)$$

For any given situation, the $(Q_{ss}+Q_i)$ term may be positive or negative depending on the surface state density and insulator charge. The values used in the present calculation give a positive value for this term. Thus, there is a linear decrease in ϕ_p with increasing d and hence a linear decrease in V_{oc}. Of course, the assumption used, that the surface state density N_{ss} and insulator charge Q_i are insulator thickness independent, may not be valid in practice. More will be said about this later, when we will compare theory with experimental results.

As can be seen from Figure 3.11, the short circuit current density is constant up to about 20 Å, after which it starts decreasing. Up to a certain thickness, the minority carrier-quasi fermi level is pinned to the metal fermi level, as shown in Figure 3.12(a). The short circuit current density for a p-type MIS solar cell is approximately given by

Figure 3.12

Schematic energy-band diagram for a p-type MIS solar cell under short circuit condition.

(a) The minority carrier quasi Fermi level is pinned to the metal Fermi level.

(b) The minority carrier quasi Fermi level is not pinned to the metal Fermi level.

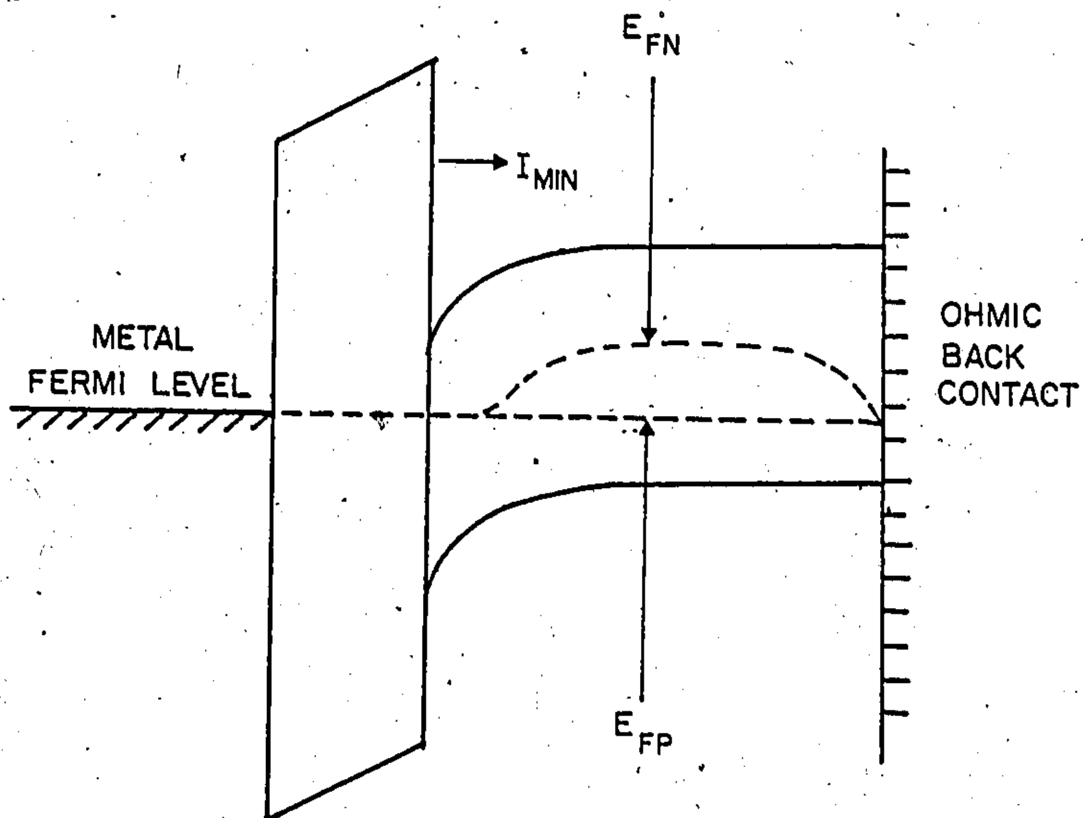

Figure 3.12(a)

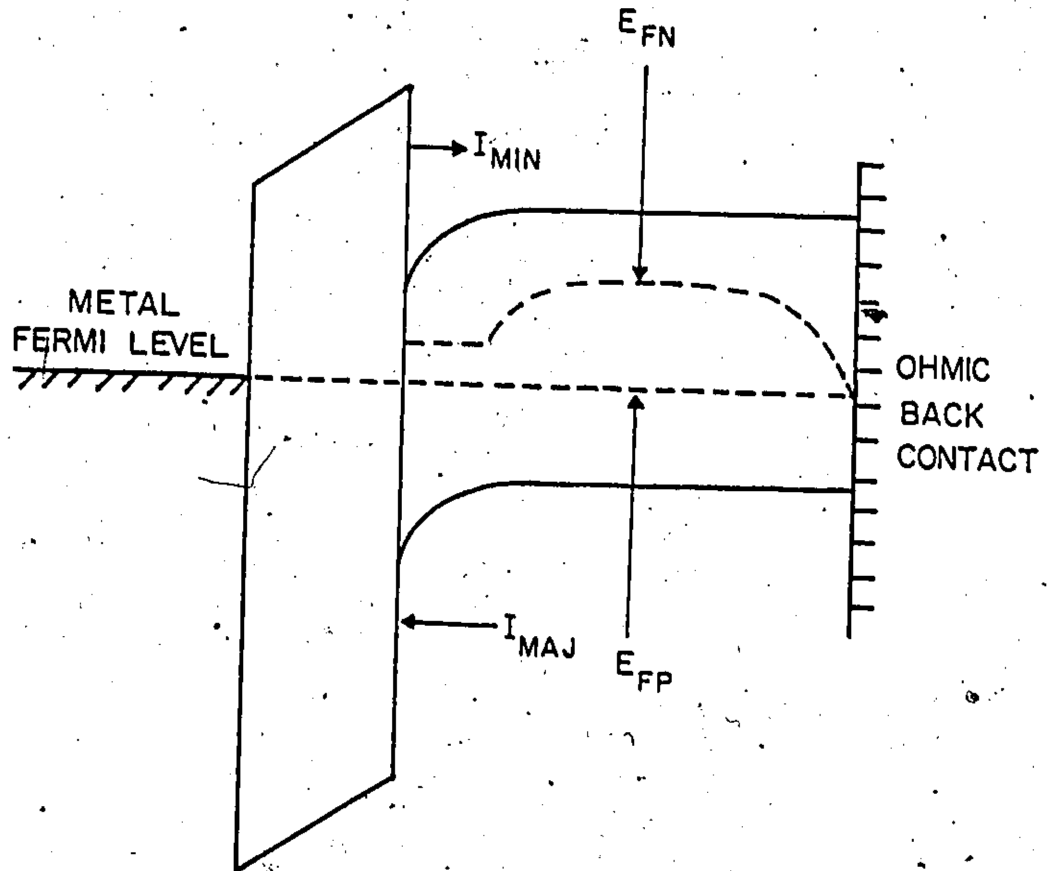

Figure 3.12(b)

$$J_{sc} \approx J_n$$

where

$$J_n = n\mu_n \frac{dE_{fn}}{dx} . \qquad (3.24)$$

The electrons reaching at the semiconductor-insulator interface that crosses the tunneling barrier, will constitute most of the short circuit current. So we can write (3.24) as

$$J_n = n_s \mu_n \frac{dE_{fn}}{dx}$$

$$n_s = N_c \exp\left[\frac{E_{fn}(0)-E_c(0)}{kT}\right] . \qquad (3.25)$$

In Figure 3.12(b) we have shown the case of an unpinned MIS solar cell under short-circuit conduction. The change in the position of minority carrier quasi fermi level is mainly responsible for decreasing J_{sc}, when the insulator thickness is increased after a certain limit (∿ 20 Å in the present case). Similar reasoning applies to SIS solar cells.

The fill factor of an MIS and SIS solar cell decreases as the insulator thickness is increased. As can be seen from Figure 3.11, below about 15 Å the fill factor decreases very slowly and is practically constant. In this region (10-15 Å), the tunnel current can flow without any significant resistance offered by the insulator layer. After about 15 Å, the fill factor starts decreasing due to the increased resistance of the insulator layer. It is worth mentioning here that in practice,

there will be some potential drop across the top layer and the sheet resistivity of the top layer will also contribute to the series resistance of the device. This effect will be treated in a later chapter covering the loss mechanism associated with SIS solar cells.

3.4.2 Effect of Substrate Resistivity

We have calculated the effect of substrate resistivity on the performance of MIS and SIS solar cells. In Figure 3.13, we have shown the conversion efficiency, open-circuit voltage, short-circuit current density and fill factor as a function of doping density. The effect of base-semiconductor resistivity on the conversion efficiency of SIS solar cells is shown in Figure 3.14. In both MIS and SIS cases the calculations have been done for a low value of insulator thickness so that the effect of the insulator is minimal. Surface states and insulator charge have been included as before.

There are several semiconductor parameters which depend on the doping level such as diffusion length (through mobility and minority carrier lifetime variation), carrier concentration, Fermi-level position and absorption coefficient. The modeling of mobility and minority carrier lifetime as a function of doping level is presented in Appendix B. The variation in carrier concentration and Fermi level is automatically calculated in the usual way as part of the calculational routine for the transport equations. We have assumed an absorption coefficient independent of impurity concentration which is reasonable over

Figure 3.13

Effect of doping density on the conversion efficiency, open-circuit voltage short circuit current density and fill factor of an Al-SiO_x-(p-type)Si solar cell. The thickness of the insulator is 14 Å and the surface states have the distribution of Figure 3.9.

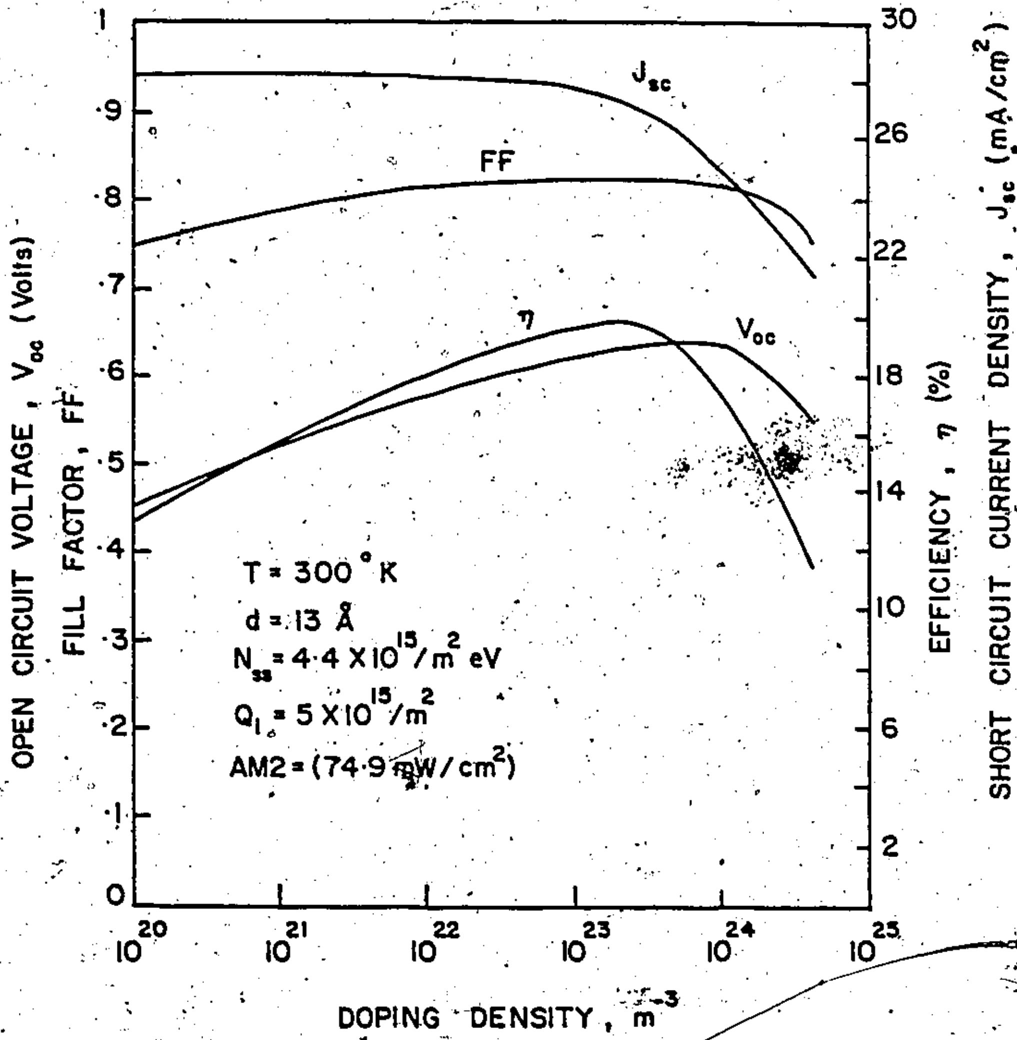

Figure 3.13

Figure 3.14

Effect of doping density on conversion efficiency of an ITO-SiO_x-(p-type)Si tunnel diode. Surface states have the distribution of Figure 3.9 and the insulator charge has the value of $5 \times 10^{15}\ m^{-2}$. All other parameters are listed in Table 3.5.

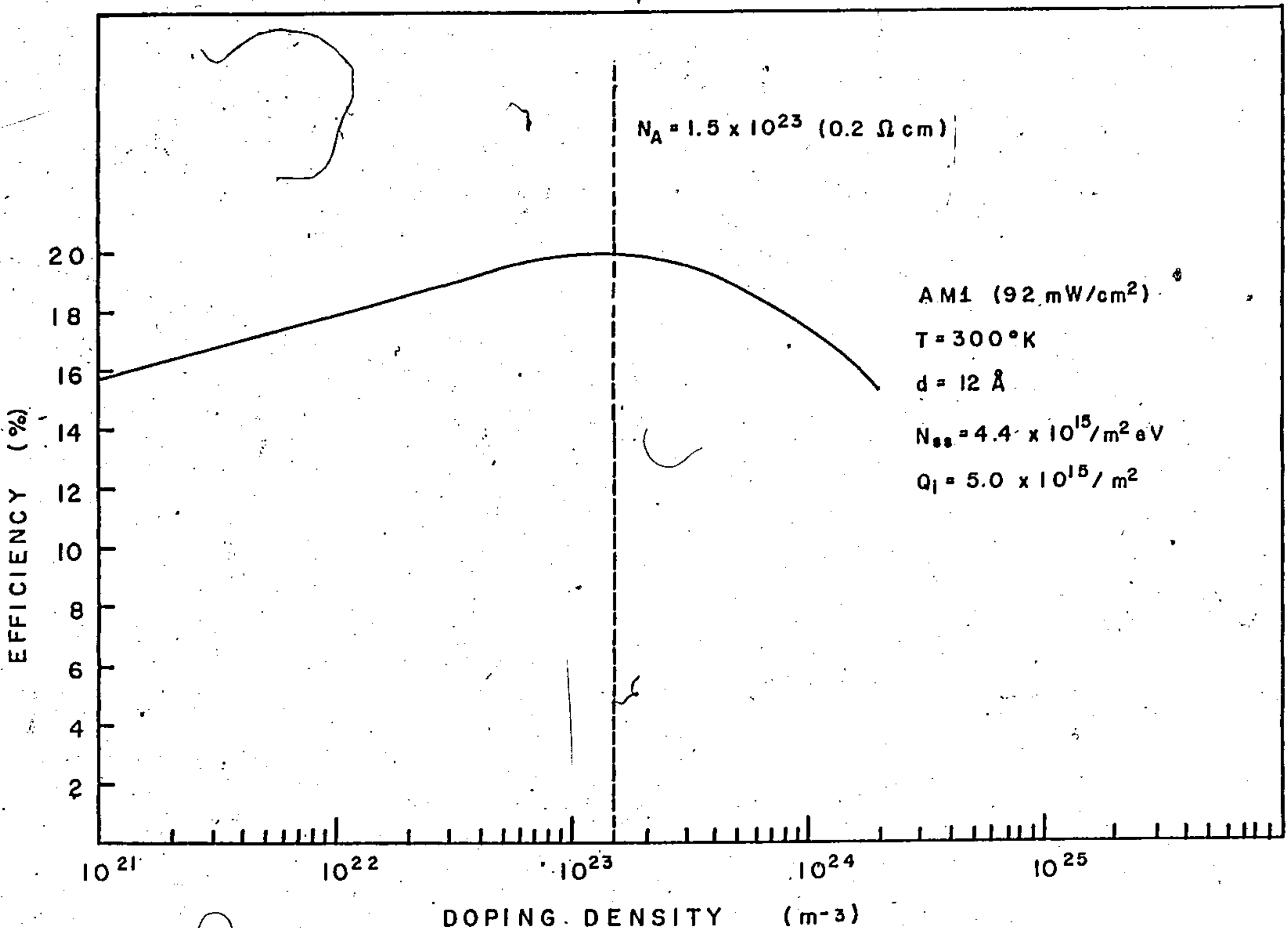

Figure 3.14

the range of our calculations.

With increase in doping intensity, the open-circuit voltage increases since the Fermi level shifts closer to the band edge, resulting in increase of the barrier height. After a certain doping density (4×10^{23} m^3), the open-circuit voltage starts decreasing as the device becomes a majority carrier device rather than a minority carrier device. In such cases, the difference of the electron and hole quasi Fermi level in the base-semiconductor will not be equal to the difference of top layer Fermi level and hole quasi Fermi level. It is worth mentioning here that the term minority carrier device implies that only at near zero bias is the minority carrier injection ratio, i.e. minority carrier current divided by total device current, about unity. After this doping density the open-circuit voltage start falling off. Although, in the present calculations at higher doping level, we have not included the Auger recombination, since the peak efficiency is not in the heavily doped region. But in any model for doping density greater than 10^{25} m^3, the band gap narrowing [64] and Auger recombination should be included.

The short circuit current density initially decreases with doping level at a very slow rate, due to the degradation in the diffusion length. In this region the device can be thought of as n^+p junction solar cell.

The short circuit current can be given approximately by [65]

$$J_{sc} = qN\alpha L\{[\frac{\exp(-\alpha W)}{1 + \alpha L} - \frac{\exp(-\alpha L)}{(\alpha L)^2 - 1}] \times$$

$$[\frac{\exp(-(1-\alpha L)(L-W)) - 1}{\sinh(L-W)}]\} \qquad (3.26)$$

where W is the width of the semiconductor depletion region plus inversion region and N is photon flux entering the semiconductor per square meter per second. The doping density at which the open-circuit voltage V_{oc} starts falling is the same as when the J_{sc} also starts falling, since in this region, the majority carrier current becomes the dominating loss for the total current of the device under illumination.

It can also be seen from Figure (3.13) that the fill factor initially rises due to the rise in V_{oc} and later it falls due to the fall in V_{oc}. The diode ideality factor also decreases the fill factor, when it increases from the ideal value of one to higher values. This effect in the present case is weak, compared to the V_{oc} effect. The combined effect of increase in V_{oc} and F F and a decrease in J_{sc} with increase in doping level results in a peak efficiency at about 2×10^{23} m^{-3}. After this doping density, the efficiency falls due to degradation in V_{oc}, J_{sc} and F F.

3.4.3 Effect of Surface States and Surface Charge

Out of the four basic electrical charges (surface states, surface charge, mobile ionic charge and ionized traps) in the MIS structure, only the first two greatly influence the properties of the insulator-semiconductor interface. The large density of surface states in a Schottky diode effectively "pins" the Fermi level in the semiconductor near the valence band, making the barrier height low, which results in a low open-circuit voltage. The introduction of a thin insulating layer [< 16 Å in the case of Al-SiO_x-(p-type)Si diode] eliminates this pinning effect, so that the minority carrier quasi-Fermi level is now pinned to the Fermi level in the metal to produce a higher open-circuit voltage. As commented earlier in Figure 3.3, the introduction of the interfacial layer results in a clean insulator-semiconductor (IS) interface, which mainly controls the device's electrical characteristics. However, in most experimental devices, the interface is hardly defect free and these defects associated with the IS interface can cause deviations from the ideal theory.

The effect of surface charge in the insulator region of the device is to change the metal to insulator work function, ϕ_{mi}. For a 15 Å SiO_x layer, a positive charge density of aoubt 1.5×10^{16} m^{-2} located near the IS interface causes an

effective reduction in ϕ_{mi} of about 0.1 eV. Surface states have the following properties:

1) they are charge storage centres,
2) they are recombination-generation centres,
3) they provide additional tunnelling paths between the metal and the semiconductors.

All of these properties of surface states and surface charge were included self-consistently in the model used to characterize tunnel MIS solar cells.

For p-type MIS solar cells, a positive surface charge and donor type surface states will have a beneficial effect on the device performance. In the case of n-type MIS solar cells, a negative surface charge and acceptor-type surface states will have advantageous effects. Thus, both surface states and insulator charge can affect the open-circuit voltage of MIS solar cells, as can be seen from Equation (3.20). A large density of surface states may also affect the short circuit current density.

In the case of thick oxides, a great deal of work has been done in understanding and controlling the interface properties. However, not much is known about ultra-thin oxides (< 40 Å). The distribution of surface states across the energy gap used in our calculations is shown in figure 3.9 and is that most commonly employed for thick oxides. The magnitude was adjusted upward or downward as necessary. States below the mid-

gap were treated as having acceptor-type properties.

The effect of surface states and surface charge on the conversion efficiency is shown in Figure 3.15, which indicates that for insulator thickness less than 14 Å, minimum surface states and surface charge results in maximum conversion efficiency. This statement is valid under our assumption that both surface state density N_{ss}, and insulator charge Q_i are related to each other and both together can be reduced significantly by annealing. Otherwise, a higher positive value of insulator charge increases the photovoltaic efficiency of p-type MIS solar cells. The surface state distribution assumed in our calculations gives a negative charge, which decreases the barrier height of the device. Minimum reduction in V_{oc} is possible only when both N_{ss} and Q_i have negligible contribution. For an insulator thickness, d, less than 14 Å, the surface states have little effect on the current density and significant changes in conversion efficiency result due to a change in open circuit voltage. For d > 14 Å, a large density of surface states gives a higher conversion efficiency as compared to the efficiency for the corresponding case of a low surface state density, since the tunnelling component of current is supplemented by recombination-generation current. However, this higher efficiency is still less than the maximum achievable efficiencies for MIS solar cells.

As we have shown earlier, the maximum efficiency for

Figure 3.15

The effect of surface state density and insulator charge on conversion efficiency versus insulator thickness of an Al-SiO_x-(p-type)Si solar cell.

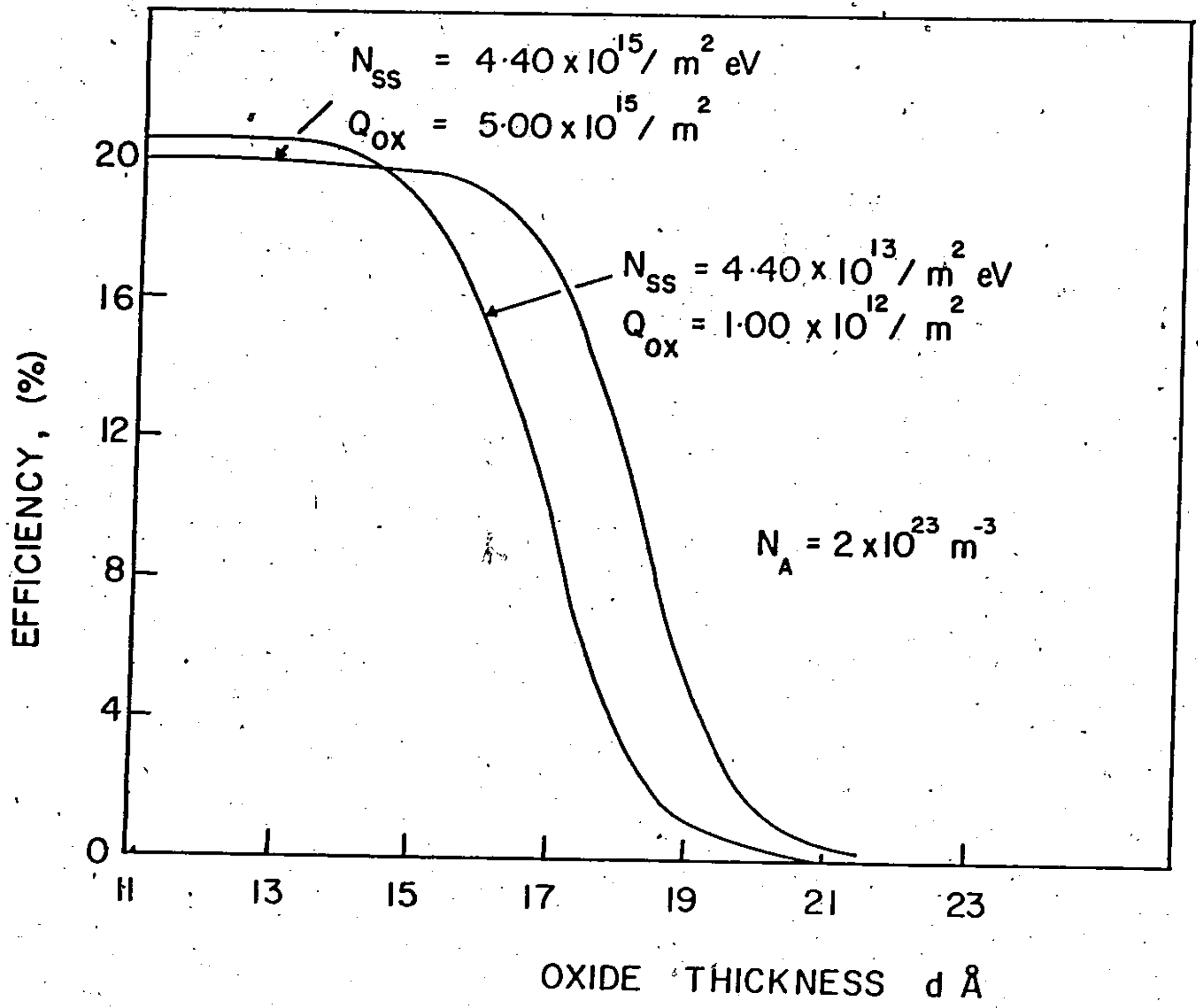

Figure 3.15

Al-SiO_x-(p-type) Si can be obtained for an insulator with a thickness less than 14 Å. Therefore, we have calculated the conversion efficiency for an insulator thickness of 12 Å as a function of insulator charge with surface state density as the variable parameter. These results are shown in Figure 3.16. The upper curve represents a very low value of N_{ss}, the middle curve represents a moderate value of N_{ss} and the bottom curve represents a high value of N_{ss}. The worst combination of low Q_i and high N_{ss} gives the lowest efficiency. In the case of low surface state density, the higher value of insulator charge does not increase the conversion efficiency by any significant amount. The saturation is due to the fact that maximum barrier heights have been obtained at moderate values of N_{ss} and Q_i, and any increase in Q_i does not increase V_{oc}.

In this section all calculations have been done for MIS solar cells. Similar results are expected for SIS solar cells.

3.4.4 Effect of Metal and Oxide-Semiconductor Work Function

As discussed earlier, minority carrier tunnel MIS and SIS diodes are formed when the metal-insulator work function, ϕ_{mi}, or oxide-semiconductor-insulator work function, ϕ_{osi}, is less than about 3.6 eV with p-type silicon as the base-semiconductor. Above 3.6 eV, majority carrier diodes are formed. We have confined our discussion so far to Al diodes with ϕ_{mi} = 3.2 eV or ITO diodes with ϕ_{osi} = 3.3 eV. However, it is of considerable interest to know how the MIS and SIS struc-

Figure 3.16

The effect of insulator charge on conversion efficiency of an Al-SiO_x-(p-type)Si solar cell with surface state density as the variable parameter. The thickness of the insulator is 12 Å.

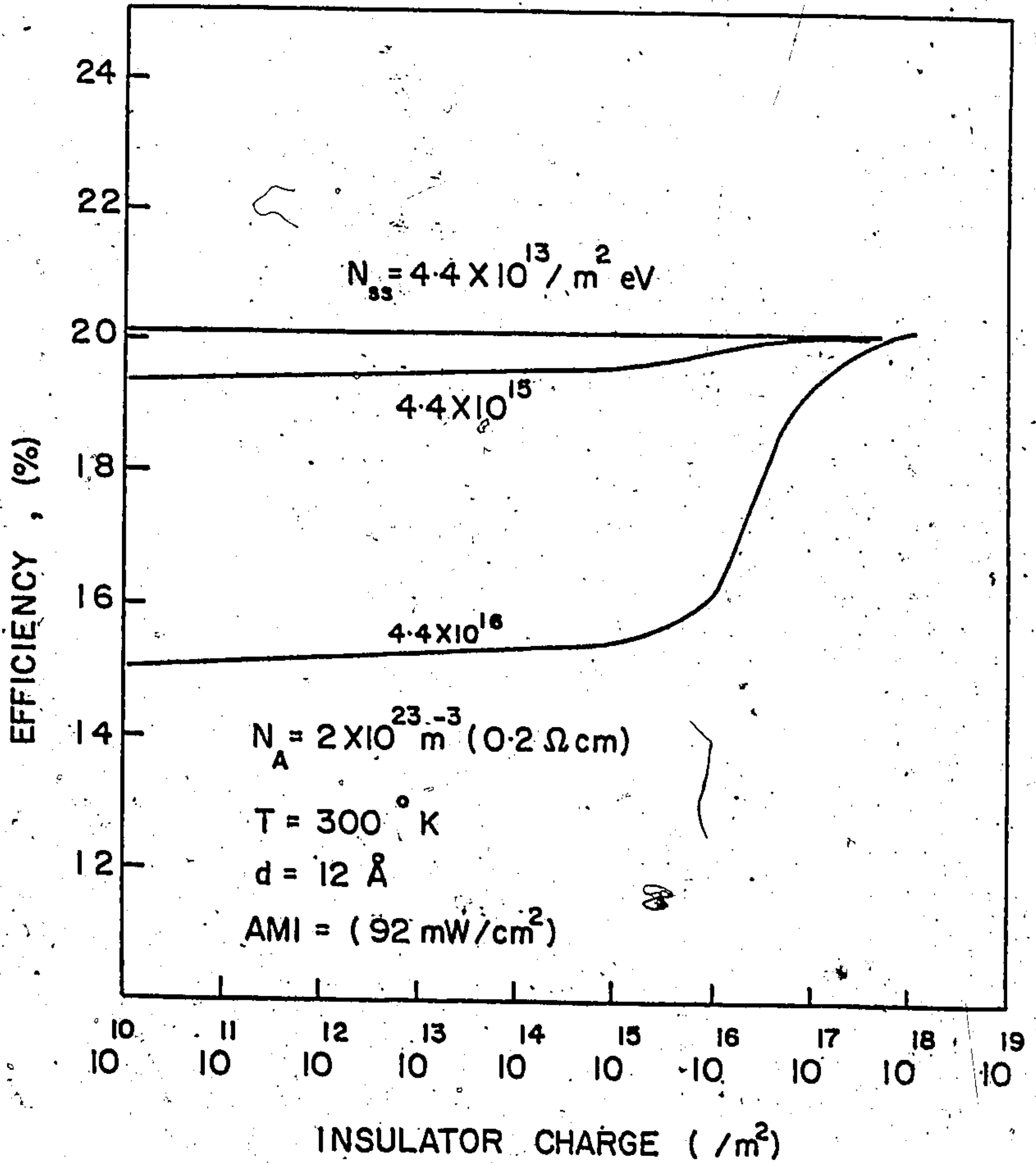

Figure 3.16

ture performs as an energy converter for top layers other than aluminum or ITO. In order to see the effect of top layer work function, let us re-examine Equation (3.22)

$$\phi_p = E_{gs} + \phi_{si} - \phi_{mi} - F_s d + q \frac{(Q_{ss}+Q_i)}{\varepsilon_i} d \qquad (3.22)$$

$$\phi_p = E_{gs} + \phi_{si} - \phi_{osi} + \Delta - F_s d + q \frac{(Q_{ss}+Q_i)}{\varepsilon_i} d. \quad (3.23)$$

These simple Equations (3.22) and (3.23) show that for p-type MIS and SIS solar cells, the metal or oxide-semiconductor work function should be less than or equal to the electron affinity of the base-semiconductor. Similarly, one can see from Equations (3.24) and (3.25) that for an n-type base-semiconductor, the metal or oxide-semiconductor work function should be greater than or equal to the sum of the electron affinity and band-gap of the base semiconductor. We have listed the desired metal work functions for some base-semiconductors in Table 3.6. The desired electron affinity for some oxide-semiconductors and base-semiconductor materials are listed in Table 3.7. One can see from Equation (3.22) that even in the case of an ideal interface with $\phi_{mi} < \phi_{si}$ (neglecting the effect of surface states and insulator charge), the surface field will decrease to give a maximum barrier height equal to the band gap of the semiconductor. As pointed out in Section 3.4.3, surface states may increase or decrease the barrier height depending

TABLE 3.6

DESIRED WORK FUNCTION OF METALS AND HIGHEST POSSIBLE AM1 EFFICIENCY FOR SOME MIS SOLAR CELLS

Semiconductor	Bandgap of the semiconductor at T = 300°K (eV)	Desired Work function of metal for p-type semiconductor (eV)	Possible Metals	Possible AM1 Efficiency	Desired work function of metal for n-type semiconductor (eV)	Possible metals	Possible AM1 Efficienc %
Si	1.12	$\leq$ 4.05	Al Cr Ta Ti Mg Be	21	$\geq$ 5.17	Ag Au Pt	21
GaAs	1.43	$\leq$ 4.07	Al Cr Ta Ti Mg Be	25	$\geq$ 5.50	Ag Au Pt	25
InP	1.34	$\leq$ 4.30	Al Cr Ta Ti Mg Be	23	$\geq$ 5.74	Ag Au Pt	23

TABLE 3.7

DESIRED ELECTRON AFFINITY OF OXIDE-SEMICONDUCTORS AND HIGHEST POSSIBLE AMI EFFICIENCY FOR SOME BASE-SEMICONDUCTORS

Base Semi-Conductor	Bandgap of the Base Semiconductor at T = 300°K (eV)	Desired Electron Affinity of Oxide semiconductor for p-type Base Semiconductor	Possible Oxide Semiconductors	Possible AM1 Efficiency	Desired Electron Affinity of Oxide Semiconductor for n-type Base Semiconductor (eV)	Possible Oxide Semiconductors	Possible AM1 Efficiency %
Si	1.12	4.05	ZnO, ITO	21	5.17	SnO_2	21
Ge	0.80	4.0	ZnO, ITO	11	4.80	SnO_2	11
InP	1.34	4.4	ZnO, ITO In_2O_3, Cd_2SnO_4	24	5.74	SnO_2	24
GaAs	1.43	4.07	ZnO, ITO	25	5.50	SnO_2	25
CdTe	1.44	4.30	ZnO, ITO Cd_2SnO_4	25	5.74	SnO_2	25
$CuInSe_2$	1.02	4.58	ZnO, ITO Cd_2SnO_4, Bi_2O_3	18	5.60	SnO_2	18

upon whether they are acceptor or donor types. Similarly, a positive insulator charge increases the barrier height for p-type MIS solar cells. This relation suggests that, for $\phi_{mi} < \phi_{si}$, little increase in the conversion efficiency will be expected. This feature has been confirmed by our calculation of efficiency as a function of metal work function for a fixed configuration of insulator thickness, substrate resistivity, insulator charge and surface state density. These results are shown in Figure 3.17 for an insulator thickness of 13 Å and 0.2 Ω-cm substrate resistivity. In our calculations, we have taken the work function of Aluminum and the electron affinity of Si as 4.1 eV. Therefore, the efficiency does increase by a great deal with ϕ_{mi} below 3.2 eV. For metals with ϕ_{mi} less than 2.7 eV, there is a complete saturation in efficiency. For metals with $\phi_{mi} > 3.2$ eV, the efficiency decreases slowly up to $\phi_{mi} = 3.4$ eV, after which it decreases rapidly due to the reduced barrier height. At $\phi_{mi} \geq 3.9$ eV, the devices become majority carrier diodes, which are not suitable for photovoltaic purposes.

In Figure 3.18, we have calculated open-circuit voltage, V_{oc}, short circuit density, J_{sc}, and fill factor, FF, for Figure 3.16. For $\phi_{mi} < 3.2$ eV, J_{sc} does not increase, since essentially all the current available out of the semiconductor is already being extracted at $\phi_{mi} = 3.2$ eV. Up to $\phi_{mi} \approx 3.6$ eV, the majority carrier current near zero bias is small, which keeps

Figure 3.17

Calculation of efficiency as a function of metal work function of an M-SiO_x-(p-type)Si solar cell. The substrate resistivity is 0.2 Ω-cm and the insulator thickness is 13 Å.

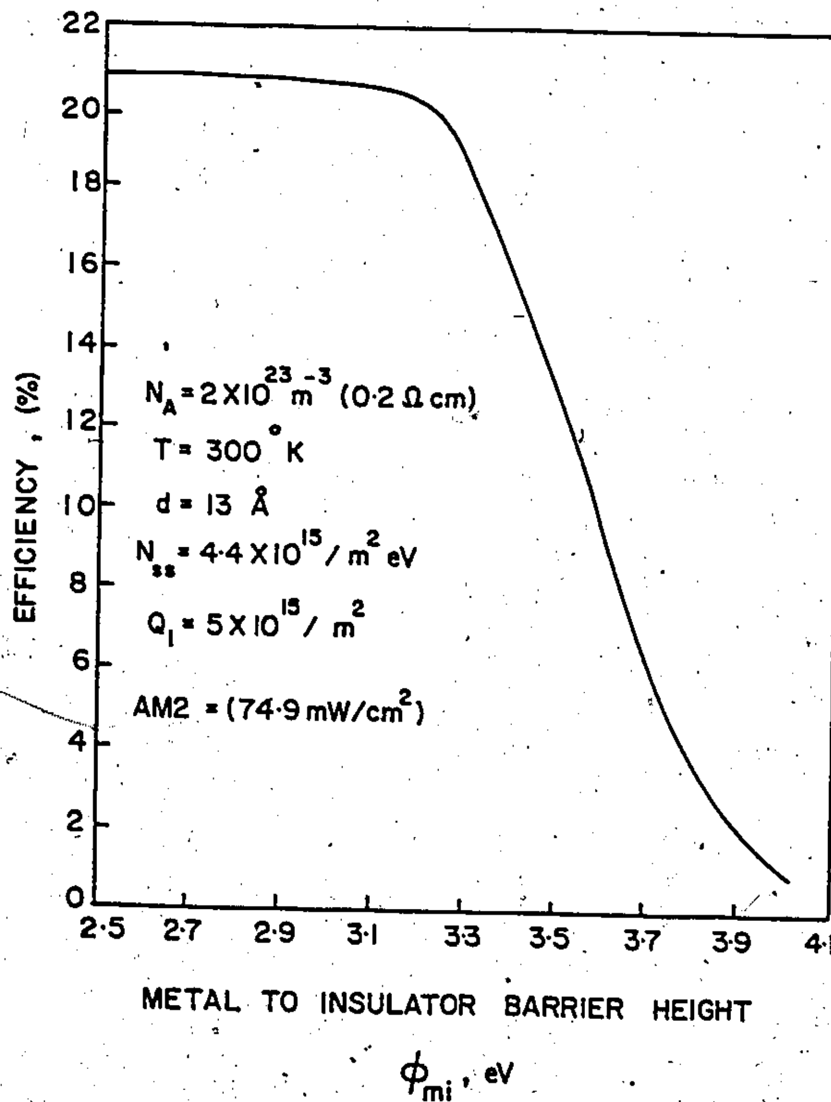

Figure 3.17

Figure 3.18

Effect of metal work function on the open-circuit voltage, short circuit current density and fill factor of an M-SiO_x-(p-type)Si solar cell. All the device parameters are the same as in Figure 3.17.

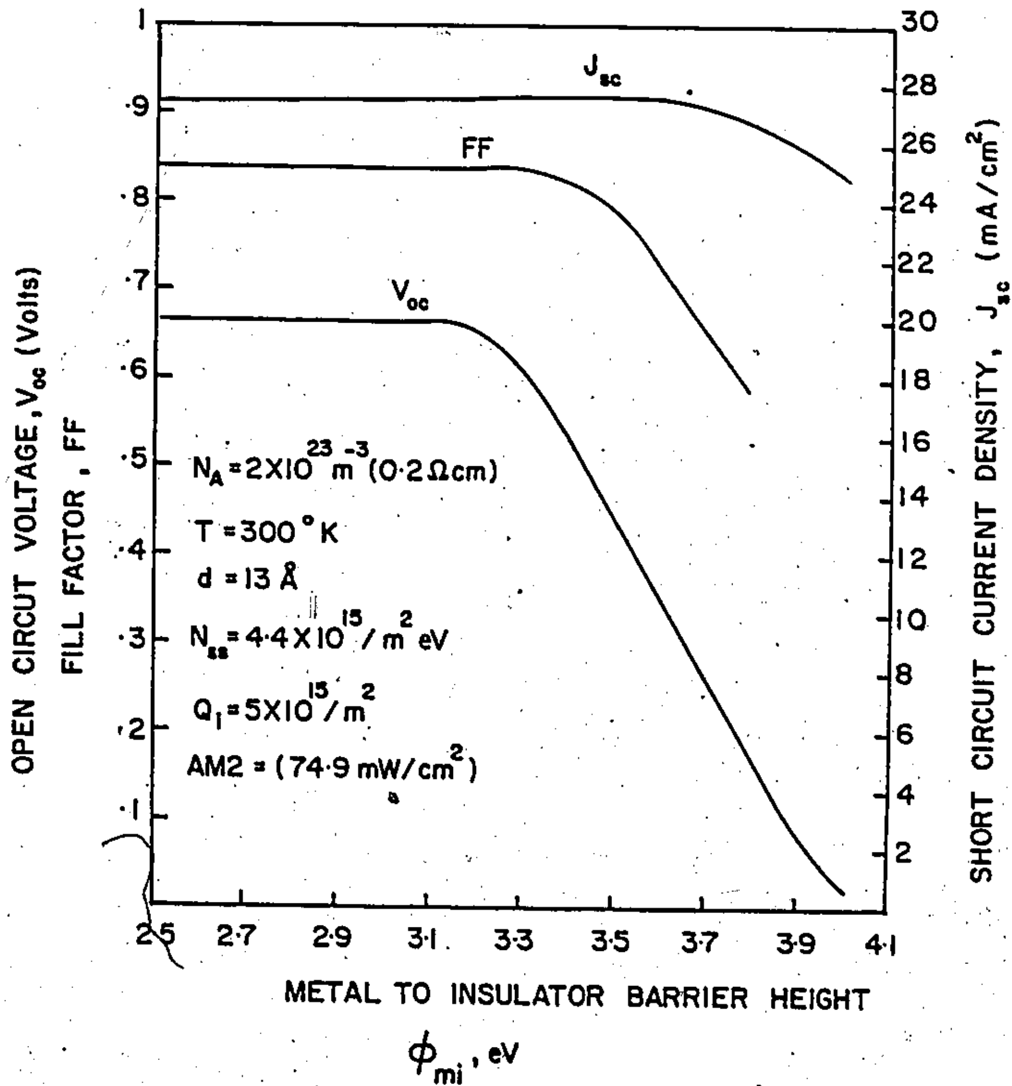

Figure 3.18

J_{sc} constant in this range of work function. After $\phi_{mi} > 3.6$ eV, J_{sc} starts falling due to the loss by majority carriers. Slight increases in efficiency for ϕ_{mi} less than 3.2 eV is due to a slight increase in V_{oc}. For $\phi_{mi} > 3.2$ eV, V_{oc} will decrease, since the barrier height decreases as predicted by equation (3.22). The decrease in fill factor with increase in metal work function is due to the fact that the dark current of the device increases as well as the ideality factor. These two factors contribute to the decrease of the fill factor. For $\phi_{mi} > 3.4$, the fill factor decreases rapidly, since V_{oc} starts decreasing by a substantial amount.

The above calculations show that efficiency of a p-type MIS solar cell does not increase greatly with ϕ_{mi} below 3.2 eV. But, the main advantage of low work-function metal is that the device performance will be less sensitive to defect density and insulator charge. The effect of surface states on the device performance, as a function of ϕ_{mi} and substrate doping, is shown in Figure 3.19. The insulator charge, Q_i, ranged from $10^{12}/m^2$ to $10^{16}/m^2$. It is seen from Figure 3.19, that the number of surface states has little effect on conversion efficiency when ϕ_{mi} is low. Lower values of ϕ_{mi} favour formation of minority carrier diodes, even at higher doping levels. The large number of minority carriers at the surface ensures that surface states are heavily occupied by these carriers (electrons in the case of

Figure 3.19

The effect of surface state density and insulator charge on conversion efficiency for various ϕ_{mi} and doping density combinations. Q_i ranged from 10^{12} m^2 to 10^{16} m^2.

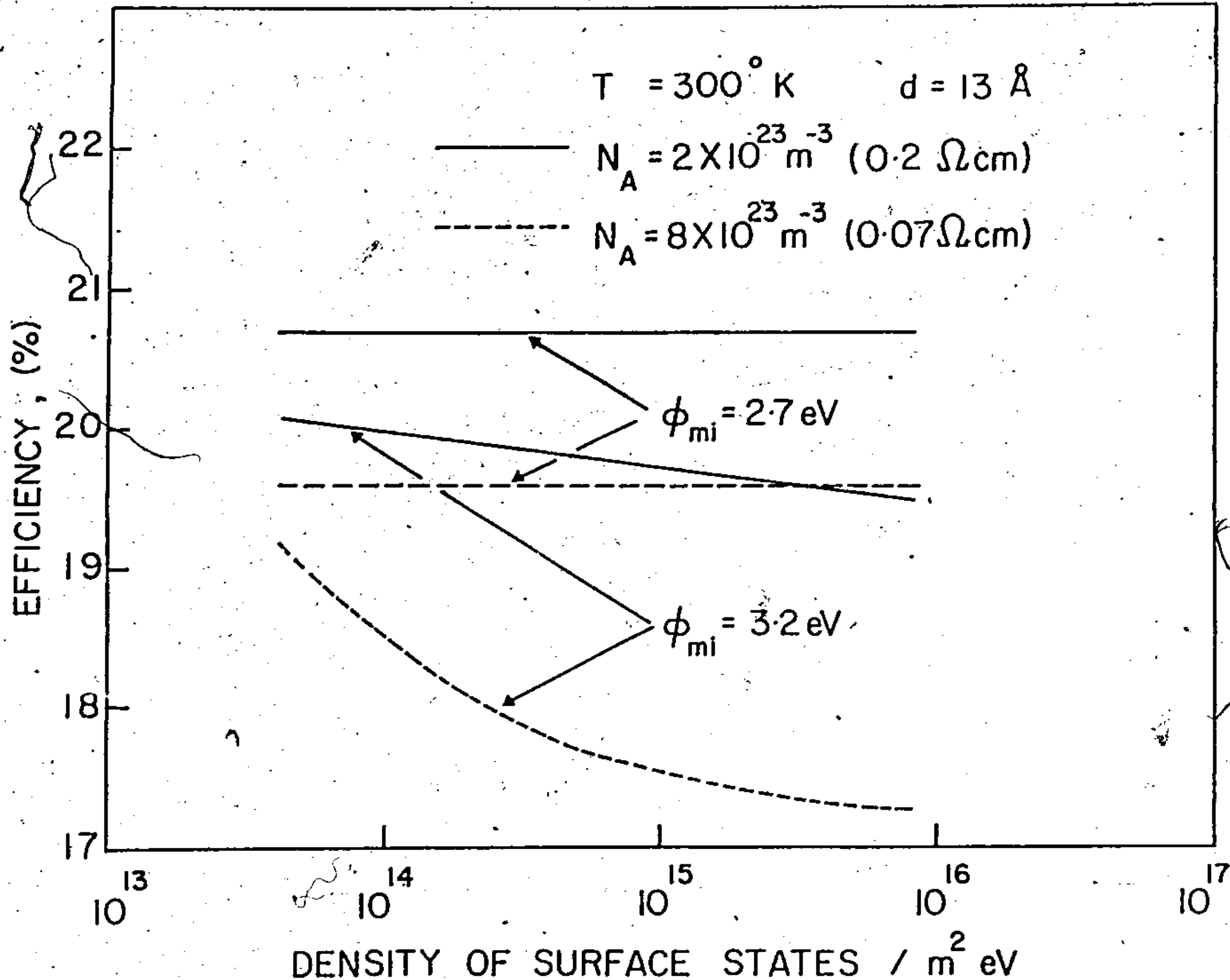

Figure 3.19

p-type MIS solar cells). The large density of electrons at the surface reduces the possibility of surface states as efficient recombination centres. Thus, with lower metal work function minority-carrier diodes can be formed even at lower substrate resistivity. The combination of a low metal work function and a high substrate resistivity for p-type semiconductors can result in MIS solar cells with efficiencies equal to that obtained by p-n junctions. The main advantage of such minority carrier MIS solar cells is that, batch after batch, we will get virtually identical devices if we use the same substrate material. Devices whose properties depend on surface states, insulator charge etc. are not likely to fare well even in a relatively benign terrestrial environment.

In Figure 3.20 we have calculated the efficiency and open-circuit voltage of an n-ITO-SiO_x-(p-type)Si solar cell as a function of ϕ_{osi} and ϕ_{si}. The variation of barrier height ϕ_{si} was studied to account for patchy insulators with an efffective lower value of ϕ_{si}. The reflection data of N. Chang [66] were used in these calculations. In case (a), the base-semiconductor to insulator work function, ϕ_{si}, is kept constant and the barrier energy on the ITO side, ϕ_{osi}, is varied. As can be seen from Equation (3.23), the open-circuit voltage and efficiency of the device are expected to decrease drastically for $\phi_{osi} > \phi_{si}$. Although for the case of $\phi_{osi} >$ 3.6 eV, there will be a good J_{sc} and fill factor, V_{oc} will be

Figure 3.20

Computed effect of barrier heights variation on the conversion efficiency η, and open-circuit voltage, V_{oc} of an ITO-Si SIS tunnel diode. In case (a), the barrier height on the ITO side is varied, while in case (c), the barrier height on the Si side is varied. Equal change in barrier heights on both sides has no effect on η and V_{oc} as shown in curve (b). These curves were calculated by M. Spitzer and are reported in reference 58.

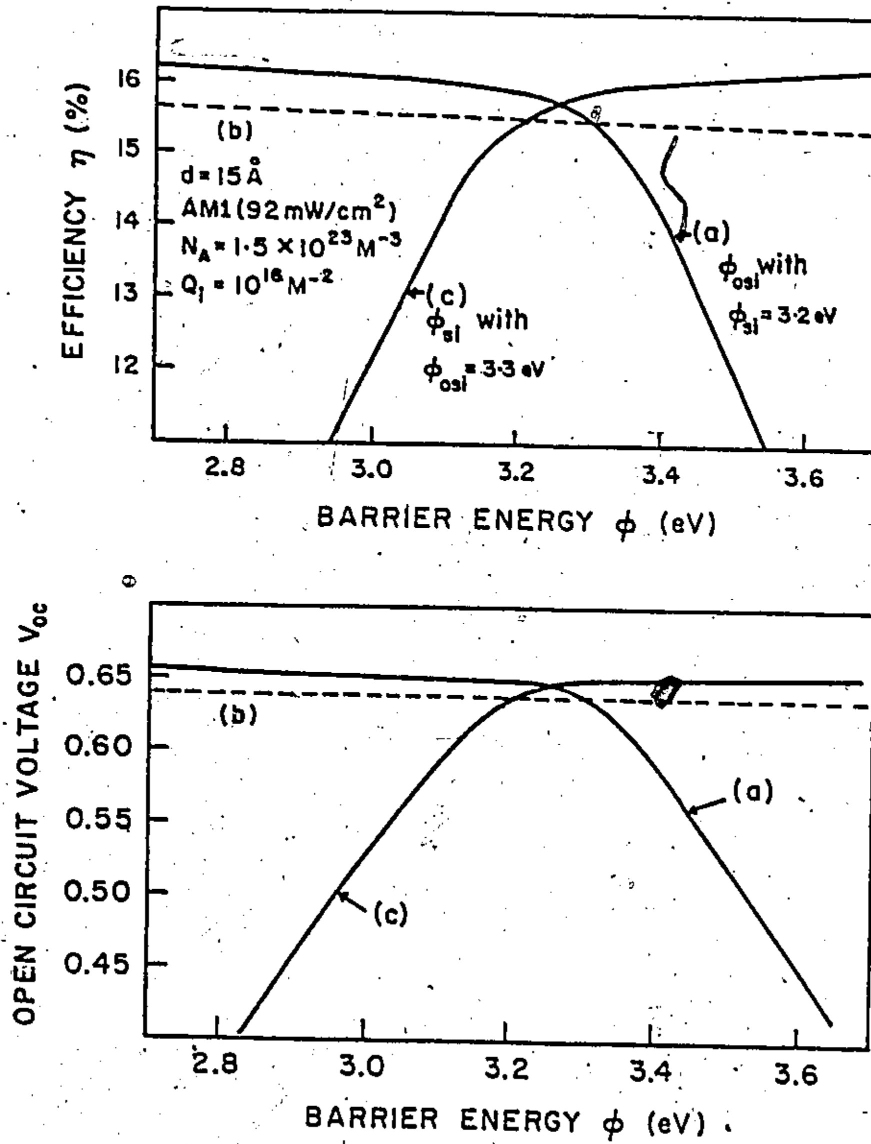

Figure 3.20

very low. For $\phi_{osi} < \phi_{si}$, the efficiency almost saturates, since no further current can be extracted from the semiconductor than at $\phi_{osi} = \phi_{si}$. Any increase in the barrier height ϕ_{osi} will be compensated by large field at the semiconductor (i.e. high potential drop across the insulator). In case (c), we have varied the barrier energy on the base-semiconductor side and kept the barrier energy on the ITO side constant. The results are a mirror-image of case (a). Relative changes in both barrier energies simultaneously does not affect the device performance, as can be seen in case (b). Fill factor and the short-circuit current density will vary in the same manner as for MIS solar cells.

3.4.5 Effect of Temperature

The variation of temperature affects the performance of MIS and SIS solar cells in two ways. Firstly, the tunnelling barrier depends on the temperature and secondly, the transport properties are changed due to change in the semiconductor parameters. We will show later in this section that for MIS and SIS solar cells with ultra thin interfacial layers (< 16 Å for Al-SiO_x-(p-type)Si and ITO-SiO_x-(p-type)Si cases), the temperature effect is governed mainly by the transport properties of the semiconductor. The important semiconductor parameters which change with temperature are energy band gap, mobility, carrier life time, intrinsic carrier concentration and absorption coefficient. In this section we shall first

discuss forward and reverse dark I-V curves at various temperatures followed by the effect of temperature on conversion efficiency, open-circuit voltage, short-circuit current density and fill factor. All the calculations have been done for SIS diodes, but the results are equally valid for the MIS case.

Figure 3.21 shows the forward dark I-V characteristics of the SIS diode as a function of temperature for a fixed insulator thickness of 15 Å. The temperature was varried from 200 to 400°K and the substrate resistivity is 0.2 Ω-cm. Solid lines in this figure represent the actual current flow for the device. Dashed lines represent the case where the current flow under forward bias can be represented by the diode equation i.e.

$$I_{dark} = \sum_{i=1}^{2} (I)_{oi} \exp\left(\frac{qV_a}{n_i kT}\right) \qquad (3.27)$$

with n equal to 2 for recombination current (low voltage) and n equal to 1 for diffusion current (intermediate voltage). As mentioned earlier, at low forward bias, the current flow in the device is semiconductor limited and the temperature dependence is similar to a p-n junction device. In this bias regime, the diode current is limited by recombination processes in the depletion region, with n approximately equal to 2. In the intermediate bias region (0.2V < V_a < 0.5V, for T = 300°K), the dominant component of current flow is minority carrier diffusion and n approaches 1. At high forward bias, the current

Figure 3.21

Effect of temperature upon the forward dark I-V characteristics of ITO-SiO_x-(p-type)Si tunnel diode. The substrate resistivity is 0.2 Ω-cm and the insulator thickness is 15 Å.

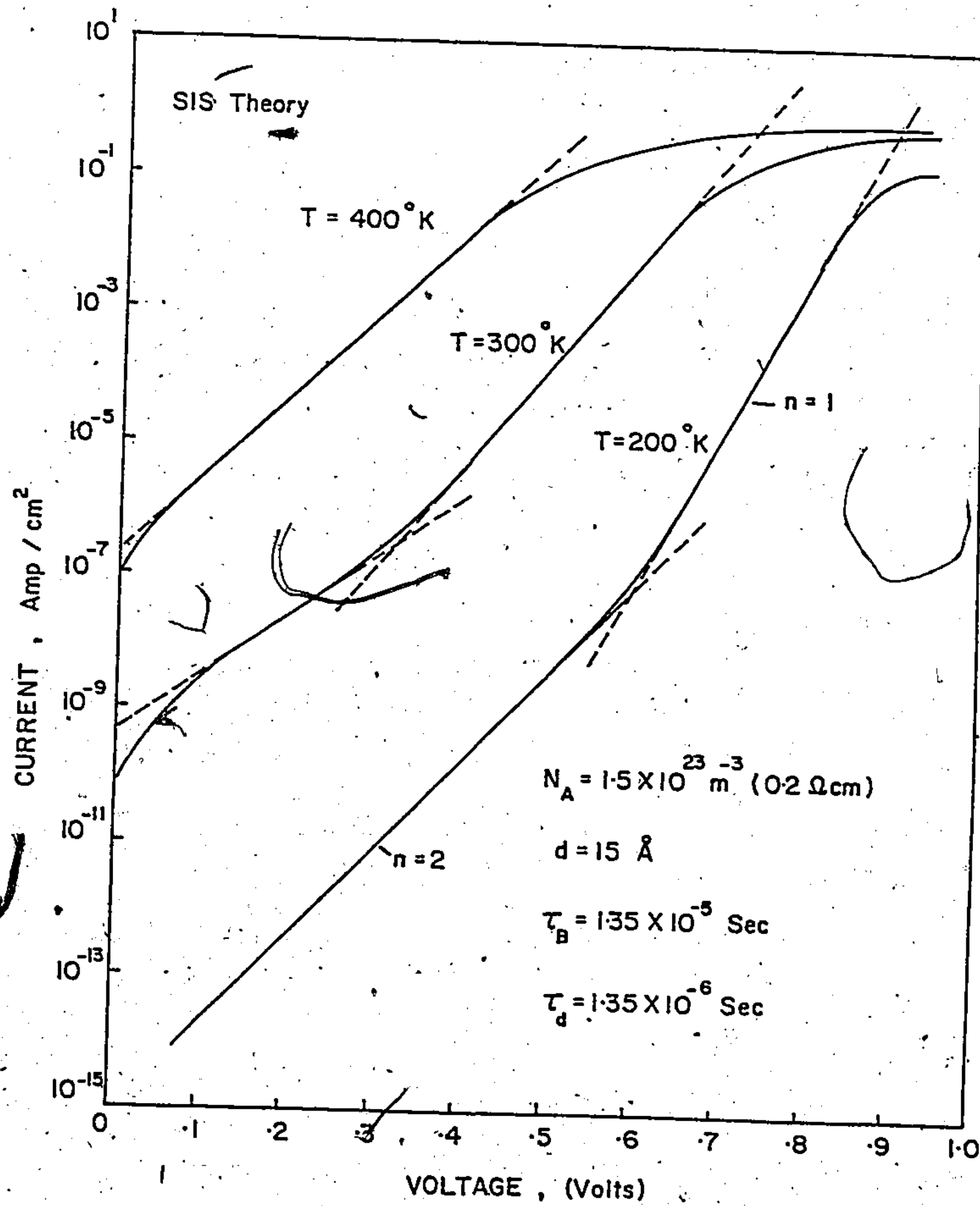

Figure 3.21

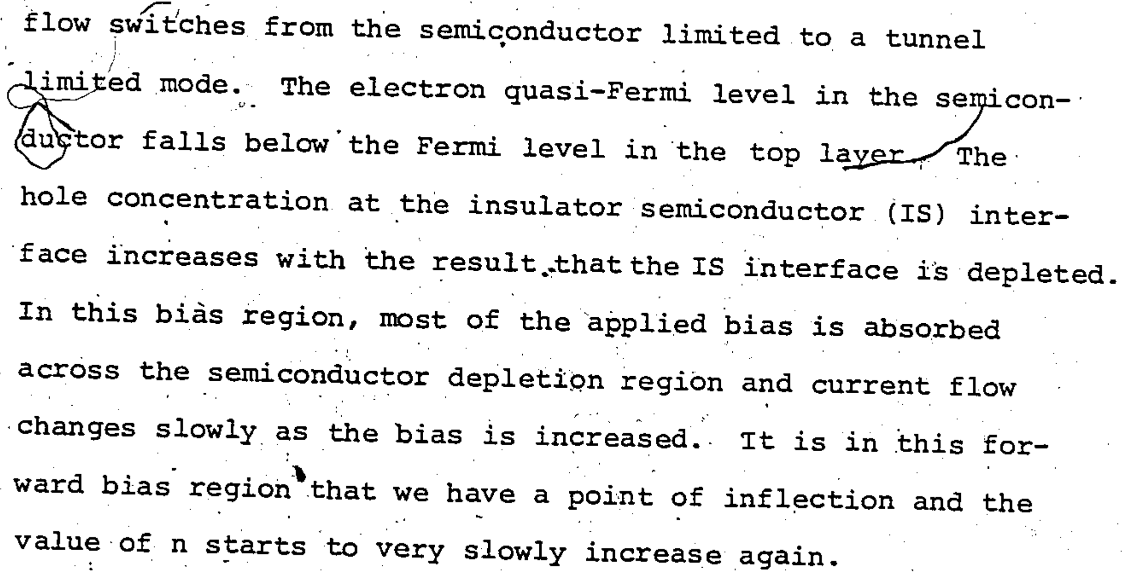

flow switches from the semiconductor limited to a tunnel limited mode. The electron quasi-Fermi level in the semiconductor falls below the Fermi level in the top layer. The hole concentration at the insulator semiconductor (IS) interface increases with the result that the IS interface is depleted. In this bias region, most of the applied bias is absorbed across the semiconductor depletion region and current flow changes slowly as the bias is increased. It is in this forward bias region that we have a point of inflection and the value of n starts to very slowly increase again.

The reverse dark I-V characteristics of the SIS diode as a function of temperature are shown in Figure 3.22. The device parameters are the same as in Figure 3.21. For minority carrier tunnel MIS and SIS diodes the base-semiconductor-insulator interface is inverted at small forward and reverse biases. Thus, the device dark I-V characteristics under reverse bias are more or less like a p-n junction device. At lower temperatures, the current will be mainly due to recombination-generation and at higher temperatures the device current will be dominated by diffusion.

Figure 3.23 shows the calculated efficiency, open-circuit voltage, short-circuit current density and fill factor as a function of temperature for an ITO-SiO_x-(p-type) Si diode. The substrate resistivity is 0.2 Ω-cm and the insulator thickness is 12 Å. The Si parameters used in this temperature study are given

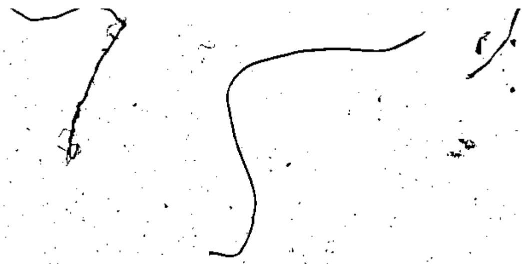

Figure 3.22

Effect of temperature upon the reverse dark I-V characteristics of ITO-SiO_x-(p-type)Si tunnel diode. The substrate resistivity is 0.2 Ω-cm and the insulator thickness is 15 Å.

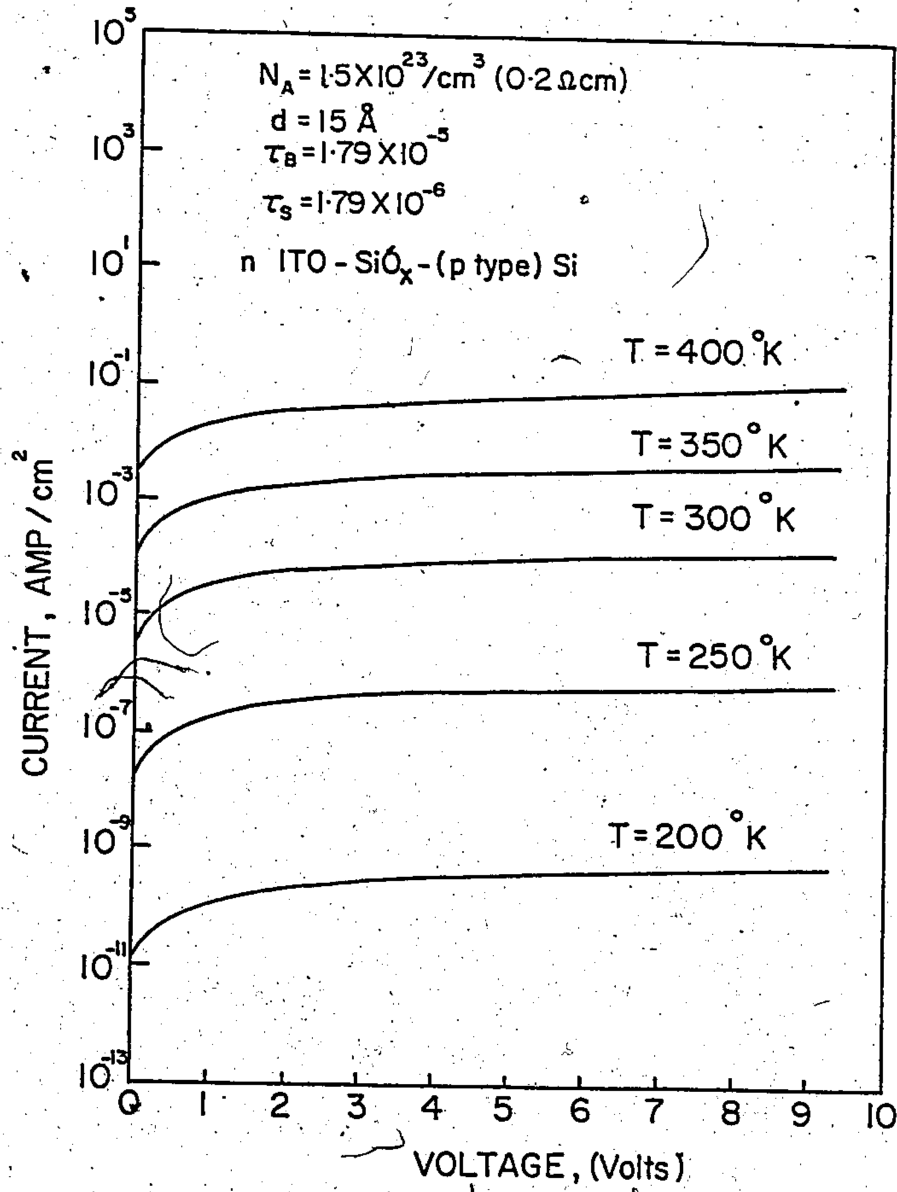

Figure 3.22

Figure 3.23

Effect of temperature on the efficiency, open-circuit voltage, short circuit current density and fill factor of an ITO-SiO_x-(p-type)Si solar cell. The insulator is 12 Å thick.

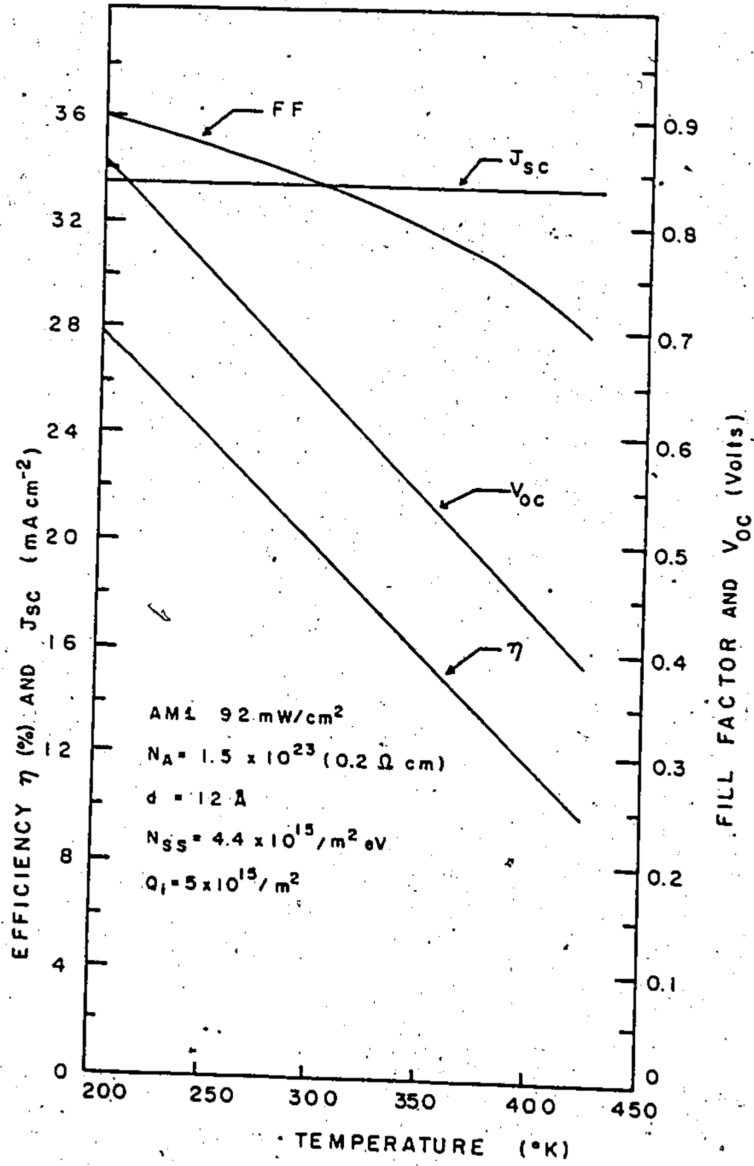

Figure 3.23

in Appendix B. The open-circuit voltage decreases with increasing temperature in a linear fashion. This result can be explained with the help of Figure 3.21, which shows that dark current increases with temperature. Using the simple relation for the open-circuit voltage of an ideal solar cell, we have

$$V_{oc} = \frac{nkT}{q} \ln \left(\frac{I_{sc}}{I_s} + 1\right) . \qquad (3.33)$$

This shows that an increase in dark current, will lead to a decrease in open-circuit voltage, as observed in Figure 3.23. The short circuit current density remains practically constant as temperature is increased. The reason for this type of behaviour is that in the present calculations we have treated the diffusion length and absorption coefficient as constants for the entire range of temperature (200-400°K). The slight increase in J_{sc} is due to the shift of the absorption edge to lower energies. The fill factor also decreases with increasing temperature, as can be seen in Figure 3.23. This behaviour is similar to the effect of the temperature on the fill factor of a p-n junction solar cell [34(b)]. The efficiency also decreases in a linear fashion, which is due to the decrease of V_{oc} and FF. The improvement in J_{sc} is negligible in this case. These results show that the temperature dependence of tunnel MIS solar cells is similar to p-n junction solar cells.

3.4.6 Effect of Intensity

In order to see the potential of MIS and SIS solar cells in concentrating systems, it is desirable to study the intensity effect. For this purpose we have calculated the intensity effect on the performance of SIS solar cells. The efficiencies of n-ITO-SiO_x-(p-type)Si solar cells as a function of illumination intensity are shown in Figure 3.24. The calculations have been done for three insulator thicknesses, i.e. 15, 16 and 17 Å. The intensity maxima increases with decrease in the thickness of the interfacial layer. These results can be explained with the calculation of the series resistance of the interfacial layer as a function of its thickness. The series resistance of the interfacial layer was estimated by using the method of Reference [67] and is given by

$$R_s = \frac{V' - V_{oc}}{I_{sc}}$$

where V' is the voltage from the forward dark I-V at the point where $I = I_{sc}$. These results are shown in Figure 3.25. It is worth mentioning here that the series resistance depends on the area of the device. In the present calculations, the device area is taken as 1 cm^2. Although in Figure 3.25 we have expressed the series resistance in the unit of ohms, in a more general sense, the unit is ohms$\times cm^2$. At normal intensity, the 15 Å interfacial layer contributes very little to the total series resistance of the device. With increase in intensity, even a 15 Å interfacial layer causes a degradation in the conversion efficiency as shown in Figure 3.24. The efficiency, open-

Figure 3.24

Calculated efficiency of nITO-SiO_x-(p-type)Si solar cell as a function of solar intensity with insulator thickness as the variable parameter. These curves were calculated by M. Spitzer and are reported in reference 153.

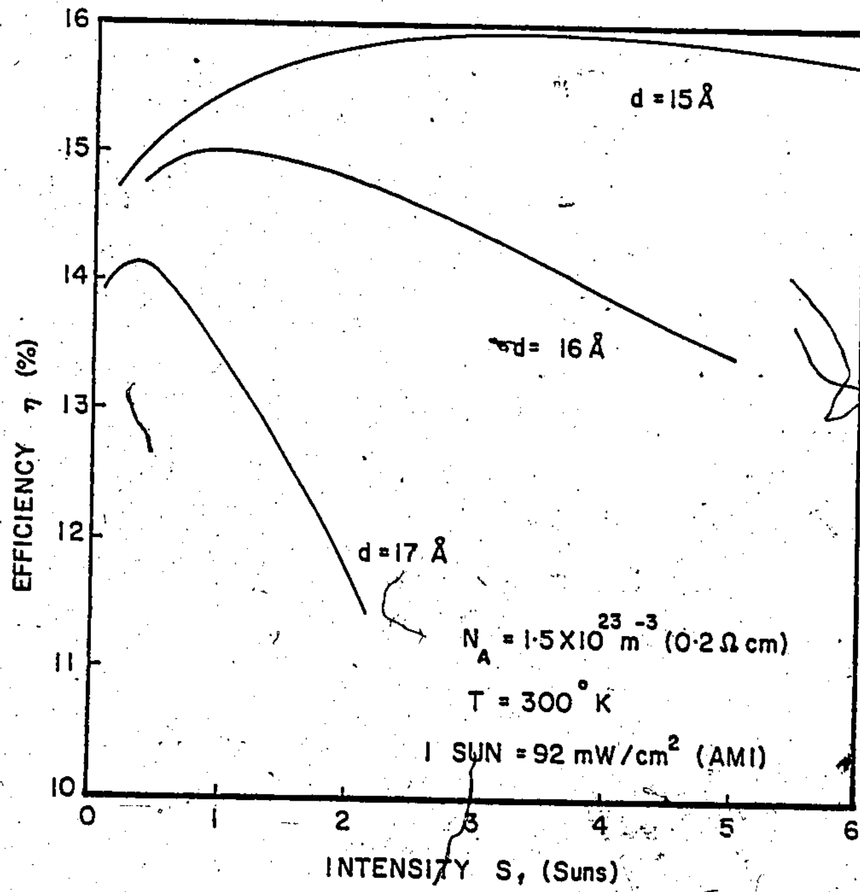

Figure 3.24

Figure 3.25

Calculated resistance of the interfacial layer as a function of its thickness. The method of reference 67 has been used and the device area is 1 cm^2.

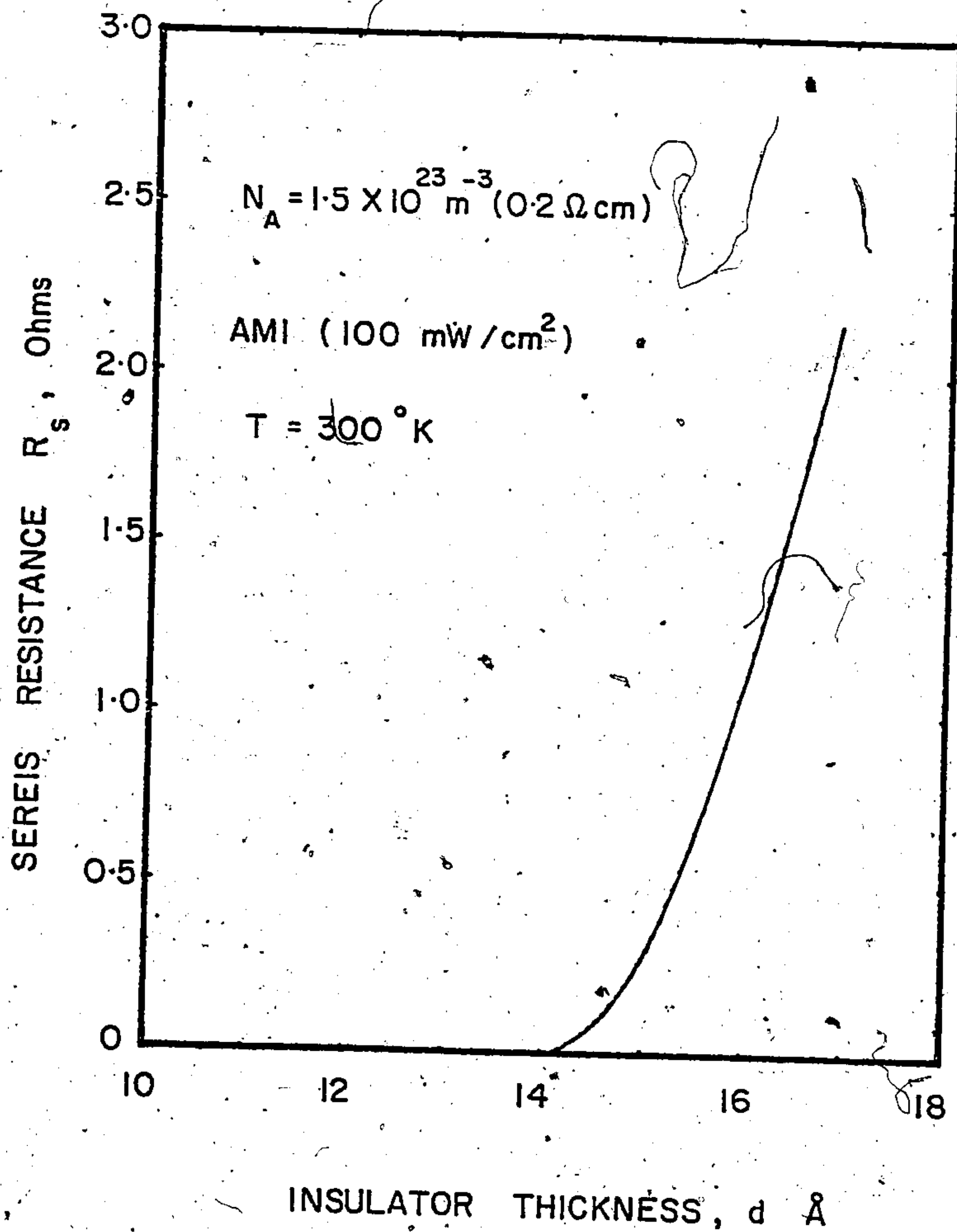

Figure 3.25

circuit voltage, short circuit current density and fill factor of an SIS solar cell, as a function of intensity for a fixed thickness of the interfacial layer, are shown in Figure 3.26 and 3.27. If it is possible to build SIS solar cells with ultra-thin interfacial layers (∿ 12 Å in the case of Si devices) and small contributions to series resistance from the top layer and back contact, these devices can be used in concentration systems up to more than 100 suns (in the case of ITO/Si cells).

The functional dependence of short-circuit current density, open-circuit voltage and fill factor of Figures 3.26 and 3.27 can be explained by considering the device as equivalent to a p-n junction diode. The short-circuit current density is proportional to the incident intensity, provided the series resistance of the interfacial layer is negligible. The open-circuit voltage increases logarithmically with increasing intensity, as shown in Figure 3.27. The fill factor will increase only if the series resistance is negligible. The efficiency of the device will increase due to increases in V_{oc} and FF. In the present calculation, the fill factor of the device decreases constantly from about 0.5 sun. Therefore the efficiency peaks between 2-3 suns. As mentioned above, for a lower thickness of the interfacial layer (10-12 Å), the efficiency continues to increase up to about 100 suns.

Figure 3.26

Calculated efficiency η and fill factor FF of ITO-Si SIS tunnel diodes as a function of solar intensity. The insulator thickness is 15 Å. These curves were calculated by M. Spitzer and are reported in reference 153.

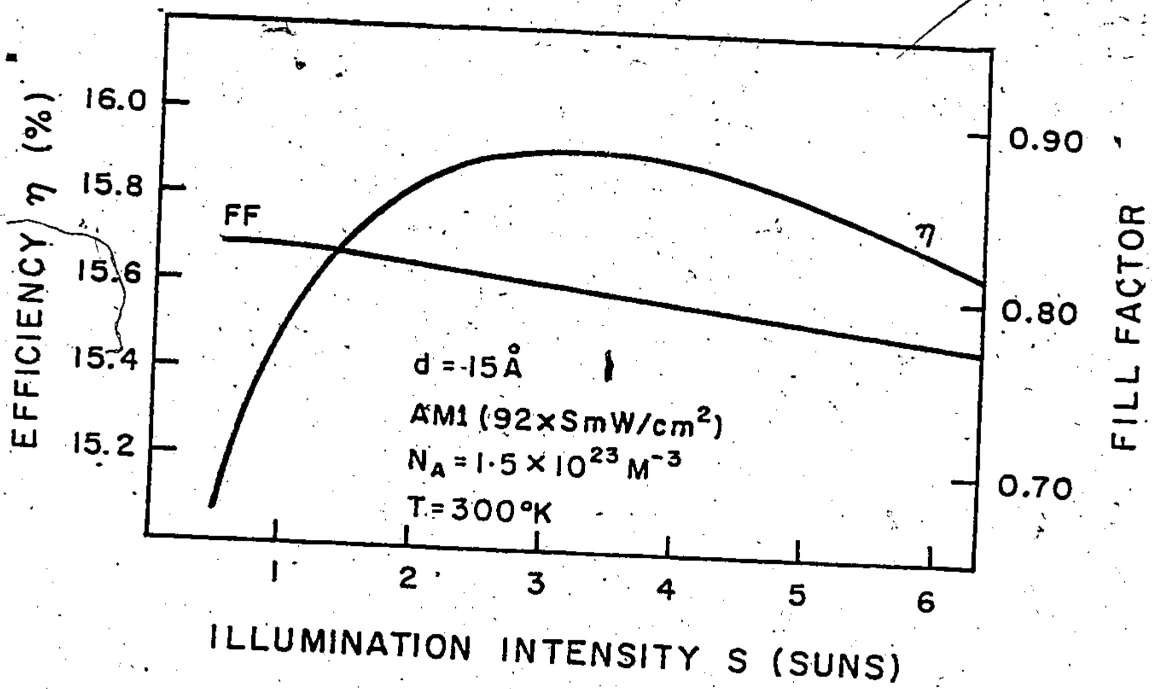

Figure 3.26

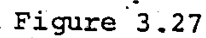

Figure 3.27

Calculated open-circuit voltage V_{oc}, and short-circuit current density, J_{SC}, of ITO-Si SIS tunnel solar cell as a function of solar intensity. All the parameters are the same as in Figure 3.26. These curves were calculated by M. Spitzer and are reported in reference 153.

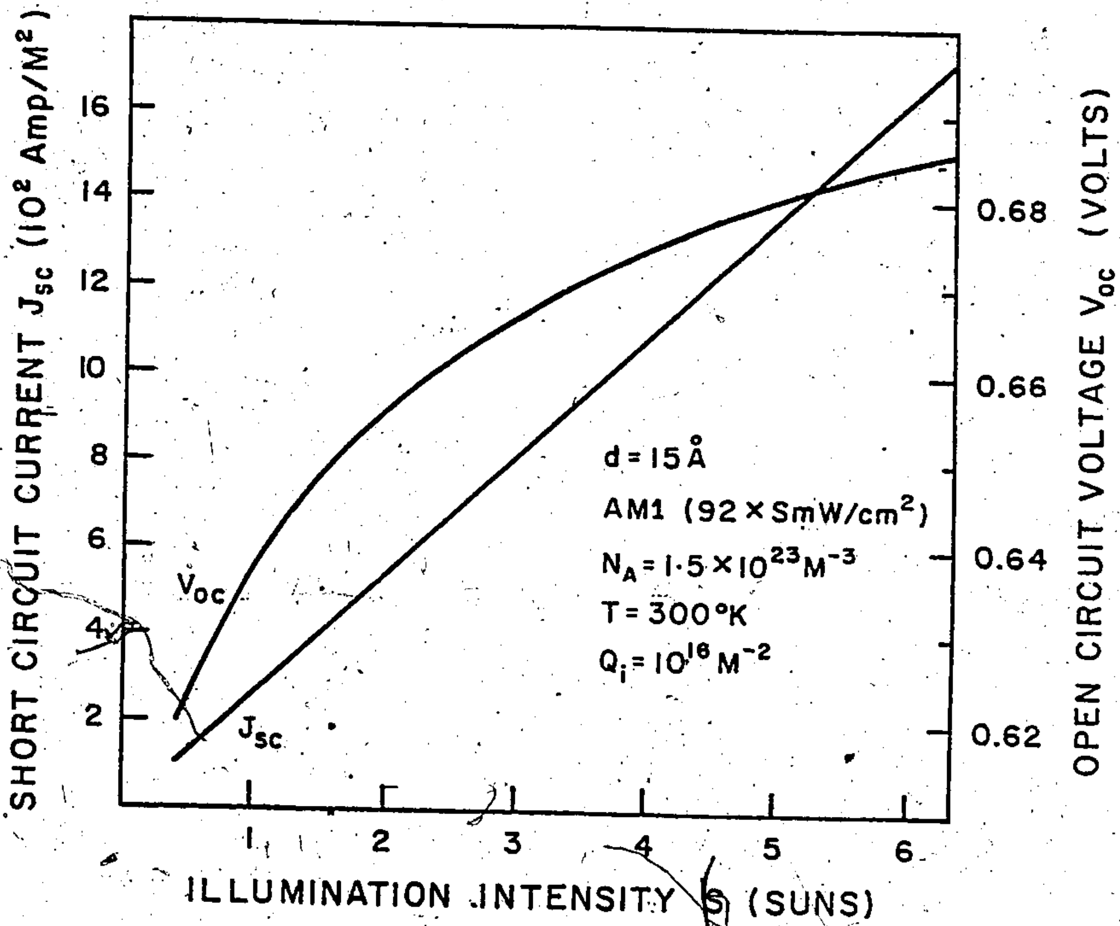

Figure 3.27

3.4.7 Effect of Minority Carrier Life Time

Based on an empirical fit of Fossum [68], the minority carrier life time for p-type silicon may be represented by

$$\tau_n = \frac{\tau_{no}}{1 + \frac{N_A}{N_{oA}}} \quad (3.30)$$

where $\tau_{no} = 3.95 \times 10^{-4}$ sec. and $N_{oA} = 7.10 \times 10^{21}$ m^{-3}. Since only low temperatures are required for growth of the thin oxides, it is highly likely that the original silicon wafer lifetime characteristics can be maintained substantially through the MOS type solar cell fabrication schedule [69].

The effect of minority carrier lifetime on conversion efficiency is shown in Figure 3.28. The lower curve, with $\tau_{no} = 3.95 \times 10^{-4}$ sec., represents Fossum's lifetime data and in the upper curve, we have assumed $\tau_{no} = 3.45 \times 10^{-3}$ sec. With present state-of-the-art processing techniques, it is possible to achieve this type of lifetime in single crystals of silicon. This curve shows that for the lower doping level, minority carrier lifetime had little effect, whereas, in the higher doping level, it affects the conversion efficiency significantly. With poor quality material, lower conversion efficiencies are expected due to short carrier lifetimes.

Figure 3.28

Effect of minority carrier lifetime on the conversion efficiency of an Al-SiO_x-(p-type)Si solar cell. The effect of surface states and insulator charge is neglected. The insulator thickness is 11 Å.

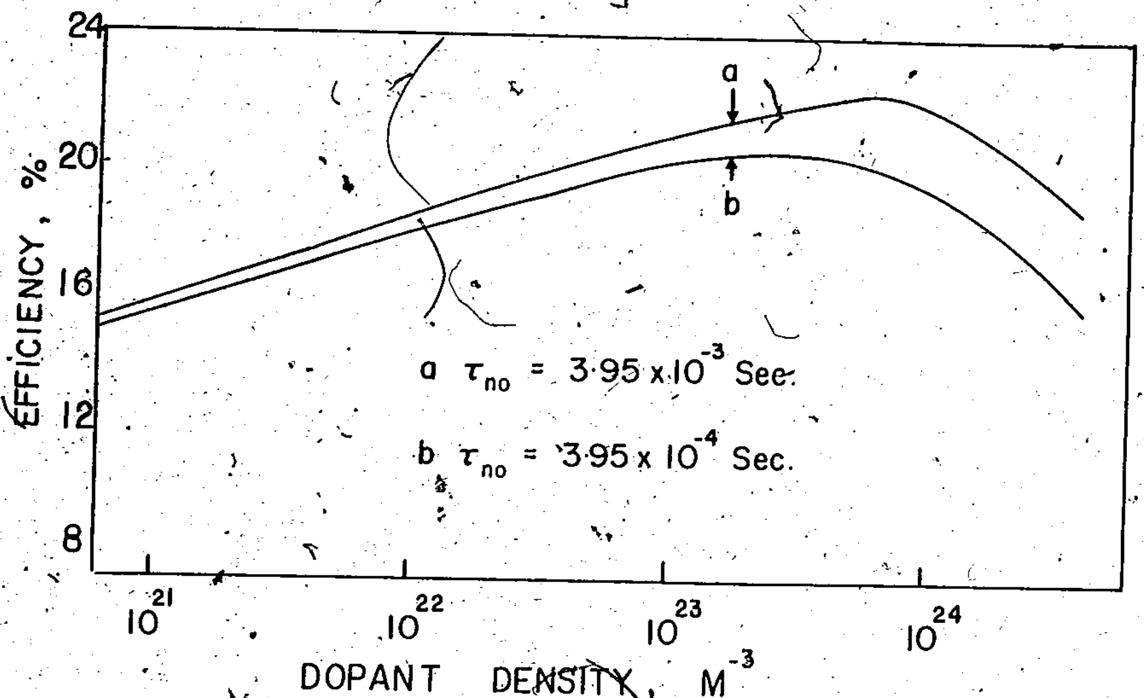

Figure 3.28

3.4.8 Effect of Crystal Orientation

It is well known that the density of surface states depends on crystallographic orientation (N_{SS} <111> > N_{SS} <110> > N_{SS} <100>). For optimized thickness of the insulator layer, the <100> orientation will give better efficiency due to a lower defect density. The tunneling probability and tunnel currents also depend on the crystal orientation. But, for the optimum insulator thickness (< 16 Å in the case of Al-SiO_x-(p-type)Si and ITO-SiO_x-(p-type)Si solar cells), the device current is semiconductor limited. Therefore, the effect of tunnel current due to crystal orientation will not be appreciable, as compared to the effect of surface states.

3.4.9 Effect of the Semiconductor Band Gap

In the previous sections we have done calculations for silicon MIS and SIS solar cells. In this section we will show that, like p-n junction solar cells, higher efficiencies can be obtained with base-semiconductors other than silicon. In this section we will calculate the conversion efficiency of InP and GaAs SIS solar cells as a function of insulator thickness. With proper choice of top layer work function and insulator thickness, the InP and GaAs MIS and SIS solar cells can yield up to 24 and 25% efficiencies respectively at AM1. It is worth mentioning here that, with increase in the band gap of the base-semiconductor, the range of useful insulator thickness

also increases. This can be explained by considering that the photocurrent remains unaffected by the presence of the interfacial layer as long as the rate of minority carriers arriving at the interface is smaller than that which can be supported by the tunneling process. The rate of minority carriers arriving at the interface depends on the particular base-semiconductor and the tunneling probability strongly depends on the interfacial layer thickness. For the sake of simplicity, let us assume that in an MIS or SIS solar cell, the low band-gap base-semiconductor (e.g. Si) is replaced by a high band-gap base-semiconductor (e.g. GaAs or InP) and all other device parameters are the same. Since, only photons with energy $h\nu > E_g$ can create electron-hole pairs in the base-semiconductor, the rate of minority carriers arriving at the interface will be smaller in the high band-gap semiconductor. This implies that, with increase in the band-gap of the base-semiconductor, the range of useful insulator thickness increases. This is indeed the case as will be shown by the calculations for InP and GaAs SIS solar cells in this section. Thus, in general, it is expected that as the band gap of the base-semiconductor is increased the useful range of the insulator thickness also increases.

3.4.9.1 ITO/InP SIS Solar Cell

Sree Harsha and co-workers [9] have reported a 14.4% (AM2) n-ITO/p-InP solar cell. They prepared devices with both amorphous and crystalline ITO, although the highest

efficiency was observed with "amorphous" ITO deposited on cooled substrates (room temperature). The question remains as to whether these junctions are heterojunctions, Schottky barriers or some interfacial layer SIS diodes. In the case of crystalline ITO, it is difficult to see how a heterojunction or Schottky model could apply, based on earlier arguments. An examination of the crystal structure and lattice parameters of the InP, In_2O_3, and SnO_2 from Table 4.1 shows that the ITO/InP systems would have too many mismatch defects at the interface to form good heterojunctions or Schottky barriers. It would be difficult to account for a 14.4% efficiency. Furthermore, the thermal expansion coefficients of InP, In_2O_3 and SnO_2 are against the formation of a good device. However, an interfacial layer could act to promote the matching of the InP to ITO, although such an interface would likely be complicated chemically and structurally. In the case of amorphous ITO, plausible arguments are even more difficult since there is very limited information available regarding amorphous ITO. The amorphous ITO could be thought of as behaving like a metal (albeit one with a large band gap with degeneracy). The requirement of crystal and lattice matching is now relaxed, so that it is easier to argue heterojunction or Schottky behaviour. In the case of tetrahedally bonded amorphous semiconductors, the bond length is approximately equal to the crystalline bonding distance [71]. Thus to a first order approximation, the lattice constant of crystalline ITO can be used

to estimate the dangling bond at the interface. Thus, defects should still be high and limit the efficiency. Furthermore, Schottky solar cells are notorious for their low open circuit voltages, but the observed V_{oc} is about 0.76 volts in the ITO/InP system. Again there is more in favour of an interfacial layer hypothesis with amorphous ITO than the other way around [72].

As to the nature of what the interface between ITO and InP may be composed of, this is even more difficult to argue. The only sensible compound is P_2O_5. The melting point of P_2O_5 is 580°C and it sublimes at 300°C [73]. If this is indeed the interface being formed, then one would have to question why the amorphous ITO cell performed better than the crystalline one. A possible explanation is that the lower substrate temperature which allows amorphous ITO fo form is also better for the formation of P_2O_5. Furthermore, in the case of the ITO-InP system, such interfacial layers can be complicated mixtures and not just simply P_2O_5. They may also be capable of accomodating in some way, which is not as yet completely understood, the strains due to crystal structure and lattice parameter mismatch, thus in effect grading one side of the junction into the other. In this grading scheme, we can think of the ITO side of the junction as dominated by In-O bonding, while the other side has In-P bonding. The transition region may consist of P-O bonding, giving rise to an interfacial layer of P_2O_5. Wilmsen and Kee [74] observed this type of bonding by

Auger analysis of indium oxide/indium phosphide interface. Alternately the transition may be a more complicated ternary compound. Figure 3.29 shows the energy band diagram of n-ITO-P_2O_5-(p-type)InP solar cell without illumination. The device is biased positively by a voltage V_a with respect to the top layer.

We have calculated the efficiency performance of the SIS n-ITO-p-InP solar cell. For these calculations we have assumed the proposed interim air-mass-two spectral distribution [63(a)]. The value of the solar constant for AM2 was taken to be 74.9 mW cm^{-2}. Data for the absorption coefficient of InP were taken from reference 75(a). The minority carrier lifetime was taken as 2 μsec [76] which is not unreasonable since present state of the art materials are considerably better. There are no published data in the literature to the best of our knowledge for the band gap and dielectric constant P_2O_5. We have estimated the dielectric constant of P_2O_5 using the following equation [77]:

$$\varepsilon = \frac{\varepsilon_1 n_1 + \varepsilon_2 n_2}{n_1 + n_2} \tag{3.31}$$

where ε, ε_1 and ε_2 are the dielectric constant of phosphosilicate glass, SiO_2 and P_2O_5 respectively. n_1 and n_2 are the concentrations of SiO_2 and P_2O_5 in mole fractions. The values of ε and ε_1 were taken from reference 78. This gives a value

Figure 3.29

Schematic energy-band diagram of the minority carrier $ITO-P_2O_5$-(p-type)InP tunnel diode system without illumination. The device is biased positively by a voltage V_a with respect to the top ITO layer.

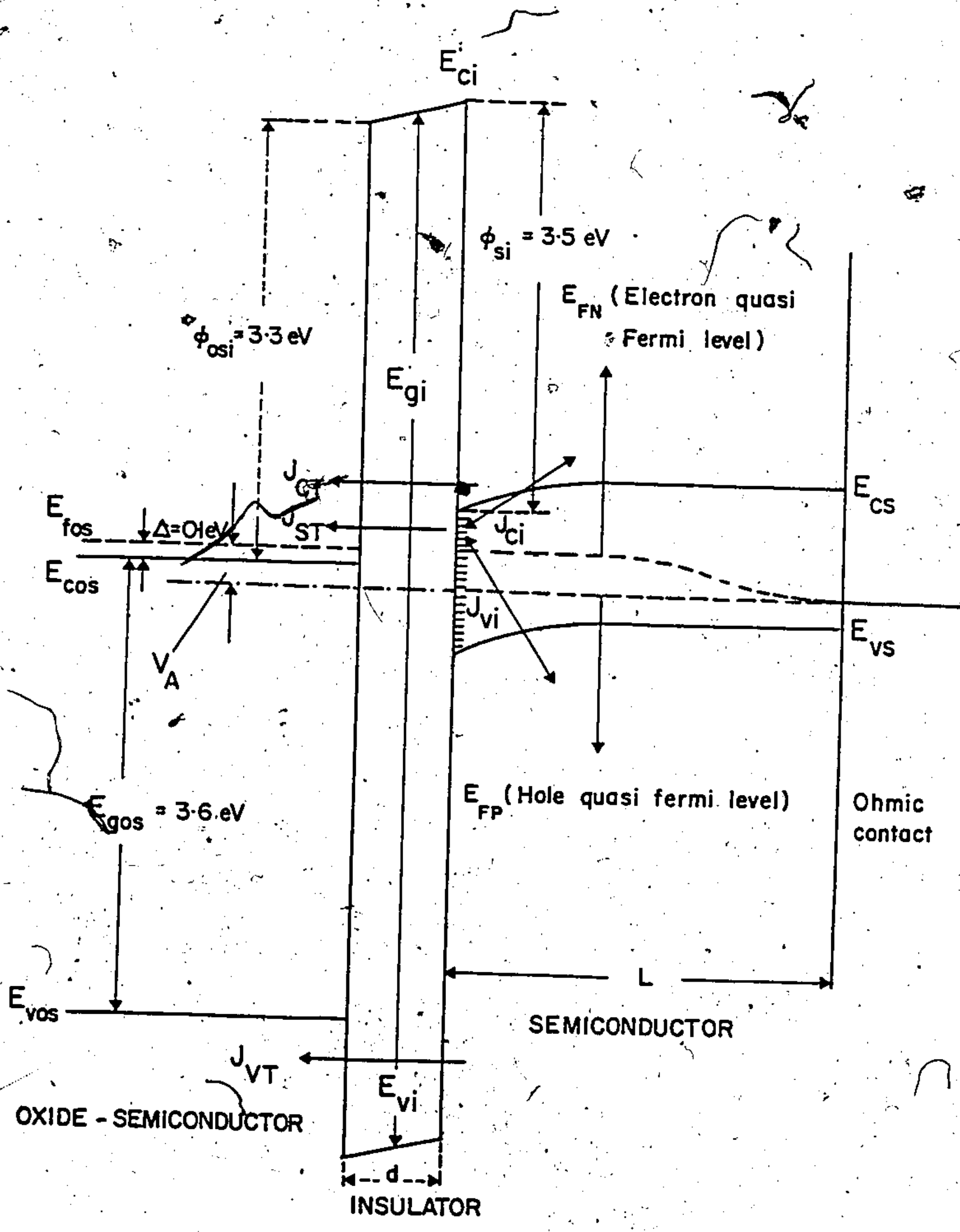

Figure 3.29

of 4.12 for ε_2, which is close tto that of SiO_2. As shown in Table 3.8, some parameters of P_2O_5 like density and magnetic susceptibility are also close to that of SiO_2. So we have assumed a value of 8.1 eV for the band gap of P_2O_5. The surface state density and the oxide charge at the P_2O_5-InP interface were taken as 3.6×10^{15} $m^{-2}eV^{-1}$ and 5.0×10^{15} m^{-2}. In a recent publication, Lile and Collins [79] reported a surface density in the range of $3\text{-}4\times10^{15}$ m^{-2} eV^{-1} for InP MIS diodes. The values of other system parameters are listed in Table 3.9. In these calculations we have assumed zero reflection loss at the front surface and zero absorption loss in the ITO. The absorption loss in the ITO is about 10% [6] and the reflection loss from ITO can be reduced by applying a suitable antireflection coating [9]. Hence, this assumption is reasonable.

Figure 3.30 shows the results of calculations of conversion efficiency as a function of insulator thickness. The efficiency is very low until the interfacial layer thickness drops below about 24 Å and then there is a rapid rise with a saturation in a plateau at about 17 Å. In the region between 17 and 24 Å, the drop in efficiency can be thought of as due to an increasing effective series resistance as the tunneling current changes exponentially and changes in the characteristic due to the transition from the semiconductor limited mode to the tunnelling limited mode. As noted, below about 18 Å, the

TABLE 3.8

SOME PROPERTIES OF SiO_2 AND P_2O_5

Material Property	SiO_2	P_2O_5
Density (kg m^{-3})	2.33×10^5	$2.39.10^5$
Magnetic susceptibility (m^3 kg^{-1})	$-.45 \times 10^9$	$-.46 \times 10^9$

TABLE 3.9

NUMERICAL VALUES ASSIGNED TO SYSTEM PARAMETERS FOR CALCULATING ITO-InP SIS SOLAR CELL PERFORMANCE

Parameter	Numerical Value
T	300°K
ϕ_{si}	3.5 eV
ϕ_{osi}	3.3 eV
E_{gi}	8.1 eV
E_{gs}	1.34 eV
E_{gos}	3.6 eV
n_i	8.0×10^{13} m^{-3}
N_c/N_v	0.049
N_A	1.5×10^{23} m^{-3}
ε_i	4.12 ε_0
ε_s	11.0 ε_0
n_1	n_i
p_1	n_i
m_i, m_{Ti}, m_{Ts}	0.65 m_0
σ_n	10^{-19} m^{-2}
σ_p	10^{-19} m^{-2}
σ_t	10^{-19} m^{-2}
v_{th}	1.17×10^5 m/sec
L	2.5×10^{-4} m
F_A	.047 eV

Figure 3.30

Computed effect of insulator thickness on conversion efficiency of an ITO-P_2O_5-(p-type)InP tunnel diode under AM2 illumination. Substrate resistivity is 0.5 Ω-cm and the temperature is 300°K.

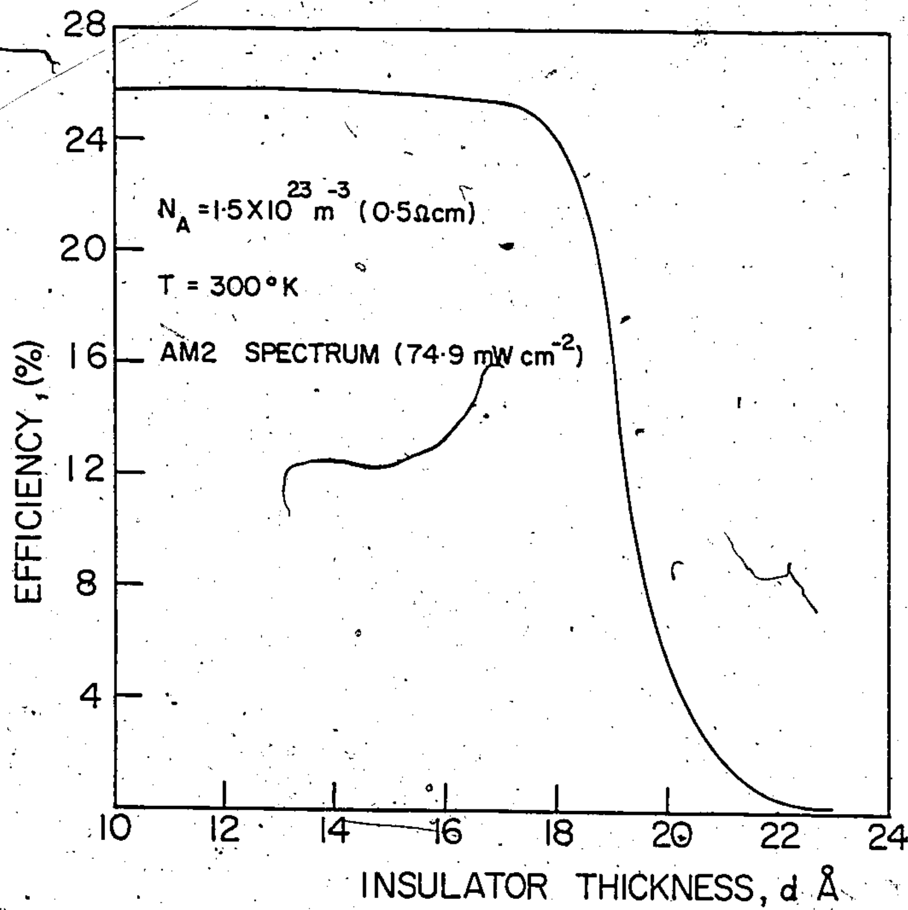

Figure 3.30

efficiency curve saturates in a plateau. The explanation is that the tunnelling occurs at such a rate that the series resistance via this process is insignificant. All possible current from the semiconductor is being extracted and changes can only occur with changes in illumination. Thus, the efficiency saturates.

Also, figure 3.30 shows that calculations have been truncated at about 10 Å. In principle it is possible to calculate the efficiency to a zero thickness limit. However, practically, it is difficult to produce devices with interfacial layers less than about 10 Å. At these levels, interfacial films become non-continuous and the operation is more appropriately described as a Schottky barrier or a p-n heterojunction.

We should mention here that the problem of making a proper interface in InP SIS solar cells may be crucial in achieving a theoretical upper limit. But, in the case of InP MIS solar cells, added dielectrics can be used in place of native grown oxides.

3.4.9.2 ITO/GaAs SIS Solar Cell

In the case of an ITO/GaAs solar cell, the possible interfacial layer could be Ga_2O_3, As_2O_3, a mixture of the two or some ternary compound. There is very limited information available regarding electron affinity and bandgap of the

native oxides of GaAs. For simplicity, we assumed the interfacial layer to be that of crystalline β-Ga_2O_3. We have taken the band gap of β-Ga_2O_3 equal to 4.6 eV from reference 80, and the electron affinity is assumed to be 0.9 eV. Data for the absorption coefficient of GaAs are taken from reference 75(b). Other system parameters are listed in Table 3.10. The efficiency of n-ITO-Ga_2O_3-(p-type)GaAs as a function of insulator thickness is shown in figure 3.31. The reflection data of N. Chang [66] were used in these calculations. In principle, one can have about 20% efficiency from an n-ITO/p-GaAs diode, if there is a wide band gap thin insulator. But, no highly efficient solar cells using GaAs and an oxide-semiconductor have been reported in the literature. One reason may be that none of the oxides present in the device fabricated to date have been suitable.

In the case of GaAs MIS solar cells about 25% efficiency (AM1) can be obtained for properly optimized structures. In place of native oxides, added dielectrics may give better device performance. The problem of making proper interface with native oxides or added dielectrics is very important for the operation of MIS and SIS solar cells.

3.5 SPECTRAL RESPONSE OF MIS AND SIS SOLAR CELLS

Since the MIS and SIS tunnel diodes are essentially surface induced diodes, one would expect a significant enhancement in the ultra-violet response of such cells. There

TABLE 3.10

NUMERICAL VALUES ASSIGNED TO SYSTEM PARAMETERS FOR CALCULATING ITO-GaAs SIS SOLAR CELL PERFORMANCE

Parameter	Numerical Value
T	300°K
ϕ_{si}	3.17 eV
ϕ_{osi}	3.3 eV
E_{gi}	4.5 eV
E_{gs}	1.43 eV
E_{gos}	3.6 eV
n_i	1.1×10^{13} m^{-3}
N_c/N_v	0.067
N_A	1.5×10^{23} m^{-3}
ε_i	3.84 ε_0
ε_s	10.9 ε_0
n_1	n_i
p_1	n_i
m_i, m_{Ti}, m_{Ts}	0.65 m_0
σ_n	10^{-19} m^{-2}
σ_p	10^{-19} m^{-2}
σ_t	10^{-19} m^{-2}
v_{th}	1.17×10^5 m/sec
L	2.5×10^{-4} m
F_A	.023 eV

Figure 3.31

Computed effect of insulator thickness on the conversion efficiency of an nITO-Ga_2O_3-(p-type)GaAs tunnel diode. This curve was calculated by M. Spitzer and is reported in reference 58.

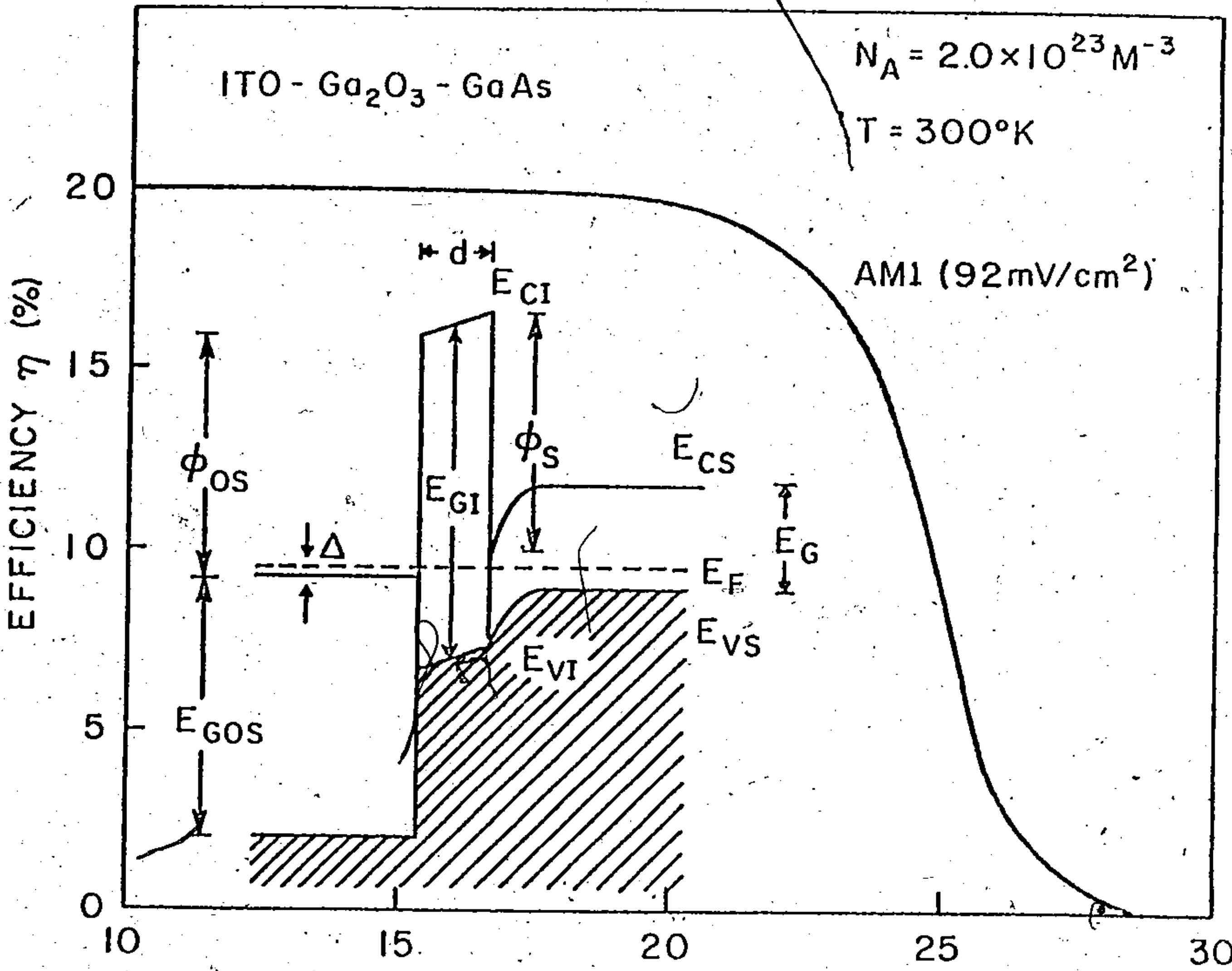

Figure 3.31

is no heavily doped layer at the surface, as with a conventional $n^{+}p$ junction, to cause an ultraviolet loss. Compared to a Schottky or heterojunction diode, the presence of the interfacial layer in MIS and SIS solar cells reduces the image force and also reduces the tunneling probability of majority carriers. Both these factors contribute to the enhancement of the ultra-violet response of MIS and SIS diodes. There will be some loss in the top layer, but this will be small and can be neglected in the theoretical calculations. Calculated spectral response (A/w) of an ITO-SiO_x-(p-type)Si solar cell is shown in Figure 3.32. As expected the blue response is high. Similar results are obtained for MIS solar cells.

3.6 CAPACITANCE-VOLTAGE (C-V) AND CONDUCTANCE-VOLTAGE (G-V) CHARACTERISTICS OF MIS AND SIS SOLAR CELLS

The method of reference 11 has been used to study the C-V and G-V characteristics of MIS solar cells. Identical results are expected for SIS solar cells. The high frequency C-V characteristics are routinely used to estimate the barrier height of the device. We have calculated the high frequency (100 KHz) C-V and G-V characteristics of p-type Si MIS solar cells as a function of insulator thickness. The substrate resistivity is 0.2 Ω-cm (optimum value for MIS and SIS solar cells) and the insulator thickness is varied from 12 to 18 Å. This range of thickness has been selected, since below about 10-12 Å, this device will show Schottky diode behaviour and

Figure 3.32

Computed spectral response (A/W) versus wavelength of an ITO-SiO_x-(p-type)Si solar cell. Substrate resistivity is 0.2 Ω-cm and the insulator thickness is 12 Å. Surface states have the distribution of Figure 3.9 and the insulator charge has the value 5×10^{15} m^{-2}. All other parameters are listed in Table 3.5.

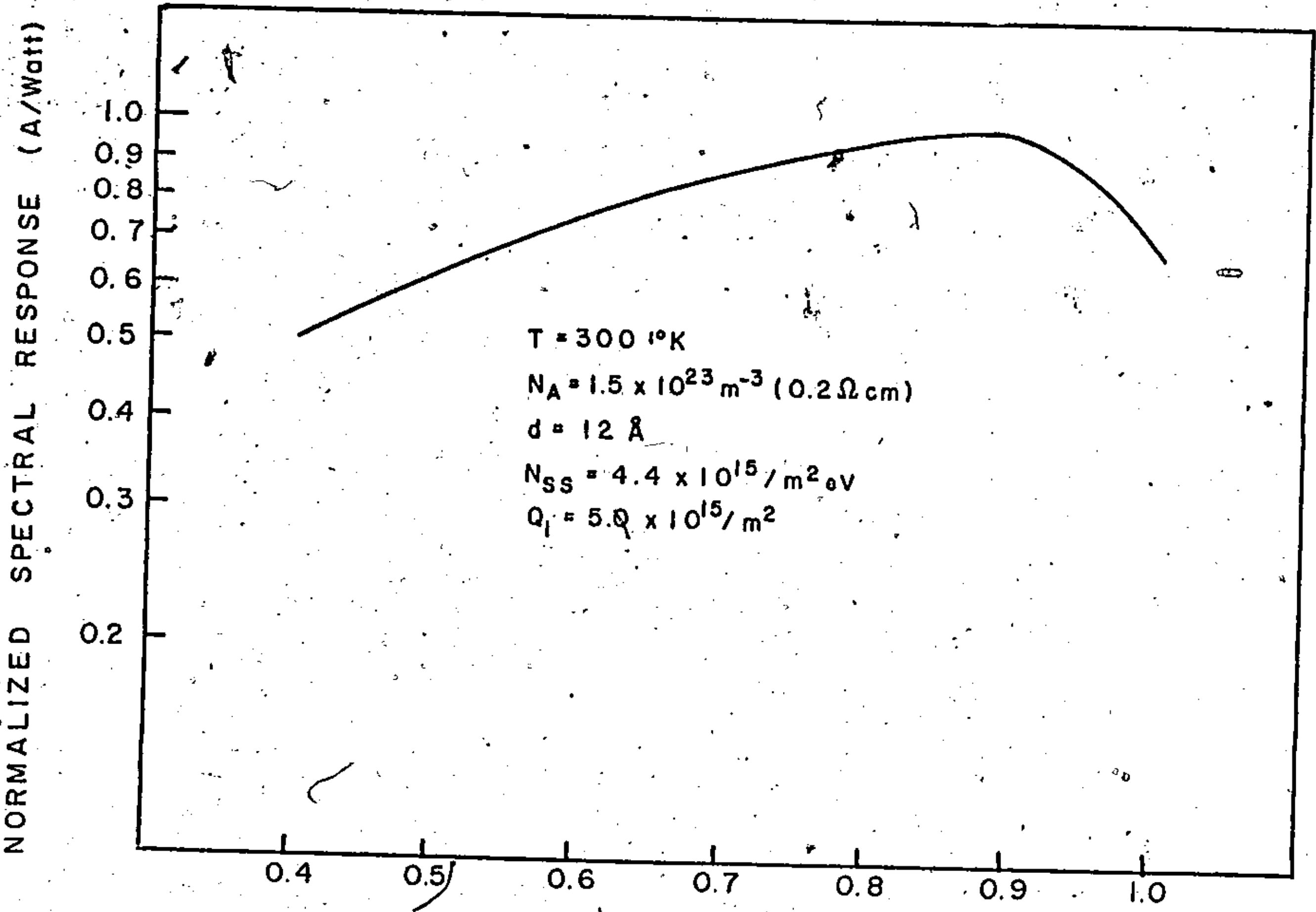

Figure 3.32

above 18 Å, the device shows almost negligible photovoltaic conversion efficiency. The calculated C-V and G-V characteristics are shown in Figures 3.33 and 3.34 respectively. In the reverse and small forward bias range, the C-V characteristics are independent of the frequency of the applied signal. In this bias range the interface is inverted and no frequency dispersion effect is observed. At about 0.45 volt, the capacitance starts increasing with applied bias and large humps appear in the characteristics. After about 0.85 volts, the characteristics show the normal behaviour of thick MIS capacitors [27(d). In the bias region between about 0.45 and 0.85, the current flow in the device is tunnel limited. With an increase in bias, the inversion layer disappears and a large hump is observed in the C-V characteristics. At lower insulator thickness, the hump is sharp due to large current flow compared to a thicker insulator device. After about 0.85 volts the interface is accumulated, and the C-V characteristics are similar to that of a thick MIS capacitor.

The G-V characteristics of Figure 3.34 can be explained in the following way. For a given insulator thickness in the reverse and small forward bias region, the minority carrier concentration does not change and the conductance increases very slowly with bias. After about 0.4 volts, the current flow increases rapidly with decreasing insulator thickness. In

Figure 3.33

Theoretical C-V characteristics of p-type MIS solar cell as a function of insulator thickness. Curves are calculated at a frequency of 100 KHz and the value of ϕ_{mi} is 3.2 eV.

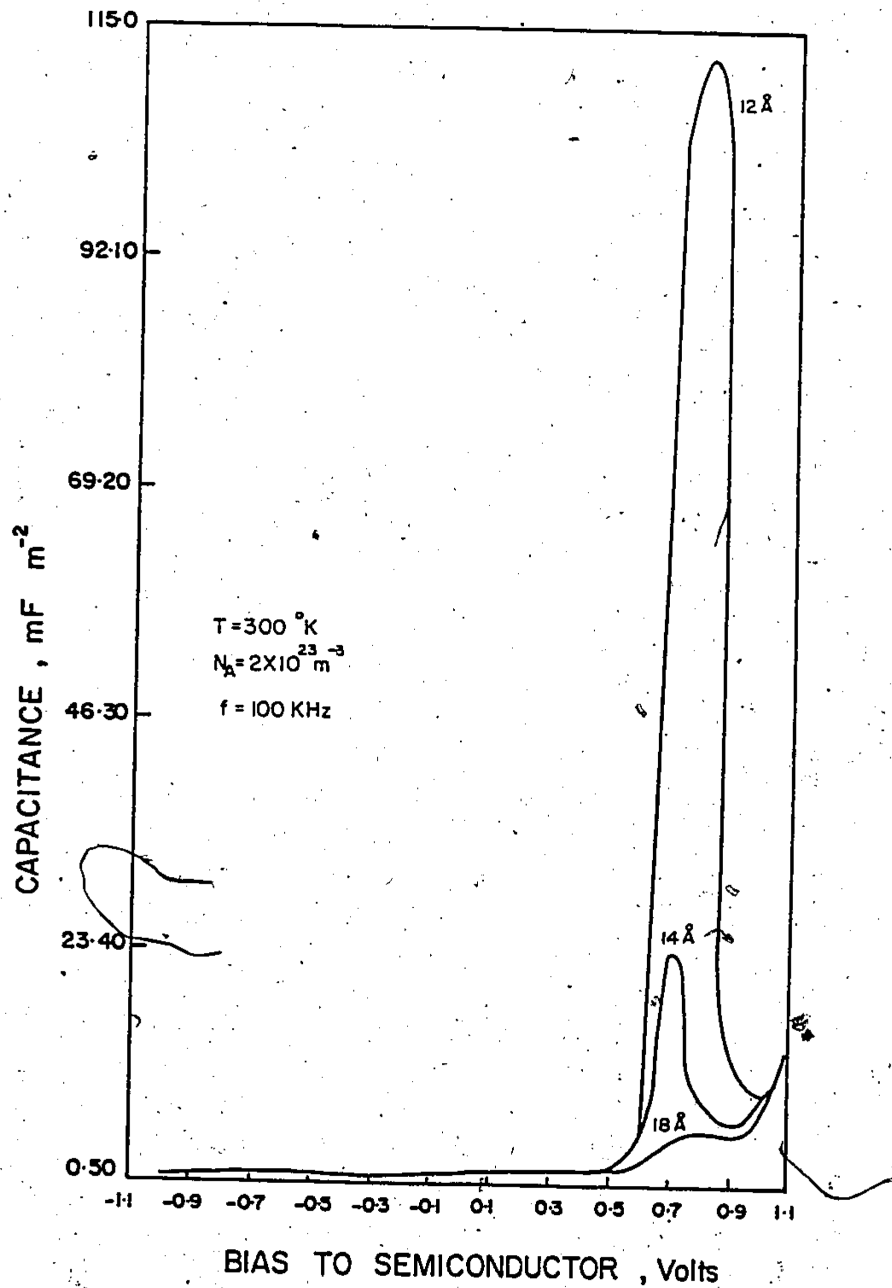

Figure 3.33

Figure 3.34

Theoretical G-V characteristics of p-type MIS solar cell as a function of insulator thickness. All the data are the same as in Figure 3.33.

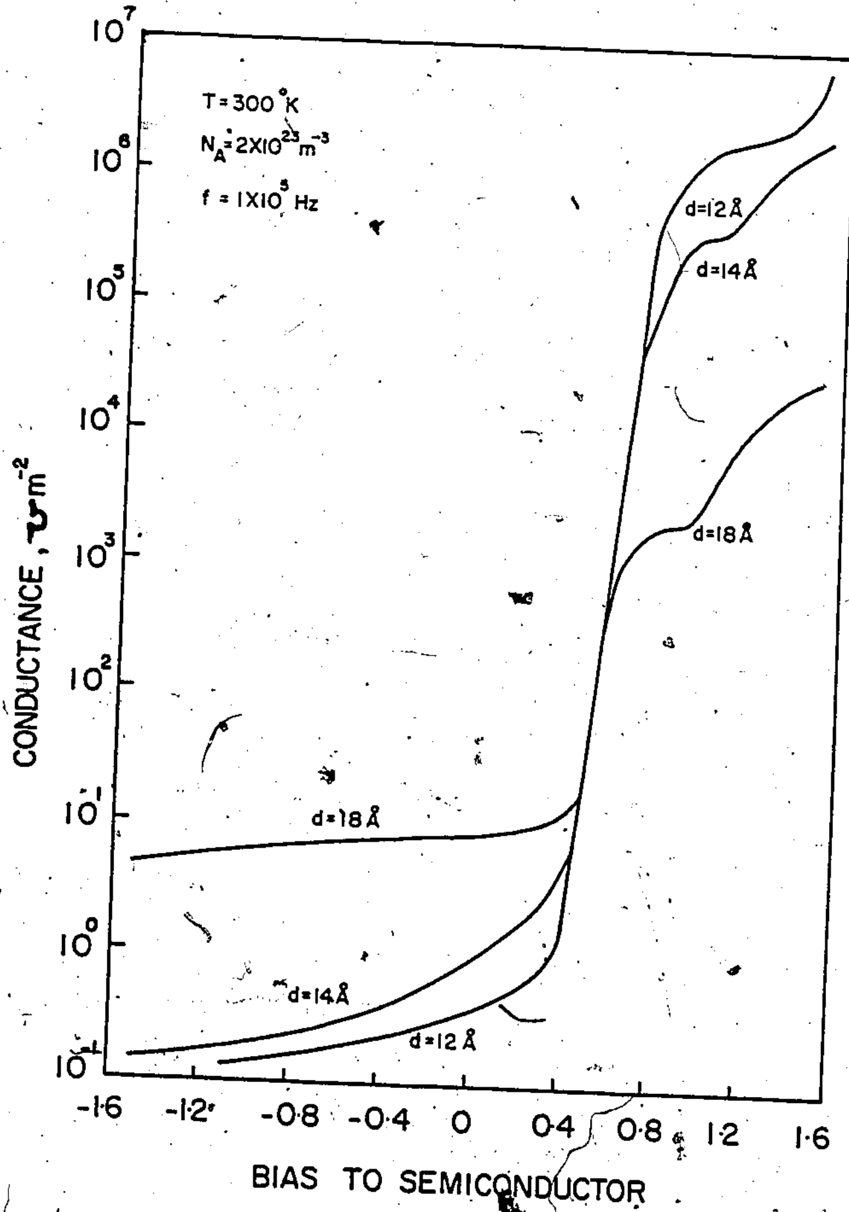

Figure 3.34

this region, the diode current is tunnel limited and varies approximately exponentially with the insulator thickness. At a given bias, in this region, a lower thickness curve shows large conductance compared to a higher thickness curve. At a higher bias (> 0.8 volt), the surface goes from depletion to accumulation and changes in bias are absorbed across the insulator resulting in a pronounced hump.

The C-V and G-V characteristics of p-type Si MIS solar cells as a function of signal frequency are plotted in Figures 3.35 and 3.36 respectively for a fixed insulator thickness of 15 Å. The C-V curves in Figure 3.35 show the clamping of the inversion layer up to about 0.4 volt, and this contributes to the device capacitance above this bias point. The voltage range over which the hump extends can be estimated by considering that, at zero bias, the surface is strongly inverted and at the high voltage side of the hump, the surface is in weak inversion. This voltage is given by [27(e)].

$$V_H \approx \psi_{in} = \frac{2kT}{q} \ln(\frac{N_A}{n_i})$$

The G-V characteristics of Figure 3.36 show the frequency dispersion in the reverse and small forward bias. The hump in the forward bias is due to the delayed response of the inversion layer as explained before. Once the interface is accumulated, the conductance increases with applied bias.

Figure 3.35

Theoretical C-V characteristics of p-type MIS solar cell as a function of signal frequency. The thickness of insulator is 15 Å and the value of ϕ_{mi} is 3.2 eV.

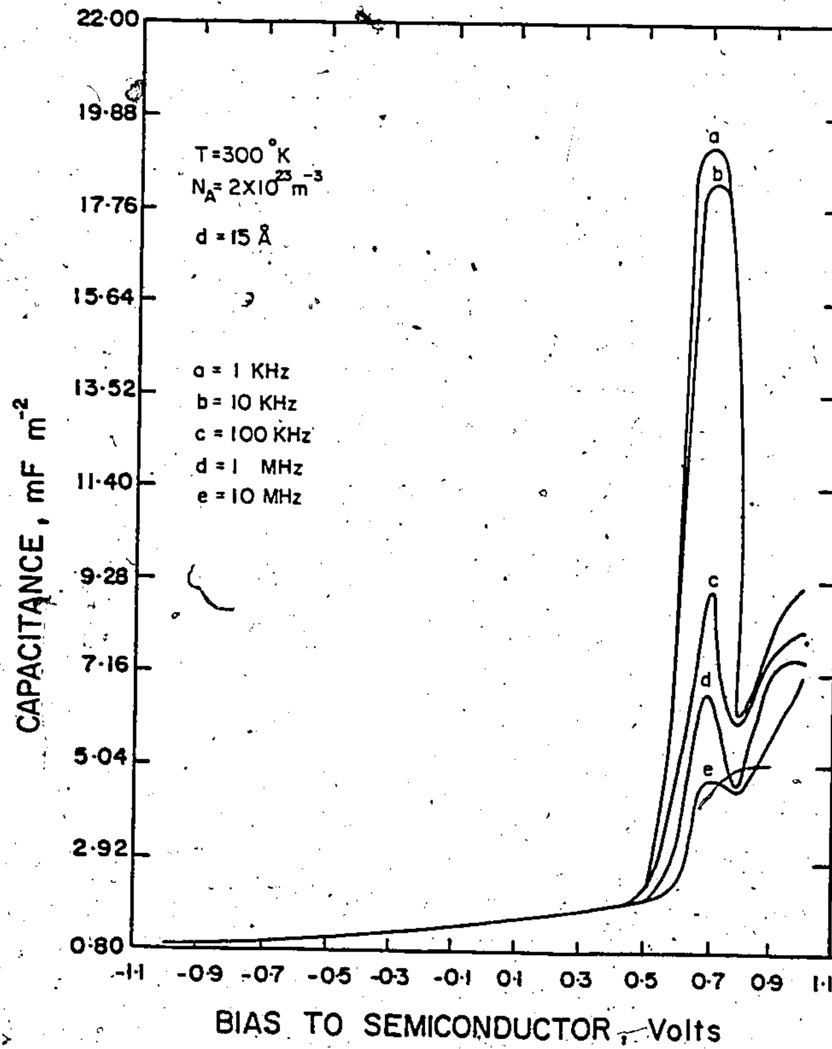

Figure 3.35

Figure 3.36

Theoretical G-V characteristics of p-type MIS solar cell as a function of signal frequency. All the data are the same as in Figure 3.35.

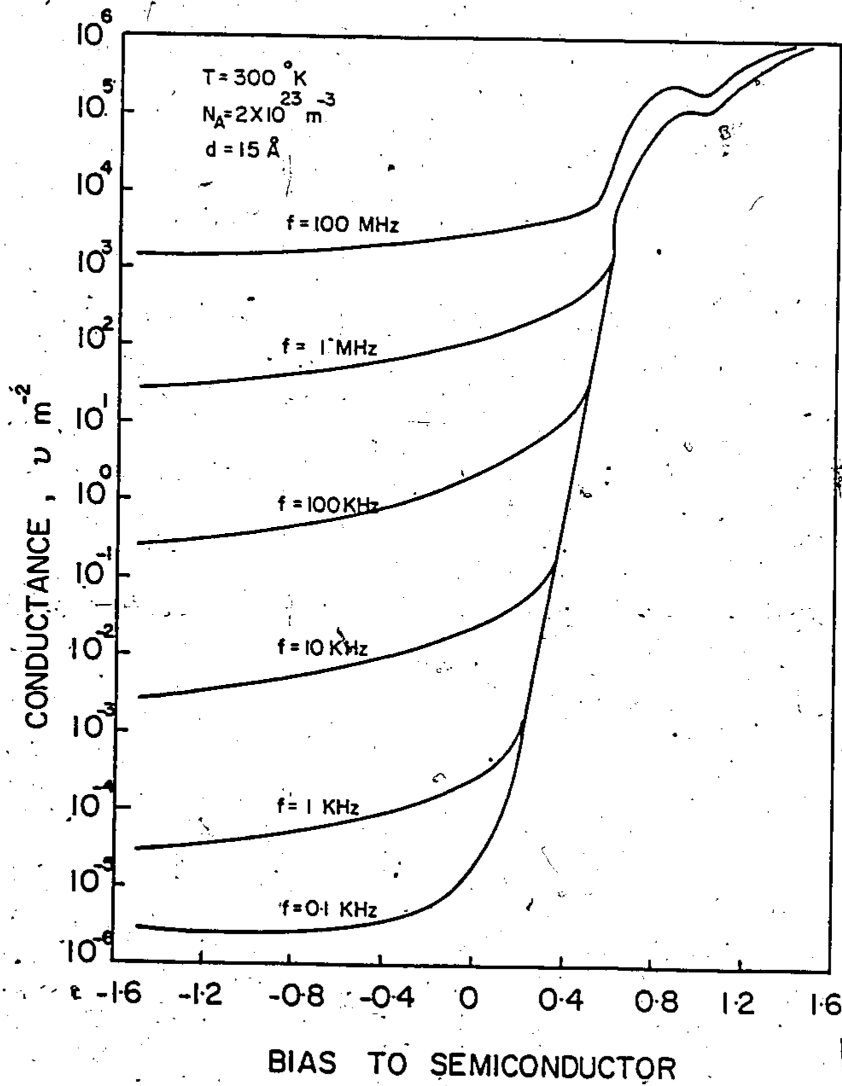

Figure 3.36

3.7 SUMMARY

In this chapter we have described the theory of tunnel MIS and SIS solar cells. The introduction of an ultra thin insulating layer between the top layer and base-semiconductor of a Schottky barrier or heterojunction solar cell results in a tunnel metal-insulator-semiconductor (MIS) or semiconductor-insulator-semiconductor (SIS) diode. Below a certain thickness of the oxide (∿ 10 Å in the case of M or S-SiO_x-(p-type)Si diodes), the device behaves as a Schottky barrier diode. Above a certain thickness, the device behaves as an equilibrium tunnel diode. For an optimum thickness of the insulating layer, the tunnel MIS and SIS solar cells behave like p-n junction devices except for the location of the depletion region. Basically, the field effect induces a p-n junction at the surface of the semiconductor under the insulating layers, and the coupling to this junction is achieved by tunneling, allowing the metal to be contacted to the induced junction.

The reason why the Schottky barrier solar cells do not have high conversion efficiencies is simple. In the MIS case, the oxide is formed by converting the first few layers of semiconductor. The oxide-semiconductor interface is therefore "clean" and a metal-oxide interface (the less important) is "dirty". In Schottky barrier solar cells, the MIS interface is "dirty".

The insulator thickness, the top layer work function and the substrate resistivity are the key parameters in the optimization of tunnel MIS and SIS solar cells. For the optimum insulator thickness, the tunneling occurs at such a rate that the series resistance via this process is insignificant. For p-type MIS and SIS solar cells, the top layer work function should be less than or equal to the electron affinity of base-semiconductor. In the case of n-type tunnel MIS and SIS solar cells, the top layer work function should be equal to or greater than the sum of electron affinity and band gap of the base-semiconductor. Regarding selection of substrate resistivity, lower resistivity wafers are desired as in conventional p-n junction solar cells. For p-type MIS and SIS solar cells, a positive surface charge and donor type surface states will have advantageous effects.

Our calculations based on real world parameters show that efficiencies comparable to p-n junction solar cells can be obtained using tunnel MIS and SIS structures. The Si and GaAs MIS and SIS solar cells are expected to yield about 20% (AM1) and 24 % (AM1) efficiency, respectively.

CHAPTER 4

COMPARISON OF MIS SOLAR CELL THEORY WITH EXPERIMENTAL WORK AND $Si\text{-}SiO_x$ INTERFACE STUDY

4.1 INTRODUCTION

In this chapter we will compare the theoretical data with the available experimental data obtained from the work done in our group and from other published work. The device fabrication details in our group are mentioned in references 26 and 81. In section 4.2.1 the effect of insulator thickness on the performance of MIS solar cells will be compared with theory, followed by the effect of substrate resistivity in section 4.2.2. The effect of metal work function on the performance of MIS solar cells will be compared in section 4.2.3. In section 4.2.4., the dark I-V characteristics as a function of temperature are compared with theory. The effect of crystal orientation on the device performance will be compared in section 4.2.5. The spectral response calculated from the theory will be compared in section 4.2.6 with the device fabricated in our laboratory.

We shall compare our theoretical work with other theories of MIS solar cells in section 4.3. Also, in the same section, we shall compare our calculations with Schottky barrier calculations. The next section of this chapter will be devoted to the study

of $Si\text{-}SiO_2$ interface. The summary of this chapter will be described in section 4.5.

4.2 COMPARISON WITH EXPERIMENTAL WORK

4.2.1 Effect of Insulator Thickness

Figure 4.1 shows the results of efficiency measurements made on $Al\text{-}SiO_x$-(p-type)Si diodes. The single crystal wafers were of 0.17-0.33 Ω-cm resistivity and <100> orientation. The dependence on thickness is functionally the same as that given by the theory (Figure 3.10(a)). Above 22 Å, the efficiency has dropped to zero and saturation is appearing below about 13 Å. The maximum efficiency is considerably lower than that predicted by theory. This is due to the fact that no anti-reflection coatings were employed on the devices we have reported here. The main loss in efficiency is due to a high reflection loss in the 60 Å of aluminum employed. The average reflection loss from 60 Å Al film is more than 50% [82]. An SiO anti-reflection coating of about 670 Å can reduce the loss to about 10% [4].

Figure 4.2 contains a plot of J_{sc} against insulator thickness. When compared to Figure 3.11(a), the behaviour is much the same as predicted by theory. The dependence of V_{oc} on thickness is shown in Figure 4.3. Also, we have plotted the effect of insulator thickness on V_{oc}, as measured by Pulfray [83] for $Al\text{-}SiO_x$-(p-type)Si diodes shown in Figure 4.4. One can see from Figures 4.3 and 4.4 that there is an interesting

Figure 4.1

The measured variation of efficiency as a function of insulator thickness for an Al-SiO_x-(p-type)Si diode with 0.2 Ω-cm Si. The Al is 60 Å thick. Temperature is 300°K. These measurements were carried out by J. St. Pierre and are reported in reference 92.

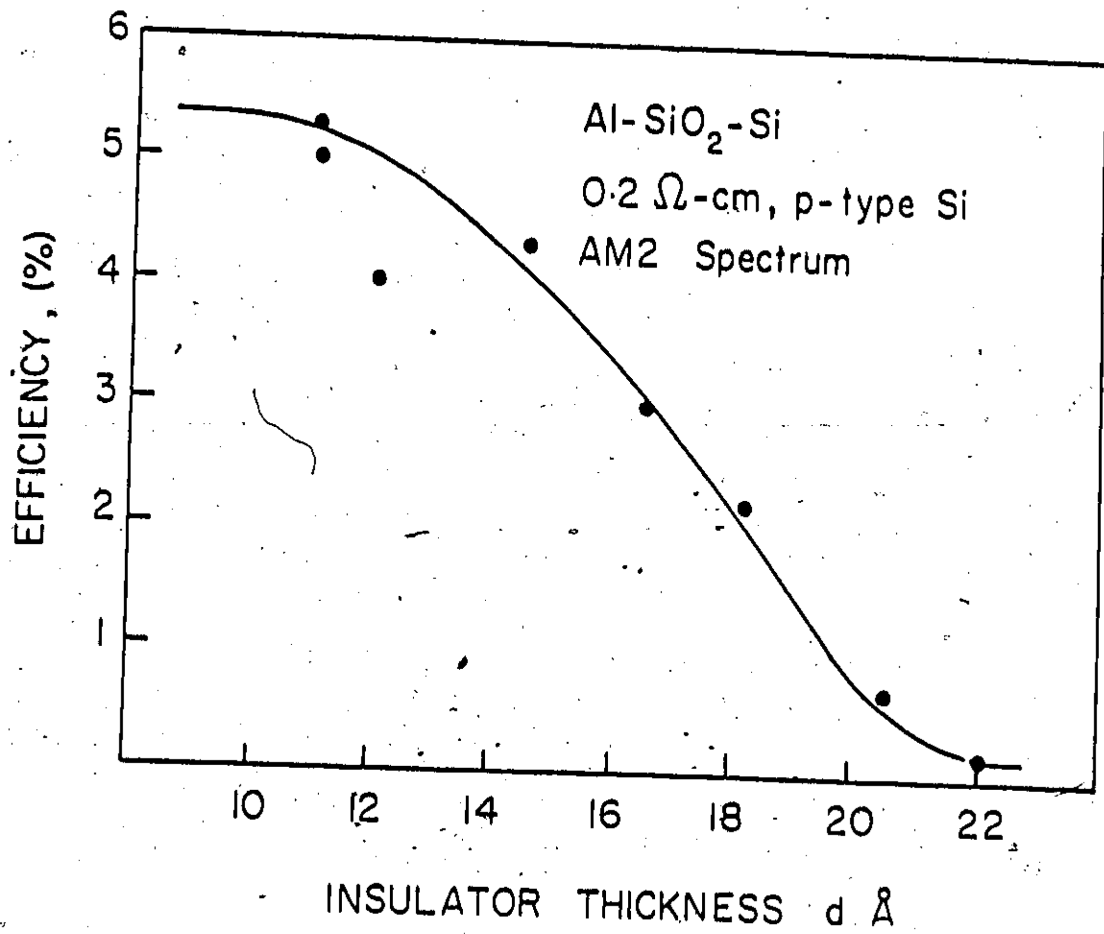

Figure 4.1

Figure 4.2

The measured dependence of J_{sc} as a function of insulator thickness for an Al-SiO_x-(p-type)Si diode with 0.2 Ω-cm Si. The Al is 60 Å thick, temperature 300°K. These measurements were carried out by J. St. Pierre and are reported in reference 92.

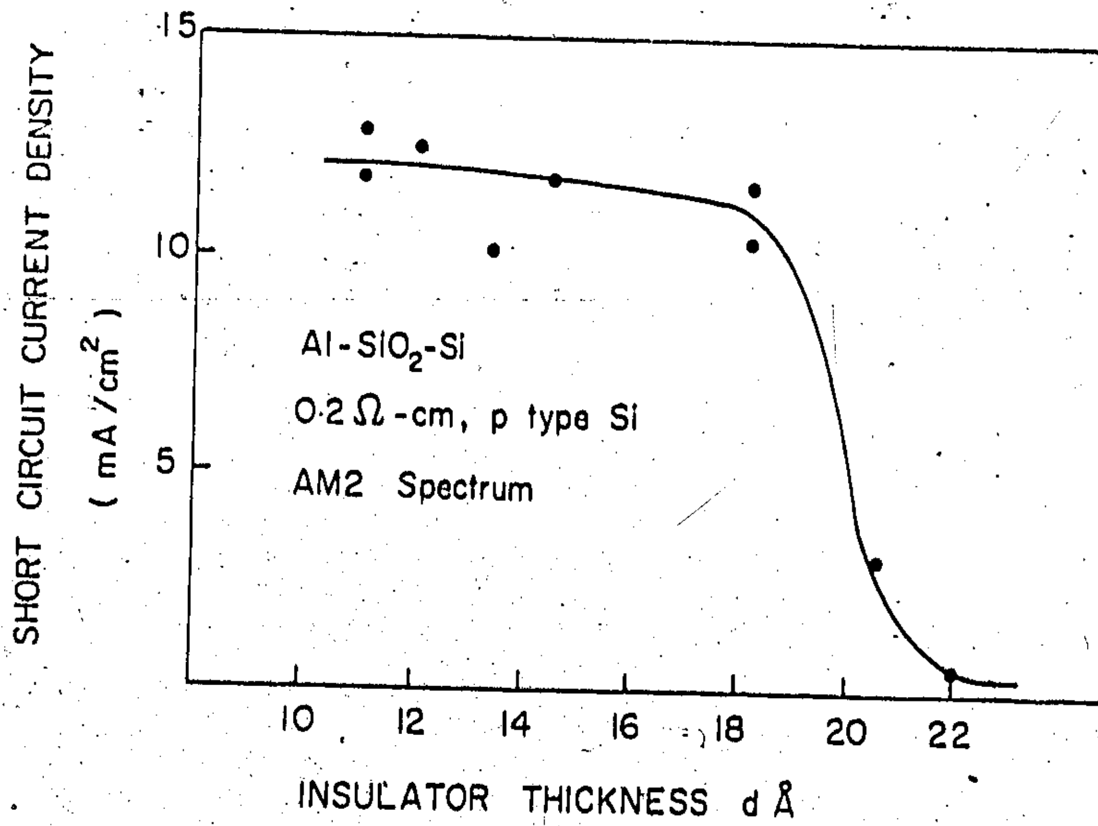

Figure 4.2

Figure 4.3

The measured dependence of V_{oc} as a function of insulator thickness for an Al-SiO_x-(p-type) diode with 0.2 Ω-cm Si. The Al is 60 Å thick and temperature is 300°K. These measurements were carried out by J. St. Pierre and are reported in reference 92.

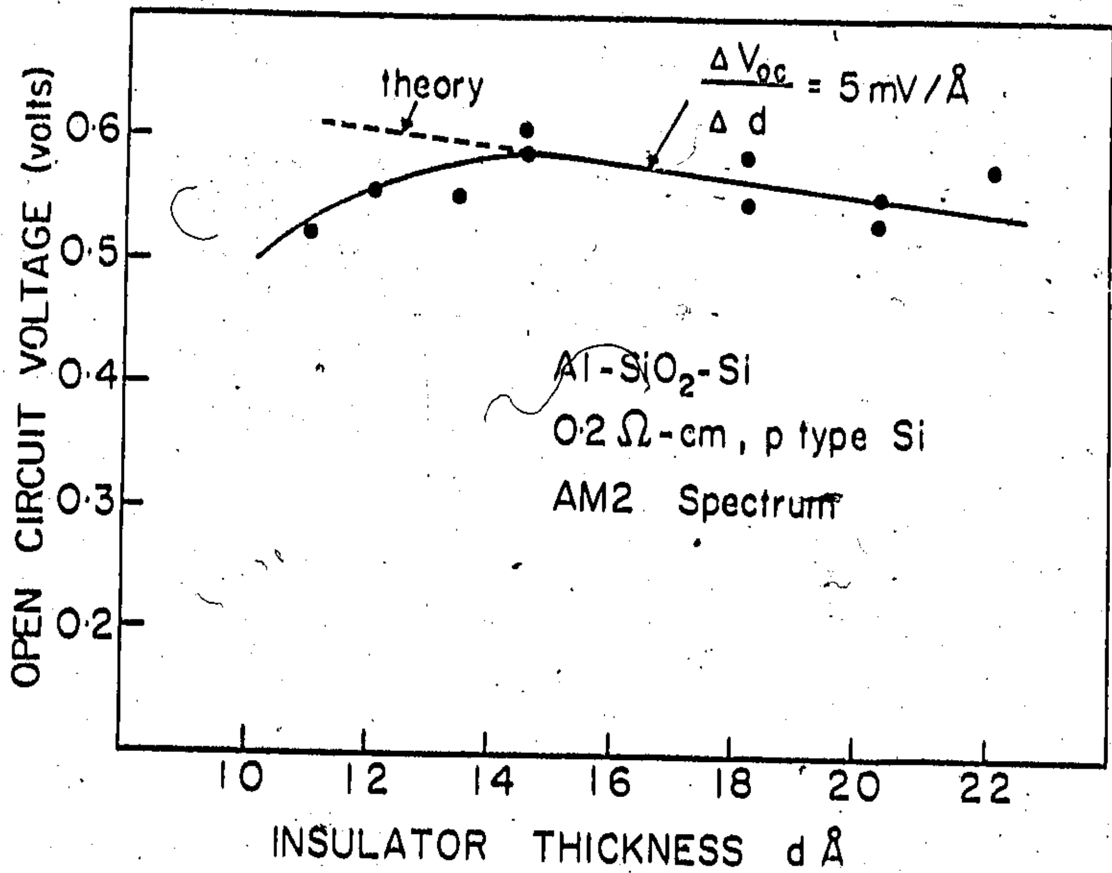

Figure 4.3

Figure 4.4

The measured dependence of V_{oc} as a function of insulator thickness for an Al-SiO_x-(p-type)Si solar cell. The data are taken from reference 83.

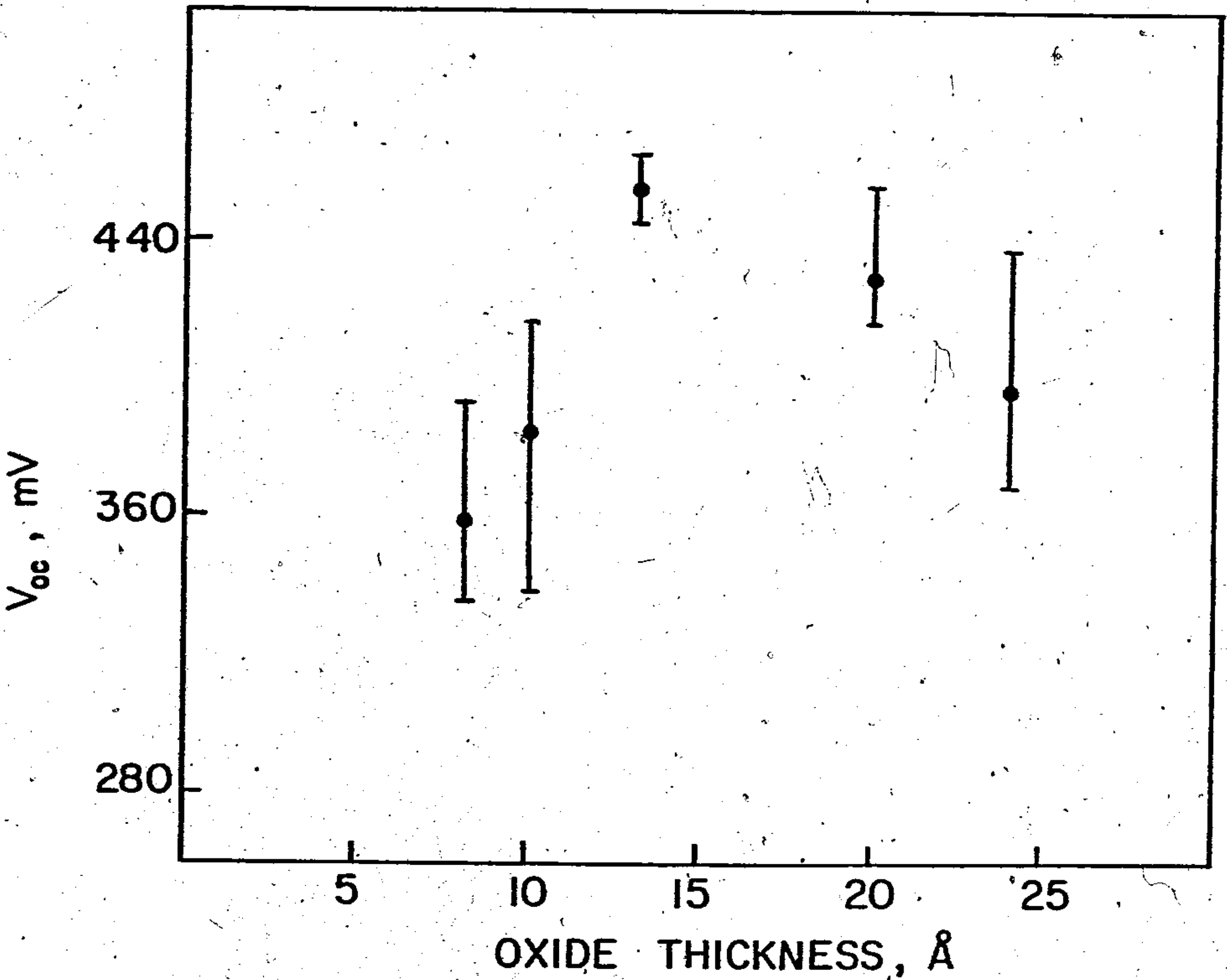

Figure 4.4

departure from theory. For an insulator thickness above 14 Å, the drop in V_{oc} is at a rate of about 3-4 mV/Å, in reasonable agreement with the theoretical value of 4 mV/Å in Figure 3.11(a), considering the calculation was for 0.07 Ω-cm material. However, the drop in V_{oc} below 14 Å is unexpected, but can be accounted for in two ways. First of all, at this low thickness, the oxide may be very patchy and we may have a mixed mode of operation of the diode, partly MIS and partly Schottky barrier [84]. Secondly, as the insulator thickness is decreased, the defect density at the interface may be rising. We have investigated both these possibilities and observed that it is the mixed mode of the diode, which is responsible for this effect. The detailed study is mentioned in section 4.4.

The effect of insulator thickness on the fill factor of experimental devices is shown in Figures 4.5 and 4.6. The first figure represents the measurements made in our group [81] and the second by Pulfrey [83]. Although, to a first approximation, both these curves show that the fill factor decreases as predicted by theory. A better comparison on these test devices is not possible due to the following reasons. The devices fabricated by Pulfrey were of about 0.06 cm^2. The measurements on these devices were made without using any mask. Thus, the area considered in the measurements is somewhat less than that used in the collection of carriers. If we assume a square

Figure 4.5

The measured dependence of FF as a function of insulator thickness for an Al-SiO_x-(p-type)Si solar cell. The data are taken from reference 81.

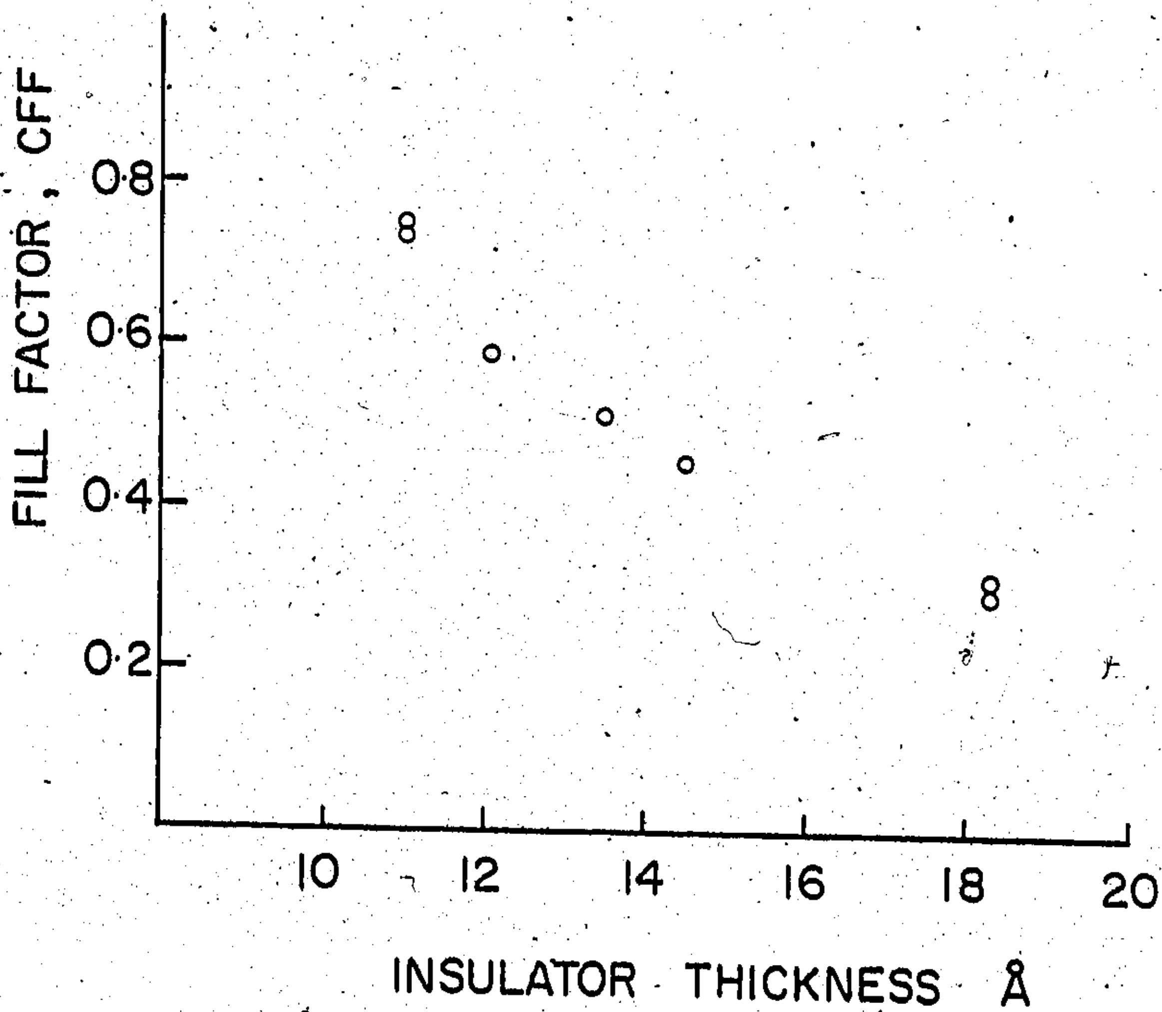

Figure 4.5

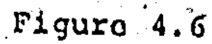

Figure 4.6

The measured dependence of FF as a function of insulator thickness for an Al-SiO_x-(p-type)Si solar cell. The data are taken from reference 83.

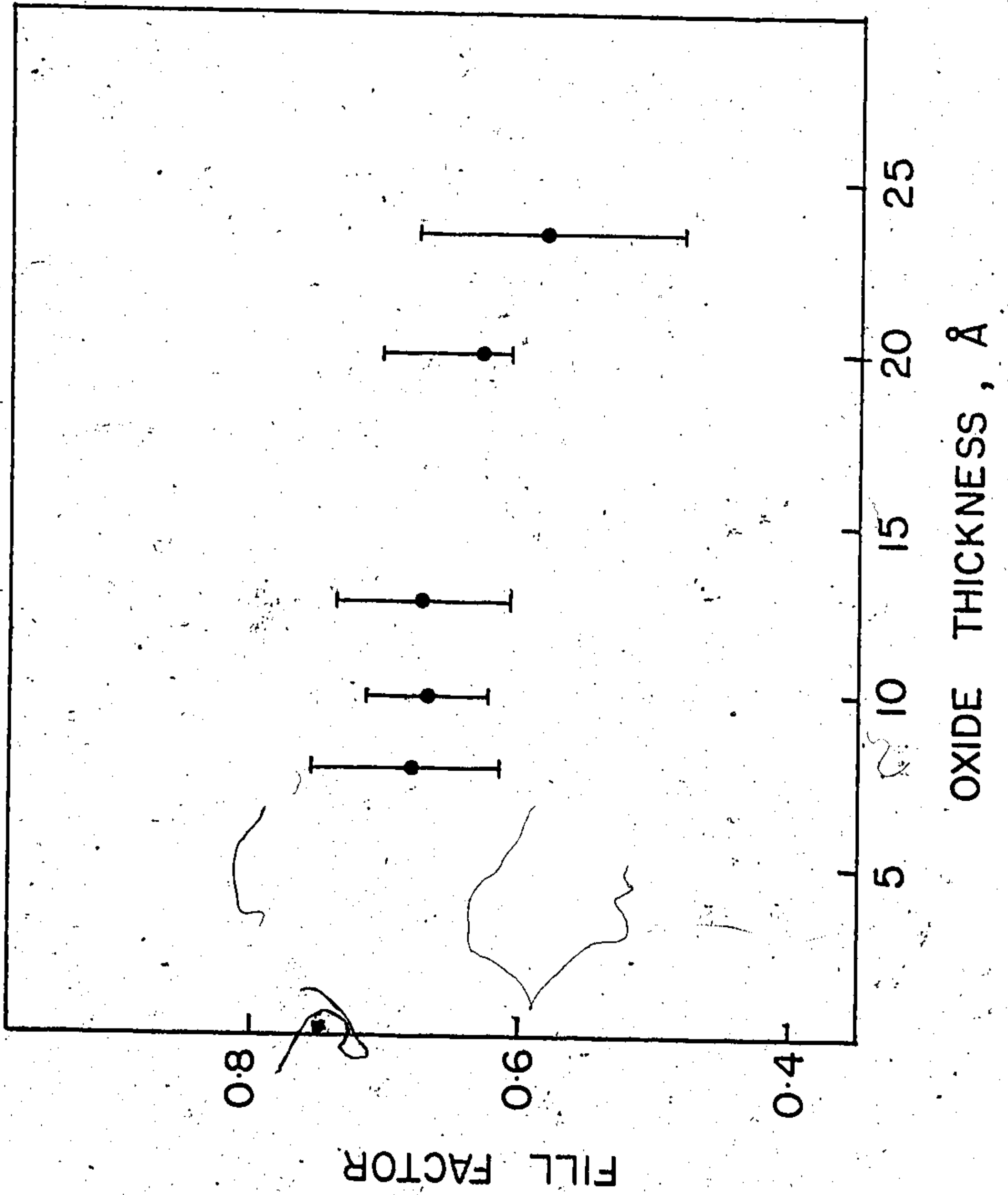

Figure 4.6

cell of side a, then the fractional increase in J_{sc} due to peripheral collection is given by

$$\frac{(a+nL_n)^2}{a^2} - 1 \approx 2n \frac{L_n}{a}$$

$$\approx N \frac{L_n}{a}$$

where L_n is the diffusion length of the solar cell and N may vary from 0 to 1 depending upon the particular solar cell. We have plotted the % increase in J_{sc} as a function of $\frac{L_n}{a}$ with N as a variable parameter. These results are shown in Figure 4.7. The authors of reference 85 have recently commented on the increase in J_{sc} of MIS solar cells by perhiperal collection. By using scanned light spot photo-response technique, Szedon and co-workers [86] have shown that for some Al-SiO_x-(p-type)Si solar cells, peripheral photocurrent collection occurs from unmetallized regions as far as 1000 μm from the edge of the metal layer.

Another problem associated with small area devices is the series resistance effect. We have calculated the fill factor in an ideal solar cell as a function of cell area, with series resistance as the variable parameter. The calculation details are given in Appendix A and the results are shown in Figure 4.8. Thus, one can see that for small area devices,

Figure 4.7

The increase in short circuit current density as a function of normalized diffusion length for small area solar cells.

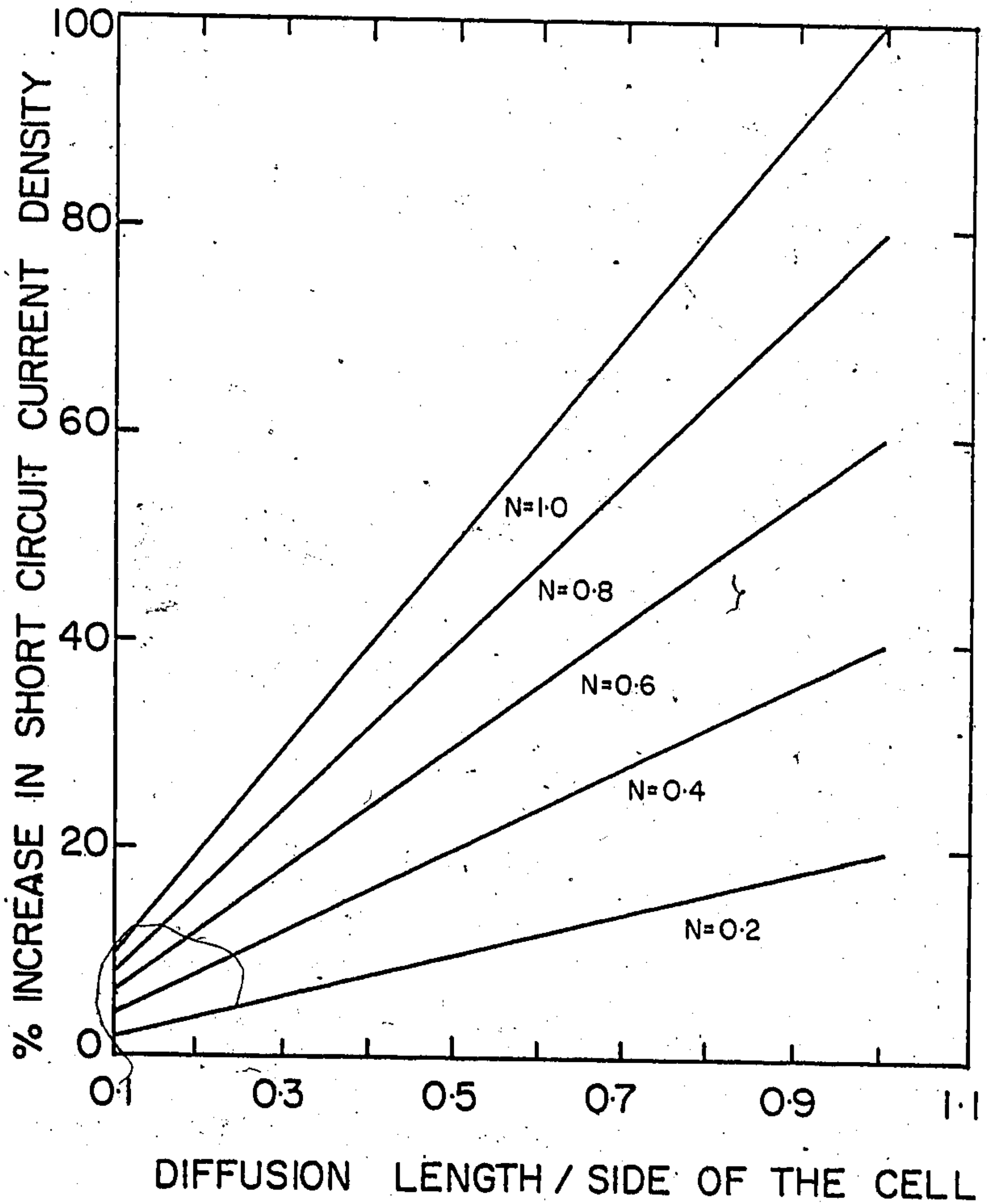

Figure 4.7

Figure 4.8

Calculated fill factor of a solar cell as a function of area, with series resistance as the variable parameter. For small area devices the fill factor is large, although the series resistance is very high.

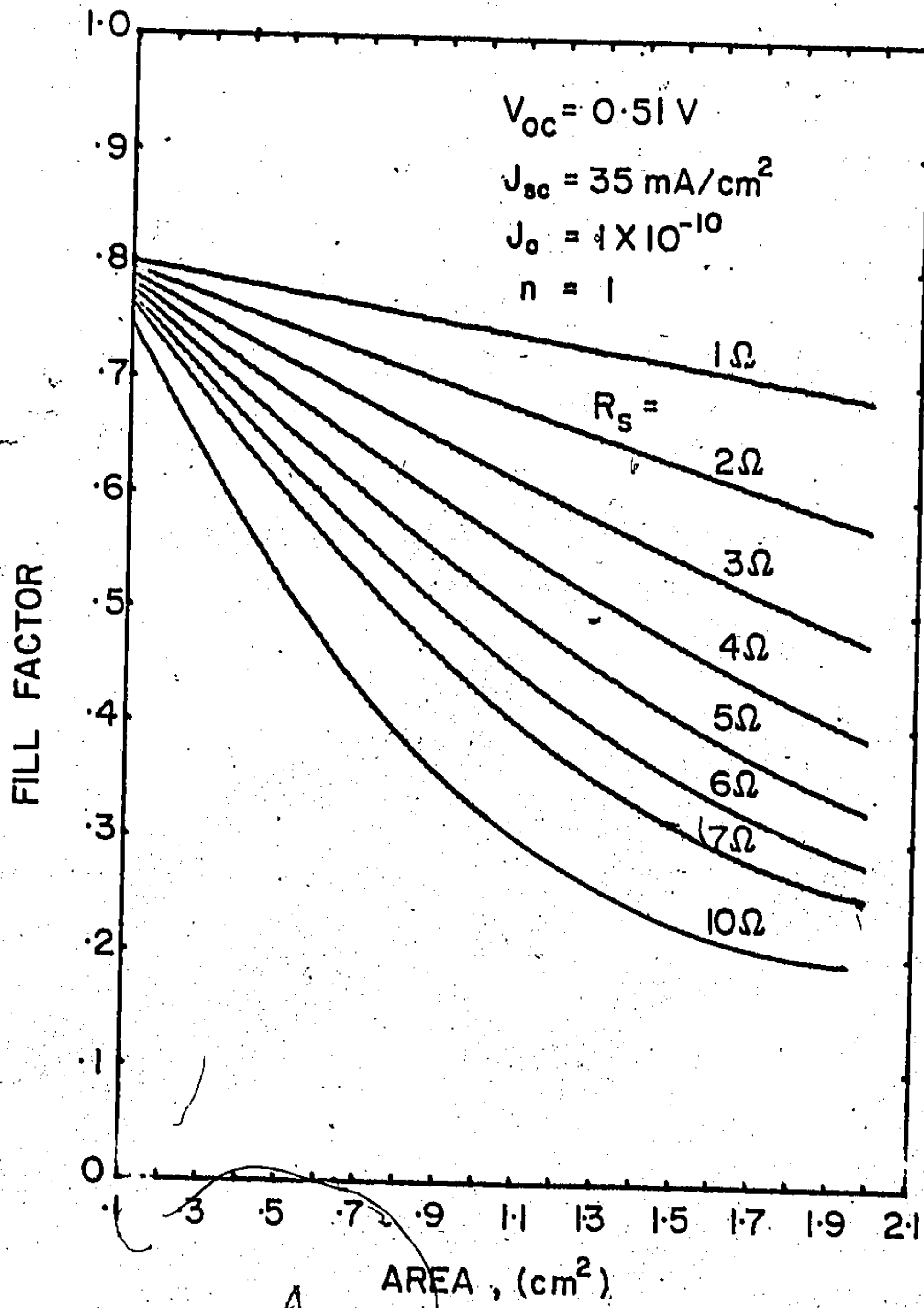

Figure 4.8

the fill factor will always be high even though the series resistance may be very high. The true characteristic parameter of a solar cell in determining the fill factor is not the resistance alone, but the product of series resistance and area. If this product is independent of area, then we can find the true behaviour of the device.

The above arguments are valid for any solar cell with small area. There are a number of publications in the literature on these small area devices [18,87-89], and the conclusion drawn from these measurements about the operating mechanism, or any other judgement, may not be true. In the light of these facts, the effect of insulator thickness on the fill factor of an MIS solar cell may be compared with the theory only when $R_s \times A$ is very small. In that case, the resistance of the insulator will be the only parameter to govern the fill factor.

4.4.2 Effect of Substrate Resistivity

The effect of substrate resistivity on the open-circuit voltage has been studied by Green and co-workers [90]. These results are shown in Figure 4.9. The functional dependence is the same as predicted by the theory (Figure 3.17). For comparison, we have also shown in Figure 4.10, the measurements made by Iles [91] on the V_{oc} of p-n junction Si solar cells. Although the measurement conditions are not the same in the two cases, one can still conclude that optimized MIS solar cells behave like p-n junction devices. The highest observed

Figure 4.9

Measured open circuit voltage of an Al-SiO_x-(p-type)Si solar cell as a function of doping density for an Al-SiO_x-(p-type)Si solar cell. The data are taken from reference 90.

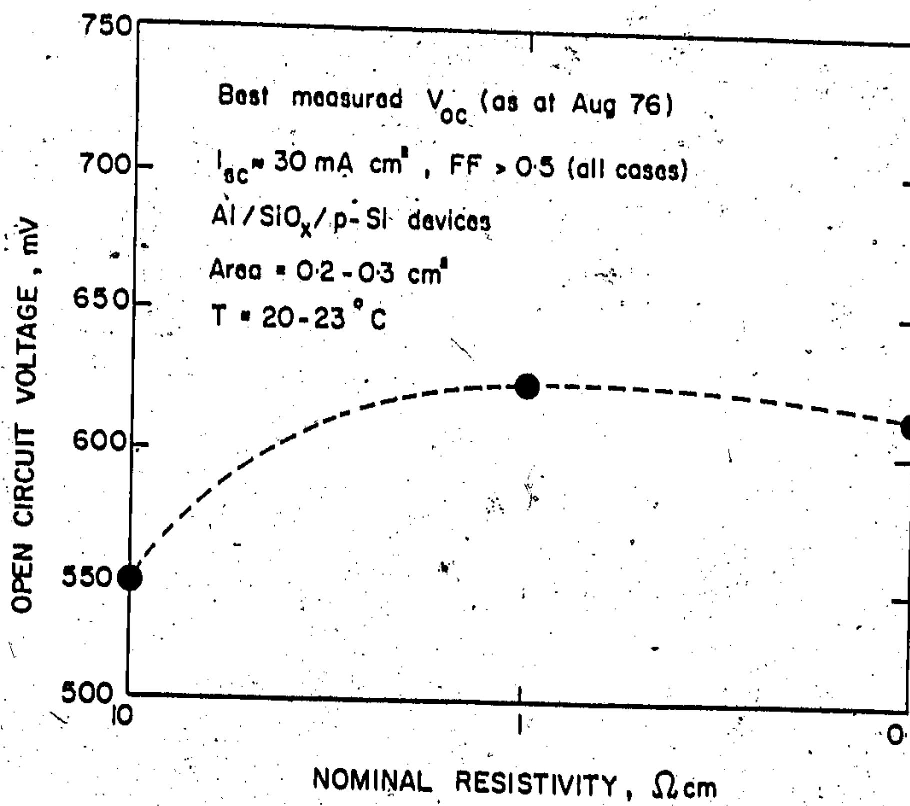

Figure 4.9

Figure 4.10

Measured short circuit current, open-circuit voltage and fill factor as a function of doping density for Si p-n junction solar cells. The data are taken from reference 91.

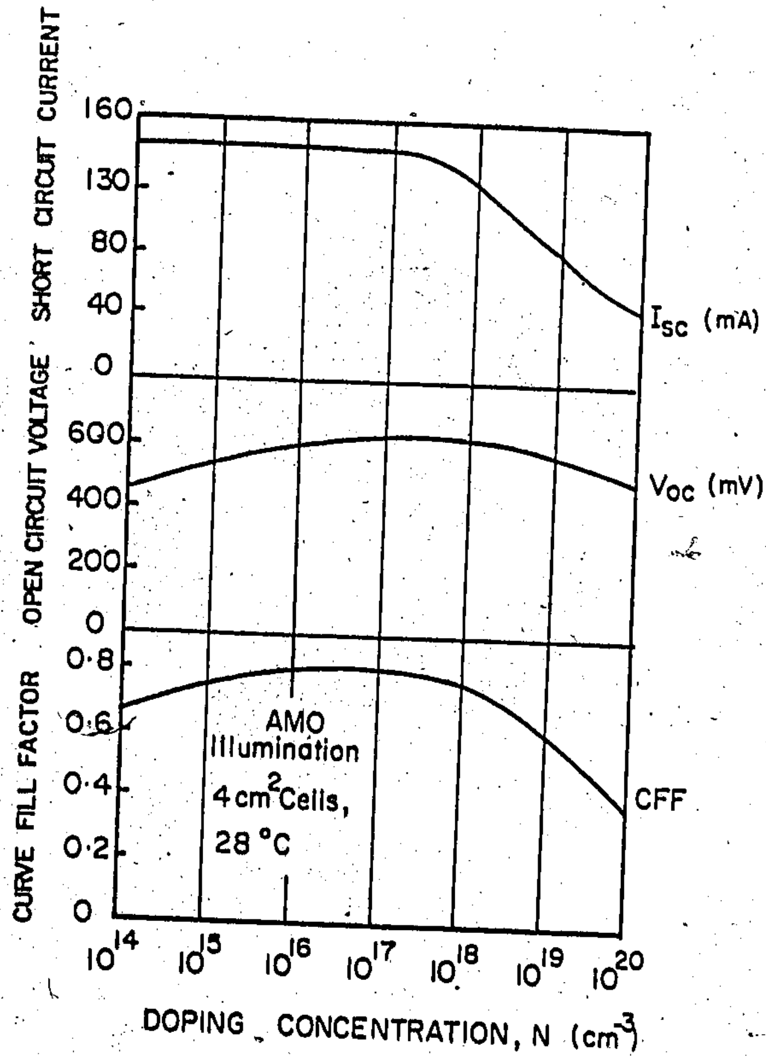

Figure 4.10

V_{oc} of 600 mV in Si MIS solar cells [92] is close to the predicted value of 650 mV by theory [5]. The 50 mV difference may be accounted for by the bandgap narrowing in Si [64], and the different solar spectrum used in calculations than for the measurements. The minority carrier lifetime may also be slightly less in the devices than the one used in calculations.

4.2.3 Effect of Metal Work Function

As we mentioned in section 3.3.4, for a p-type MIS solar cell, the metal work-function should be less than or equal to the electron affinity of the semiconductor. In the case of n-type MIS solar cell, the metal work function should be equal to the sum of the band-gap and electron affinity of the semiconductor. Based on these criteria, the suitable metals for p-type Si and GaAs solar cells are Al, Cr, Ta, Ti, Be and Mg while for n-type devices, Au, Ag, Cu, Ni and Pt may be used. Since work function depends on the surface properties of metal films, the reported values in the literature may vary among various workers. In a recent publication, Michaelson [93] has compiled the work functions of various metals, and these may be used to estimate the metal to insulator barrier height for a particular combination of metal and insulator.

In Table 4.1, the experimental results on single-crystal MIS solar cells are shown. We have included only those results

TABLE 4.1

EXPERIMENTAL DATA ON SINGLE CRYSTAL Si AND GaAs MIS SOLAR CELLS

Substrate	Barrier Metal	Illumination	AR Coating	Device Area (cm^2)	V_{oc} (mV)	J_{sc} mA/cm^2	FF	Efficiency %	Reference
p-Si	Al Mg	AM1	SiO	3.1	610	33.3	0.74	15.1	25
p-Si	Cr	AM1	SiO	2.03	600	26.4	0.77	12.2	96
p-Si	Ti	AM1	TiO_2	2.6	550	33.0	0.66	11.7	95
p-Si	Al	AM1	SiO	0.29	552	21.3	0.7	9.2	26
p-Si	Al	AM1	SiO +ZnS	0.026	470	26.5	-	8.0	87
p-Si	Al	AM1	-	0.06	470	5.5	-	-	83
p-Si	Be	85 mW/cm^2 Sunlight	-	0.68	540	24.6	0.61	9.5	96
p-Si	Au	95 mW/cm^2 Sunlight	-	0.019	400	43.7	0.53	10.5	88
p-Si	Al	AM1	SiO	-	455	28.4	0.79	10.2	97
n-Si	Au	AM1	-	0.33	410	25.0	0.66	6.5	19

(Continued next page)

TABLE 4.1 (continued)

Substrate	Barrier Metal	Illumination	AR Coating	Device Area (cm^2)	V_{oc} (mV)	J_{sc} mA/cm^2	FF	Efficiency %	Reference
n-Si	Pt	82 mW/cm^2 Tungsten Lamp	In_2O_3	0.12	410	29.2	0.6	8.8	20
n-Si	Ag	–	–	–	455	28.4	0.79	10.2	98
n-Si	Au	–	–	0.01	410	32.0	–	9.0	18
n-Si	Au	AM1	–	0.18	550	22.0	0.72	9.0	99
n-GaAs	Ag	AM1	Sb_2O_3 Ta_2O_5	1.0	795	25.9	0.804	16.6	100
n-GaAs	Au	AM1	Sb_2O_3 Ta_2O_5	1.0	794	25.7	0.795	16.2	101

where a barrier metal and some output characteristics of the device are given. As we mentioned earlier in section 4.4.2, the conclusions drawn from devices having less than 0.2-0.3 cm^2 may be misleading. For example, the current density reported in reference 88 is greater than the theoretical limits. In the absence of sufficient experimental data, it is hard to compare the effect of metal work function with the theory. However all the high efficiency and large area devices shown in Table 4.1 confirm the basic prediction of our model, i.e. low work function metals are required for p-type substrate and high work function metals for n-type substrate.

4.2.4 Effect of Temperature

Recent experimental work on single crystal silicon MIS solar cells [25,94] supports our theoretical predictions [1,5] that these structures can approach p-n junction performance. Over a certain bias range, MIS solar cells operate as classical p-n junctions, with diffusion in the bulk of the semiconductor governing carrier transport and hence determining the I-V characteristics of the device. The high efficiency behaviour reported in references 25 and 94 indicates that the device dark current consists of minority carriers and not of majority carriers. A study of dark I-V characteristics as a function of temperature can be used to confirm the diffusion dominated p-n junction behaviour of MIS solar cells. In this section we report on an

experimental study of dark I-V characteristics as a function of temperature for Al-SiO_x-(p-type)Si solar cells.

Tunnel MIS solar cells were fabricated using <100> p-type (Boron doped) single-crystal silicon wafers of 1-3 Ω-cm resistivity. The thickness of the oxide is about 10-15 Å. The details of the device fabrication are given in reference 26. After fabrication, the following parameters were measured for a typical device (No. N-08-01) under AM1 (100 mw/cm^2) illumination:

$$V_{oc} = 0.552 \text{ V}$$
$$I_{sc} = 6.265 \text{ mA}$$
$$FF = 0.766$$
$$A = 0.29 \text{ cm}^2$$
$$\eta = 9.2\% .$$

No attempt was made to optimize devices for efficiency through a better collection grid or AR coating.

The experimentally observed dark I-V characteristics for a typical MIS solar cell are shown in Figure 4.11 as a function of temperature. An inspection of the curves shows that the dark I-V consists of three regions: One at low bias, one in the intermediate bias range and the other of high bias range. The low bias regime is complicated consisting undoubtedly of depletion layer recombination current as well as other defect current flow such as surface channel currents [70]. The intermediate bias region corresponds to diffusion dominated current and the high bias region is the result of tunnel limited current [5]

Figure 4.11

Measured forward bias current-voltage characteristics for a typical Al-SiO_x-(p-type)Si solar cell as a function of temperature. These measurements were carried out by D. Burk and are reported in reference 26.

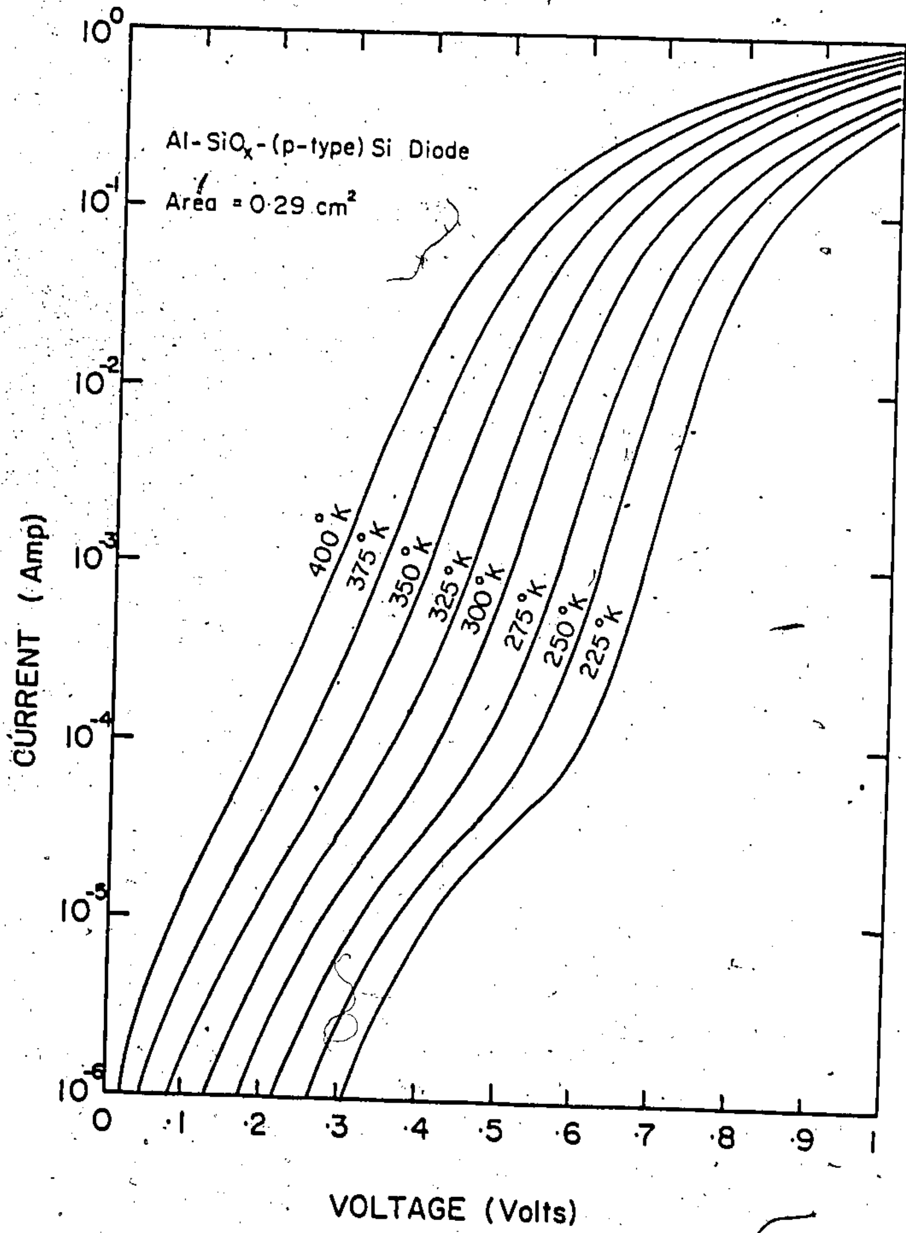

Figure.4.11

and series resistance. For solar cell application, it is the first two regions in which we are principally interested, since the open-circuit voltage for silicon solar cells is generally less than 0.7 volt. As shown by Hovel [102], the influence of the depletion region recombination current on the conversion efficiency of Si p-n junction solar cells is negligible. The same applies to other defect currents which show up. The arguments are also true for tunnel MIS solar cells. Thus, it is primarily the diffusion region current that controls the output I-V characteristics of MIS solar cells. It is also seen in Figure 4.11 that for the lower bias region there is a "crowding" of the characteristics at lower temperatures unlike that expected from theory. This feature is not unusual and has been observed on Si p-n junction solar cells [103,104]. Again this is the influence of the other defect currents mentioned.

In principle, the computer calculated curves obtained from our MIS solar cell theory [5] can be used to fit the experimental data. However, we know that we are dealing with pseudo p-n junctions and it is particularly illustrative and just as effective to use the lumped diode model approximations. The experimentally observed data of Figure 4.11 were fitted by using the following equations:

$$I - \frac{V-IR_s}{R_{sh}} = I_{01}[\exp q(\frac{V-IR_s}{n_1kT}) - 1] + I_{02}[\exp q(\frac{V-IR_s}{n_2kT}) - 1] \quad (4.2)$$

where

$$I_{01} \propto T^3 \exp\left(\frac{-E_g}{n_1 kT}\right) \quad \text{(diffusion)} \qquad (4.3)$$

$$I_{02} \propto T^{5/2} \exp\left(\frac{-E_g}{n_2 kT}\right) \quad \text{(recombination)}. \qquad (4.4)$$

I_{01} is the reverse saturation current associated with the diffusion component and I_{02} is the reverse saturation current for the defect current at low biases which, for simplicity, we have taken to be all depletion recombination current [103]. This approximation is warranted since the region of the excess defect current is not known and we have argued that, in any event, it does not influence the output characteristics of the solar cell. As shown in Table 4.2, the average value of n_1 from the experimental data is 1.18. We take $n_2 = 2$. To obtain a fit we adjust the magnitude of the saturation current to agree with the experimental data. It is, however, about two orders of magnitude larger than one gets from the MIS theory. As can be seen from Figure 4.12 an excellent fit is obtained with $R_s \cong 0.5\ \Omega$ and $R_{Sh} = 1\times10^8\ \Omega$.

Next we attempted to fit the experimental curves by assuming that the dark current in the intermediate region consists of thermionic emission current. The barrier height ϕ_b was determined by plotting $\frac{I_{01}}{T^2}$ vs. 1/T and a value of 0.83 eV was obtained. In this situation we have

TABLE 4.2

MEASURED n VALUES AND SATURATION CURRENTS AS A FUNCTION OF TEMPERATURE FOR Al-SiO_x-(p-type)Si SOLAR CELLS

T°K	n_1	I_{01} (Amp)
400	1.14	2.81×10^{-7}
375	1.15	1.02×10^{-7}
350	1.18	1.32×10^{-8}
325	1.20	5.04×10^{-9}
300	1.23	2.51×10^{-10}
275	1.27	7.20×10^{-12}
250	1.28	1.35×10^{-13}
225	1.30	4.64×10^{-15}

Figure 4.12

Theoretical fit to the experimental data in Figure 4.11, using the diffusion current dominated tunnel MIS theory of reference 5.

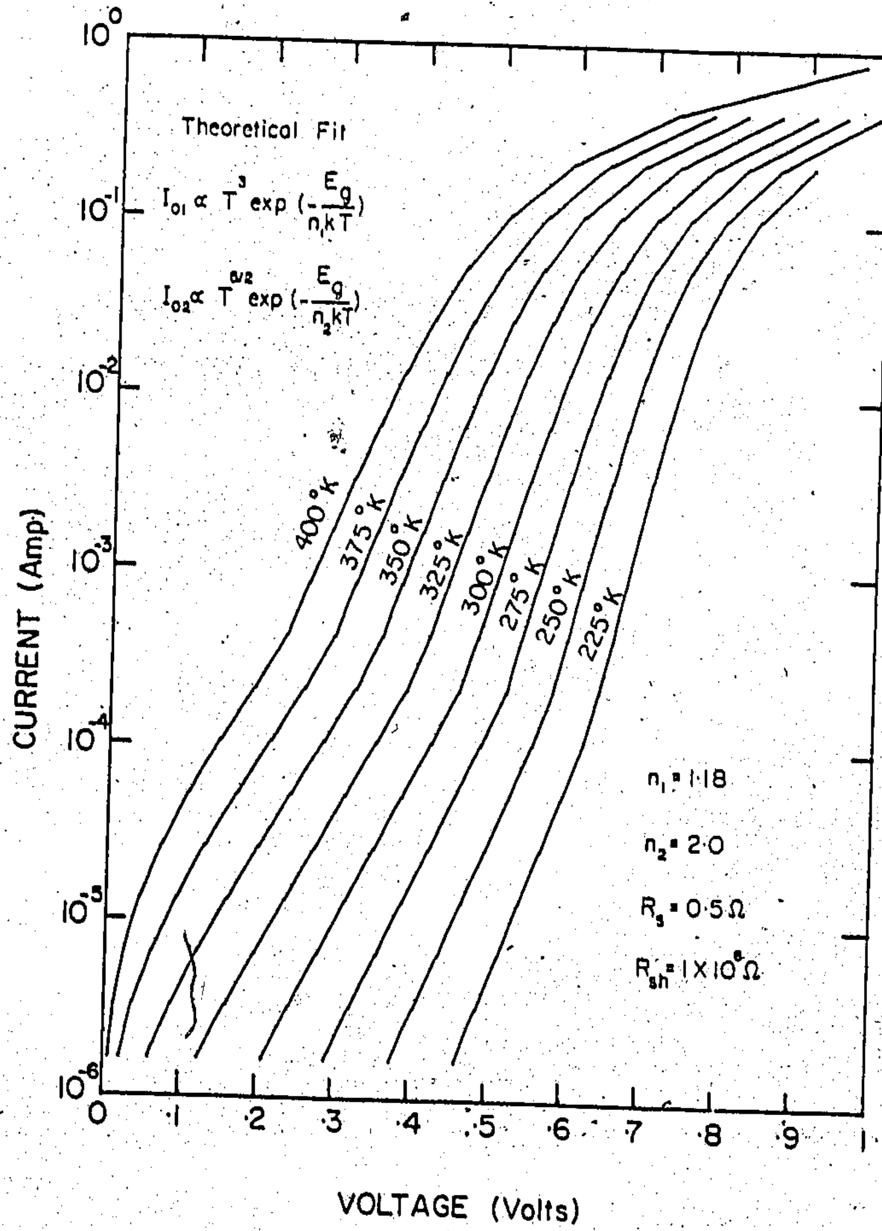

Figure 4.12

$$I_{01} \propto T^2 \exp(\frac{-\phi_b}{kT}) \quad \text{(thermionic-emission)} \qquad (4.5)$$

$$I_{02} \propto T^{5/2} \exp(\frac{-E_g}{n_2 kT}) \quad \text{(recombination)}.$$

The values of $n_1 = 1.18$, $n_2 = 2$, $R_s = 0.5\ \Omega$ and $R_{sh} = 1\times10^8\ \Omega$ were used as in the previous case. The results of this curve fitting are shown in Figure 4.13 and it can be seen that the fit is quite poor.

In conclusion, the experimental data shows that the current conduction mechanism in MIS solar cells is as predicted by our theory. Optimum MIS solar cells behave like pseudo p-n junctions and there is no support for the thermionic emission current mechanism as proposed by various investigators [22-24].

4.2.5 Effect of Crystal Orientation

Figure 4.14 shows the I-V characteristics of two MIS solar cells of different crystal orientation [81]. The top metal is Al and no AR coatings were applied. The substrate resistivity and the thickness of the interfacial layers are nearly the same. The upper curve represents <100> orientation device and the lower curve represents the <111> orientation device. As we mentioned in section 3.3.7, the device perfor-

Figure 4.13

Attempted theoretical fit to the experimental data in Figure 4.11, using the thermionic emission current model.

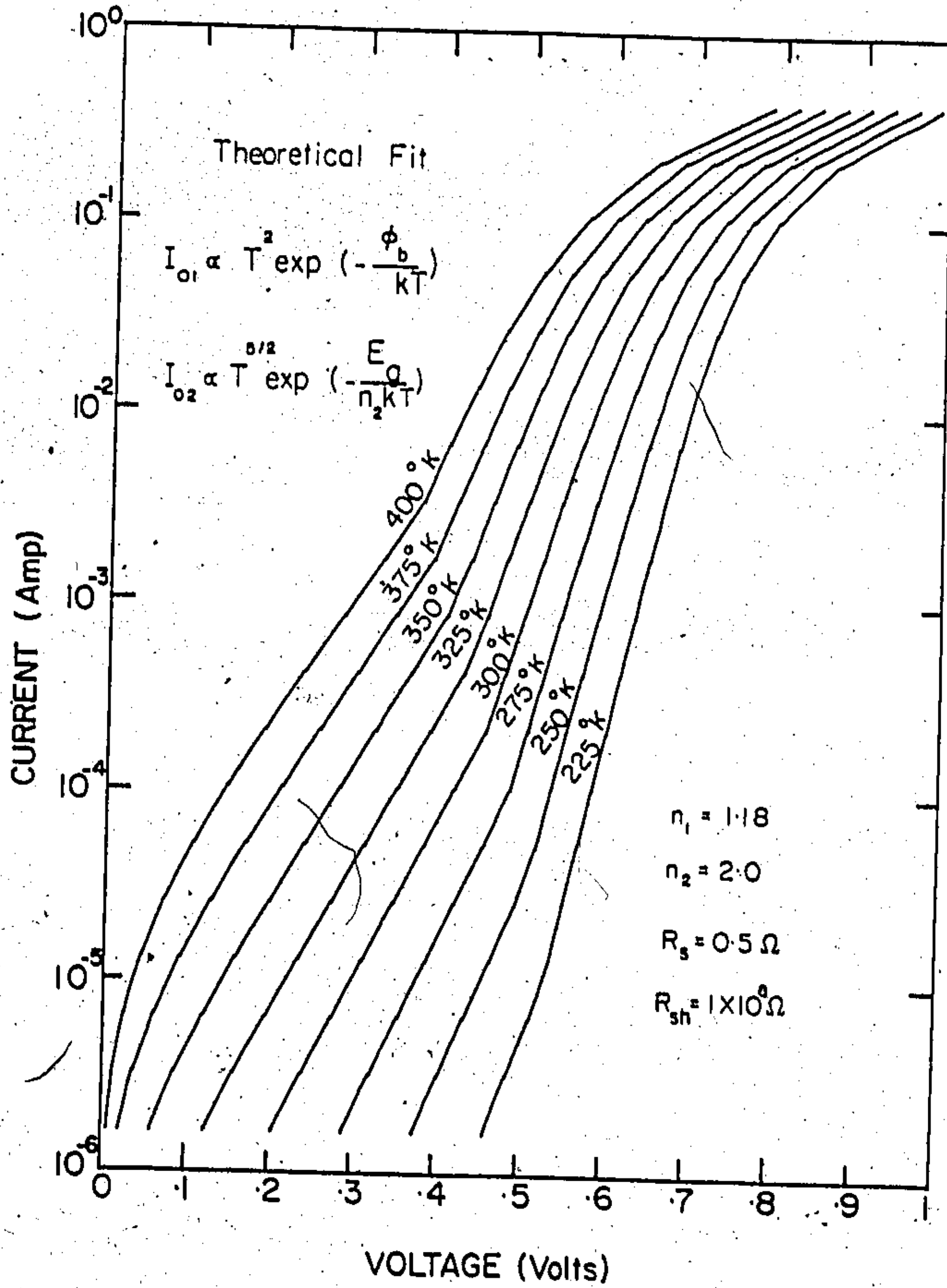

Figure 4.13

Figure 4.14

I-V characteristics under solar illumination for Al-SiO_x-(p-type)Si solar cells. Lower curve is for <111> orientation and the upper curve is for <100> orientation. These data are taken from reference 81.

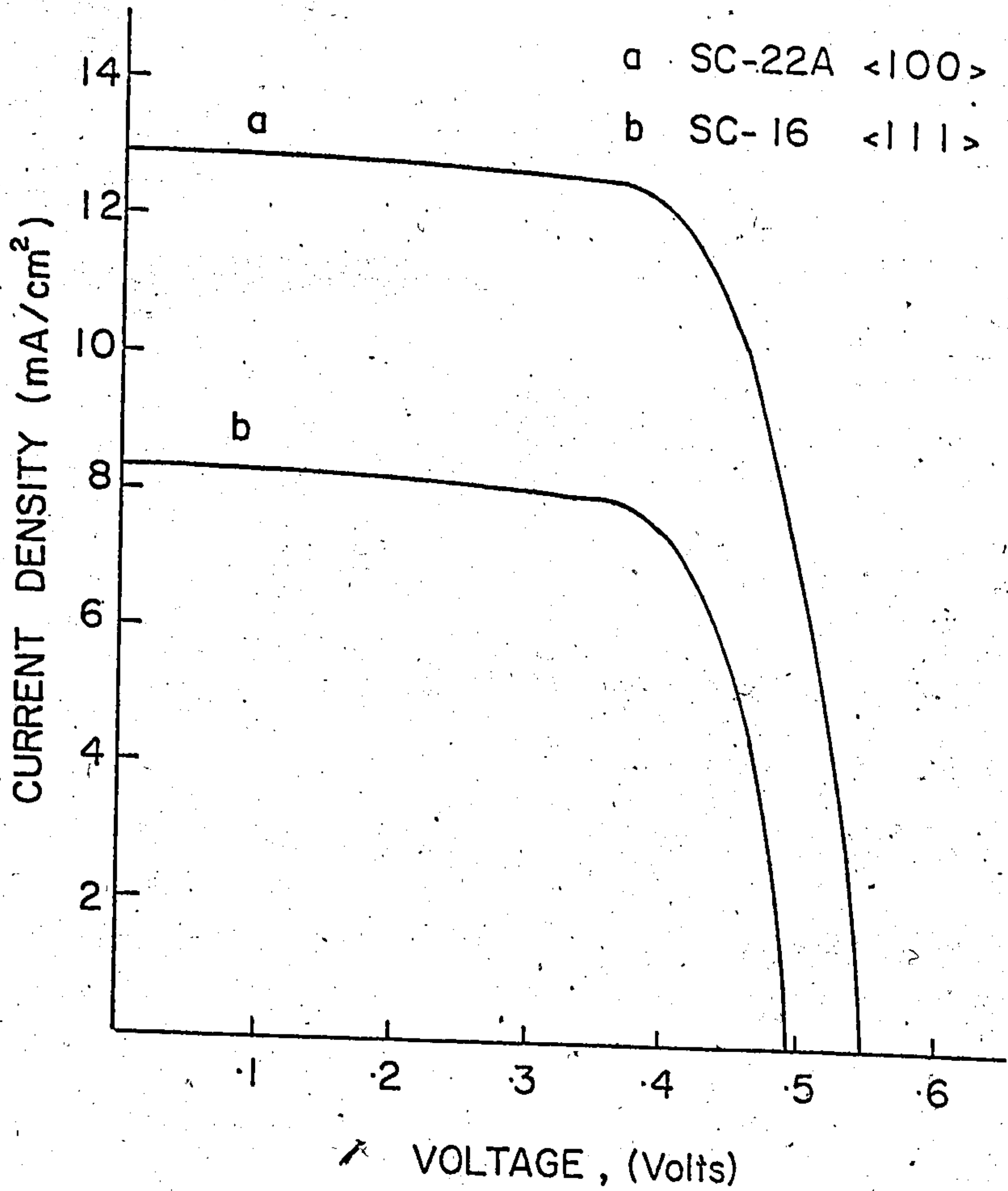

Figure 4.14

mance is better in the case of <100> orientation. Similar results are reported in references A and 105.

4.2.6 Spectral Response

Since the tunnel MIS diode is essentially a surface induced diode, one would expect a significant enhancement in the ultra-violet response of such cells. There is no heavily doped or dead layer at the surface as with conventional n^+p junctions to cause an ultraviolet loss. Theoretical calculations of spectral response (amperes/watt) for an Al-SiO_x-(p-type)Si diode are shown in Figure 4.15. The substrate resistivity is 0.2 Ω-cm and the insulator thickness is 13 Å. Experimental measurements were carried out on a 0.17-0.30 Ω-cm Si MIS solar cell [92]. These results are also shown in Figure 4.15. The agreement is quite good. By way of comparison, a diffused n^+p junction made in our laboratories was measured at the same time. This data is also plotted in Figure 4.15. Since the junction depth is about 3 μm, the ultraviolet side of the response should be considerably suppressed and this is the case. The enhanced infra-red response is due to a back pp^+ junction.

Figure 4.15

Normalized spectral response (amperes/watt) versus wavelength. Measurements were performed on 0.2 Ω-cm Si. The diffused junction had a depth of about 3μ. Measurements were carried out by J. St. Pierre and are reported in reference 92.

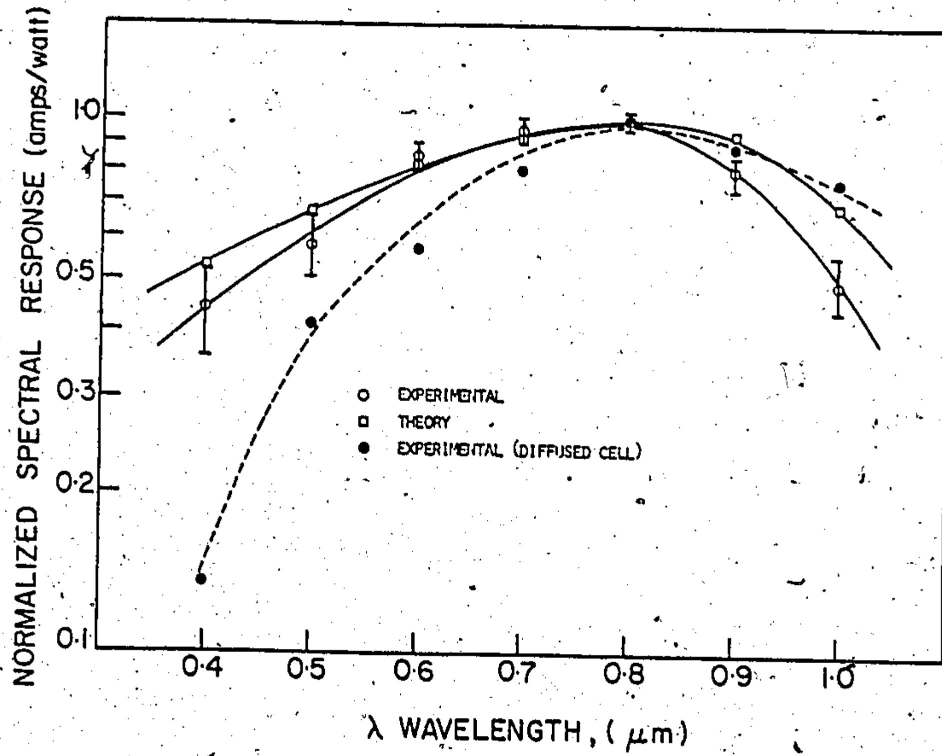

Figure 4.15

4.3 COMPARISON WITH MIS AND SCHOTTKY BARRIER CALCULATIONS

4.3.1 Comparison with Other MIS Solar Cells Models

Various semi-empirical approaches have been made to explain the operation of MIS solar cells [22-24,106]. The main assumption in most of these works is that like a Schottky barrier device, the dark current of MIS solar cells consists of majority carriers. The dark current of a Schottky barrier diode is given by

$$J = AT^2 \exp(-\frac{\phi_b}{kT})[\exp \frac{qV_a}{nkT} - 1] . \qquad (4.6)$$

The addition of interfacial layer introduces an additional attenuation factor, so the majority carrier current of an MIS solar cell is given by

$$J_{maj} = AT^2 \exp-(\frac{\phi_b}{kT}) \exp(- \chi^{1/2}\delta) [\exp \frac{qV_a}{nkT} - 1] . \qquad (4.7)$$

The major difference between our work and other works is about the dominant current conduction mechanism of the device. We do not take any assumption in our model about dominance of minority or majority carrier current. The set of coupled equations is solved numerically to get the self-consistent solutions, which satisfy the equations describing tunneling through the insulator and carrier transport in the semiconductor.

In conclusion, our theoretical work is based on real world situations and explains the experimental work done on MIS solar cells. Major features of the theory have already been confirmed. More experimental work in the near future will show that only our theory can explain the operation of MIS solar cells.

4.3.2 Comparison with Schottky Barrier Solar Cell Calculations

Although it is well known that Schottky barrier solar cells have very low photovoltaic conversion efficiency, there are some workers [107] who still think that Schottky barrier solar cells can approach p-n junction solar cell performance. These conclusions are based on the calculations of Pulfrey and McOut on Schottky barrier solar cells. For this reason it is relevant to compare our results with calculations by Pulfrey and McOut [167] which indicate that a maximum theoretical efficiency of 22-24% should be possible with silicon. While these efficiencies are comparable to those for our MIS diodes, it is important to realize that these Schottky diode calculations require some unusual physical conditions which cannot be readily met in practice. For example, a quantum efficiency of unity is required, as well as a barrier height equal to the energy gap. Using very recent data [108] for barrier heights on n type silicon, the two metals which would yield the highest barrier heights are platinum at 1.022 eV

and gold at 0.822 eV. Gold would result in a Schottky barrier diode efficiency of approximately 11% and platinum of 17.8%. Unfortunately, the electrical resistivity of Pt is 10 μ ohm-cm compared to Au at 2.44 μ ohm-cm [109]. Hence in the case of Pt one would expect a considerably reduced efficiency due to high sheet resistivity effects. Our calculations on MIS tunnel diodes are based on real world parameters which can be easily met in the laboratory.

4.4 Si-SiO_x INTERFACE STUDY

4.4.1 Introduction

Recent experimental work on the interface of thermally grown thick silicon oxide on silicon reveals the existence of a transition region with a composition of SiO_x, where x varies from one to two across the transition region. Various diagnostic techniques have been used to estimate the width and stoichiometry of this transition layer. It is apparent from Table 4.3 that the non-stoichiometric region extends to about 20 Å from the interface. In the case of MIS devices involving ultra thin oxides (10-20 Å), such as MIS solar cells, the oxide thickness is comparable to the non-stoichiometric transition region and the device properties are expected to be dependent on the thickness and the composition of the oxide. In addition, since the ultra-thin oxide of 10-20 Å consists of

TABLE 4.3

ESTIMATION OF THE WIDTH OF TRANSITION LAYER AT THE INTERFACE BY VARIOUS DIAGNOSTIC TECHNIQUES

Oxide thickness and type of Si	Ambient	Technique used	Transition region	Reference
<30 Å p <100>, 2 Ω-cm	23°-850°C, O_2, O_2+N_2 and and boiling (HNO_3 $+H_2O_2+H_2O$)	x-ray photoemission spectroscopy	12 Å	111
<30 Å p <111>, 2Ω -cm	-do-	-do-	15 Å	
6328 Å, n <111>, 10 Ω-cm	600-900°C, steam or O_2	ESCA	15-20 Å	112
15-100 Å, p <100>, 6-13 Ω-cm	600°C, steam-HCl	Low-energy (keV) ion scattering	15-20 Å	113
700 Å, ion-thinned 200-300 Å, <100>	900°C, HCl steam	Transmission electron microscopy	No evidence for phase separation	114
700 Å n <111>, 5 Ω-cm n <100>, 0.9 Ω-cm p <111>, 13 Ω-cm	Wet stream (95°C) of N_2 at 800°C for 90 min.	Backscattering experiments with 600 keV He ions	15-50 Å	115

(continued next page)

TABLE 4.3 (continued)

Oxide thickness and type of Si	Ambient	Technique used	Transition region Width	Reference
1000 Å <100>	1200°C, dry O_2	Auger electron spectroscopy	20 Å	116
1090 Å n <100>, 10 Ω-cm	1050°C, dry O_2	Field-dependent internal photoemission	4 Å	117
13-1500 Å n <111>	920-1000°C, dry O_2	Backscattering with 2.0 MeV He ions	<2000 Å (concluded)	118
10-40 Å p <100> 6-13 Ω-cm	600°C, dry O_2	Contact angle of water drops	30 Å	119
1400 Å p <100> 24 Ω-cm	110°C, dry O_2	High resolution electron microscopy	10 Å	120

only a few atomic layers, it can be heavily defected with large pin-hole density, therefore, the device performance will also depend on the quality of the oxide. In this section, we shall describe the use of Al-SiO_x-(p-type)Si solar cells to study the transition layer associated with a thermally grown SiO_x layer. The oxide thickness dependence of open-circuit voltage, V_{oc}, below a particular oxide thickness can be interpreted to give information regarding the properties of the transition layer. In particular, by using the Maxwell-Garnett relation, the complex dielectric constant of the transition layer has been estimated as a function of its thickness. A phenomenonological model will be described which takes into consideration the effects of pin holes which are expected to be present in the ultra thin oxides involved in the MIS solar cells [110].

4.4.2 <u>Effect of Oxide Thickness on Open Circuit Voltage</u>

Figure 4.16 shows experimentally observed V_{oc} as a function of oxide thickness in the range of 10-20 Å. The data shows a decrease in V_{oc} with increasing thickness at approximately 1 mV/Å above about 12 Å and a rapid increase below 12 Å.

In order to explain the observed oxide thickness dependence of V_{oc} we examined whether or not our theory of MIS solar cells could give a similar functional behaviour. For this purpose, we varied the oxide and interface parameters

Figure 4.16

Experimental and theoretical open circuit voltage of tunnel MIS solar cell as a function of oxide thickness.

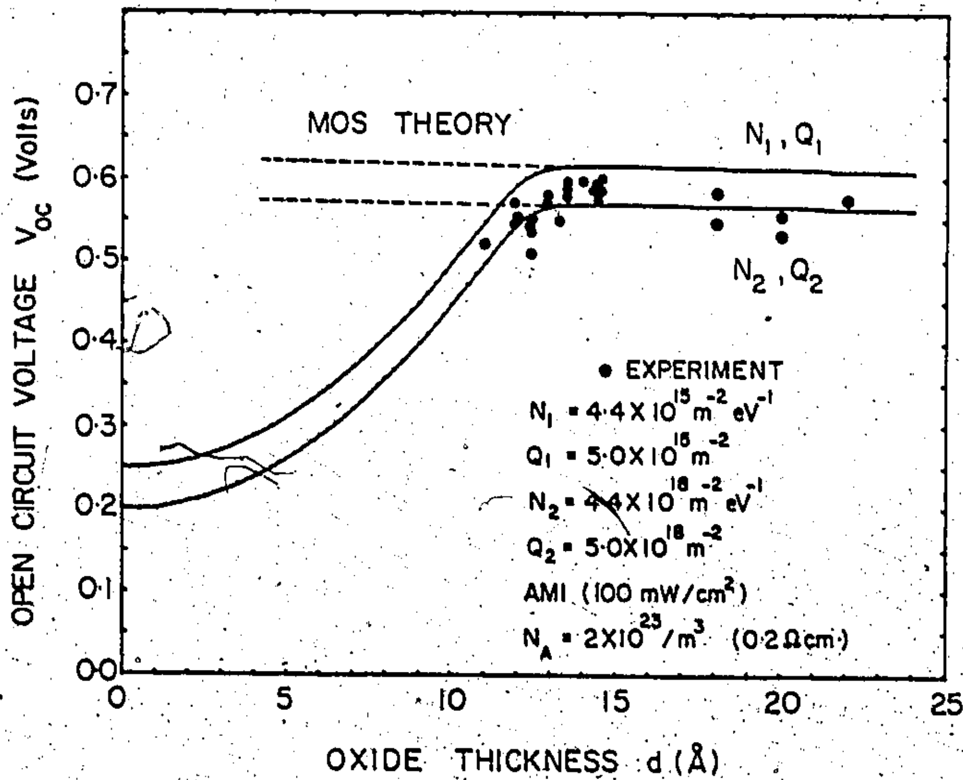

Figure 4.16

within suitable upper and lower limits, to account for the non-stoichiometry of ultra thin oxide layers. The parameters related to the $Si-SiO_x$ interface and oxide layer are surface state density, oxide charge, dielectric current, band gap and electron affinity of SiO_x, effective mass of carriers in SiO_x and surface state capture cross section. On varying the dielectric constant from 2 (for SiO_2) to 4 (for SiO), V_{oc} changes only by 6 mV. This change is negligibly small compared to the observed change of about 100 mV in V_{oc}, when the oxide thickness is varied from about 20 Å to about 10 Å. Other parameter such as the effective mass of carriers, band gap [121] and electrons affinity of SiO_x are expected to change with the stoichiometry, but they also do not affect the V_{oc} by any significant amount. The surface state capture cross sections do not seem to vary in the range of 10-20 Å, since in this range of oxide thickness, the observed short circuit current density remains practically constant [92]. For thin oxides, the measured surface state capture cross-section for p-type Si in the <100> direction is 3.1×10^{-20} m^2 [122]. We are already assuming a larger cross section of 10^{-19} m^2, therefore the possible change in capture cross-section due to stoichiometric changes was neglected. In the light of the above facts, it appears that possible changes in dielectric constant, band gap and electron affinity of SiO_x, effective mass of carriers and capture cross-sections due to stoichiometric changes are not

sufficient to explain the observed V_{oc} variation. The dielectic constant of the oxide was therefore taken as 3.84 ε_0, which is the value obtained by our ellipsometric measurements on the oxides of 10-20 Å thickness. Thus, the only remaining parameters to be varied are surface state density N_{ss}, and oxide charge Q_{ox}.

A simplified model [123] regarding the origin of N_{ss} and Q_{ox} suggests that both these charges may result from either defects in the interfacial region between the Si and SiO_x or due to the impurities in this region, or both. Under the controlled growth of 10-20 Å thin oxides, it is the change in the stoichiometry of the oxide which is responsible for the change in N_{ss} and Q_{ox}. The dangling bond density for Si-SiO is more than for Si-SiO_2. Also, the surface state density is related to the dangling bond density at the interface. Hence, the N_{ss} for Si-SiO_2 should be less than for the Si-SiO interface. In the present calculations, we have varied N_{ss} at the mid-gap of silicon from 4.4×10^{15} m^2 eV^{-1} to 4.4×10^{18} m^{-2} eV^{-1}. The lower limit of N_{ss} taken here is usually obtained in the laboratory, although the minimum achievable density may be more than two orders less than this value for thick oxides [124]. The upper limit of N_{ss} taken here is roughly the dangling bond density for the <100> Si-SiO_x system.

There are reports in the literature which indicate that both N_{ss} and Q_{ox} have common origins with a linear relationship between them [123,125,126]. Although it is still not

well established which of the N_{ss} and Q_{ox} values has the higher magnitude, there is evidence that the larger of the two is 1-2 times greater than the other one [125,127]. It is our feeling that, by proper annealing, N_{ss} could be reduced more easily than the fixed oxide charges. Therefore, we have assumed $Q_{ox} > N_{ss}$ [128] and have taken the proportionality constant between them to be 1.2 [127]

As mentioned earlier, the surface states have the following properties (a) they are charge storage centers, (b) they are recombination-generation centers, and (c) they provide a tunneling path between the metal and the semiconductor. All of these properties were included self-consistently into the MIS solar cell model [5] to characterize these surface states. In the case of the Al-SiO_x-(p-type)Si structure, negative charges will be stored in the surface states above the mid-gap, since the interface is in strong inversion for reverse and small forward bias. For the Si-SiO_x interface, the oxide charge, Q_{ox}, is always positive. Therefore, total charge at the interface is $Q_{ox} + Q_{ss}$, where Q_{ss} is the charge in the surface states. This sum is always positive for Al-SiO_x-(p-type)Si under the assumption that $N_{ss} < Q_{ox}$. Thus, due to the charge storage properties of surface states and the oxide charge, the metal work function is effectively changed and is given by

$$\phi'_{mi} = \phi_{mi} - \frac{q(Q_{ox}+Q_{ss})d}{\varepsilon_{ox}} \qquad (4.8)$$

where d is the oxide thickness and ε_{ox} is the oxide dielectric constant. It is evident from section 3.3.4 that for p-type Si, a lower value of ϕ'_{mi} will give higher barrier height and hence high V_{oc}. Thus, the theoretical curve of V_{oc} versus oxide thickness gives a negative slope of about 1 mV and, if N_{ss} and Q_{ox} are increased by three orders of magnitude, V_{oc} is decreased by about 30 mV under the assumption $|Q_{ox}| \approx |N_{ss}|$. These results are plotted in Figure 4.16. A comparison of experimental results with these theoretical curves reveals a distinct deviation from theory below about 12-13 Å. These deviations must be accounted for by some mechanism related to the structure of the oxide layer.

4.4.3 Composite Model of MIS Solar Cells

In the light of the above discussion, it seems that a mere variation in the oxide and interface parameters is not sufficient to explain the positive slope of V_{oc} versus oxide thickness at low thickness. From Figure 4.16 it is apparent that below an oxide thickness of about 13 Å, the barrier height of the device is considerably reduced giving a low V_{oc}. Card [129] has published experimental data which shows a linear decrease of barrier height in Al-SiO_x-(p-type)Si system, when the

oxide thickness is reduced from 20 Å to 5 Å. Qualitatively, similar results have been obtained by Kasprzak and co-workers [130] although they used degenerate Si. One possible way of accounting for this positive slope may be the presence of pin holes associated with ultra thin oxides.

It is a well known fact that as the thickness of the oxide is reduced, it becomes more and more patchy, i.e. pin hole density increases and the variation in oxide thickness across the surface increases. In principle, thick oxides are also not totally pin hole free, but the effect of pin holes will be seen only on devices with ultra thin oxides because of their large surface density which may even cause patches in the oxide layer. Therefore, in any realistic model of MIS devices with ultra thin oxides, the effect of structural defects due to a large pin hole density should also be taken into account.

This situation can be visualized as several solar cells in a parallel combination, some of them having a large barrier height and others having a small barrier height. It should be noted however, that it is difficult to assign a particular distribution for the variation of oxide thickness and hence, of the barrier height across the entire surface due to pin holes. To overcome this problem, we have, somewhat arbitrarily at present, assumed only two barrier heights. One corresponds to the ideal MIS structure for the region with minimum pin holes and the other for a "Schottky" diode in a

region where either no oxide exists or pin hole density is so large that there is virtually no oxide. The exact nature of the metal-semiconductor contact is not well understood, but a survey of the literature reveals that for Si Schottky barrier solar cells, the maximum open-circuit voltage under normal sunlight intensities is about 0.2-0.3 volts [17-20]. Under the same level of illumination, the theoretical V_{oc} for an Al-SiO_x-(p-type)Si solar cell of 13 Å oxide thickness is about 0.65 V [5]. Therefore, a parallel combination of ideal MIS and "Schottky" diodes will give V_{oc} between 0.2-0.3 V and 0.65 V. To account for the fact that an increase in oxide results in a reduction of the pin hole density and an increase in the barrier height, we have assumed a Gaussian distribution of pin holes as given below:

$$\rho_{pin} \sim [\exp-(\frac{d}{2do})^2 + \rho_o] . \qquad (4.9)$$

Here d is the oxide thickness and do is the Si-O bond length equal to 1.62 Å [131]. ρ_o takes into account the fact that, even for very thick oxides, there are some pin holes present. There are reports in the literature [132-134] which indicate that the fractional pin hole area is about 10^{-7}. In our model we have taken this fractional area as ρ_o. The fractional

pin hole area obtained by Equation 4.9 is plotted against the oxide thickness in Figure 4.17. To perform the actual calculations, we have assumed that for both the "MIS" and "Schottky" parts, the series and shunt resistance effects are negligible and carriers are generated in a similar manner. The diode ideality factors were taken as the same for both cases. Also, we have assumed that if the fractional area of pin holes is x, then out of a total light generated current I_L, (xI_L) would be due to pin holes and $(1-x)I_L$ due to ideal MIS parts. The total open-circuit voltage is given by

$$V_{oc}^{total} = \frac{nkT}{q} \ln \left[\frac{1}{\dfrac{\{\exp-(\frac{d}{2do})^2+\rho_o\}}{\{\exp \frac{qV_{oc}^S}{nkT} - 1\}} + \dfrac{\{1-\exp-(\frac{d}{2do})^2-\rho_o\}}{\{\exp \frac{qV_{oc}^M}{nkT} - 1\}}} + 1 \right]. \quad (4.10)$$

The derivation of the above relation is given in appendix C. Here V_{oc}^M varies with oxide thickness as

$$V_{oc}^M(d) = V_{oc}^M(o) - \alpha d \quad (4.11)$$

where α is a parameter depending on the interface properties and base material. A more general form of Equation (4.10) is

$$V_{oc}^{total}(d) = \frac{nkT}{q} \ln \left[\int_o^d \frac{1}{\dfrac{\rho(t)dt}{\exp \frac{qV_{oc}}{nkT} - 1}} + 1 \right] \quad (4.12)$$

where $\rho(t)$ is the distribution function for estimating ρ_{pin}. Equation (4.10) combined with equation (4.11) is plotted in Figure 4.16. We have varied V_{oc}^{M} and V_{oc}^{S} to account for the possible changes due to variation in surface states, oxide charges etc. in the MIS regions and work function variation in the Schottky regions. α in equation (4.11) has been taken as 1 mV/Å, the value obtained by our theoretical calculations on MIS solar cells. The ideality factor, n, has been taken to be unity, which is the value obtained by the theory of MIS solar cells. The experimental values are usually slightly larger than unity, but not much different. It should be noted that, for each combination of V_{oc}^{M} and V_{oc}^{S}, these curves peak or saturate at about 13-14 Å of oxide thickness, much as the experimental data points out. Most of the experimental points lie between the curves for $N_{ss} = 4.4\times10^{15}\ m^{-2}\ eV^{-1}$ and $N_{ss} = 4.4\times10^{18}\ m^{-2}\ eV^{-1}$. This is in agreement with our hypothesis that the observed variation in the V_{oc} with oxide thickness is due to pin holes in the ultra thin oxide. The positive slope below about 12 Å is mainly due to pin holes, although some contributions due to stoichiometric variation will be present, primarily around the peak in Figure 4.16. It is worth mentioning here that the peak around 13-14 Å is roughly the width of the transition region as obtained by Raider and Flitsch [111].

4.4.4 Dielectric Properties of the Interface

The above conclusion also leads to another result concerning the dielectric constant of the thin oxide layer in MIS structures. Because of the pin holes in the oxide layer, the top layer metallic particles will be embedded in the silicon oxide film in a similar density as the pin holes. This will lead to modifications in the dielectric constant of the oxide layer. The effective dielectric constant of a "mixture" is given by the Maxwell-Garnett relation [135]

$$\frac{\varepsilon_e - \varepsilon_h}{\varepsilon_e + 2\varepsilon_h} = q\,\frac{\varepsilon_f - \varepsilon_h}{\varepsilon_f + 2\varepsilon_h}$$

where ε_e is the effective dielectric constant, ε_h is the dielectric constant of the host material (SiO_x in our case), ε_f is the dielectric constant of foreign particles (Al in our case for the Al-SiO_x-Si structure) and q is the fraction of foreign particles in the mixture (fractional density of pinholes). We have plotted results for the Al-SiO_x-Si structure in Figure 4.17. In principle, the dielectric constant of an intermediate layer could be deduced from ellipsometric measurements on a complicated MIS structure. The curves of Figure 4.17 predict a sharp rise in n and k values around 2 Å of oxide thickness with a return to values associated with SiO_x at about 5 Å oxide thickness. The peak position is governed

Figure 4.17

Calculated n,k of SiO_x as a function of oxide thickness. Percent pin hole area is calculated from equation 4.11 of the text. These curves were calculated by K. Rajkanan and are reported in reference 110.

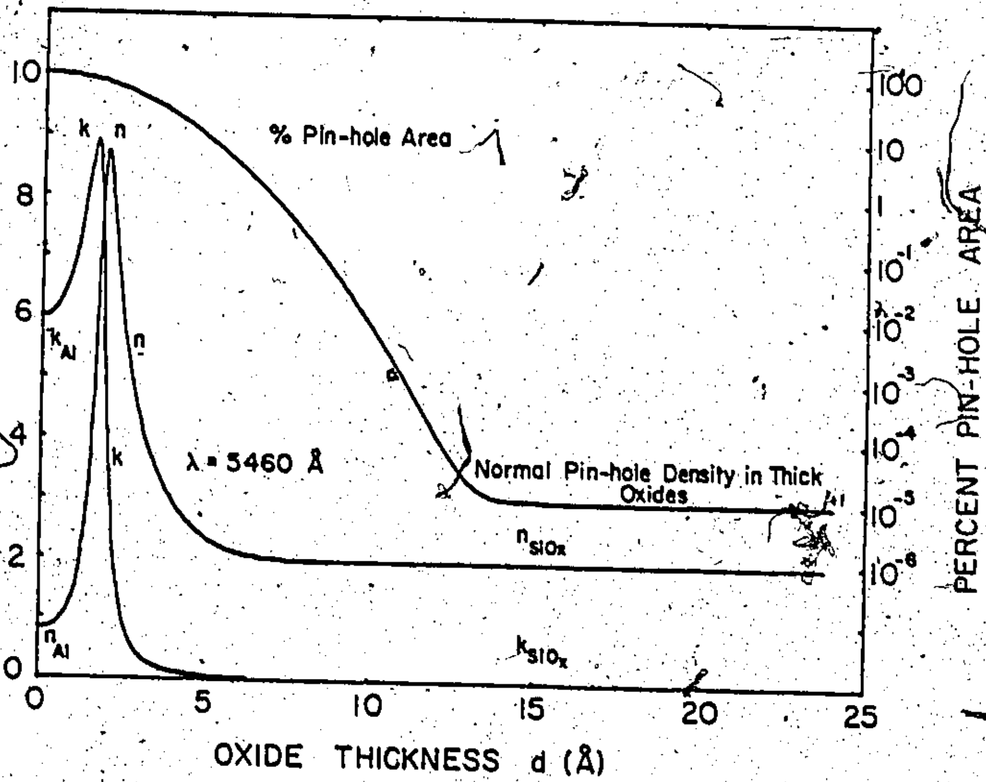

Figure 4.17

by the dipole-dipole interaction between metal and oxide and will therefore change for different metals. At about 5 Å oxide thickness the pin hole area is about 10% and this thickness represents the growth of about two monolayers. At this point the oxide layer begins to be effective in separating the silicon substrate from the metal layer. Therefore, it is expected that after about 5 Å, the n and k values will saturate, as observed in Figure 4.17.

4.5 SUMMARY

The theory of tunnel MIS solar cells has been compared with the available experimental data. In particular the effect of insulator thickness on the conversion efficiency, short circuit current density, open circuit voltage and fill factor of an MIS solar cell has been compared with the theory. The open circuit voltage below certain thickness of the insulating layer shows slight deviation from theory. In a later section, these deviations have been accounted for by taking into consideration the pin holes, which are generally present in ultra thin films of oxides. A composite model has been developed to explain the open-circuit voltage of these ultra thin oxides. Based on this model we have predicted the complex dielectric constant of SiO_x films in the range of 10-20 Å. The general behaviour of insulator thickness on the device performance is similar to that expected by the theory. The effect of substrate resistivity on the open-circuit voltage of

an Al-SiO_x-(p-type) Si solar cell has been compared with the theory. For comparison, we have shown the effect of substrate resistivity on the open-circuit voltage of p-n junction solar cells. These results show that tunnel MIS solar cells behave like p-n junction solar cells.

The effect of metal work function has been compared with the theory. The functional dependence of the metal work function on the behaviour of tunnel MIS solar cells could not be compared due to a lack of experimental data. However, all the experimental work supports our concept of low and high work function metals required to fabricate p-type and n-type MIS solar cells.

The forward dark I-V characteristics of Al-SiO_x-(p-type)Si solar cells as a function of temperature have been used to study the current conduction mechanism of these devices. These results show that the dark current consists of minority carriers and not of majority carriers. These results show that optimum MIS solar cells behave like pseudo p-n junctions.

The effect of crystal orientation on the device performance is also compared. Due to large surface state density, the <100> crystal oriented device has a higher output compared to the device employing <111> crystal orientation.

The spectral response calculated from the theory has been compared with the experimentally observed data for an Al-SiO_x-(p-type)Si solar cell. The agreement between theory and ex-

periment is quite good. We have also compared the spectral response of tunnel MIS solar cells with diffused n^+-p junction. As expected, the ultraviolet response of the MIS solar cell is higher compared to n^+-p junction response in that region. The infra-red response of n^+-p junction is enhanced due to a back pp^+ junction.

We have also compared our theory of tunnel MIS solar cells with other theoretical work. The major difference is that other workers assume the dark current of MIS solar cells to be dominated by majority carriers, similar to Schottky barrier devices. No such assumption is taken in our work and the optimum MIS solar cells behave like non-equilibrium minority carrier tunnel MIS diodes.

In general, compared with the available experimental data, the major features of the theory are confirmed. There is every reason to believe that in the near future the experimental devices will approach the upper limit predicted by the theory.

CHAPTER 5

COMPARISON OF SIS SOLAR CELL THEORY WITH EXPERIMENTAL WORK

5.1 INTRODUCTION

In this chapter, experimental data will be presented on SIS solar cells for comparison with the theoretical work mentioned in Chapter 3. In section 5.2, we will begin with the existence of the interfacial layer. The effect of insulator thickness on the device performance will be described in section 5.2.2. The effect of temperature and intensity on the device characteristics will be compared in sections 5.2.3 and 5.2.4 respectively. In section 5.2.5, the effect of oxide-semiconductor work function on SIS solar cells will be discussed. Calculated spectral response of n-ITO/p-Si solar cells will be compared in section 5.3. The various loss mechanisms associated with SIS solar cells are discussed in section 5.4. At the end of this chapter, we will show that simple methods based on the electrical measurements of oxide-semiconductor/base-semiconductor systems often lead to incorrect results about the electron affinity of oxide-semiconductors. The summary of this chapter is described in section 5.6.

5.2 EFFECT OF VARIOUS PARAMETERS ON SIS SOLAR CELL PERFORMANCE

5.2.1 Existence of the Interfacial Layer

The critical feature determining SIS solar cell performance is the interfacial layer between the oxide-semiconductor and the base-semiconductor. In the case of ITO/Si solar cells, Auger analysis [51] not only shows the presence of an interfacial SiO_2 but that such a layer is practically unavoidable under the present fabrication procedure. For ITO/InP solar cells, we have proposed that the interfacial regions consist of P-O bonding, giving rise to an interfacial layer of P_2O_5 [72]. This has been confirmed by the experimental work of reference 44, where the presence of P-O bonds in the interfacial layer has been indicated by Auger analysis. The presence of the interfacial layer has been commented on by most workers [6-8,12, 36-41,43-44,48-49], and it appears to be an essential feature of the oxide-semiconductor/base-semiconductor systems resulting in an SIS configuration.

5.2.2 Effect of Insulator Thickness

One of the major features of the theory is the rather large sensitivity of cell efficiency on insulator thickness. For ITO-SiO_x-(p-type)Si diodes the efficiency remains constant and near optimum for thicknesses up to about 16 Å and then falls rapidly to zero by about 22 Å. The experiments have not yet reached the state of sophistication where the interfacial layer

thickness can be controlled on the scale required. However, the dependence on thickness has been qualitatively confirmed. Cells fabricated with substrates at room temperature or under process condition in which the interfacial layer was not allowed to form (at least appreciably), exhibited low efficiency or low open circuit voltages. Behavior was more indicative of Schottky barrier operation with high short circuit current possible but low open circuit voltages. On the other hand, cells manufactured at high substrate temperatures (> 400°C) also showed poor efficiency and a low fill factor, consistent with too thick an oxide layer, at the interface [51].

5.2.3 Effect of Temperature

For any solar cell, the effect of temperature on the dark I-V characteristic may be used to understand the current conduction mechanism of that device. In Figure 5.1 we have calculated the dark I-V as a function of temperature for n-ITO-SiO_x-(p-type)Si diode. The temperature was varied from 200°K-400°K. The depletion layer lifetime was taken to be one order of magnitude less than the bulk semiconductor lifetime. The calculated curve shows two distinct regions of slope 1 and 2 in the voltage range of interest for solar cells. At lower temperatures, the recombination-generation current in the depletion region dominates, while at the higher temperature, the diffusion current dominates.

Figure 5.1

Calculated effect of temperature upon the forward dark I-V characteristics of ITO-SiO_x-(p-type)Si tunnel diode. The substrate resistivity is 0.2 Ω-cm, and the insulator thickness is 15 Å.

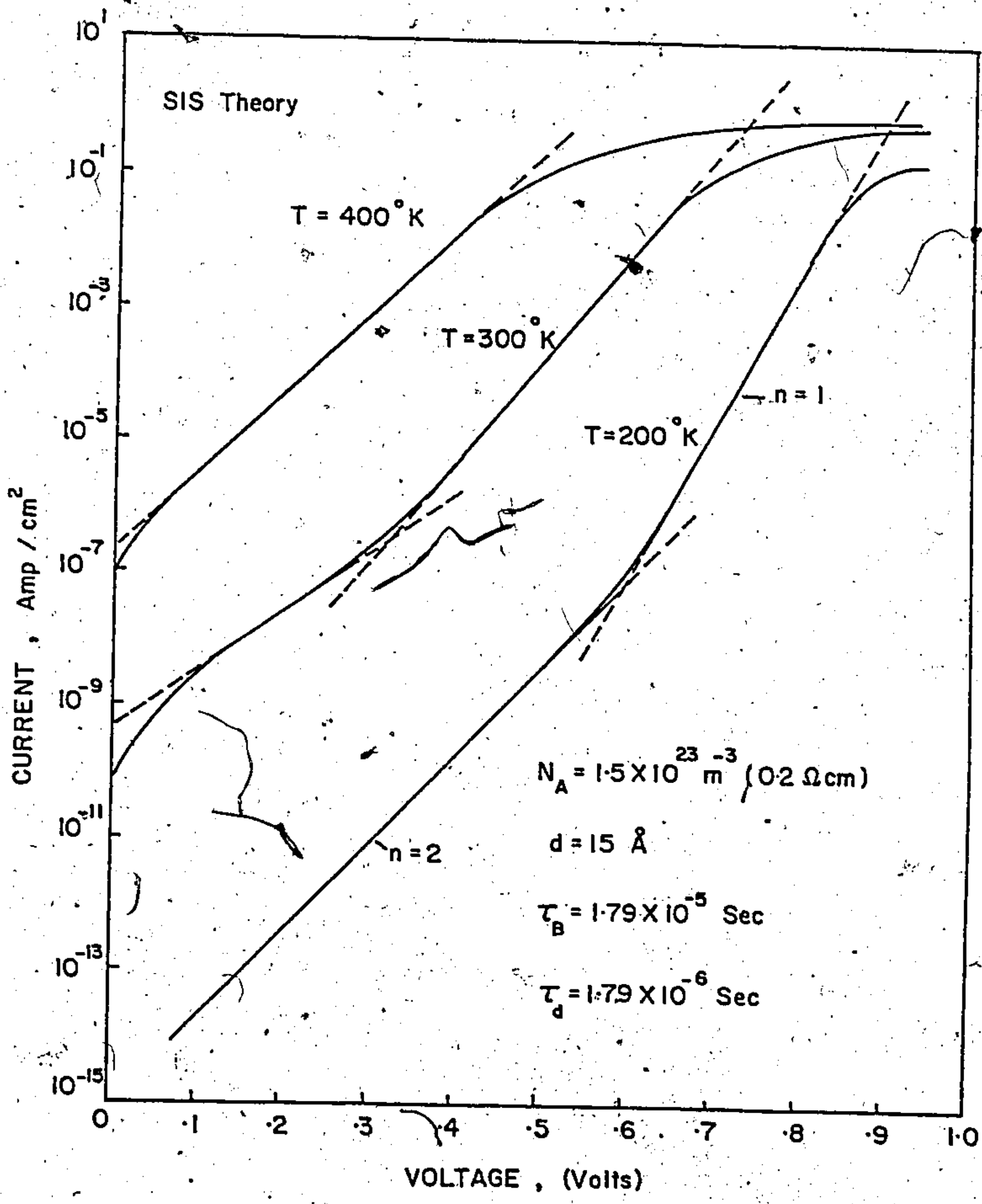

Figure 5.1

The experimentally observed dark I-V characteristics are shown as a function of temperature for a typical nITO-p-Si diode (12-G) in figure 5.2. A careful inspection of Table 5.1 shows that the dark I-V consists of two regions, one with slope $n_1 \approx 1.3$ and the other with slope $n_2 \approx 2.0$ Following parameters were measured for this device under AM1 (100 mW/cm^2) illumination:-

$$V_{oc} = .52 \text{ V}$$
$$I_{sc} = 3.6 \text{ mA}$$
$$A = 0.2 \text{ cm}^2$$
$$FF = 0.78$$
$$\eta = 7.3\%$$

The series resistance of this device was measured by the following method [67]

$$R_s = \frac{V' - V_{oc}}{I_{sc}} \quad (5.1)$$

where V' is the voltage from the dark I-V at the point where $I = I_{sc}$. A series resistance of about 5 Ω was calculated for the diode 12-G.

The computer calculated curves could be used to fit the experimental data, but since we know that we are dealing with diffusion processes, it is simpler to use the lumped diode model approximation with appropriate equations. The experimentally observed data of Figure 5.2 were fitted by using the following equations:

Figure 5.2

Experimentally measured forward dark forward I-V characteristics of ITO-(p-Si) solar Cells No. 12-G as a function of temperature. These measurements were carried out by D. Burk and are reported in reference 58.

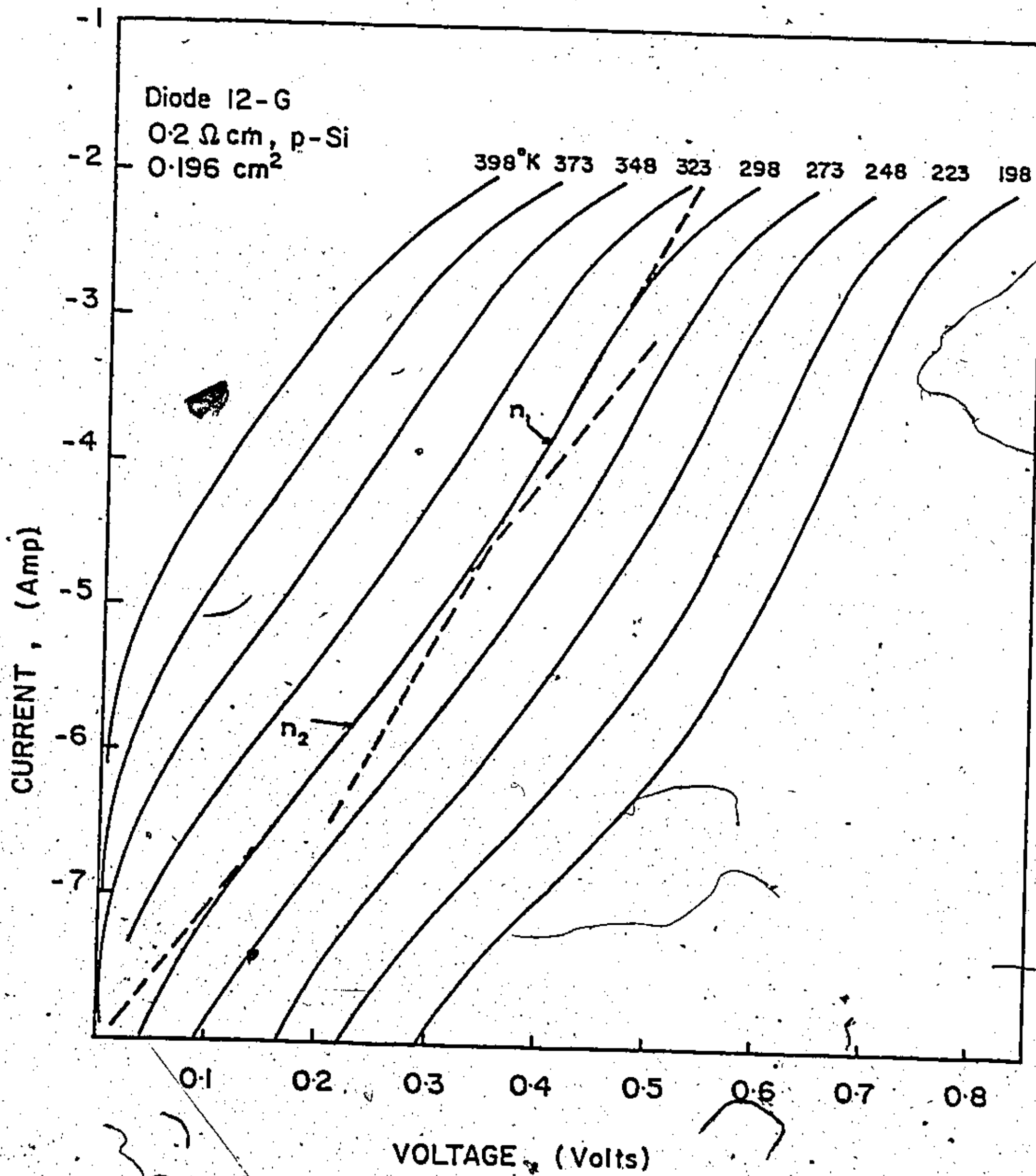

Figure 5.2

TABLE 5.1

MEASURED n VALUES AND SATURATION CURRENTS AS A FUNCTION OF TEMPERATURE FOR ITO ON (0.2 Ω-cm) P-TYPE Si DIODE NO. 12-G

	Diffusion		Recombination	
T°(K)	n_1	I_{01} (Amp)	n_2	I_{02} (Amp)
398	1.15	4.02×10^{-6}	–	–
373	1.17	1.90×10^{-6}		
348	1.20	1.00×10^{-7}	1.50	1.61×10^{-7}
323	1.23	1.00×10^{-8}	1.70	3.37×10^{-8}
298	1.25	6.19×10^{-10}	1.73	6.47×10^{-9}
273	1.27	2.03×10^{-11}	1.96	1.84×10^{-9}
248	1.32	8.89×10^{-13}	1.97	5.45×10^{-10}
223	1.36	1.20×10^{-14}	2.10	2.15×10^{-11}
198	1.39	1.06×10^{-16}	2.24	8.79×10^{-12}

$$I - \frac{V-IR_s}{R_{sh}} = I_{01}[\exp(\frac{V-IR_s}{n_1 kT})q-1]$$

$$+ I_{02}[\exp(\frac{V-IR_s}{n_2 kT})q-1] \quad (5.2)$$

where

$$I_{01} \propto T^3 \exp(\frac{-Eg}{n_1 kT}) \quad \text{(diffusion)} \quad (5.3)$$

$$I_{02} \propto T^{5/2} \exp(\frac{-Eg}{n_2 kT}) \quad \text{(recombination)} \quad (5.4)$$

The reverse saturation current given by equation (5.3) is the diffusion current and equation (5.4) represents the recombination-generation current in the depletion layer [103]. The values of $n_1 = 1.3$, $n_2 = 2$, $R_s = 5\ \Omega$ and $R_{sh} = 5\times10^7\ \Omega$ were used to fit the experimental curve. It is observed that a fairly reasonable fit is obtained, as shown in Figure 5.3.

The above method of fitting forward dark I-V as a function of temperature has been applied to a number of ITO/Si diodes and very good fits have been obtained in each case. The experimentaly observed dark I-V characteristics as a function of temperature for diode No. 170 are shown in Figure 5.4. Measured n values and saturation currents as a function of temperature for this diode are shown in Table 5.2. The values of $n_1 = 1.2$, $n_2 = 1.7$, $R_s = 5\ \Omega$ and $R_{sh} = 1\times10^8\ \Omega$ were used to fit the experimental curve of Figure 5.4. As shown in Figure 5.5, the fit is excellent.

The reverse I-V characteristics of diode No. 170 as a function of temperature are shown in Figure 5.6. Theoretically

Figure 5.3

Theoretical fit to the experimental data of Figure 5.2.

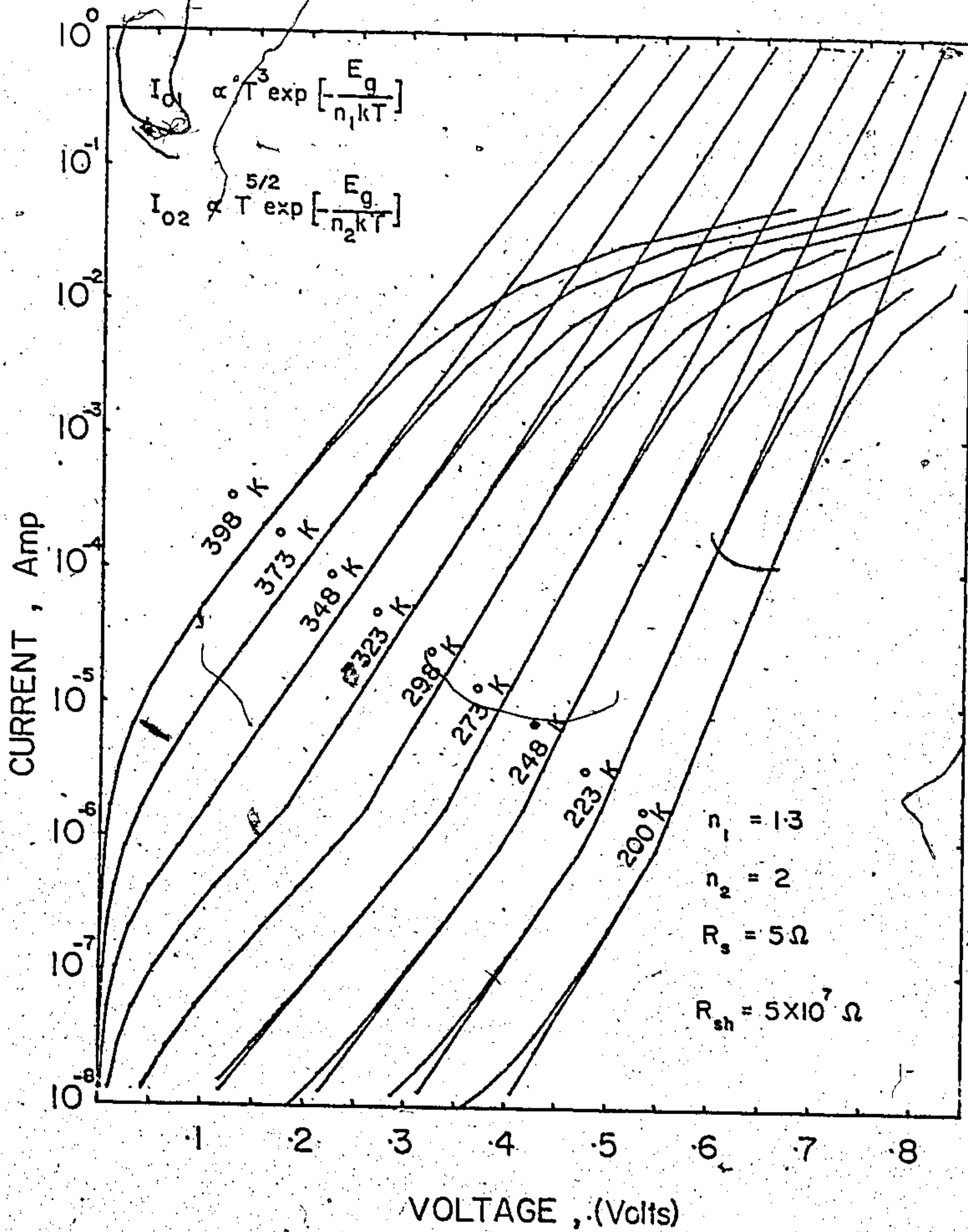

Figure 5.3

Figure 5.4

Experimentally measured forward dark forward I-V characteristics of ITO-(p-Si) solar cell No. 170. These measurements were carried out by D. Burke.

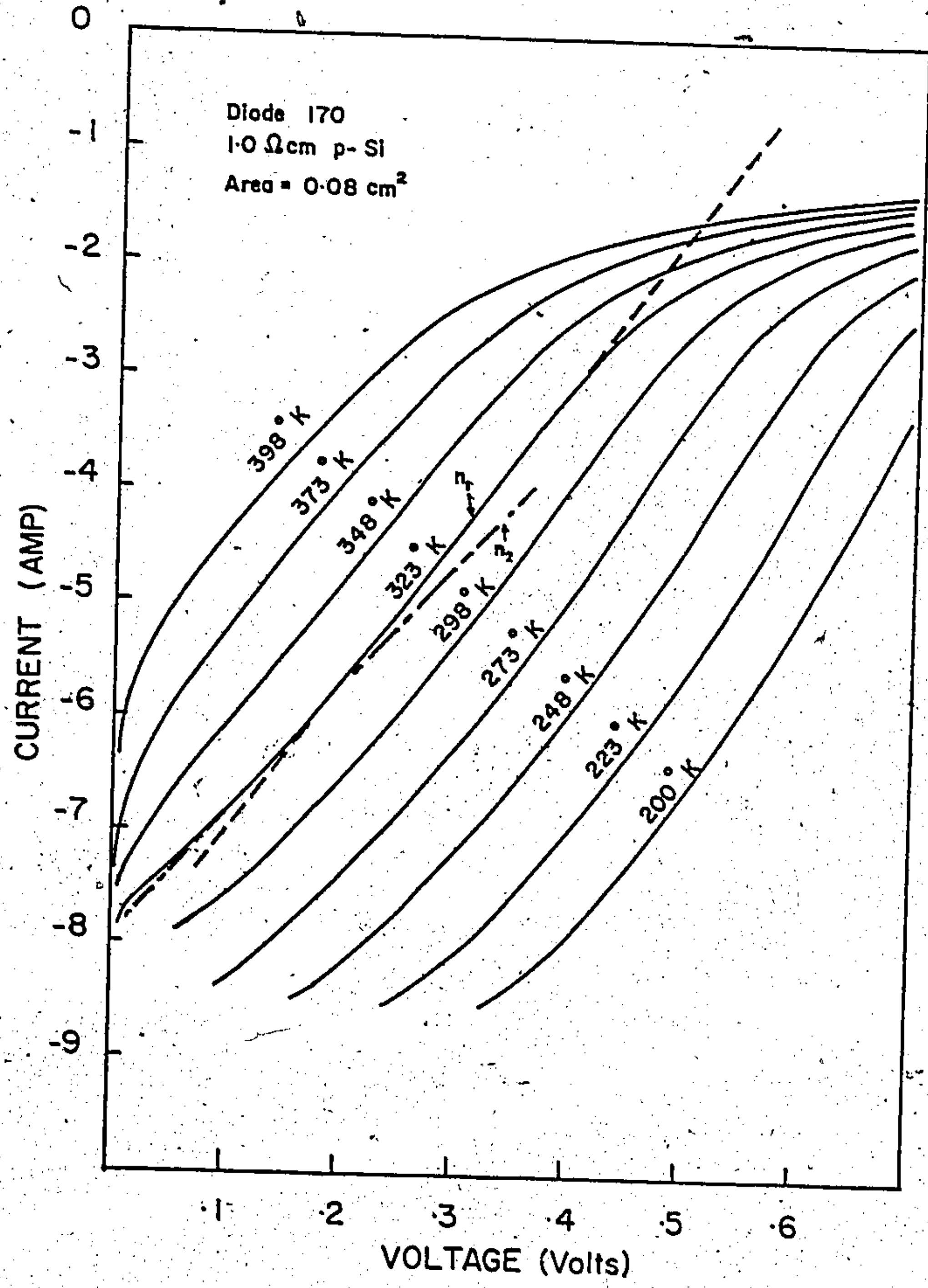

Figure 5.4

TABLE 5.2

MEASURED n VALUES AND SATURATION CURRENTS AS A FUNCTION OF TEMPERATURE FOR ITO ON (1.0 Ω-cm) P-TYPE Si DIODE NO. 170

	Diffusion		Recombination	
T°(K)	n_1	I_{01} (Amp)	n_2	I_{02} (Amp)
398	1.02	3.00×10^{-6}	–	–
373	1.07	3.30×10^{-7}	–	–
348	1.11	4.50×10^{-8}	–	–
323	1.12	3.00×10^{-9}	1.75	1.50×10^{-8}
298	1.19	3.00×10^{-10}	1.75	2.00×10^{-9}
273	1.19	8.20×10^{-12}	1.75	1.00×10^{-10}
248	1.20	2.54×10^{-13}	1.8	2.00×10^{-11}
223	1.23	2.20×10^{-15}	1.8	5.70×10^{-13}
200	1.29	1.68×10^{-17}	1.93	7.40×10^{-14}

Figure 5.5

Theoretical fit to the experimental data of Figure 5.4.

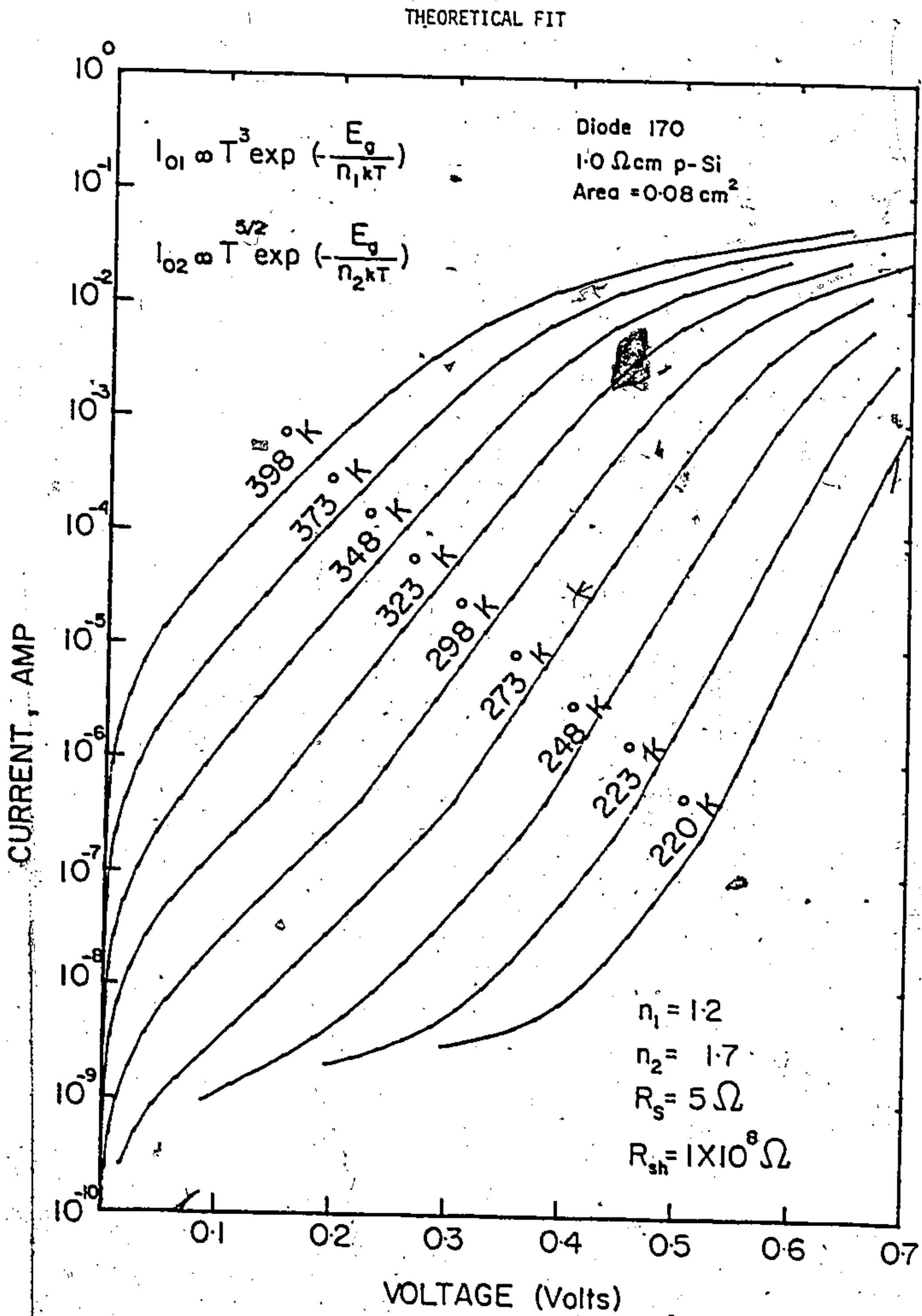

Figure 5.5

Figure 5.6

Experimentally measured reverse dark I-V characteristics of ITO-(p-Si) solar cell No. 170. These measurements were carried out by D. Burk.

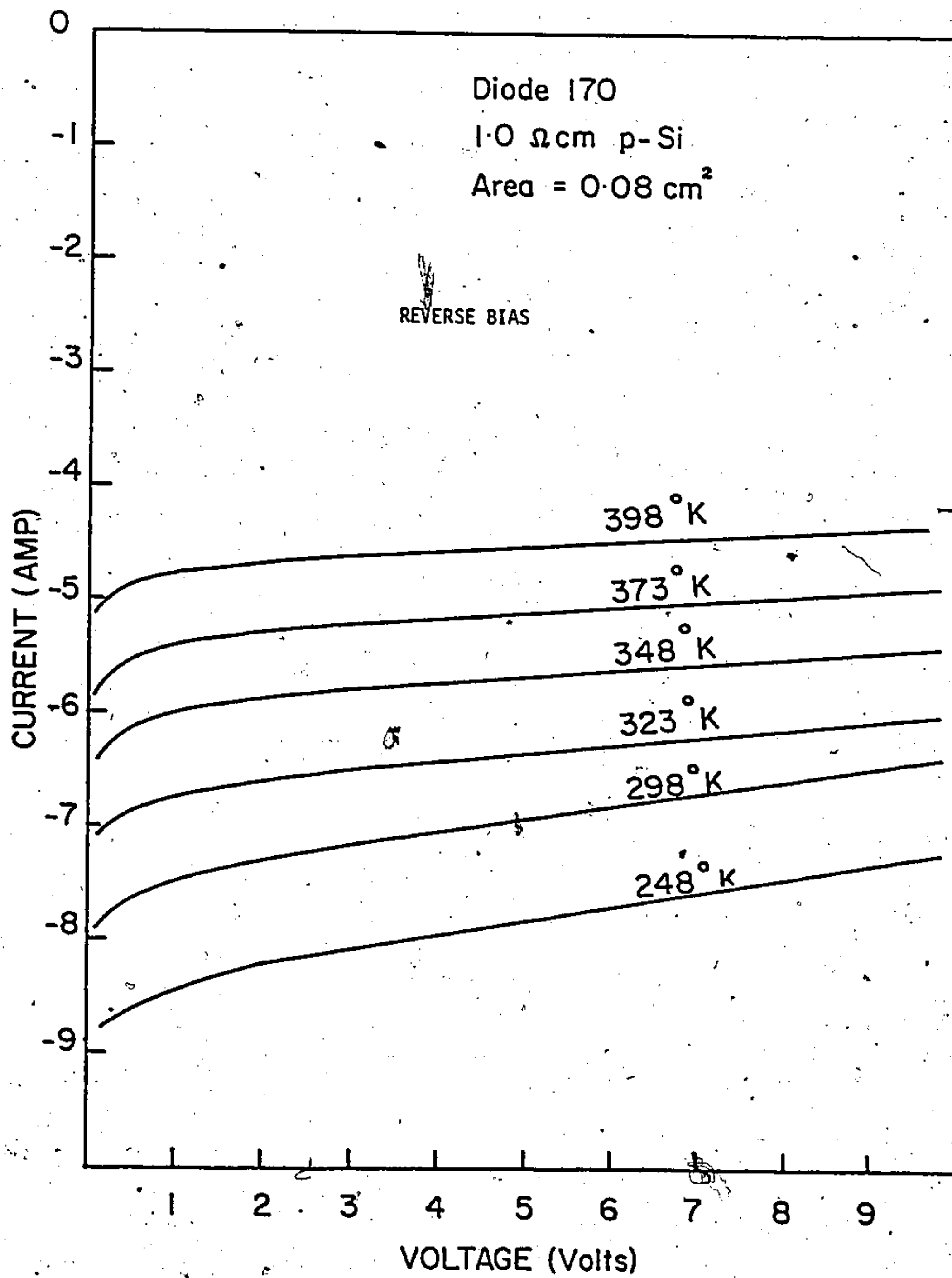

Figure 5.6

calculated reverse I-V characteristics from the SIS model are shown in Figure 5.7. At first glance, above room temperature the experimentally observed data have the same shape as obtained by theory, although they differ by many orders of magnitude. By using a scale factor of 4×10^{-5}, the theoretical data at T = 398°K has almost the same shape and magnitude as observed experimentally at this temperature. Using this scale factor of 4×10^{-5}, $R_s = 5\ \Omega$ and $R_{sh} = 1 \times 10^{8}\ \Omega$, the data of Figure 5.7 are transformed into the fit as shown in Figure 5.8. We also tried the method of forward I-V to fit the experimental data of reverse bias. This fit was not as good as that obtained by the approach described above. This demonstrates that the SIS diode characteristics can be represented by a semi-empirical relation for a limited range of applied bias. This is indeed the case as shown by a plot of reverse current at 1 volt as a function of 1/T in Figure 5.9. At lower temperatures, the current is dominated by recombination in the depletion region and at higher temperatures, the diffusion current dominates.

The excellent fit obtained in the forward and reverse bias modes confirms the general behaviour of theoretical SIS diodes. As noted above, both in forward and reverse bias, the dark current obtained by the SIS model is many orders of magnitude smaller than the experimentally observed value. This is because of the uncertainty in the device parameters. For example, a higher value of ϕ_{osi}, a lower value of minority carrier life time and a large defect density at the interface will provide additional majority carrier current and will shift the charac-

Figure 5.7

Calculated effect of temperature upon the reverse dark I-V characteristics of ITO-SiO_x-(p-type)Si tunnel diode. the substrate resistivity is 0.2 Ω-cm and the insulator thickness is 15 Å.

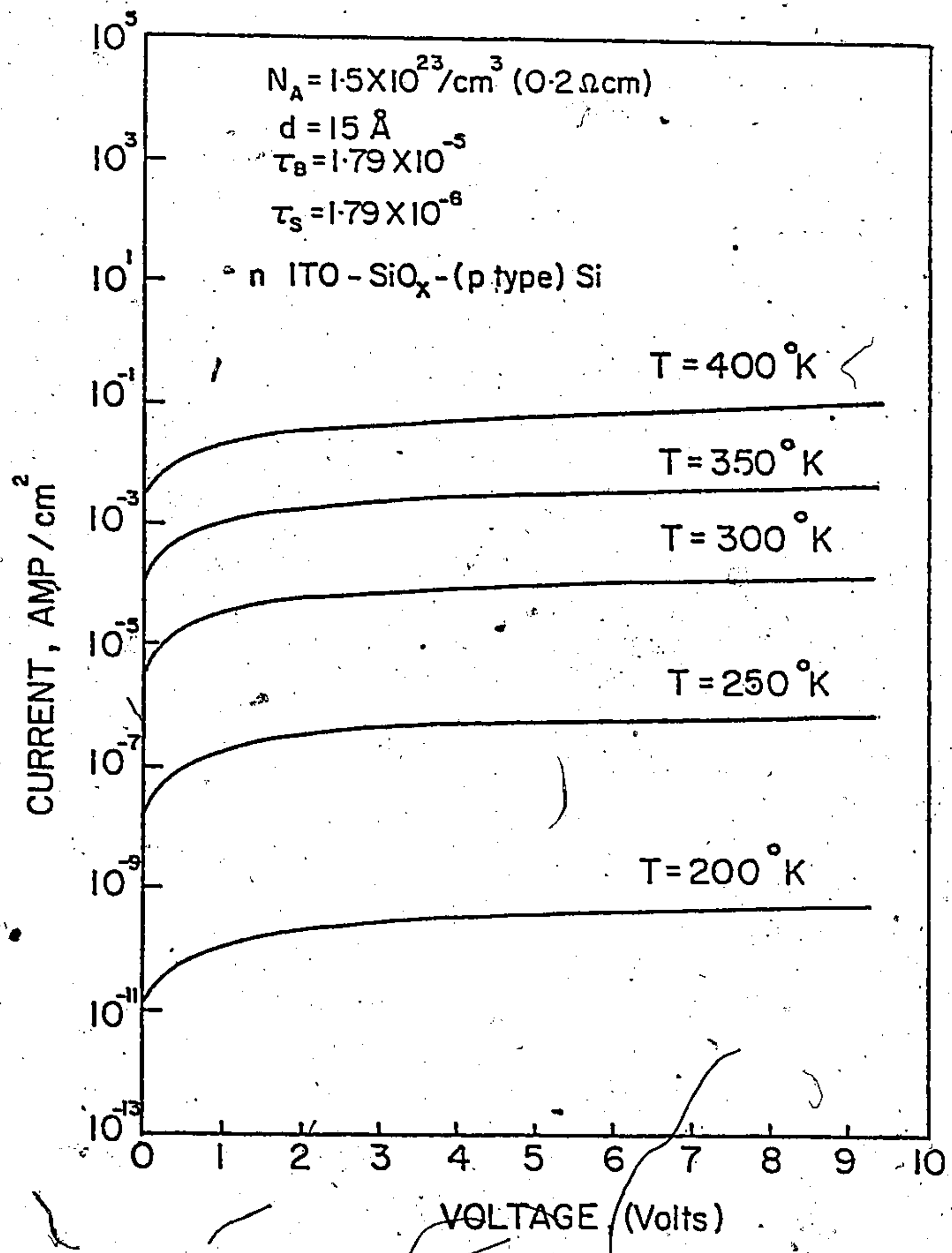

Figure 5.7

Figure 5.8

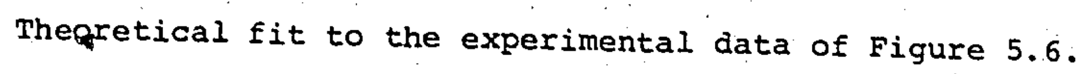

Theoretical fit to the experimental data of Figure 5.6.

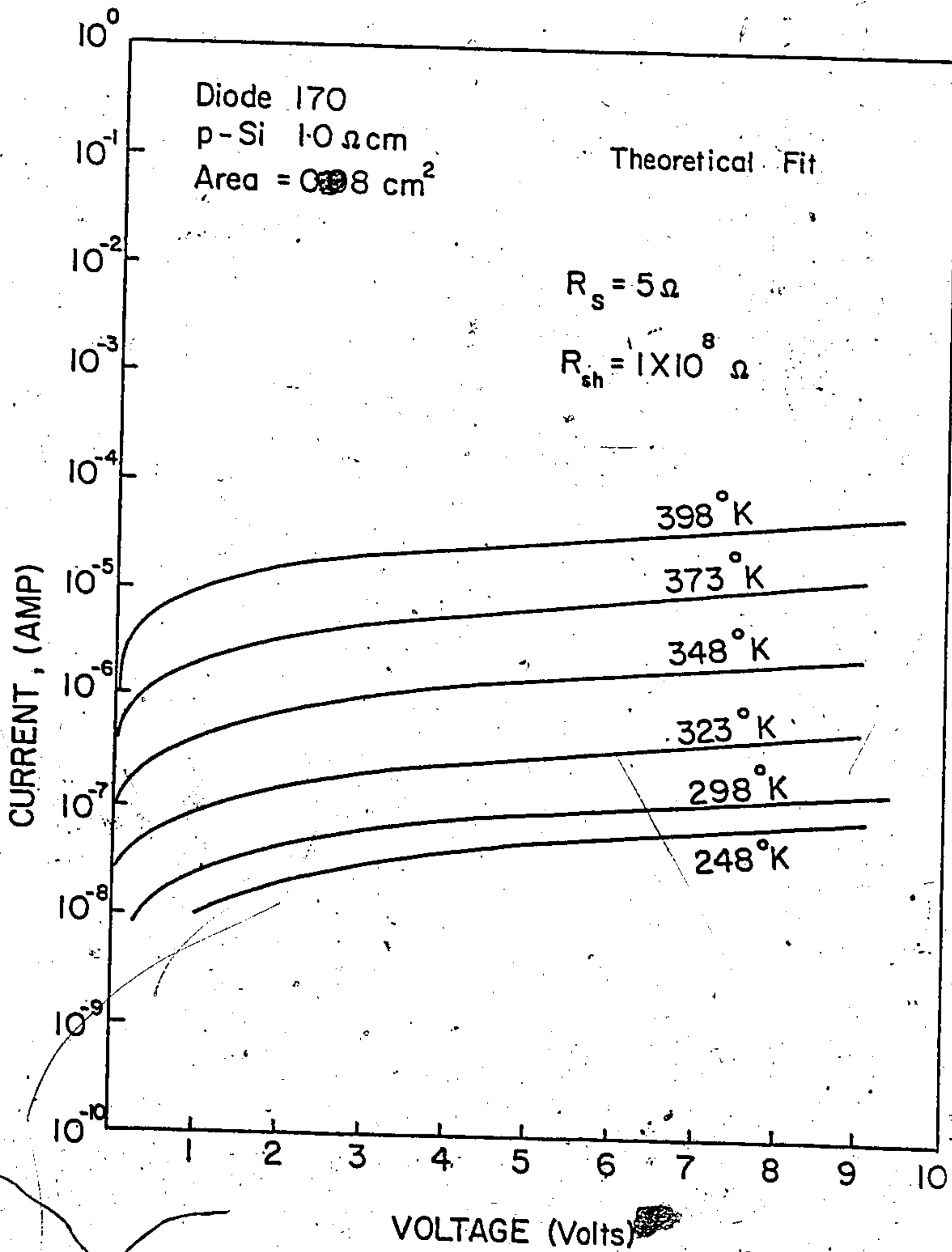

Figure 5.8

Figure 5.9

Reverse current at V_R = 1 volt as a function of temperature for diode No. 170. Continuous lines represent primarily diffusion-current type, dashed lines represent recombination current type I-V characteristics.

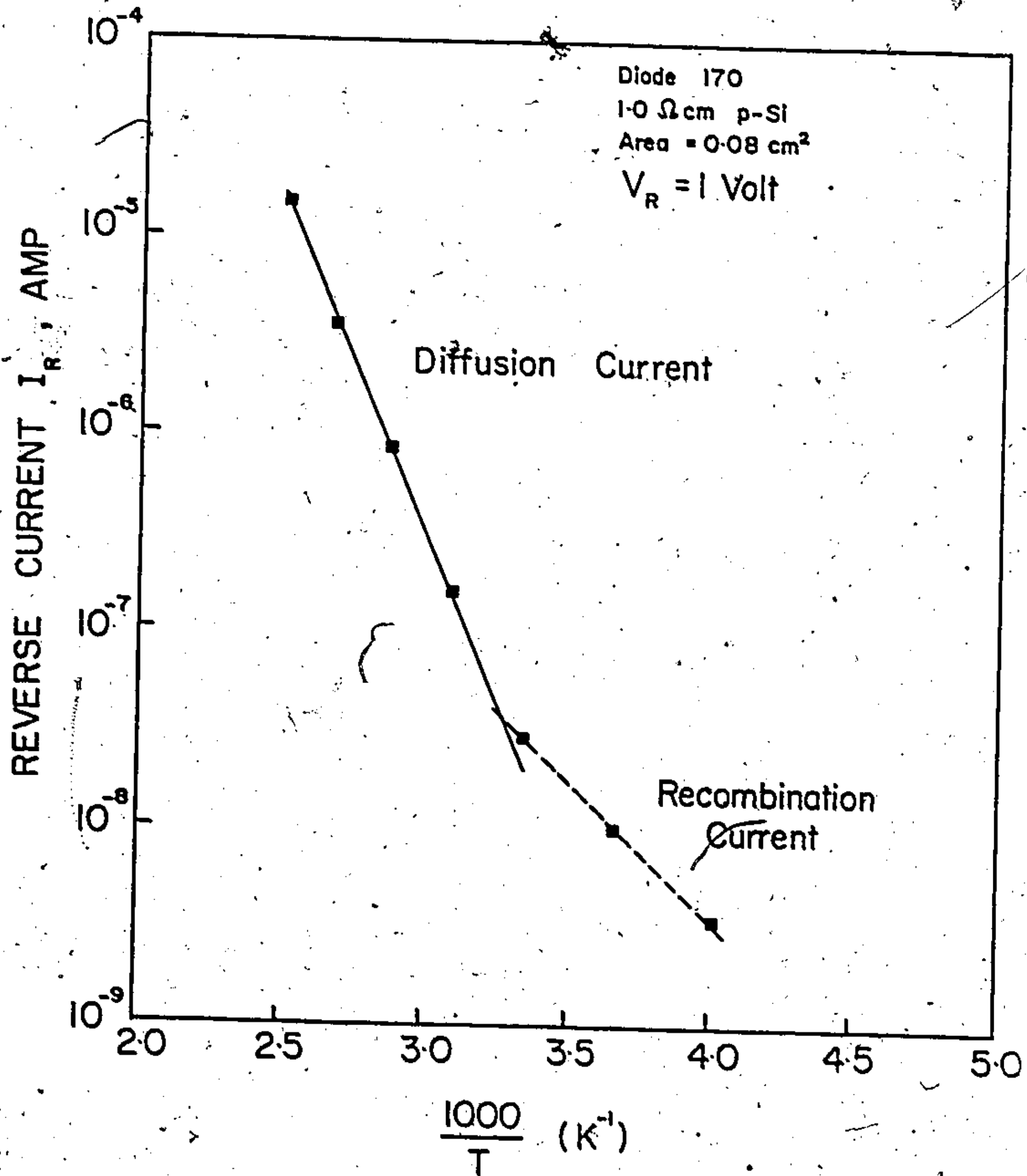

Figure 5.9

teristics toward the experimental ones. Such a laborious exercise, along with other parameter variations, could effect an exact fit, but would not reveal any new information about the device properties.

A more conclusive argument for the adequacy of the tunnel SIS theory can be made by studying the functional dependence of η, J_{sc}, V_{oc} and FF as a function of temperature. Theory and experiment are shown in Figure 5.10. Direct magnitude matching is not possible since the experimental data was measured at 120 mW/cm^2 on 2 Ω-cm material for a less than ideal diode and the calculations are for AM1 illumination (92 mW/cm^2) on 0.2 Ω-cm material for a "best case" converting diode. However, it is the functional dependence which is most important. Theory predicts a constant J_{sc} which is exactly that observed experimentally. The FF experimental curve varies approximately linearly and is in fair agreement with theory which shows some curvature. The V_{oc} and η curves are predicted to have linear dependences with coefficients of 2.3 mV/°C and .08%/°C respectively. These are in good agreement with experimentally measured values of 2.4 mV/°C and .07%/°C. The overall assessment is that good fits between theory and experiment are possible.

5.2.4 Effect of Intensity

The experimentally measured effect of intensity on the efficiency, open-circuit voltage, short-circuit current density and the fill factor is shown in Figure 5.11. As mentioned earlier,

Figure 5.10

Effect of temperature on the efficiency, open-circuit voltage, short-circuit current density and fill factor of n-ITO/p-Si solar cell.

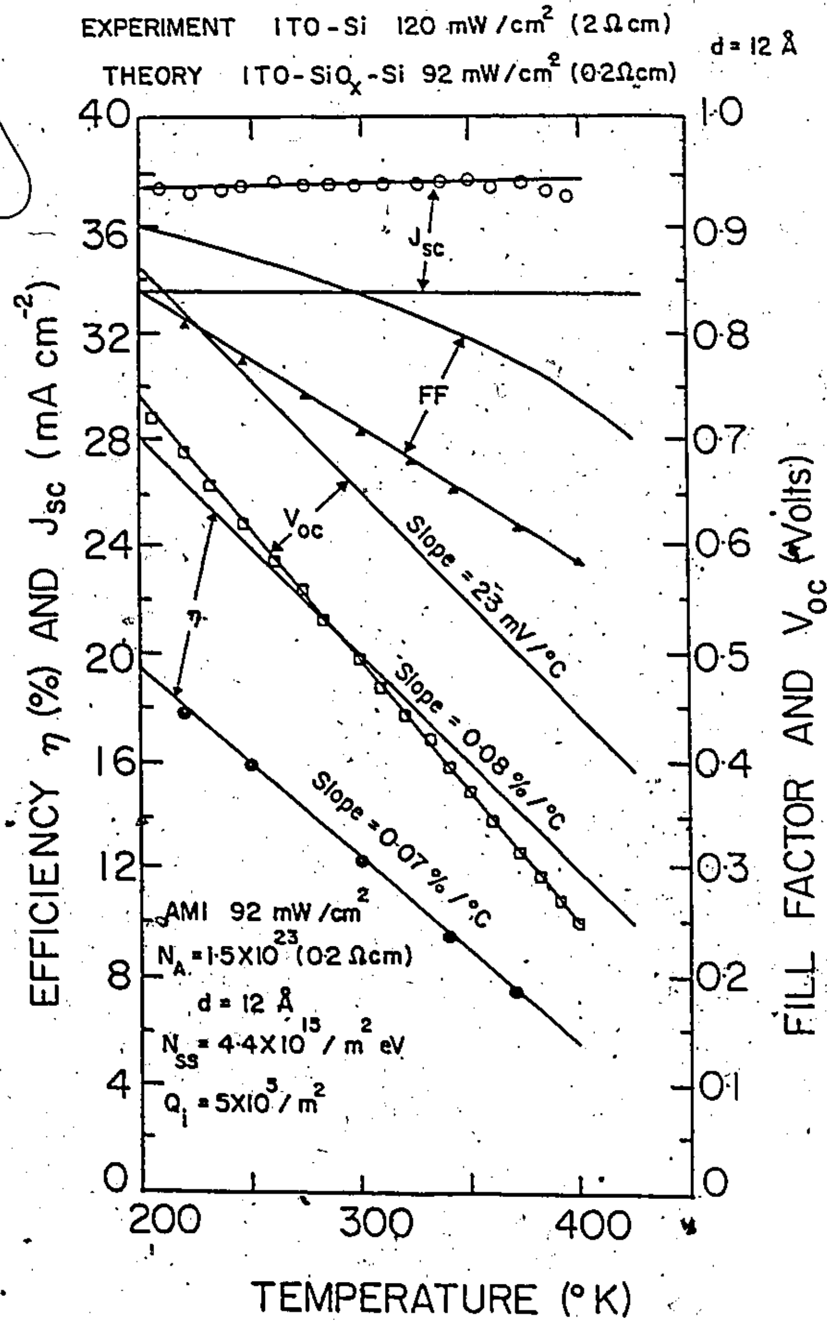

Figure 5.10

Figure 5.11

Experimentally measured effect of intensity on the efficiency, open-circuit voltage, short-circuit current density and fill factor of an nITO/p-Si solar cell. Measurements were carried out by D. Burke and are reported in reference 153.

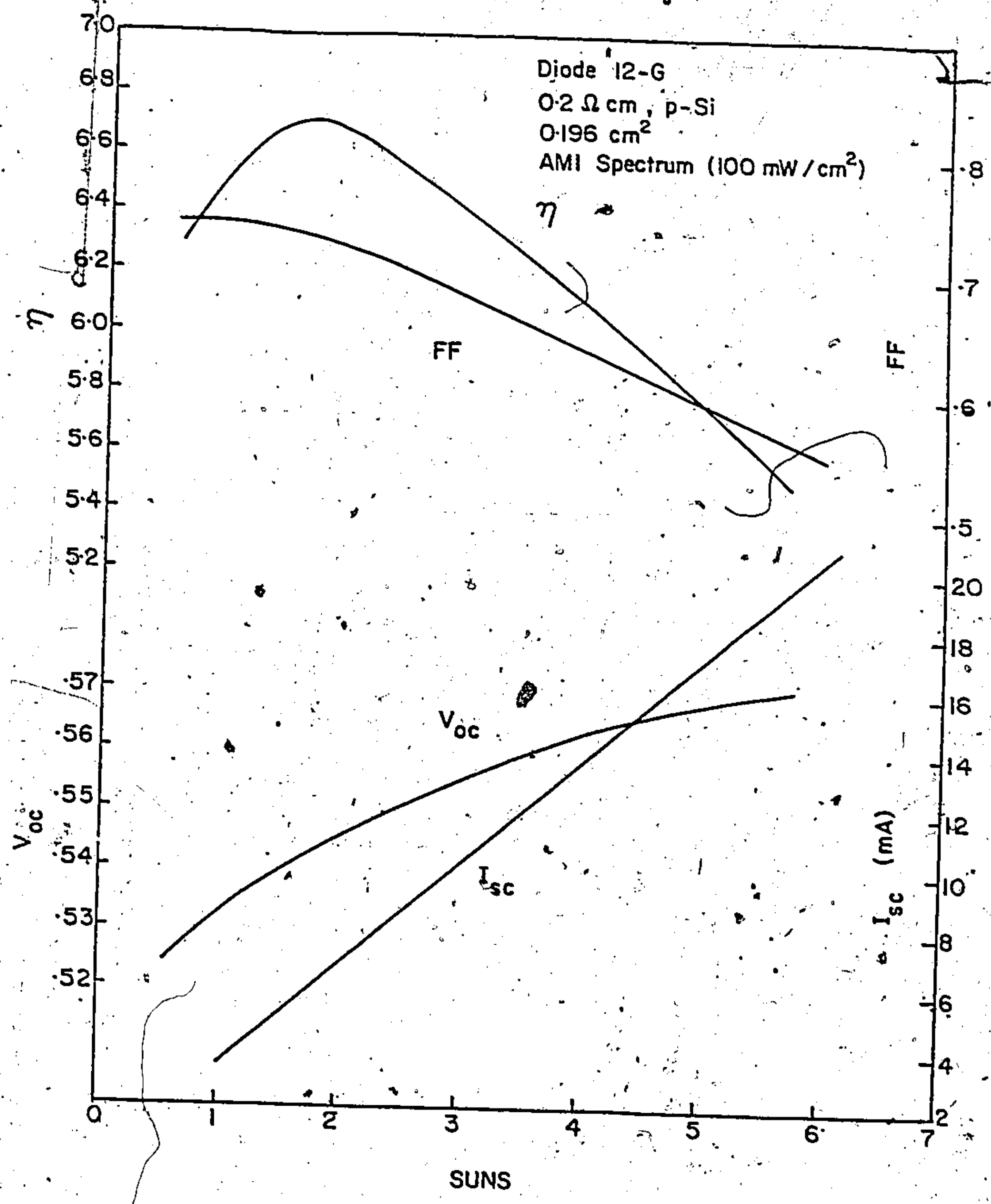

Figure 5.11

the maxima in efficiency depends on the insulator thickness. By comparison of these experimental curves with the theoretical curve of Figure 5.11, we may infer that an interfacial layer of about 15.5 Å is present in the device. However, the theoretical calculations do not take into account the resistance from the ITO layer. Thus, the interfacial layer may be less than 15.5 Å. The functional dependence of V_{oc}, I_{sc} and FF is the same as shown in Figures 3.26 and 3.27 for a 15 Å SIS diode. These measurements demonstrate that SIS diodes can be used in concentrating systems provided that the interfacial layer is very thin (12 Å). Also, the intensity measurements can be used to estimate the interfacial layer thickness, provided the series resistance component from the top layer of ITO and grid etc. is negligible.

5.2.5 <u>Effect of Oxide-Semiconductor Work Function</u>

We have listed the experimental results on SIS solar cells in Table 5.3. The oxide-semiconductors In_2O_3, ITO and ZnO are low work function materials, while SnO_2 is a high work function material. All the experimental results show that low-work function oxide-semiconductors are required for p-type base-semiconductor solar cells and high work function oxide-semiconductors are required for n-type base-semiconductor solar cells. The only exception to this conclusion is the experimental work of reference 41, where the authors have reported ITO solar

TABLE 5.3

EXPERIMENTAL RESULTS ON SIS SOLAR CELLS

Base-semi-conductor	Oxide Semicon-ductor	Possible Inter-facial layer	Illumina-tion	AR Coating	Device Area (cm^2)	V_{oc} (mV)	J_{sc} mA/cm^2	PF	Effi-ciency %	Re-ference
p-Si	ITO	SiO_x	AM 1.2 92 mW/cm^2	-	.07	510	32	0.70	12	6
p-Si	SnO_2	SiO_x	AM1 100 mW/cm^2	-	-	-	-	-	1-1.5	7
p-Si	ITO	SiO_x	AM1 100 mW/cm^2	-	0.13	120-200	-	-	0.3	12
p-Si	In_2O_3	SiO_x	AM0	-	-	340	22	0.48	-	47
n-Si	SnO_2	SiO_x	AM1 100 mW/cm^2	-	1	521	29	0.64	9.9	7
n-Si	ITO	SiO_x	AM1 100 mW/cm^2	-	1.5	480	32	0.63	9.1	41
n-Si	ITO	SiO_x	Sunlight 82 mW/cm^2	-	0.13	380	-	-	.1	37
n-Si	In_2O_3	SiO_x	10^3 lux	-	0.98	160	0.73	0.53	-	35
n-Si	SnO_2	SiO_x	AM1 100 mW/cm^2	-	3.84	615	29.1	0.685	12.12	43
p-InP	ITO	P_2O_5	AM2 75 mW/cm^2	MgF_2	0.20	760	21.55	0.76	14.4	9
p-InP	In_2O_3	P_2O_5	AM2 75 mW/cm^2	-	-	-	-	-	7	44

(continued next page)

TABLE 5.3 (continued

Base-semiconductor	Oxide Semiconductor base	Possible Interfacial layer	Illumination	AR Coating	Device Area (cm^2)	V_{oc} (mV)	J_{sc} mA/cm^2	FF	Efficiency %	Reference
p-Inp	ITO	P_2O_5	Aml 85 mW/cm^2	–	.04	690	23.4	0.65	12.4	45
n-InP	In_2O_3	P_2O_5	AM0	–	–	18	0.6	0.35	–	47
p-GaAs	In_2O_3	Ga_2O_3	AM0	–	–	82	6.17	0.40	–	47
p-GaAs	ITO	Ga_2O_3	AM2 75 mW/cm^2	–	–	500	13.5	–	–	44
n-GaAs	SnO_2	Ga_2O_3	AM0	–	–	33	11.4	0.43	–	42
p-Ge	In_2O_3	Ge_2O_2	AM0	–	–	55	3	0.25	–	47
n-Ge	SnO_2	GeO_2	AM0	–	–	77	3.8	0.30	–	42
p-CdTe	ITO	TeO_2	AM1 82 mW/cm^2	–	0.15	820	14.5	0.55	8	48
p-CdTe	ZnO	TeO_2	AM1 92 mW/cm^2	–	0.1	370	19.5	0.54	4.6	48
p-CaInSe$_2$	ITO	CaO	AM1 100 mW/cm^2	–	0.13	500	30.2	0.55	8.5	49

cells with n-type Si as the base-semiconductors. This surprising result may be explained by assuming that the ITO films deposited by the spray method probably have a higher electron affinity compared to those obtained by the ion-beam sputtering method. The electron affinity of the oxide-semiconductor consists of two parts, i.e.

$$\chi_{os} = \chi_{os}^{(e)} + \chi_{os}^{(p)} \quad . \qquad (5.7)$$

The contribution from the polarization part $\chi_{os}^{(p)}$ is the work against the image force and the contribution from the electrostatic part is the work against any permanent dipole layers at the oxide-semiconductor surface [136]. The surface of oxide-semiconductors prepared by different methods may be different, which will result in different contributions to the electrostatic part, $\chi_{os}^{(e)}$. It is not possible to generalize, at present, for all oxide-semiconductors, but at least in the case of ZnO, films prepared by two different methods have been observed to behave differently [48].

5.3 SPECTRAL RESPONSE

Since the SIS tunnel diode is essentially a surface induced diode, one would expect a significant enhancement in the ultra-violet response of such cells. There is no heavily doped layer at the surface, as with a conventional n^+p junction, to cause an ultra-violet loss. There will be some loss in the

top semiconductor (ITO) but this will be small and can be neglected in the theoretical calculations. Calculated and measured spectral response curves are shown in Figure 5.12. The agreement is quite good, almost exact to within experimental error. There is some reduction in blue response in the experimental diode, perhaps due to some surface damage or other surface imperfections. This might disappear with improved processing.

5.4 LOSS MECHANISM IN SIS SOLAR CELLS

Theoretically, we predicted a 20% efficiency (AM1) using 0.2 Ω-cm p-type silicon with a 12 Å interfacial layer for n-ITO-SiO_x-(p-type)Si solar cells. In general, the SIS solar cells can reach the efficiency close to that which will be obtained by using the base-semiconductors alone as a p-n junction solar cell. However, the experimentally observed efficiencies have not reached this limit. The highest efficiency reported for Si is that obtained by Feng et. al. [43] at 12.24% (AM1) for a 3.84 cm^2 device. In the case of nITO/p-InP, a 14.14% (AM2)) efficiency device has been obtained [9]. An outstanding question is, thus, the nature of the losses which seem to be impeding the achievement of 20% efficiency in the case of Si devices. In this section we will identify the various possible loss mechanisms and the

Figure 5.12

Calculated and experimentall measured spectral response of n-ITO/p-Si solar cell.

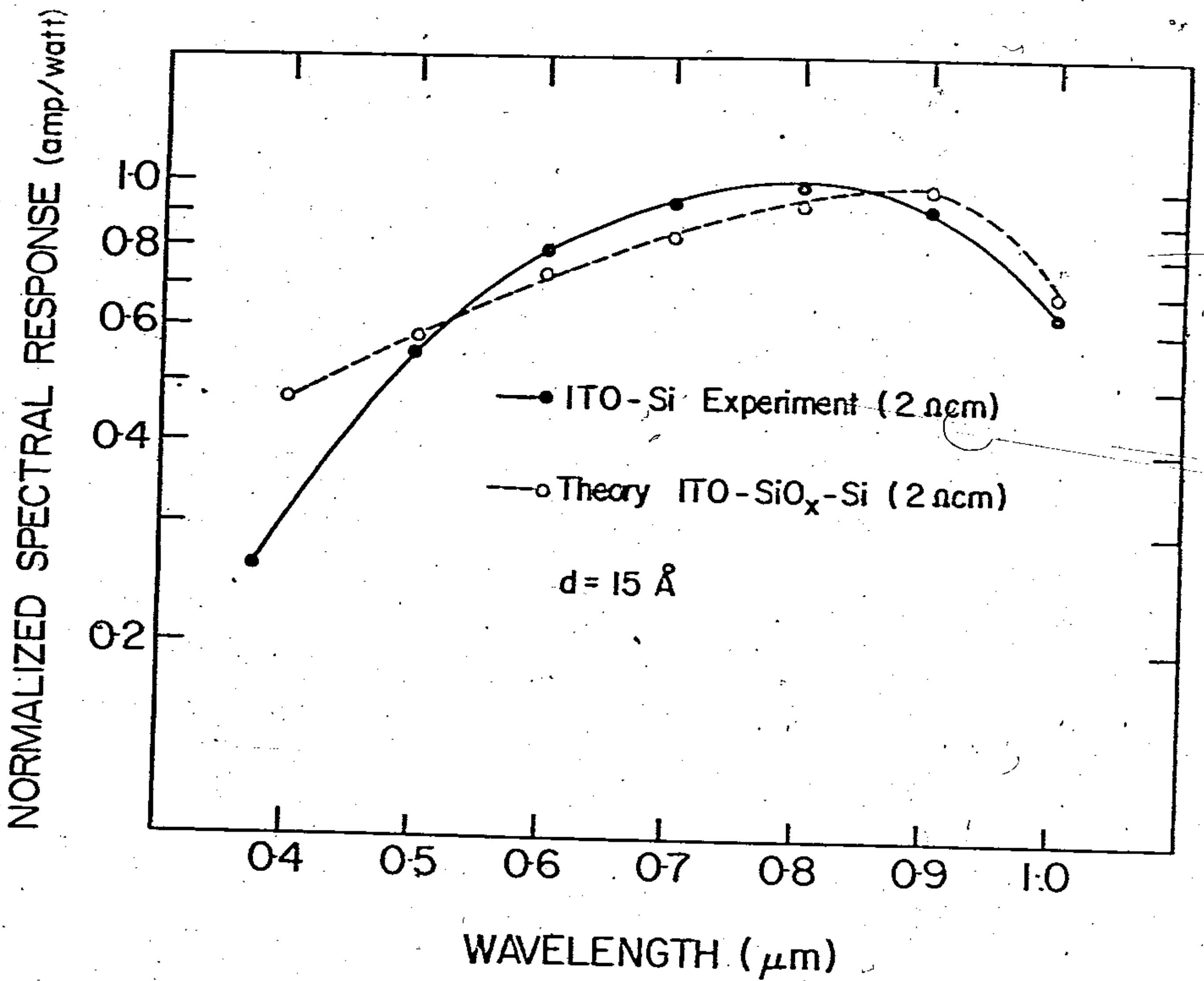

Figure 5.12

magnitude that can be attributed to them. The following are the main loss mechanisms in SIS solar cells:

(i) transmission-reflection loss associated with the oxide-semiconductor layer.

(ii) recombination in the surface depletion layer

(iii) lowering of the open circuit voltage

(iv) series and shunt resistance losses.

5.4.1 Transmission-Reflection Loss Associated with the Oxide Semiconductor

The sources of optical loss in oxide-semiconductors are absorption, scattering and transmission. Out of these three losses, the reflection loss is the dominant one. The transmission data on ITO films used in the fabrication of solar cells were measured by N. Chang [66]. For comparison we have also collected transmission-reflection data from the literature reported by two other workers [137,138]. These aresults are shown in Figure 5.13. In all three cases, the ITO films are deposited by sputtering and the film thickness is approximately 3000 Å. On the average, 80-90% transmission can be obtained for ITO films. This will lead to the reduction of I_{sc} and eventually to a decrease in the overall efficiency. A rough estimation gives an efficiency loss of 2-4%.

We have carried out an actual calculation for nITO-SiO_x-(p-type)Si solar cells taking reflection loss from ITO into consideration. For this purpose the transmission data of N. Chang were used. The efficiency was reduced from 19.92%

Figure 5.13

Typical transmission and reflection curves for argon sputtered indium-tin-oxide films (10% Sn) of approximately the same thickness ($\sim$ 3000 Å).

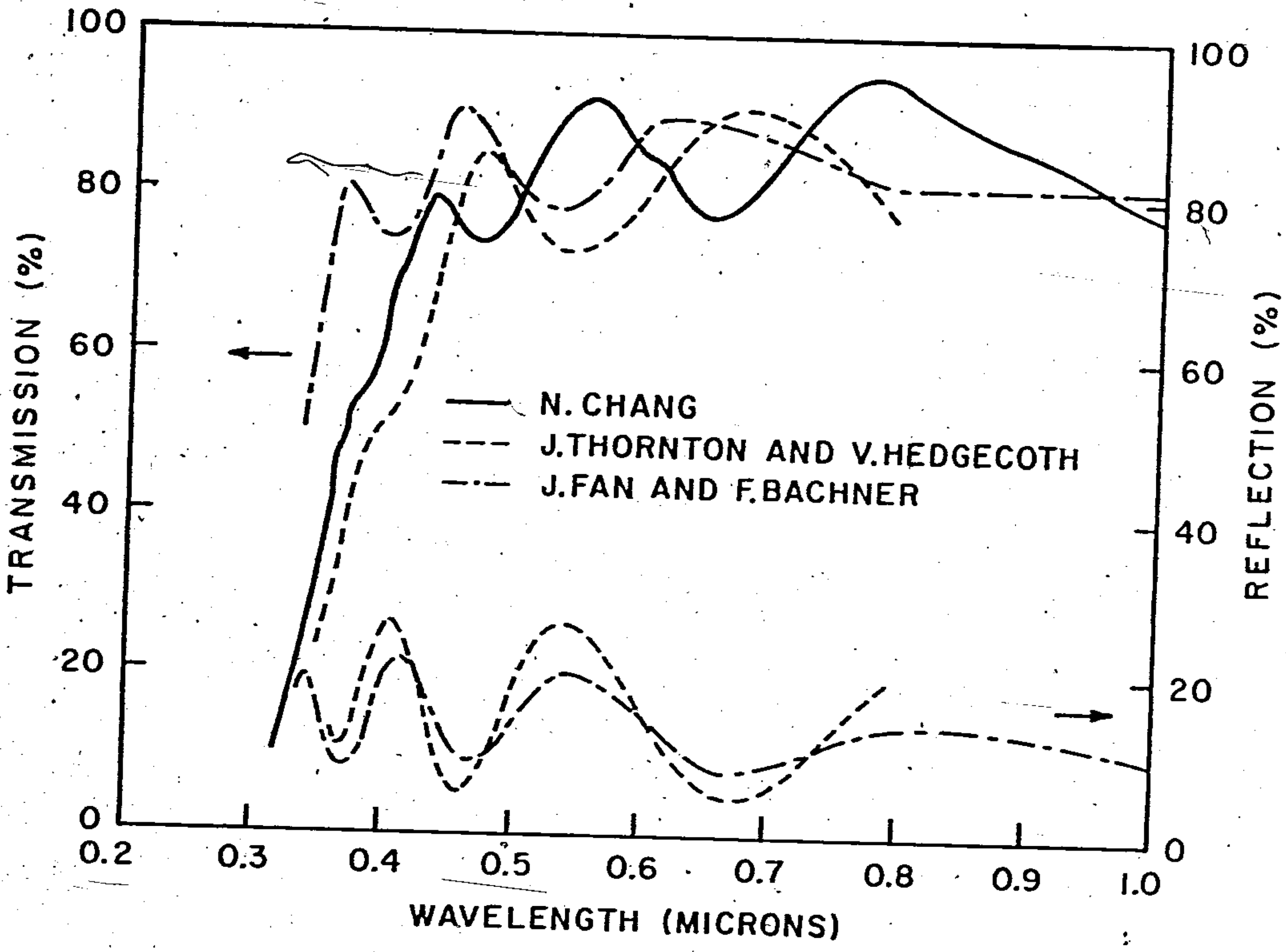

Figure 5.13

(AM1/92 mW/cm^2) to 15.5%. Thus, without the application of an anti-reflection coating, only 15-16% can be expected from n-ITO/p-SI SIS solar cells. Similar reflection losses are expected for other SIS solar cells.

As mentioned earlier, the oxide-semiconductor layer in SIS solar cells serves as a partial AR coating. This requires the thickness of the top layer to be in the order of 600-700 Å. However, a practical device may have a thicker oxide-semiconductor layer in order to keep its sheet resistivity low, and in such cases, the reflection losses may be more than 10-20% of the incident light. Therefore, this device requires an anti-reflection coating to improve the transmittance of the top layer. The main materials used as AR coating are SiO, Ta_2O_5, TiO_2, MgF_2, CeO_2, Al_2O_3 and Si_3N_4 [34(c)]. The index of refraction for these materials is given in Table 5.4. It can be seen from Table 5.4 that the average index of refraction for these materials is about 2. The simplest way to estimate the thickness of the AR coating is to have a knowledge of the spectral response of the device and the spectrum of the light source. The maximum of the product of the spectral response and the spectral irradiance can be obtained at a certain wavelength and a quarter of this wavelength is divided by the refractive index of AR coating to get its thickness [139]. For example, if the maximum of the product of the spectral response and the spectral irradiance is at 6000 Å, and the index of refraction is taken as 2, the thickness of the AR coating will be 750 Å.

TABLE 5.4

LIST OF SOME ANTI-REFLECTION COATING MATERIALS AND THEIR INDEX OF REFRACTION

Material	Index of Refraction
SiO_2	1.90
Ta_2O_5	2.40
TiO_2	2.40-2.70
MgF_2	1.40
CeO_2	-
Al_2O_3	1.86
Si_3N_4	2.10
Sb_2O_3	2.09

5.4.2 Recombination in the Surface Depletion Layer

Most of the oxide-semiconductors used in the fabrication of SIS solar cells have been deposited by sputtering methods. The energy of ion beam is typically 700 eV for etching and 500 eV for sputtering [51]. The sputtering process may introduce defects at the surface of the base-semiconductor. Although the role of the ion beam (usually argon ions) in the creation of these defects is not clear, the following possibilities exist:

i) defects due to accidental Ar ion implantation

ii) electron penetration effects

iii) stress induced effects.

Argon implantation may be ruled out based on the work of Johnson, Speir and Strausse [140], who have estimated the penetration of 1 keV Ar ions in Si to be about 6 Å. Electron penetration effects are not so easily interpreted. In some sputtering systems, an electron plasma is used to neutralize the ion beam. 1 keV electrons lose virtually all of their energy within 500 Å of the surface. Appreciable neutralizing current can damage the surface, however, there has been no conclusive experiment which shows the effect of electron damage on the electrical properties of solar cells.

The effect of beam induced stress has been reported by Dearsly [141]. In this process, impurities which reside on or near the surface can be driven into the substrate rather than

being sputtered off during cleaning. Accidently, impurity gradients caused by sputtering can cause the migration of impurities. The net result is an increased number of traps and recombination centers near the surface.

In order to characterize the defects introduced by sputtering, we have modified our calculational program to take into account the spatially dependent life-time. We introduced two lifetimes in the base-semiconductor (a) depletion region life time τ_D, and (b) bulk life time τ_B. In the nITO-SiO_x-(p-type)Si solar cells, depletion occurs in the silicon, typically within 900 Å of the interface. The depletion layer also includes the inversion layer. The recombination in the depletion region was modelled by using Sah-Noyce-Shockley (SNS) model [142]. Figure 5.14 shows the dark I-V characteristics with depletion lifetime, as the variable parameter. Case (a) represents the depletion lifetime equal to the bulk lifetime. In other cases (b), (c) and (d), the depletion lifetime is reduced successively by one order of magnitude. The reduction of lifetime in the depletion region represents the increase in the number of recombination centers. One can see from Figure 5.14 that decreasing the lifetime of the depletion region increases the range of voltage over which the recombination current dominates. In the last case, (d), the I-V curve up to about 0.7 volt is dominated by recombination current. An SIS diode with such characteristics will give a low photovoltaic output compared to the case where the depletion and bulk

Figure 5.14

Calculated dark I-V characteristics of n-ITO/p-Si tunnel diode with depletion lifetime as the variable parameter. These curves were calculated by M. Spitzer and are reported in reference 154.

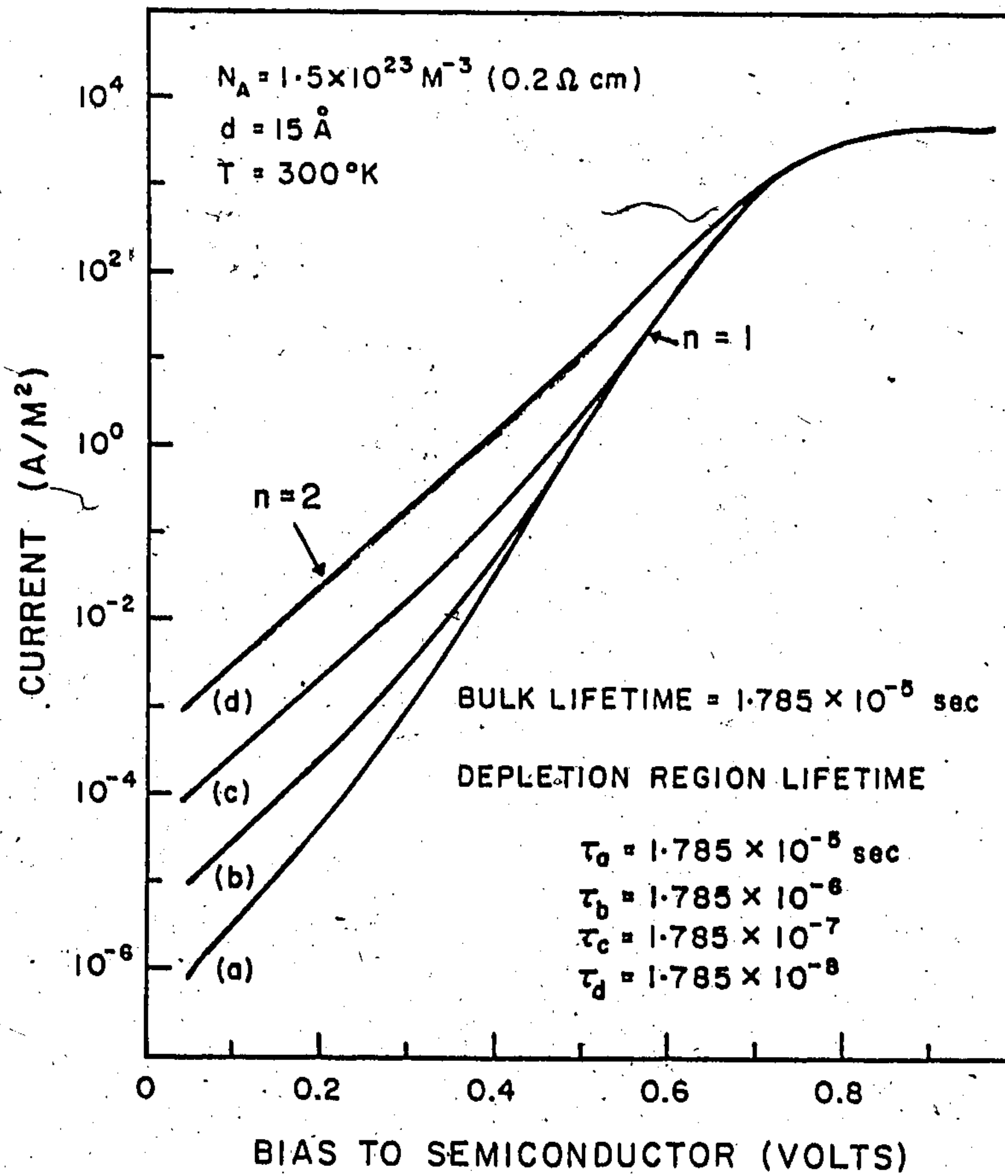

Figure 5.14

lifetimes are the same.

We have calculated the conversion efficiency of nITO-SiO_x-(p-type)Si solar cells as a function of depletion region lifetime, with bulk lifetime as the variable. These results are shown in Figure 5.15. In case (a), the bulk lifetime is 17.85 μsec and represents the best value reported in the itera- ture for single crystals of Si. Case (b) represents a moderate value of 1.79 μsec while case (c) represents low grade Si with a bulk lifetime of 0.18 μsec. In low-grade materials the efficiency is reduced by a large amount, if the depletion lifetime is very low. It is observed from Figure 5.15 that if the depletion lifetime is an order smaller than the bulk lifetime, the conversion efficiency is almost unchanged. Such results are not surprising and the same conclusion was drawn by Hovel in a study of Si p-n junction solar cells [102].

In order to estimate the loss in conversion efficiency by sputtering, we compared the experimentally observed dark I-V characteristics of nITO/p-Si solar cells with the theore- tically calculated one. The forward I-V characteristics of a typical diode No. 12G are shown in Figure 5.16. On comparison, we observed that the experimental dark I-V may be fitted by picking up case (b) of Figure 5.14. Overall loss by this mechanism is estimated to be between 0.1 to 1.0%.

Figure 5.15

Calculated conversion efficiency of n-ITO/p-Si SIS solar cell as function of depletion region lifetime, with bulk life time as the variable. These curves were calculated by M. Spitzer and are reported in reference 154.

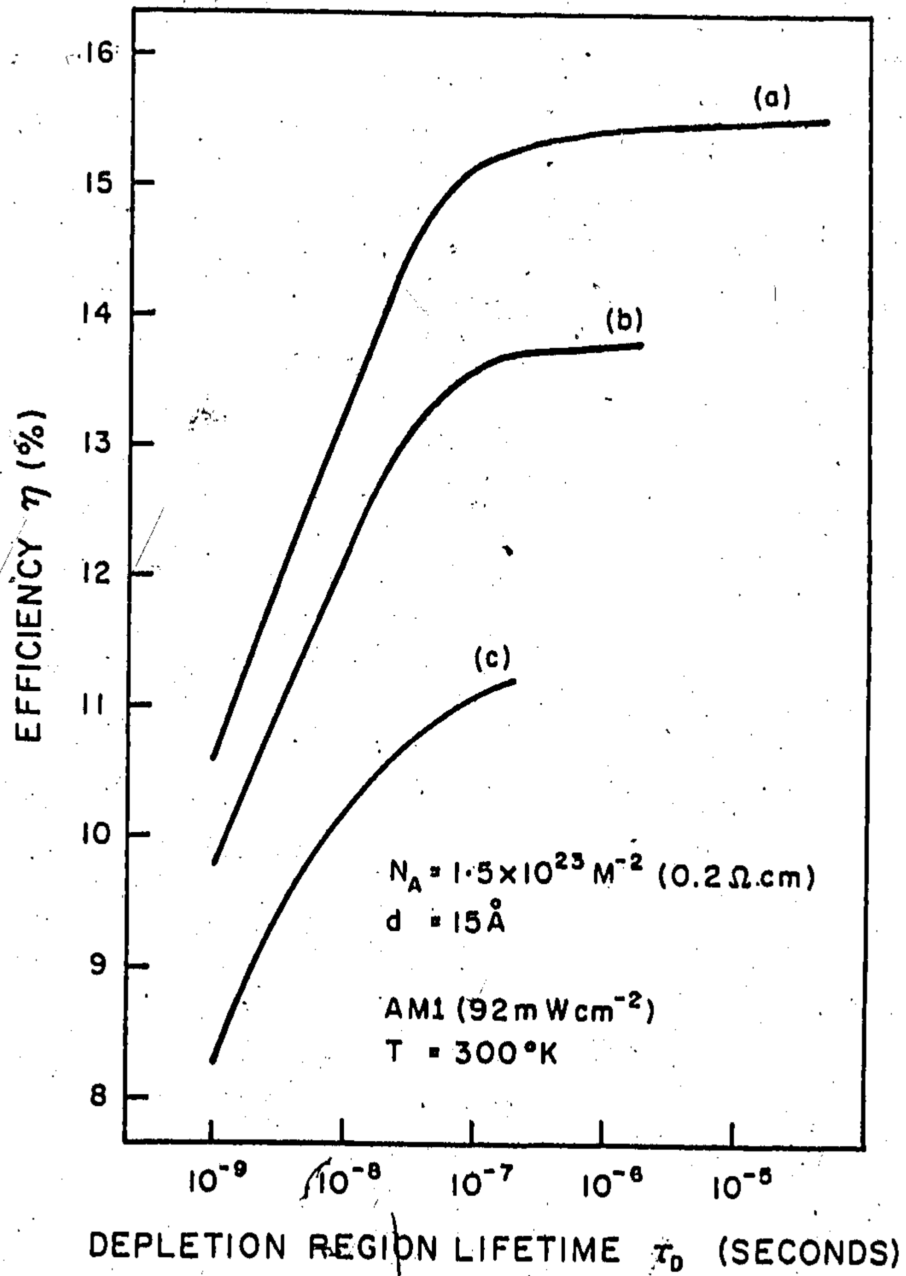

Figure 5.15

Figure 5.16

Experimentally measured forward dark I-V characteristics of n-ITO/p-Si solar cell at 298° K. These measurements were carried out by D. Burk.

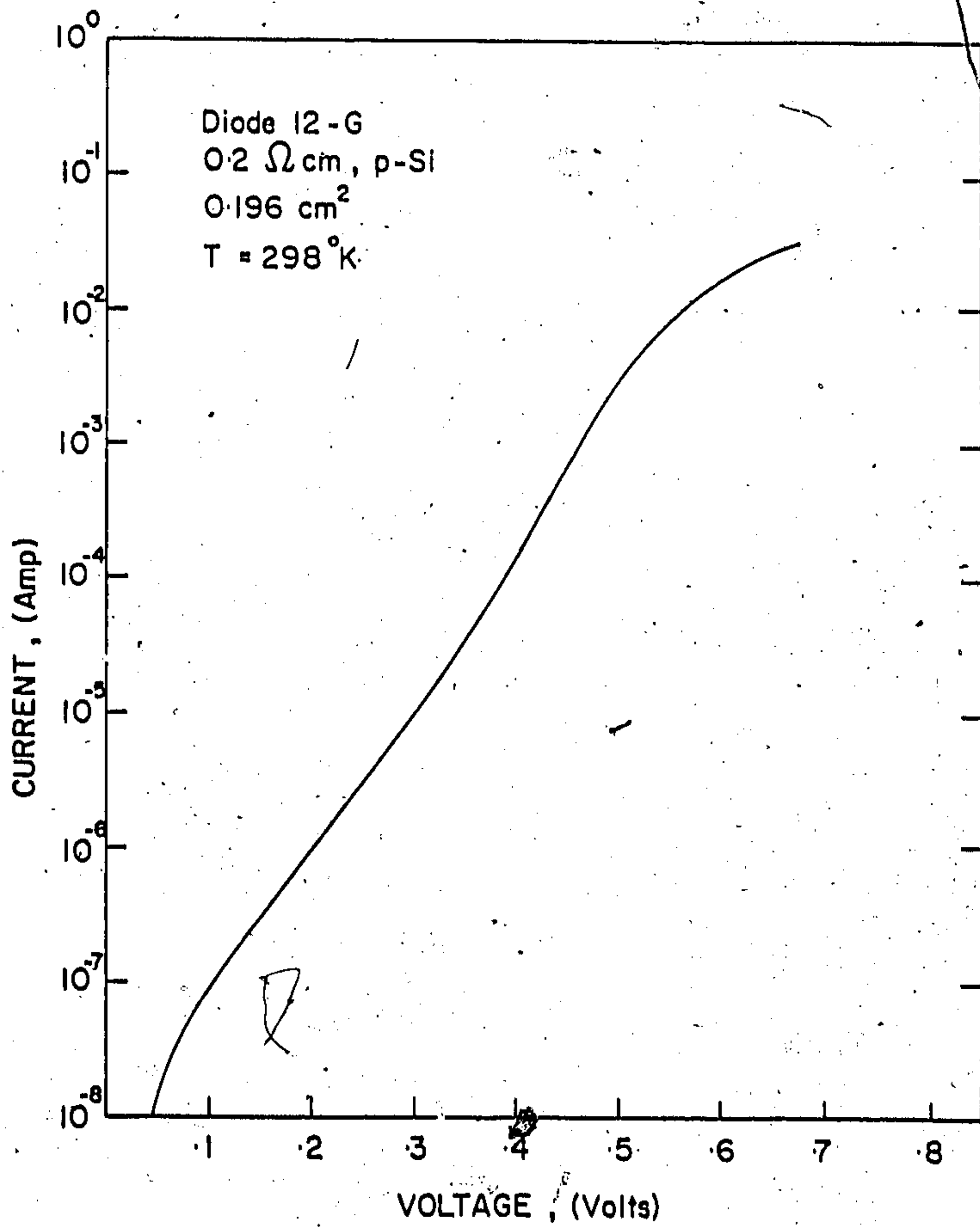

Figure 5.16

5.4.3 Lowering of Open-Circuit Voltage

There are various mechanisms, which may be responsible for lowering the open-circuit voltage of SIS solar cells. The open-circuit voltage V_{oc} is governed by the "barrier height" of the device, given by Equation (3.23)

$$\phi_b = E_{gs} + \phi_{si} - \phi_{osi} + \Delta - V_i + q\left(\frac{Q_s + Q_i}{\varepsilon_i}\right)d$$

This relation shows that an increase in ϕ_{osi} and a decrease in ϕ_{si} and Δ may decrease the barrier height of the device. The barriers ϕ_{osi} and ϕ_{si} are related to the electron affinity of the oxide-semiconductor and base-semiconductor respectively, while Δ depends on the degree of degeneracy in the oxide-semiconductor. However, the presence of pin-holes in ultra-thin interfacial layers may lead into another reduction in V_{oc} [110]. Nevertheless, for generality, we may conclude this mechanism for the lowering of ϕ_{si}. The loss due to increase in ϕ_{osi} is estimated to be 4-10%. The decrease in ϕ_{si} may account for 4-5% loss and the ITO doping may reduce 2-4% of the conversion efficiency.

5.4.4 Series and Shunt Resistance Losses

The shunt resistance degrades the open-circuit voltage, and the series resistance degrades short-circuit current density and fill factor of the device. Since the highest V_{oc}

reported for SnO_2/n-Si devices and ITO/p-Si devices are 0.615 V [43] and 0.52 V [50] respectively, it appears that shunt resistance losses in SIS solar cells are very small. Thus, series resistance appears to be the main loss. The series resistance of an SIS solar cell will consist mainly of the following parts: (i) resistance of the top layer, (ii) resistance of the interfacial layer, and (iii) resistance of back contact. Assuming that true ohmic back contacts can be made, the first two will be responsible for most of the series resistance of the device. We have calculated the series resistance of the insulating layer for the nITO-SiO_x-(p-type)Si solar cell. The method of reference 67 was used and the results are shown in Figure 5.17. The series-resistance contributed by the insulating layer is negligible up to about 15 Å, after which a reduced fill factor will be observed due to high value of resistance. This effect is shown in Figure 3.10(b) which shows efficiency as a function of insulator layer thickness. Thus, if one can build devices with ultra-thin interfacial layers (< 15 Å), the only resistance will be that of the top layer. A grid with a large number of lines may be used to reduce this part of the series resistance. The overall loss is estimated to be between 1-10% for non-optimized devices.

Figure 5.17

Calculated resistance of the interfacial layer as function of its thickness. The method of reference 67 has been used and the device area is 1 cm^2.

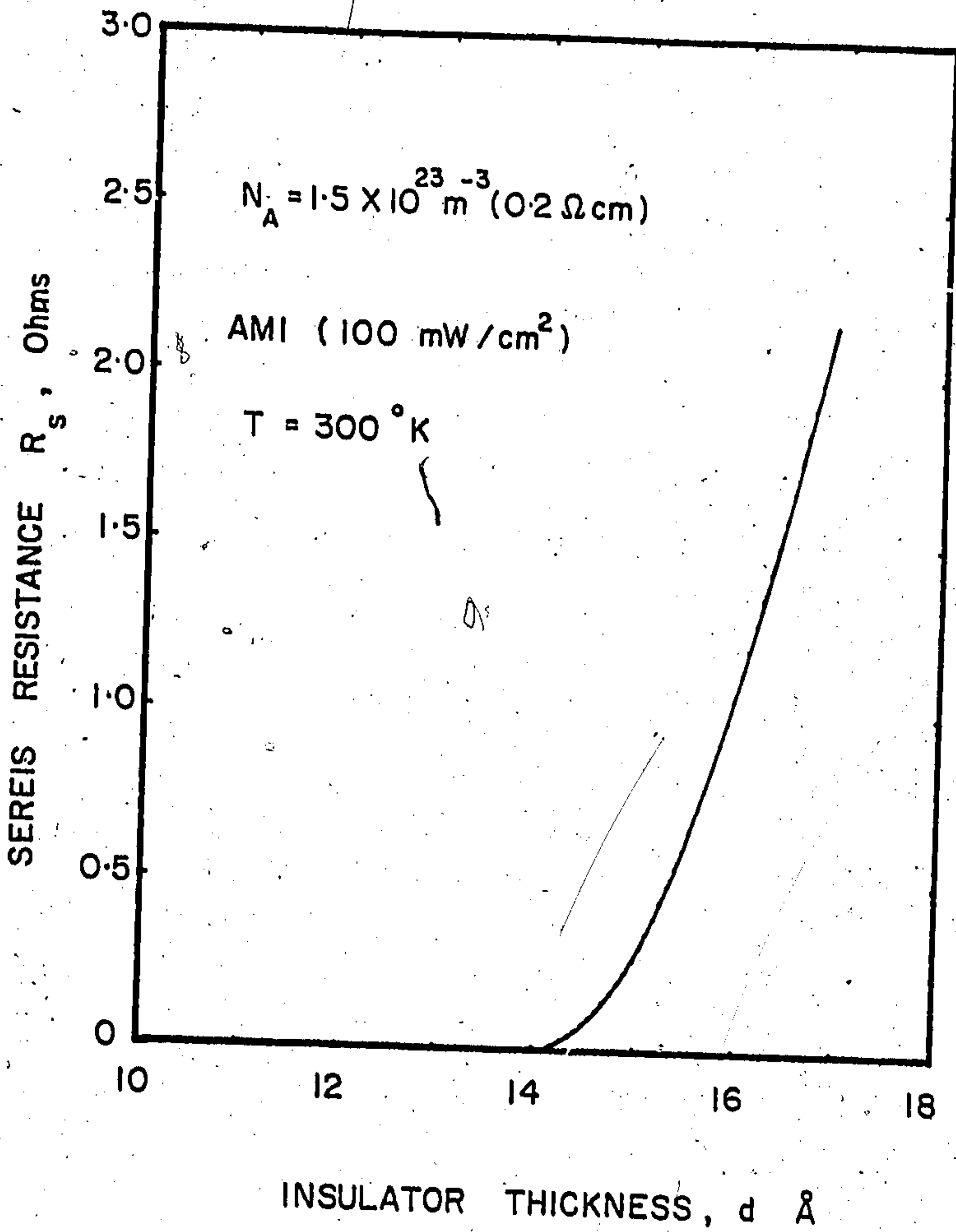

Figure 5.17

5.5 THE IMPORTANCE OF THE ELECTRON AFFINITY OF OXIDE SEMI-CONDUCTORS

The electron affinity of oxide-semiconductors (SnO_2, In_2O_3 etc.) is a topic of considerable theoretical and experimental attention. This interest has been sparked by the application of these oxide-semiconductors in opto-electronic devices, particularly solar cells. In this section we will show that simple methods based on the electrical measurements of oxide-semiconductor/base-semiconductor systems often lead to incorrect results, due to the uncertainty in the Fermi level position in the oxide-semiconductors and other interface parameters [13].

Very recently, Thompson and Anderson [12] reported that the electron affinity of indium-tin oxide (ITO) is about 4.5 eV. they also concluded that due to its electron affinity, ITO is not suitable material for making solar cells on either n or p-type silicon. Such conclusions are based on their own electrical measurements of ITO/Si solar cells and may not be warranted. For example, the presence of an interfacial layer formed during the fabrication of an oxide-semiconductor/base-semiconductor solar cell can invalidate the simple heterojunction analysis applied in reference 12. Furthermore, if we also ignore the interface, then we can argue a good case for the electron affinity of ITO being 4.3 eV based on our experimental data to be presented here. With an interface, the value can be 4.2 eV. The difference between 4.5 and 4.3 or 4.2, while small, is very

important. It can account for the reason why some investigators find efficient solar cells and others do not.

n-ITO/p-Si solar cells have been fabricated at Colorado State University using the ion beam sputtering method [51]. The composition of ITO was 91 mole % in In_2O_3 and 9 mole % SnO_2. Dark I-V characteristics as a function of temperature were measured in the temperature range of 200-400°K and those results are shown in Figure 5.2. From a careful inspection of this data, we observed that the dark I-V consists of two regions, one with slope $n_1 \sim 1.3$ and the other with slope $n_2 \sim 2.0$. If one assumes that the forward current consists of components due to thermionic emission and depletion-recombination, the I-V relation can be written semi-empirically as

$$I - \frac{V-IR_s}{R_{sh}} = I_{01}[\exp(\frac{V-IR_s}{n_1 kT})q-1] + I_{02}[\exp(\frac{V-IR_s}{n_2 kT})q-1] \quad (5.10)$$

where

$$I_{0i} = \frac{4\pi qm(kT)^2 A}{h^3} \exp(-\frac{\phi_b}{kT}) , \quad (5.13)$$

and

$$I_{02} = \frac{qn_i WA}{\tau_D} \quad (5.14)$$

with the symbols having their usual significance.

We have plotted (I_{01}/T^2) vs 1/T in Figure 5.18. The slope of this curve is about 0.85 eV, and represents the "barrier height" of the device. Due to the large band-gap of ITO, minority

Figure 5.18

Semi-log plots of I_{01}/T^2 and I_{01}/T^3 vs $10^3/T$ for n-ITO/p-Si solar cells. The lower curve represents diffusion current and the upper curve represents thermionic emission current.

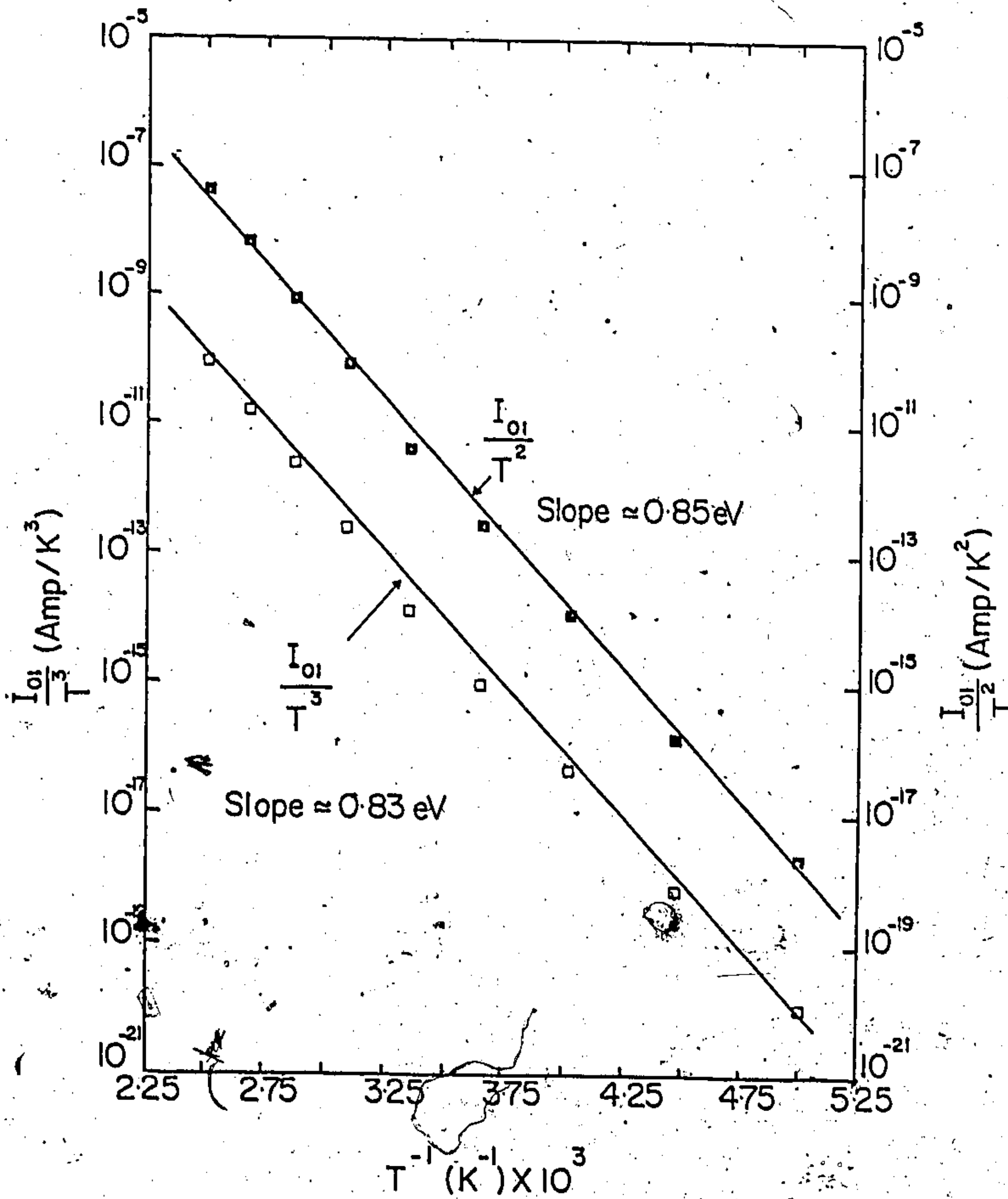

Figure 5.18

carriers will be photo-generated in p-type Si upon absorption of light. Thus, we have neglected the depletion layer in n-ITO. Such a simple heterojunction model is given in Figure 5.19. Using the notation of Figure 5.19, the electron affinity of oxide-semiconductor (ITO in this case) is given by

$$X_{os} = X_s + \Delta + E_{gs} - \phi_b \tag{5.15}$$

where

$$\phi_b = V_D + \delta. \tag{5.16}$$

This relation is valid only when we assume that the interface is free of surface states. An inspection of Table 3.1 shows that for any combination of oxide-semiconductor and base-semiconductor, large numbers of defects will be present due to a mismatch of crystal structure, lattice constant and coefficient of thermal expansion. In order to make a comparison with reference 12, we ignore these limitations for the time being.

Taking the values of $\Delta = 0$, $X_s = 4.05$ eV, $E_{gs} = 1.1$ eV (the same as in reference 12), the electron affinity of ITO is about 4.3 eV. This value for the electron affinity is close to the optimum value required to have a negligible heterojunction discontinuity for n-ITO/p-Si solar cells. Thus, it is obvious that the uncertainty in the value of Δ may lead one to incorrect conclusions about the electron affinity of indium tin oxide and, in general, about other materials, if care is not taken. Changes

Figure 5.19

Simple equilibrium energy-band diagram for n-oxide-semiconductor/p-base-semiconductor solar cell, neglecting the presence of an interfacial layer.

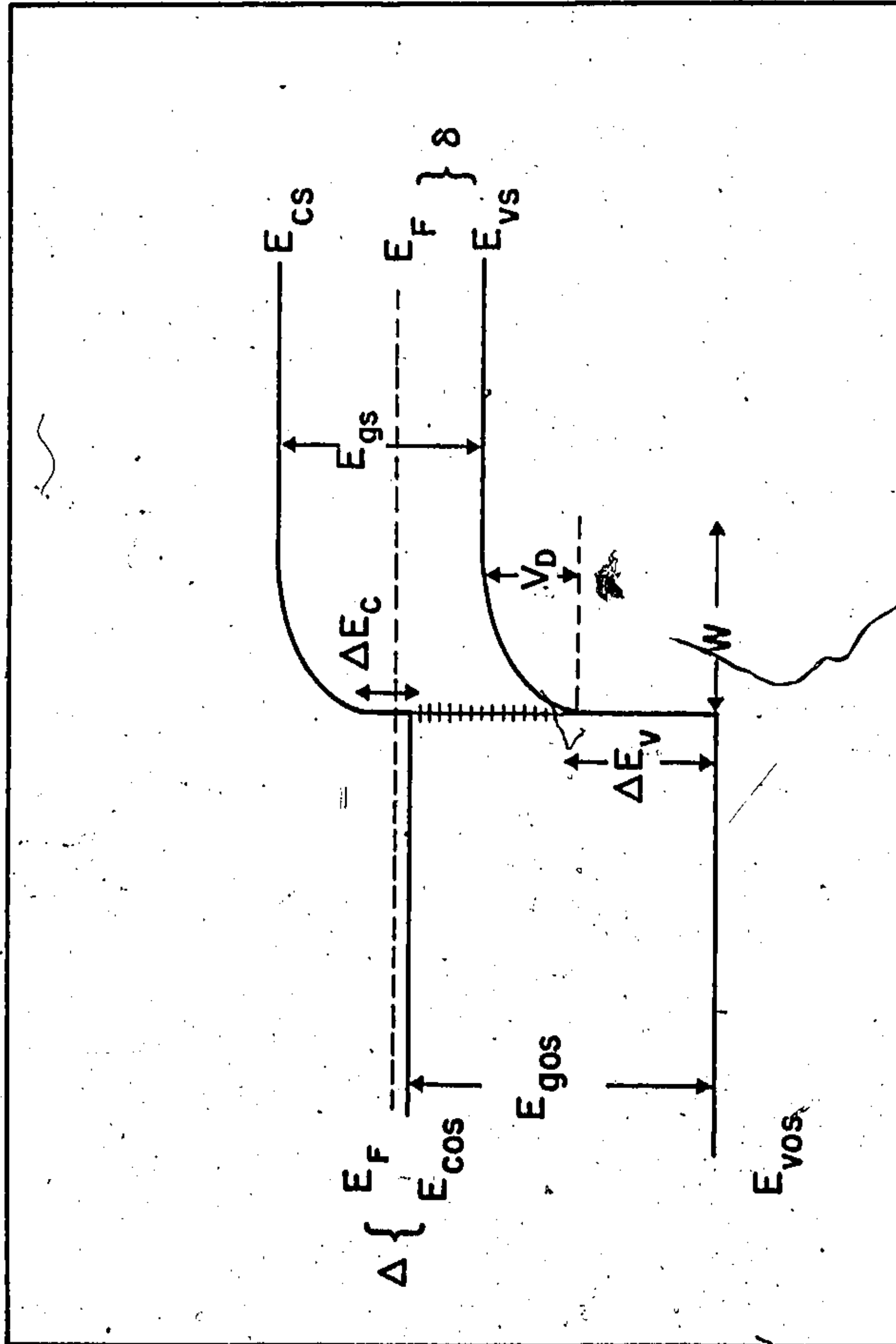

Figure 5.19

as great as 0.4 eV have been reported in the value of Δ for various heat treatments of ITO films [143]. Such heat treatments are necessary in some cases to reduce the sheet resistivity of oxide semi-conductors. Thus, there may be different types of "ITO" in terms of electron affinity and these differences may be due to chemical composition.

The presence of an interfacial layer adds additional terms in equation (5.15). Using our semiconductor-insulator-semiconductor (SIS) model, the electron affinity of the oxide-semiconductor is given by Equation (3.23) i.e.

$$X_{os} = X_s + \Delta + E_g - \phi_b - V_i + q\left(\frac{Q_s+Q_i}{\varepsilon_i}\right)d \quad (5.17)$$

Here V_i is the potential drop across the insulator, Q_s is the charge in the surface states and Q_i is the fixed charge in the insulator.

As mentioned in section 3.2, the dominant current in SIS solar cells of proper insulator thickness (< 16 Å for nITO-SiO_x-(p-type)Si system) consist of diffusion and depletion layer recombination components. We have also plotted (I_{01}/T^3) vs 1/T in Figure 5.18. The slope of this curve is about 0.83 eV. In the ideal case, this activation energy is equal to the band gap of the silicon. In our case, this represents approximately the barrier height of the device since we have a relatively high n value device. Assuming an SiO_x interfacial

layer of 15 Å, and the surface state and insulator charge data of reference 10, we have calculated the electron affinity from equation (5.17). Again, taking $\Delta = 0$, $X_s = 4.05$ eV, $E_{gs} = 1.1$ eV, the value of X_{os} is equal to 4.2 eV. These calculations demonstrate that the presence of the interfacial layer introduces another uncertainty in the estimation of X_{os}. However, as we have explained, an interfacial layer SIS solar cell can be highly efficient. This may not be the case for a heterojunction where the interface is mismatched and dominates. A thin interfacial layer on the other hand can promote matching.

In conclusion, we have shown that attempts to find the electron affinity of oxide-semiconductors from simple electrical data on barriers may not reveal the true potential of these materials. However, the suitability of a particular oxide-semiconductor as a heterojunction pair depends critically on its electron affinity. Therefore, the electron affinity of the oxide-semiconductor should be measured by methods other than those which use electrical characteristics of the device before any judgement is passed.

5.5 SUMMARY

In this chapter the theory of semiconductor-insulator-semiconductor (SIS) solar cells has been compared with the available experimental data. Most of the experimental data is presented for n-ITO/p-Si solar cells. The presence of the interfacial layer has been confirmed by Auger spectroscopy in the

case of n-ITO/p-Si and n-ITO/p-InP solar cells and the effect of the interfacial layer thickness on the performance of n-ITO/p-Si solar cell has been described. We have studied the effect of temperature on the forward and reverse dark I-V characteristics in length, and the theoretical fit to the experimental data is very good. The measured parameters of n-ITO/p-Si solar cell as a function of temperature are compared with the theory and match well. The measured effect of intensity has been compared with theoretical calculations and the functional dependence of device parameters agrees fairly well. These data demonstrate that the resistance of the interfacial layer has to be reduced by fabricating thin interfacial layer devices if these devices are to be used in the concentration systems. If the series resistance component from the top layer is very small, the intensity measurements can be used to estimate the interface thickness. The experimental data of various oxide-semiconductor/base-semiconductor solar cells supports our concept of low and high work function materials for p-type and n-type base-semiconductor.

The measured spectral response for an n-ITO/p-Si solar cell is in good agreement with the theory. As expected, there is no loss in the ultra-violet spectral response. We have also studied the various loss mechanisms associated with SIS solar cells. The following are the main loss mechanisms in these devices: (i) transmission-reflection loss associated with the

oxide-semiconductor layer, (ii) recombination in the surface depletion layer, (iii) lowering of open-circuit voltage and (iv) series and shunt resistance losses. Each loss mechanism was studied in detail and a possible range of efficiency loss for n-ITO/p-Si solar cells is mentioned. At the end of this chapter we have shown that simple methods based on the electrical measurements of oxide-semiconductor/base-semiconductor solar cells often leads to incorrect results about the electron affinity of oxide-semiconductors due to the uncertainty in the Fermi level position in the oxide-semiconductor and other interface parameters.

CHAPTER 6

CONCLUSION

The work presented in this thesis has been concerned with investigating the theory of metal-insulator-semiconductors (MIS) and semiconductor-insulator-semiconductor (SIS) solar cells. In both MIS and SIS solar cells, the insulator is thin (< 40 Å) and the current flow between the top layer and the base-semiconductor has been described by the quantum mechanical tunneling process. The tunneling was described using the independent electron approach of Harrison. Although this general approach can be criticized on a number of theoretical grounds [32], it is capable of explaining the experimental characteristics of tunnel MIS and SIS solar cells.

The first part of this thesis was concerned with the theory of MIS solar cells. In order to calculate the photovoltaic response of MIS tunnel diodes, the calculation program of Ref. 58 was modified to include the generation of electron-hole pairs in the continuity equations. The theory of SIS solar cells is an expansion of the MIS theory. The metal has the property of a variable band gap which can be set at any value from zero to several electron volts. The theory is valid where the top layer is an amorphous or heavily doped

(degenerate) wide-gap semiconductor. The wide gap of the top layer blocks those majority carriers which might consider band to band tunneling.

The photovoltaic response of SIS solar cells is identical to MIS solar cells, and the effect of various parameters on the performance of MIS and SIS solar cells was studied. The insulator thickness and the top layer (metal or oxide-semiconductor) work function are the most important parameters in the optimization of MIS and SIS solar cells. Below a certain thickness of the interfacial layer (10 Å in the case of M or S-SiO_x-(p-type)Si solar cells), the device behaves like a Schottky barrier or heterojunction solar cell. For p-type semiconductors, a low work function is required while for n-type high work function top layers are required. As in the case of p-n junction solar cells, low positive and negative insulator charges have beneficial effects on the performance of p-type and n-type MIS and SIS solar cells, respectively. The surface states may have adverse or beneficial effects, depending upon their type (donor or acceptor) and the type of base-semiconductor (p-type or n-type). Since both surface states and the insulator charges are related to each other, it is desirable to keep them low during device fabrication. If the top layer work function is sufficiently low (for p-type MIS and SIS solar cells) or sufficiently high (for n-type MIS and SIS solar cells) true minority carrier non-equilibrium tunnel

MIS and SIS solar cells can be formed, whose electrical characteristics are independent of both these charges.

The main difference between Schottky barrier and MIS solar cells is that the dominant dark current is a majority carrier current in the Schottky case, whereas, it is a minority carrier current in the tunnel diode case. The introduction of the insulating layer results in a relatively "clean" insulator-semiconductor (IS) interface in the case of tunnel MIS solar cells. In the case of Schottky barrier solar cells, the interface is "grubby" and results in low photovoltaic conversion efficiency.

The theory of tunnel MIS solar cells has been compared with the available experimental data. The effect of insulator thickness on the efficiency, open-circuit voltage, short circuit current density and the fill factor has been compared. The open-circuit voltage, below a certain thickness of the insulator, shows slight departure from the theory. This has been accounted for by taking into consideration the pin-holes associated with ultra thin oxides and a composite model has been developed. This model assumes that such devices with ultra thin oxides behave partially like an MIS solar cell and partially like a Schottky barrier solar cell. Based on this model and by using the Maxwell-Garnett theory [135], we have calculated the complex dielectric constant of SiO_x as a function of its thickness. The effect of substrate resistivity is also

compared with the theory. As expected, the agreement is good. The measured dark I-V characteristics as a function of temperature not only confirm the MIS solar cell theory, but also discard any model based on the thermionic emission approach. Calculated spectral response has been compared with the experimental data for Al-SiO_x-(p-type)Si solar cells. The short wave length response is superior to a diffused p-n junction Si solar cell. All the experimental work on MIS solar cells supports our concept of the importance of a low and high work function in the selection of a metal.

The last part of this thesis is concerned with the comparison of SIS solar cell theory with available experimental data. This includes the temperature dependence of the dark and light I-V characteristics, intensity effect, insulator thickness effect and the spectral response of the n-ITO/p-Si solar cells. In all cases, an excellent agreement between theory and experiment is observed. The experimental data on the oxide-semiconductor/base-semiconductor solar cells supports our concept of low and high work function materials for p-type and n-type base-semiconductors. Various loss mechanisms associated with SIS solar cells are also discussed. In the end of this chapter we have shown that simple methods based on the electrical measurements of oxide-semiconductor/base-semiconductor solar cells often lead to incorrect results about the electron affinity of oxide-semiconductors.

The major contributions of this thesis are threefold. Firstly, we have presented the theory of single-crystal MIS solar cells. The optimum parameters have been used in the fabrication of MIS solar cells. Experimental results as high as 15% [25] have been obtained and in the near future they will reach the theoretical limit. The second contribution of this thesis is the presentation of the operational mechanism of a relatively new class of devices, namely semiconductor-insulator-semiconductor (SIS) solar cells. The model is able to explain that in spite of mismatch of crystal structure, lattice constant and coefficient of linear expansion, certain oxide-semiconductor/base-semiconductor solar cells yield efficient photovoltaic devices while others do not. The third contribution is that this work can be extended further to develop the theory of polycrystal and amorphous MIS and SIS solar cells. In the case of polycrystalline devices, as a first order we can assume that the lifetime of minority carriers will be reduced. Some physical mechanism relating the grain size to the minority carrier lifetime can do the job [144]. In the case of amorphous devices, Harrison's tunneling approach has to be replaced by some other form, which will depend on the density of states in amorphous semiconductors. Experimental work on amorphous MIS solar cells [145] supports the major features of our theory. Thus, it is fair to conclude that this thesis will contribute greatly towards the fabrication of low-cost solar cells for terrestrial applications.

APPENDIX A

EFFECT OF SERIES RESISTANCE ON THE SOLAR CELL PERFORMANCE

In this appendix, the effect of series resistance on the short-circuit density and fill factor of solar cells will be discussed. Although, in order to understand the effect of various components of series resistance, a two dimensional analysis is required. However, in the most usual formulation the series resistance, R_s, may be treated in series with the load and in a classical sense results in a power loss I^2R_s when a current I is drawn from the cell. Neglecting the effect of shunt resistance, the I-V characteristics of a solar cell can be described semi-empirically by the following relation:

$$I = I_0[\exp \frac{(V-IR_s)}{V_{th}} - 1] - I_L . \qquad \text{(A1)}$$

Substituting, V = 0, we get $I = I_{sc}$ from the above relation.

$$I_{sc} + I_0 + I_L = I_0[\exp(- \frac{I_{sc}R_s}{V_{th}})] . \qquad \text{(A2)}$$

The solution of the above transcendental equation can be used to see the effect of series resistance on the short-circuit current of solar cells. In Figure A1, we have plotted short-circuit current density as a function of solar cell area with

Figure A1

Calculated effect of series resistance on the short-circuit current density of a solar cell.

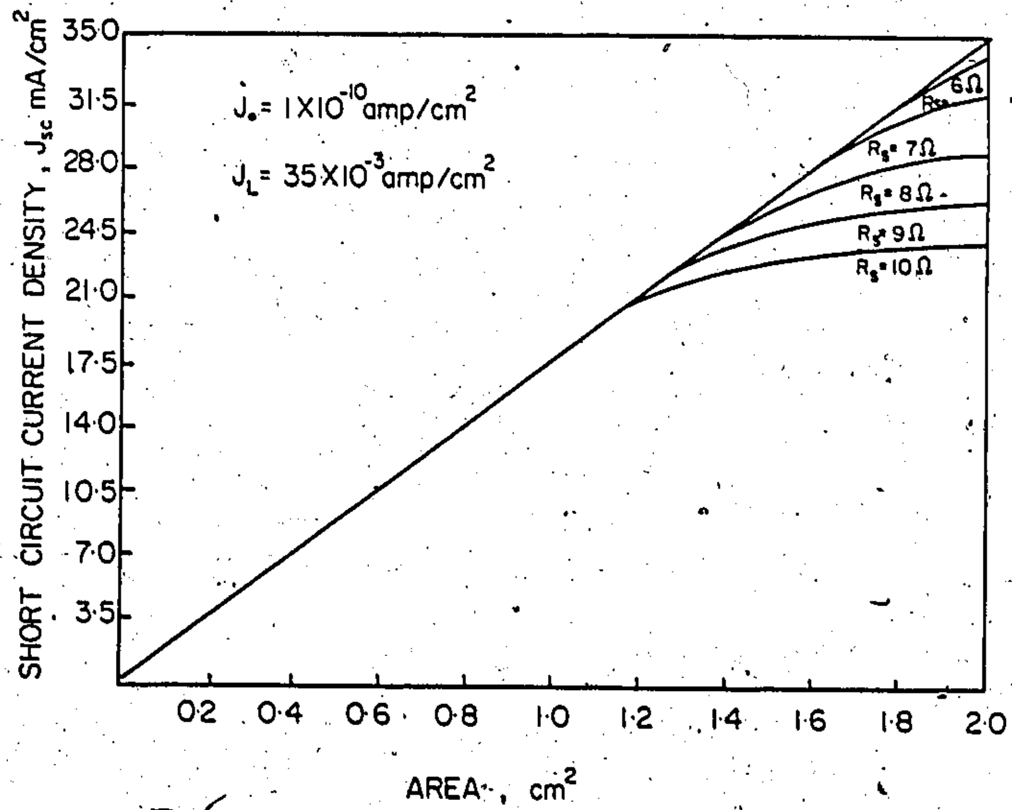

SHORT CIRCUIT CURRENT DENSITY, J_{sc} mA/cm²
J_o = 1X10⁻¹⁰ amp/cm²
J_L = 35X10⁻³ amp/cm²
35·0
31·5
28·0
24·5
21·0
17·5
14·0
10·5
7·0
3·5
0·2
0·4
0·6
0·8
1·0
1·2
1·4
1·6
1·8
2·0
AREA, cm²
R_s= 6Ω
R_s= 7Ω
R_s= 8Ω
R_s= 9Ω
R_s= 10Ω

series resistance as the variable parameter. For the particular set of parameters taken in Figure A1, it can be seen that up to about a 1 cm^2 area device, a series resistance of about 10 Ω has no effect in reducing the value of J_{sc} from its ideal value of J_L. For large area devices or for higher values of series resistance, the value of J_{sc} will be reduced. These calculations are consistent with the experimental observation of Si p-n junction solar cells [34(d)].

A simple way of calculating the effect of series resistance on the fill factor of a solar cell is given in reference 146. The following expression was used to calculate the fill factor

$$FF = \frac{IV}{I_{sc}V_{oc}} = \frac{I}{I_{sc}} \{(1 - \frac{I}{I_{sc}} \frac{I_{sc}R_s}{V_{oc}}) + \frac{V_{th}}{V_{oc}} \times \ell n[1 - \frac{I}{I_{sc}} (1 - \exp(\frac{V_{oc}}{V_{th}} (\frac{I_{sc}R_s}{V_{oc}} - 1)))]\} . \quad (A3)$$

The ratio I/I_{sc} was varied to find the maximum value of the quantity on the left hand side and is equal to the fill factor. The effect of series resistance on the fill factor of a solar cell has been recently commented on by a number of workers [146-147]. However, no authors have reported the effect of the solar cell area on the device fill factor, with series resistance as the variable parameter. We have mentioned this effect in section 4.2.1 of the text. In the context of MIS and SIS solar cells,

we have calculated the effect of series resistance on a 1 cm^2 area device and these results are shown in Figure A2. These simple calculations demonstrate the necessity of reducing the series resistance to a very low value to obtain high efficiency devices, even for a 1 cm^2 area device.

Figure A2

Effect of series resistance on the fill factor and efficiency of optimized MIS and SIS solar cells.

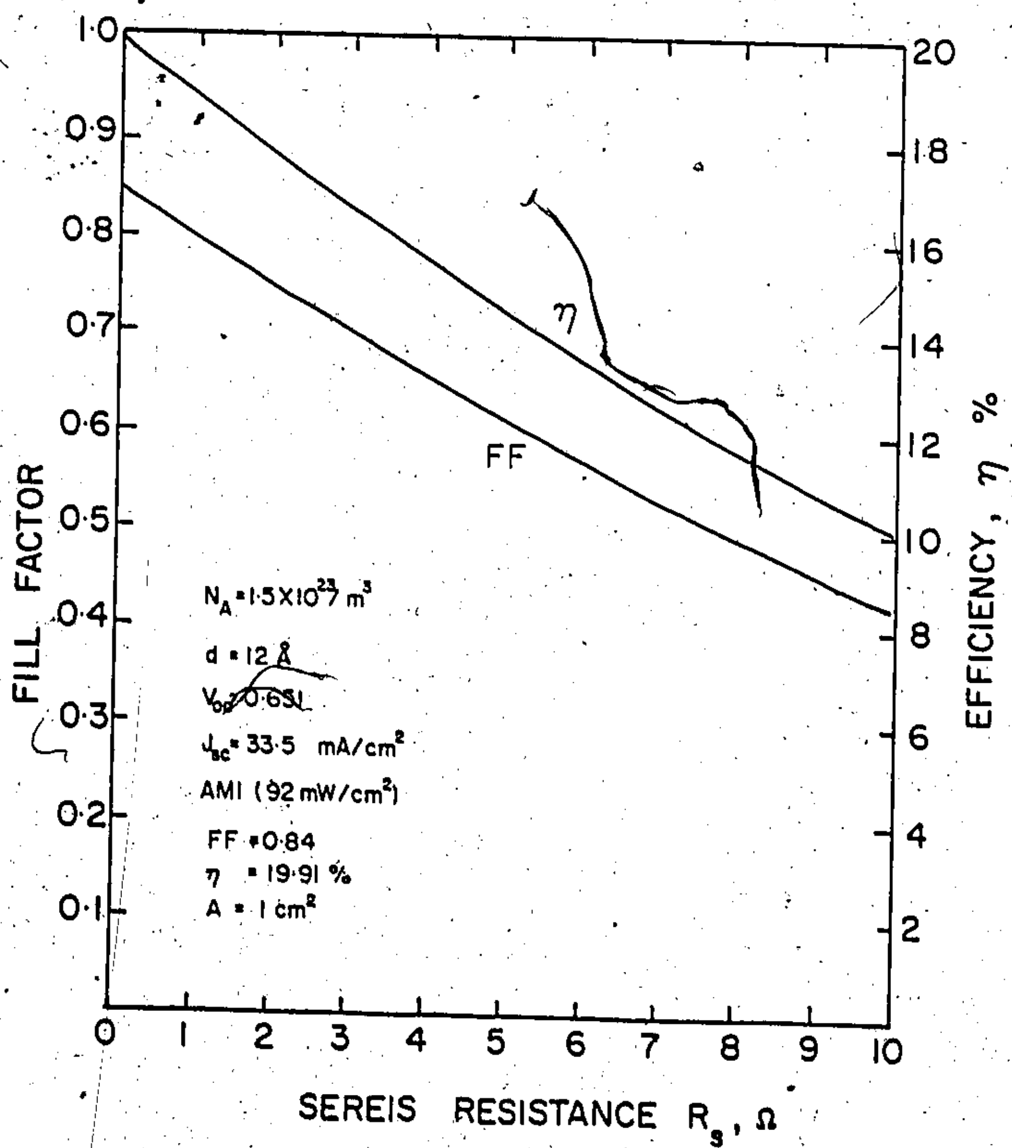

Figure A2

APPENDIX B

SILICON PARAMETERS AND SOLAR SPECTRUMS USED IN THE CALCULATIONS

(1) MODELLING OF SILICON PARAMETERS

(a) Doping Density Variations

The electron lifetime (for p-type silicon) used in our calculations is based on the following empirical relation given by Fossum [68]

$$\tau_n = \frac{\tau_{no}}{1 + \frac{N_A}{N_{OA}}} \tag{B1}$$

where $\tau_{no} = 3.95\times10^{-4}$ sec. and $N_{OA} = 7.1\times10^{21}\ m^{-3}$.

At 300°K, the electron and hole mobilities for various doping densities are given by the following analytical expression [148]

$$\mu = \mu_{min} + \frac{\mu_{max} - \mu_{min}}{1 + (\frac{N}{N_{OB}})^{\alpha}} . \tag{B2}$$

Here N is the doping density (N_A or N_D) and the value of other parameters is given in Table B1.

(b) Temperature Variations

In general, at any temperature, the drift mobilities (for holes or electrons) can be obtained by combining the lattice and impurity mobilities according to the relation [149]

$$\mu = \mu_L[1 + M^2\{CiM \times \cos M + SiM \times \sin M - \frac{\pi}{2} \sin M\}] , \tag{B3}$$

TABLE B1

PARAMETERS USED IN THE CALCULATION OF Si MOBILITY

	Electron	Holes	Units
μmin	9.2×10^{-3}	4.77×10^{-3}	$m^2v^{-1}sec^{-1}$
μmax	0.136	0.0495	$m^2v^{-1}sec^{-1}$
N_{OB}	1.3×10^{23}	6.3×10^{22}	m^{-3}
α	0.91	0.76	

where $M^2 = 6\mu_L/\mu_I$; Ci and Si are the integral cosine and sine respectively.

The lattice mobilities are taken from reference [148] and given by

$$\mu_{nL} = 1.43\times10^5\ T^{-2.42}\ m^2\ v^{-1}\ sec^{-1}\ , \qquad (B4)$$

and

$$\mu_{pL} = 1.35\times10^4\ T^{-2.20}\ m^2\ v^{-1}\ sec^{-1}\ . \qquad (B5)$$

The impurity mobilities are calculated by using the following relation [149]

$$\mu_I = \frac{64\sqrt{\pi}\ \varepsilon_s^2 (2kT)^{3/2}}{N_I q^3 m_{eff}^{1/2} \ln[1 + (\frac{12\pi\varepsilon_s kT}{q^2 N_I^{1/3}})^2]}\ , \qquad (B6)$$

where N_I is the ionized impurity density and ε_s is the permittivity.

We have assumed a constant diffusion length in the temperature range of 200-425°K. This approximation is very close to the real situation in good quality silicon solar cells [34(e)]. Carrier mobilities were calculated at various temperatures and the lifetimes adjusted so that at all temperatures we have constant values of diffusion length (L_n = 177.76 μm for $N_A = 1.5\times10^{23}\ m^{-3}$ L_n = 810.29 μm for $N_A = 7\times10^{21}\ m^{-3}$).

Also, we have assumed a constant absorption coefficient in this temperature study. This has negligible effect on the generation rate in the temperature range considered here.

The variation of energy band gap of silicon with temperature is given by [150]

$$E_g(T) = E_g(0) - AT^2/(T + B),$$

$E_g(0) = 1.1557$ eV, $A = 7.021\times10^{-4}$ eV/°K, and $B = 1108$°K.

The intrinsic carrier concentration at any temperature is given by [151]

$$n_i = 3.873\times10^{22}\ T^{3/2}\ \exp(-.605/kT),$$

which gives

$$n_i = 1.44\times10^{16}\ m^{-3} \text{ at } T = 300°K.$$

(ii) Data for AM0, AM1 and AM2 Solar Spectrums:

Although we have done all the calculations for AM1 and AM2 solar spectrums, we have listed phonon density in the interval of 0.005 μm for the three most commonly used air masses, AM0, AM1 and AM2. These data were taken from references 63 and 151 and are listed in Table B2. The solar constant for AM0, AM1 and AM2 are 135.3 mw cm^{-2}, 92.4553 mw cm^{-2} and 74.9054 mw cm^{-2} respectively. The data in references 63 and 151 are given for solar spectral irradiance in a non-uniform interval. The data of Table B2 were generated by the method of linear interpolation and the following relation between solar irradiance E, and number of photons N, was used

$$N = \frac{E\lambda d\lambda}{hc}.$$

TABLE B2

AM0, AM1 AND AM2 SPECTRAL DISTRIBUTION

Wavelength μm	Number of Photons per sec per m^2		
	AM0	AM1	AM2
.295	3.924E+18	0.	0.
.300	4.111E+18	1.498E+16	0.
.305	4.252E+18	5.711E+16	0.
.310	5.000E+18	1.625E+17	3.870E+15
.315	5.714E+18	4.365E+17	3.540E+16
.320	6.369E+18	1.131E+18	2.318E+17
.325	7.326E+18	1.924E+18	5.073E+17
.330	8.383E+18	2.494E+18	7.419E+17
.335	8.955E+18	3.017E+18	1.017E+18
.340	9.153E+18	3.496E+18	1.338E+18
.345	9.237E+18	3.841E+18	1.595E+18
.350	9.455E+18	4.120E+18	1.793E+18
.355	9.653E+18	4.401E+18	2.010E+18
.360	9.678E+18	4.621E+18	2.209E+18
.365	1.034E+19	4.986E+18	2.477E+18
.370	1.070E+19	5.485E+18	2.812E+18
.375	1.036E+19	5.794E+18	3.066E+18
.380	1.082E+19	5.896E+18	3.221E+18
.385	1.068E+19	5.984E+18	3.359E+18
.390	1.071E+19	6.150E+18	3.531E+18
.395	1.130E+19	6.644E+18	3.912E+18
.400	1.310E+19	7.894E+18	4.757E+18
.405	1.557E+19	9.569E+18	5.976E+18
.410	1.741E+19	1.087E+19	6.785E+18
.415	1.830E+19	1.161E+19	7.361E+18
.420	1.850E+19	1.192E+19	7.682E+18
.425	1.829E+19	1.197E+19	7.838E+18
.430	1.793E+19	1.192E+19	7.930E+18
.435	1.797E+19	1.215E+19	8.206E+18
.440	1.912E+19	1.313E+19	9.019E+18

(continued next page)

.445	2.078E+19	1.450E+19	1.011E+19
.450	2.212E+19	1.567E+19	1.110E+19
.455	2.314E+19	1.659E+19	1.189E+19
.460	2.374E+19	1.716E+19	1.241E+19
.465	2.395E+19	1.746E+19	1.272E+19
.470	2.401E+19	1.764E+19	1.297E+19
.475	2.424E+19	1.796E+19	1.331E+19
.480	2.475E+19	1.849E+19	1.381E+19
.485	2.459E+19	1.852E+19	1.395E+19
.490	2.409E+19	1.828E+19	1.388E+19
.495	2.423E+19	1.854E+19	1.419E+19
.500	2.443E+19	1.885E+19	1.434E+19
.505	2.442E+19	1.895E+19	1.471E+19
.510	2.428E+19	1.892E+19	1.474E+19
.515	2.396E+19	1.875E+19	1.467E+19
.520	2.388E+19	1.876E+19	1.474E+19
.525	2.423E+19	1.911E+19	1.507E+19
.530	2.452E+19	1.941E+19	1.537E+19
.535	2.453E+19	1.949E+19	1.549E+19
.540	2.436E+19	1.944E+19	1.551E+19
.545	2.415E+19	1.935E+19	1.550E+19
.550	2.397E+19	1.928E+19	1.550E+19
.555	2.395E+19	1.932E+19	1.559E+19
.560	2.396E+19	1.938E+19	1.567E+19
.565	2.407E+19	1.952E+19	1.582E+19
.570	2.440E+19	1.983E+19	1.613E+19
.575	2.472E+19	2.014E+19	1.641E+19
.580	2.496E+19	2.038E+19	1.665E+19
.585	2.512E+19	2.056E+19	1.694E+19
.590	2.523E+19	2.070E+19	1.699E+19

(continued next page)

.595	2.522E+19	2.074E+19	1.707E+19
.600	2.518E+19	2.075E+19	1.711E+19
.605	2.512E+19	2.079E+19	1.724E+19
.610	2.509E+19	2.088E+19	1.736E+19
.615	2.508E+19	2.097E+19	1.753E+19
.620	2.503E+19	2.104E+19	1.767E+19
.625	2.498E+19	2.110E+19	1.782E+19
.630	2.492E+19	2.116E+19	1.796E+19
.635	2.489E+19	2.124E+19	1.812E+19
.640	2.488E+19	2.134E+19	1.829E+19
.645	2.484E+19	2.141E+19	1.845E+19
.650	2.476E+19	2.145E+19	1.858E+19
.655	2.471E+19	2.149E+19	1.871E+19
.660	2.470E+19	2.155E+19	1.882E+19
.665	2.465E+19	2.159E+19	1.891E+19
.670	2.459E+19	2.160E+19	1.897E+19
.675	2.452E+19	2.161E+19	1.904E+19
.680	2.446E+19	2.163E+19	1.912E+19
.685	2.441E+19	2.165E+19	1.920E+19
.690	2.437E+19	2.169E+19	1.936E+19
.695	2.429E+19	2.077E+19	1.823E+19
.700	2.418E+19	2.073E+19	1.925E+19
.705	2.410E+19	2.163E+19	1.943E+19
.710	2.405E+19	2.163E+19	1.945E+19
.715	2.397E+19	2.159E+19	1.945E+19
.720	2.387E+19	2.153E+19	1.942E+19
.725	2.379E+19	2.076E+19	1.850E+19
.730	2.373E+19	2.075E+19	1.851E+19
.735	2.365E+19	2.144E+19	1.942E+19
.740	2.353E+19	2.137E+19	1.939E+19
.745	2.343E+19	2.131E+19	1.937E+19

(continued next page)

.750	2.335E+19	2.137E+19	1.937E+19
.755	2.327E+19	2.017E+19	1.799E+19
.760	2.318E+19	1.797E+19	1.519E+19
.765	2.309E+19	1.790E+19	1.515E+19
.770	2.299E+19	2.001E+19	1.792E+19
.775	2.289E+19	2.103E+19	1.931E+19
.780	2.279E+19	2.096E+19	1.928E+19
.785	2.269E+19	2.090E+19	1.924E+19
.790	2.258E+19	2.083E+19	1.921E+19
.795	2.246E+19	2.077E+19	1.917E+19
.800	2.235E+19	2.070E+19	1.914E+19
.805	2.224E+19	1.977E+19	1.801E+19
.810	2.214E+19	1.905E+19	1.712E+19
.815	2.204E+19	1.939E+19	1.760E+19
.820	2.193E+19	1.973E+19	1.808E+19
.825	2.182E+19	2.007E+19	1.857E+19
.830	2.171E+19	2.019E+19	1.879E+19
.835	2.159E+19	2.011E+19	1.872E+19
.840	2.147E+19	1.804E+19	1.63[illegible]E+19
.845	2.135E+19	1.393E+19	1.152E+19
.850	2.122E+19	1.180E+19	9.022E+18
.855	2.111E+19	1.157E+19	8.553E+18
.860	2.102E+19	1.154E+19	8.681E+18
.865	2.093E+19	1.121E+19	8.331E+18
.870	2.083E+19	1.067E+19	7.801E+18
.875	2.073E+19	1.038E+19	7.511E+18
.880	2.063E+19	1.038E+19	7.527E+18
.885	2.052E+19	1.043E+19	7.606E+18
.890	2.042E+19	1.048E+19	7.684E+18
.895	2.031E+19	1.055E+19	7.764E+18

(continued next page)

.900	2.020E+19	1.051E+19	7.943E+18
.905	2.013E+19	1.072E+19	7.973E+18
.910	2.012E+19	1.088E+19	8.149E+18
.915	2.011E+19	1.104E+19	8.320E+18
.920	2.009E+19	1.005E+19	7.361E+18
.925	2.008E+19	7.869E+18	5.253E+18
.930	2.006E+19	6.117E+18	3.630E+18
.935	2.004E+19	6.009E+18	3.562E+18
.940	2.002E+19	7.174E+18	4.560E+18
.945	2.000E+19	7.674E+18	4.398E+18
.950	1.998E+19	7.500E+18	4.835E+18
.955	1.991E+19	7.744E+18	5.071E+18
.960	1.990E+19	8.242E+18	5.555E+18
.965	1.969E+19	8.576E+18	5.899E+18
.970	1.958E+19	1.025E+19	7.750E+18
.975	1.946E+19	1.327E+19	1.113E+19
.980	1.934E+19	1.463E+19	1.265E+19
.985	1.922E+19	1.430E+19	1.227E+19
.990	1.910E+19	1.431E+19	1.225E+19
.995	1.897E+19	1.457E+19	1.269E+19
1.000	1.884E+19	1.[illegible]3E+19	1.311E+19
1.005	1.873E+19	1.540E+19	1.353E+19
1.010	1.862E+19	1.577E+19	1.396E+19
1.015	1.852E+19	1.614E+19	1.439E+19
1.020	1.842E+19	1.627E+19	1.453E+19
1.025	1.831E+19	1.615E+19	1.440E+19
1.030	1.820E+19	1.603E+19	1.426E+19
1.035	1.809E+19	1.591E+19	1.412E+19
1.040	1.797E+19	1.578E+19	1.398E+19
1.045	1.786E+19	1.566E+19	1.384E+19
1.050	1.774E+19	1.553E+19	1.369E+19

(continued next page)

1.055	1.762E+19	1.540E+19	1.355E+19
1.060	1.750E+19	1.527E+19	1.340E+19
1.065	1.738E+19	1.514E+19	1.325E+19
1.070	1.725E+19	1.500E+19	1.309E+19
1.075	1.712E+19	1.486E+19	1.294E+19
1.080	1.700E+19	1.473E+19	1.278E+19
1.085	1.686E+19	1.443E+19	1.257E+19
1.090	1.673E+19	1.396E+19	1.230E+19
1.095	1.660E+19	1.399E+19	1.238E+19
1.100	1.646E+19	1.441E+19	1.301E+19
1.105	1.635E+19	1.365E+19	1.246E+19
1.110	1.628E+19	1.179E+19	1.049E+19
1.115	1.620E+19	9.918E+18	8.497E+18
1.120	1.612E+19	8.028E+18	6.490E+18
1.125	1.604E+19	6.121E+18	4.464E+18
1.130	1.596E+19	4.898E+18	3.113E+18
1.135	1.587E+19	4.512E+18	2.657E+18
1.140	1.579E+19	4.769E+18	2.389E+18
1.145	1.570E+19	5.186E+18	3.225E+18
1.150	1.562E+19	5.752E+18	3.772E+18
1.155	1.553E+19	6.813E+18	4.798E+18
1.160	1.544E+19	7.882E+18	5.833E+18
1.165	1.535E+19	8.951E+18	6.378E+18
1.170	1.525E+19	1.005E+19	7.931E+18
1.175	1.516E+19	1.115E+19	8.992E+18
1.180	1.507E+19	1.185E+19	9.726E+18
1.185	1.497E+19	1.216E+19	1.013E+19
1.190	1.487E+19	1.263E+19	1.099E+19
1.195	1.477E+19	1.291E+19	1.162E+19
1.200	1.467E+19	1.285E+19	1.153E+19

(continued next page)

1.205	1.458E+19	1.280E+19	1.145E+19
1.210	1.451E+19	1.274E+19	1.136E+19
1.215	1.444E+19	1.269E+19	1.127E+19
1.220	1.436E+19	1.263E+19	1.119E+19
1.225	1.428E+19	1.262E+19	1.119E+19
1.230	1.421E+19	1.265E+19	1.130E+19
1.235	1.413E+19	1.267E+19	1.141E+19
1.240	1.405E+19	1.254E+19	1.131E+19
1.245	1.397E+19	1.225E+19	1.101E+19
1.250	1.389E+19	1.195E+19	1.071E+19
1.255	1.380E+19	1.165E+19	1.041E+19
1.260	1.372E+19	1.134E+19	1.010E+19
1.265	1.363E+19	1.124E+19	1.004E+19
1.270	1.355E+19	1.134E+19	1.022E+19
1.275	1.346E+19	1.143E+19	1.041E+19
1.280	1.337E+19	1.153E+19	1.049E+19
1.285	1.328E+19	1.165E+19	1.046E+19
1.290	1.319E+19	1.158E+19	1.029E+19
1.295	1.310E+19	1.134E+19	9.926E+18
1.300	1.300E+19	1.110E+19	9.553E+18
1.305	1.293E+19	1.086E+19	9.176E+18
1.310	1.288E+19	1.061E+19	8.799E+18
1.315	1.283E+19	1.011E+19	8.261E+18
1.320	1.278E+19	9.362E+18	7.561E+18
1.325	1.273E+19	8.605E+18	6.857E+18
1.330	1.268E+19	7.842E+18	6.148E+18
1.335	1.263E+19	7.073E+18	5.433E+18
1.340	1.257E+19	6.368E+18	4.826E+18
1.345	1.252E+19	5.726E+18	4.327E+18
1.350	1.246E+19	5.079E+18	3.824E+18
1.355	1.241E+19	4.427E+18	3.317E+18

(continued next page)

1.360	1.235E+19	3.771E+18	2.807E+18
1.365	1.229E+19	3.109E+18	2.293E+18
1.370	1.224E+19	2.442E+18	1.774E+18
1.375	1.218E+19	1.770E+18	1.252E+18
1.380	1.212E+19	1.096E+18	7.246E+17
1.385	1.206E+19	7.986E+17	4.733E+17
1.390	1.200E+19	8.818E+17	5.012E+17
1.395	1.193E+19	9.656E+17	5.292E+17
1.400	1.187E+19	1.052E+18	5.575E+17
1.405	1.182E+19	1.138E+18	5.860E+17
1.410	1.177E+19	1.224E+18	6.147E+17
1.415	1.173E+19	1.312E+18	6.435E+17
1.420	1.168E+19	1.400E+18	6.725E+17
1.425	1.164E+19	1.488E+18	7.019E+17
1.430	1.159E+19	1.577E+18	7.312E+17
1.435	1.154E+19	1.772E+18	8.509E+17
1.440	1.149E+19	2.071E+18	1.064E+18
1.445	1.144E+19	2.375E+18	1.278E+18
1.450	1.139E+19	2.680E+18	1.494E+18
1.455	1.134E+19	2.985E+18	1.711E+18
1.460	1.129E+19	3.118E+18	1.503E+18
1.465	1.124E+19	3.079E+18	1.769E+18
1.470	1.119E+19	3.040E+18	1.734E+18
1.475	1.114E+19	3.239E+18	1.957E+18
1.480	1.108E+19	3.682E+18	2.438E+18
1.485	1.103E+19	4.127E+18	2.922E+18
1.490	1.098E+19	4.577E+18	3.409E+18
1.495	1.092E+19	5.030E+18	3.899E+18
1.500	1.086E+19	5.484E+18	4.393E+18
1.505	1.081E+19	5.943E+18	4.690E+18

APPENDIX C

EXPRESSIONS FOR THE OPEN-CIRCUIT VOLTAGE OF A COMBINED MODEL OF THE SCHOTTKY BARRIER AND MIS SOLAR CELLS

In this appendix, an expression will be derived for the open-circuit voltage of a combined model of Schottky barrier and MIS solar cells. As mentioned in Chapter 4, we have neglected the series and shunt resistance effects and the diode ideality factors are the same for both cases. The device characteristics may be obtained by using a lumped diode model approximation. With these assumptions, the I-V characteristics for a parallel combination of a Schottky and MIS diode can be expressed as:

$$I^{total} = I_o^M(\exp \frac{qv}{nkT} - 1) + I_o^S(\text{ext} \frac{qv}{nkT} - 1) - (A^M + A^S)J_L$$

$$= (I_o^M + I_o^S)(\exp \frac{qv}{nkT} - 1) - I_L \ . \qquad (C1)$$

Here A^M and A^S are the effective areas of the "MIS" and "Schottky" parts of the device. Substituting I=0 in the above relation, the total open-circuit voltage of the device is given by

$$V_{oc}^{total} = \frac{nkT}{q} \ln[\frac{I_L}{I_o^M + I_o^S} + 1] \ . \qquad (C2)$$

We can express I_o^M and I_o^S in terms of V_{oc}^M and V_{oc}^S. Let

us assume that if the fractional area of pin holes is x, then out of a total light generated current I_L, (xI_L) would be due to pin holes and $(1-x)I_L$ due to MIS parts. Since we are treating each pin hole area as a "Schottky" device, the currents for Schottky and MIS parts are given by

$$I_o^S = \frac{xI_L}{(\exp \frac{q\, V_{oc}^S}{nkT} - 1)} \tag{C3}$$

$$I_o^M = \frac{(1-x)I_L}{(\exp \frac{q\, V_{oc}^M}{nkT} - 1)} , \tag{C4}$$

As we have assumed pin hole density $\rho \sim \exp-(\frac{d}{2do})^2 + \rho_o$, thus combining Equations (C2), (C3) and (C4) we get

$$V_{oc}^{total} = \frac{nKT}{q} \ln \left[\frac{1}{\frac{\{\exp-(\frac{d}{2do})^2 + \rho_o\}}{\{\exp \frac{q\, V_{oc}^S}{nkT} - 1\}} + \frac{\{1-\exp-(\frac{d}{2d0})^2 - \rho_o\}}{\{\exp \frac{qV_{oc}^M}{nkT} - 1\}}} + 1 \right]. \tag{C5}$$

Here V_{oc}^M varies with oxide thickness as

$$V_{oc}^M(d) = V_{oc}^M(o) - \alpha d \tag{C6}$$

where α is a parameter depending on the interface properties and base material. A more general form of equation (C5) is

$$V_{oc}^{total}(d) = \frac{nkT}{q} \ln \left[\frac{1}{\sum_i \frac{\rho_i}{\exp \frac{qV_{oc}^i}{nkT} - 1}} + 1 \right]$$

$$= \frac{nkT}{q} \ln \left[\frac{1}{\int_0^d \frac{\rho(t)dt}{\exp \frac{qV_{oc}(t)}{nkT} - 1}} + 1 \right] . \quad \text{(C7)}$$

Here $\rho(t)$ is the distribution function for finding the oxide thickness, d.

REFERENCES

1. R. Singh and J. Shewchun, J. Vac. Sci. Technol. 14, 89 (1977).

2. J. Shewchun, M. A. Green and F. D. King, Solid State Electron. 17, 563 (1974).

3. R. J. Stirn and Y.C.M. Yeh, Appl. Phys. Lett. 27, 95 (1975).

4. W.A. Anderson, S.M. Vernon, A.E. Delahoy, K.K. Ng, P. Mathe and T. Poon, International Electron Devices, 1975 Meeting, Washington, D.C., p. 217 (1975).

5. J. Shewchun, R. Singh and M.A. Green, J. Appl. Phys. 48, 765 (1977).

6. J.B. Dubow, D.E. Burk and J.R. Sites, Appl. Phys. Lett. 29, 494 (1976).

7. S. Franz, G. Kent and R.L. Anderson, Journal of Electronics Material 6, 107 (1977).

8. A.K. Ghosh, C. Fishman and T. Feng, J. Electrochem. Soc. 124, 317C (1977).

9. K.S. Sree Harsha, K.J. Bachmann, P.H. Schmidt, E. G. Spencer and F.A. Thiel, Appl. Phys. Lett. 30, 645 (1977).

10. J. Shewchun, J.B. Dubow, A. Myszkowski and R. Singh, J. Appl. Phys. 49, 855 (1978).

11. M.A. Green and J. Shewchun, Solid State Electron. 17, 941 (1974).

12. W.G. Thompson and R.L. Anderson, Solid State Electron. 21, 603 (1978).

13. R. Singh and J. Shewchun, Appl. Phys. Lett. 33, 601 (1978).

14. W. Shockley, Bell Syst. Tech. J., 28, 435 (1949).

15. J.J. Loferski, J. Appl. Phys. 27, 777 (1956).

16. D.L. Pulfrey and R.F. McOuat, Appl. Phys. Lett. 24, 167 (1974).

17. W. A. Anderso and A.E. Delahoy, Proc. IEEE, 60, 1457 (1972).

18. S. Shevenock, S. Fonash, and J. Geneczko, Proc. International Electron Devices Meeting, Washington, D.C., p.211, 1975.

19. D.R. Lillington and W.G. Townsend, Appl. Phys. Lett. 28, 97 (1976).

20. H. Matsunami, S. Matsumoto, and T. Tanaka, Japan, J. Appl. Phys. 16, 1491 (1977).

21. R. Singh and J. Shewchun, Appl. Phys. Lett. 28, 512 (1976).

22. S. Fonash, J. Appl. Phys. 47, 3597 (1976).

23. H.C. Card, Solid State Electron. 20, 971 (1977).

24. S. Kar, J. Appl. Phys. 49, 5278 (1978).

25. R.B. Godfrey and M.A. Green, Appl. Phys. Lett. 33, 637 (1978).

26. J. Shewchun, R. Singh, D. Burk and A. Kazandjian, "Temperature Dependence of the Current-Voltage Characteristics of Silicon MIS Solar Cells", submitted for publication in Appl. Phys. Lett.

27. S.M. Sze, 'Physics of Semiconductor Devices', Wiley, New York (1969).
(a) Ibid. p. 65; (b) Ibid. p. 378; (c) Ibid. p. 469.
(d) Ibid. p. 436; (e) Ibid. p. 432.

28. (a) W. Shockley and W.T. Read, Phys. Rev. 87, 835 (1952).
(b) R.N. Hall, Phys. Rev. 87, 387 (1952).

29. P. Schnupp, Phys. Stat. Sol. 25, 455 (1968).

30. W.A. Harrison, Phys. Rev. 123, 85 (1961).

31. G.D. Mahan, Many Body Theory of Tunneling, 'Tunneling Phenomena in Solids', edited by E. Burstein and S. Lundquist, Plenum Press, New York, 1969, p. 305.

32. C.B. Duke, 'Tunneling Phenomena in Solids', Academic Press, New York (1969).
(a) Ibid. p. 28; (b) Ibid. p. 53.

33. A. Rothwarf and K.W. Boer, Prog. in Solid State Chem. 10, 71 (1975).

34. H.J. Hovel, 'Solar Cells' Semiconductor and Semimetals, Vol. 11, edited by R.K. Willardson and A.C. Beer, Academic Press, New York (1975).
(a) Ibid. p. 120; (b) Ibid. p. 171; (c) Ibid. p. 203;
(d) Ibid. p. 62; (e) Ibid. p. 167.

35. T. Nagatomo and O. Omoto, Japan J. Appl. Phys. 15, 199 (1976).

36. T. Mizrah and D. Adler, Appl. Phys. Lett. 29, 682 (1976).

37. T. Mizrah and D. Adler, IEEE Trans. Electron Devices ED-24 458 (1977).

38. W.G. Thompson, S.L. Franz, R.L. Anderson and O.H. Winn, IEEE Trans. Electron Devices ED-24 463 (1977).

39. T. R. Nash and R.L. Anderson, IEEE Trans. Electron Devices ED-24, 468 (1977).

40. A.K. Ghosh, C. Fishman and T. Feng, J. Appl. Phys., 49, 3490 (1978).

41. J.C. Manifacier and L. Szepessy, Appl. Phys. Lett. 31, 459 (1977).

42. E. Y. Wang and R.N. Legge, IEEE Trans. Electron Devices, ED-25, 800 (1978).

43. T. Feng, C. Fishman and A.K. Ghosh, Proc. 13th Photovoltaic Specialists Conf., IEEE, NEw York, 1978, p. 519.

44. K.J. Bachmann, W.R. Sinclair, F.A. Thiel, H. Schreiber Jr., P. H. Schmidt, E. G. Spencer, E. Buehler and K. Sreeharsha, Proc. 13th Photovoltaic Specialists Conf., IEEE, New York, 1978, p. 524.

45. H. M. Manasevit, K. L. Hess, P. D. Dapkus, R.P. Ruth, J. J. Yang, A. G. Campbell, R.E. Johnston, L. A. Moudy, R. H. Bube, L. B. Fabick, A. L. Fahrenbruch and M. J. Tsai, Proc. 13th Photovoltaic Specialists Conf., IEEE, New York, 1978, p. 165.

46. E. Y. Want and R. N. Legge, Proc. 12th Photoboltaic Specialists Conf., IEEE, New York, 1976, p. 967.

47. L. Hsu and E. Y. Yang, Proc. 13th Photvoltaic Specialists Conf., IEEE, New York, 1978, p. 536.

48. A.L. Fahrenbruch, J. Aranovich, F. Courreges, T. Chynoweth, and R.H. Bube, Proc. 13th Photovoltaic Specialists Conf., IEEE, New York, 1978, p. 281.

49. L.L. Kazmerski and P. Sheldon, Proc. 13th Photovoltaic Specialists Conf., IEEE, New York, 1978, p. 541.

50. J. Shewchun, R. Singh, D. Burk, M. Spitzer, J. Loferski and J. Dubow, Proc. 13th Photovoltaic Specialists Conf., IEEE, New York, 1978, p. 528.

51. J. DuBow, J. Shewchun, C.W. Wilmsen, R. Singh, D. Burk and J.F. Wager, "The Operation of Semiconductor-Insulator-Semiconductor (SIS) Solar Cells: Experiment", Accepted for publication in J. App. Phys.

52. M.A. Green and J. Shewchun, Solid State Electron. 17, 349 (1974).

53. V. Heine, Phys. Rev. 138, A1689 (1965).

54. B. Pellegrini, Solid St. Electron. 17, 217 (1974).

55. W.E. Dahlke and S.M. Sze, Solid St. Electron. 10, 865 (1967).

56. H. C. Card and E. H. Rhoderick, J. Phys. D.: Appl. Phys. 4, 1589 (1971).

57. S. Kar and W. E. Dahlke, Solid State Electron. 15, 221 (1972); 15, 869 (1972).

58. M.A. Green, F.D. King and J. Shewchun, Solid State Electron. 17, 551 (1974).

59. R.A. Clarke and J. Shewchun, Solid State Electron. 14, 957 (1971).

60. V.A.K. Temple, M.A. Green and J. Shewchun, J. Appl. Phys. 45, 4934 (1974).

61. H.K. Gummel, IEEE Trans. Electron Devices ED-11, 355 (1964).

62. L.B. Freeman and W. E. Dahlke, Solid State Electron 13, 1483 (1970).

63. (a) H. Brandhorst, J. Mickey, H. Curtis and E. Ralph, NASA TM X-71771 (1975).

(b) H. Curtis, NASA-Lewis, private communication; 1977.

64. M.P. Godlewski, H.W. Brandhorst Jr. and C.R. Baraona, Proc. 11th Photovoltaic Specialists Conf. IEEE, New York, 1975, p. 32.

65. M. Wolf, Proc. IRE 48, 1246 (1960).

66. N. Chang, M.Sc. Thesis, Colorado State University (1977).

67. K. Rajkanan and J. Shewchun, "A Better Approach to the Evaluation of the Series Resistance of Solar Cells and Area Dependence of Performance Characteristics", Accepted for publication in Solid St. Electron.

68. J. G. Fossum, Solid State Electron. 19, 269 (1976).

69. R. Singh and J. Shewchun, Proc. of the International Symposium on Solar Energy, Electrochemical Society Meeting, Washington, D.C., 1976, p. 290.

70. C. T. Sah, IRE Trans. on Electron Devices, ED-9, 91 (1962).

71. K. Weiser, Prog. Solid State Chem. 11, 403 (1976).

72. R. Singh and J. Shewchun, J. Appl. Phys. 49, 4588 (1978).

73. C. W. Wilmsen, Thin Solid Films, 39, 105 (1976).

74. C. W. Wilmsen and R. W. Kee, J. Vac. Sci. Technol. 14, 953 (1977).

75. B. O. Seraphin and H. E. Bennett, Optical Properties of III-V Compounds Semiconductors and Semimetals, Vol. 3, R. K. Willardson and A. C. Beer, Eds., New York, Academic Press, (1967).
(a) Ibid. p. 529; (b) Ibid. p. 518.

76. O. Madelung, Physics of III-V Compounds, J. Wiley and Sons, New York (1964) p. 313.

77. M. A. Matveev, G. M. Matveev and B. N. Frenkel, Electrical, Optical and Thermal Properties of Glass, Ordentlich, P. O. Box 275 Holon, Israel, 1975, p. 14.

78. E. H. Snow and B. E. Deal, J. Electrochem. Soc. 113, 263 (1966).

79. D. L. Lile and D. A. Collins, Appl. Phys. Lett. 28, 554 (1976).

80. H. H. Tippins, Phys. REv. 140, A316 (1965).

81. J. St. Pierre, M. Eng. Thesis, McMaster University (1976).

82. H. J. Hovel, J. Appl. Phys. 47, 4968 (1976).

83. D. L. Pulfrey, Solid State Electron. 20, 455 (1977).

84. J. Shewchun, R. Singh, J. St. Pierre and J. J. Loferski, Proc. National Workshop on Low Cost Polycrystalline Silicon Solar Cells, SMU, Dallas, Texas, 1976, p. 390.

85. R. B. Godfrey and M. A. Green, Appl. Phys. Lett. 31, 705 (1977).

86. J. R. Szedon, T. W. O'Keefe and T. A. Temofonote, Proc. 13th Photovoltaic Specialists Conf. IEEE, New York, 1978, p. 774.

87. E. J. Charlson and J. C. Lien, J. Appl. Phys. 46, 9 (1975).

88. A. H. Kipperman and M. H. Omar, Appl. Phys. Lett. 28, 620 (1976).

89. H. Matsumami, S. Matsumoto and T. Tanako, Proc. 12th Photovoltaic Specialists Conf., IEEE, New York, p. 917 (1976).

90. M. A. Green, R. B. Godfrey and L. W. Davies, Proc. 12th Photovoltaic Specialists Conf. IEEE, New York, 1976, p. 896.

91. P. A. Iles and S. I. Soclof, Proc. 11th Photovoltaic Specialists Conf. IEEE, New York, 1975, p. 19.

92. J. St. Pierre, R. Singh, J. Shewchun and J. J. Loferski, Proc. 12th Photovoltaic Specialists Conf. IEEE, New York, 1976, p. 897.

93. H. B. Michaelson, J. Appl. Phys. 48, 4729 (1977).

94. W. A. Anderson, A. E. Delahoy, J. K. Kim, S. H. Hylend, and S. K. Dey, Appl. Phys. Lett. 33, 588 (1978).

95. E. Fabre, J. Michel and Y. Baudet, Proc. 12th Photovoltaic Specialists Conf. IEEE, New York, 1976, p. 904.

96. Y. Malda, Appl. Phys. Lett. 33, 301 (1978).

97. S. Kar, S. Varma and S. Bhattacharya, Proc. 13th Photovoltaic Specialists Conf. IEEE, New York, 1978, p. 667.

98. E. J. Charlson and W. F. Richardson, Proc. 13th Photovoltaic Specialists Conf. IEEE, New York, 1978, p. 656.

99. J. P. Ponpon and P. Siffert, J. Appl. Phys. 47, 3248 (1976).

100. R. J. Stirn, U.S. A. Department of Energy Advanced Materials, R & D Branch Review Meetings, Washington, D.C. April 1978.

101. R. J. Stirn, Y.C.M. Yeh, E. Y. Wang, F. P. Ernest, and C. J. Wu, Technical Digest International Electron Device Meeting, IEEE, New York, 1977, p. 48.

102. H. J. Hovel, Proc. 10th Voltaic Specialists Conf. IEEE, New York, 1973, p. 34.

103. M. Wolf, G. T. Noel and R. J. Stirn, IEEE, Trans. ED-24, 419 (1977).

104. J. Kukulka, J. Schewchun, A. Kazandjian and D. Burk, Proc. 13th Photovoltaic Specialists Conf. IEEE, New York, 1978, p. 268.

105. P. Viktorovitch, G. Kamarinos, P. Even and E. Fabre, Phys. Stat. Sol. (a), 48, 137 (1978).

106. P. T. Landsvert and C. Klimpke, Proc. R. Soc. Lond. A354, 101 (1977).

107. J. M. Hess, P. H. Nguyen, B. Lepley and S. Ravelet, Phys. Stat. Sol. (a) 46, K55 (1978).

108. B. Pellegrini, J. Phys. D., Appl. Phys. 9, 55 (1976).

109. Handbook of Chemistry and Physics, CRC Press, 53rd Edition, p. E72.

110. R. Singh, K. Rajkanen and J. Shewchun, Proc. Onternational Topical Conf. on the Physics of SiO_2 and its Interfaces, Academic Press, New York, 1978, p. 396.

111. S. I. Raider and R. Flitsch, J. Vac. Sci. Technol. 13, 58 (1976).

112. R. A. Clarke, R. L. Tapping, M. A. Hopper and L. Young, J. Electrochem. Soc., 122, 1347 (1975).

113. W. L. Harrington, R. E. Honig, A. M. Goodman and R. Williams, Appl. Phys. Lett. 27, 644 (1975).

114. J. Blanc, C. J. Buiocchi, M. S. Abrahams and W. E. HAm, Appl. Phys. Lett. 30, 120 (1977).

115. P. Offerman, J. Appl. Phys. 48, 1890 (1977).

116. C. R. Halms, C. M. Garner, J. Miller, I. Lindan, S. Schwarz and W. E. Spicer, IEEE Trans. on Electron Devices, ED-24, 1208 (1977); J. S. Johannemen, W. E. Spicer and Y. E. Strausser, J. Appl. Phys. 47, 3028 (1976).

117. T. H. Distefano, J. Vac. Sci. Technol. 13, 856 (1976).

118. T. W. Sigmon, W. K. Chu, E. Lugutto and J. W. Mayer, Appl. Phys. Lett. 24, 105 (1974).

119. R. Williams and A. M. Goodman, Appl. Phys. Lett. 25, 531 (1976).

120. O. L. Krivanek, T. T. Sheng and D. C. Tsui, Appl. Phys. Lett. 32, 437 (1978).

121. H. R. Philipp, J. Phys. Chem. Solids, 32, 1935 (1971); J. of Non-crystalline Solids 8-10, 627 (1972).

122. M. Hirose, S. Hiraki, T. Nakashita and Y. Osaka, Japanese J. Appl. Physics, 14, 999 (1975).

123. B. E. Deal, J. Electrochem. Soc. 121, 198C (1976).

124. A. Goetzberger, E. Klausmann, M. J. Schulz, CRC Critical Reviews in Solid State Sciences, 6, 1 (1976).

125. W. M. Werner, J. Electrochem. Soc. 123, 540 (1976).

126. Proc. of the Third International Symposium on Silicon Materials Science and Technology, Semiconductor Silicon, 1977, edited by H. R. Huff and E. Sirte ECS, Proc. Volume 77-2, p. 276, 1977.

127. D. J. Breed and R. P. Kramer, Solid St. Electron. 19, 897, (1976).

128. E. Arnoed, J. Ladell and G. Abowitz, Appl. Phys. Lett. 13, 413 (1978).

129. H. C. Card, IEEE Trans. on Electron Devices, ED-23 538 (1976).

130. L. A. Kasprzak, R. B. Laibowitz and M. Ohring, J. Appl. Phys. 48, 4281 (1977).

131. H. F. Wolf, Semiconductors, Wiley-Interscience, New York, 1971, p. 336.

132. S. W. Ing, Jr., R. E. Morrison and J. E. Sandor, J. Electrochem. Soc. 109, 221 (1962).

133. E. F. Duffek, E. A. Benjamini and C. Myerbie, Electrochem. Technol. 3, 75 (1965).

134. V. I. Prokhorov and L. M. Sorohin, Inor. Matter 9, 28 (1973).

135. J. C. Maxwell Grrnett, Roy. Soc. Phil. Trans. A203, 385 (1904).

136. H. C. Kroemmer, Crit. Rev. Solid State Sci. 5, 555 (1975).

137. J. Thornton and V. Hedgecoth, J. Vac. Sci. Technol. 13, 117 (1976).

138. J. Fan and F. Bachner, J. Electrochem. Soc. 122, 1719 (1975).

139. P. A. Iles, J. Vac. Sci. Technol. 14, 1100 (1977).

140. J. S. Johannessen, W. E. Spicer and Y. E. Strausser, J. Vac. Sci. Technol. 13, 849 (1976).

141. G. Dearnally, Appl. Phys. Lett. 28, 244 (1976).

142. C. T. Sah, R. N. Noyce and W. Schockley, Proc. IRE, 45, 1228 (1957).

143. W. G. Haines and R. H. Bube, J. Appl. Phys. 49, 304 (1977).

144. R. Singh, T. N. Bhar, J. Shewchun, and J. J. Loferski, "Effect of Grain Boundaries on the Performance of Tunnel MIS Solar Cells" Accepted for publication in J. Vac. Sci. Technol.

145. J. O. B. Wilson and P. Robinson, Solid St. Electron. 21, 489 (1978).

146. M. A. Green, Solid State Electron. 20, 265 (1977).

147. D. L. Pulfrey, Solid State Electron. 21, 519 (1978).

148. C. Jacobini, C. Canali, G. Ottaviani and A. Albergi Quaranta, Solid State Electron. 20, 77 (1977).

149. P. P. Debye and E. M. Conwell, Phys. Rec. 93, 693 (1954).

150. Y. P. Varshni, Physica 34, 149 (1967).

151. M. Wolf, Silicon Semiconductor Data, Pergamon Press, New York, 1969, p. 178.

152. Handbook of Chemistry and Physics, CRC Press, 53rd Edition, p. F-168.

153. R. Singh, J. Shewchun, M. Spitzer and D. Burk "Operation of the Semiconductor-Insulator-Semiconductor Solar Cell: Intensity Dependence", submitted for publication in Solid-St. Electron.

154. J. Shewchun, D. Burk, R. Singh, M. Spitzer and J. Dubow, "The Semiconductor-Insulator-Semiconductor (Indium Tin Oxide-on-Silicon Solar Cell): Characteristics and Loss Mechanisms". Accepted for publication in J. App. Phys.